Visualization of Complex Hydrocarbon Reaction Systems

John H. Shinn, Chevron Research and Technology Company, Richmond, CA 94802

Abstract

Many hydrocarbon reactions of interest involve either poorly characterized reactants and products and/or large numbers of simultaneous reactions. An important step in understanding the behavior of such systems is to develop quantitative pictures of the feeds and products and the transformations which connect them. The processes for constructing these reaction visualizations is illustrated by examining the construction of a molecular model for coal liquefaction and subsequent conversion to distillate products, and the construction of a video simulation of catalytic petroleum naphtha reforming. New techniques which are permitting advances in these visualizations are discussed.

Introduction

When studying feedstocks such as coal or reactions such as those used in converting petroluem to commercial products one must confront an overabundance of information concerning chemical composition and molecular transformations. The essential features which govern the behavior of a material or process may be lost in the detail. In such cases, the production of a simple picture, or visualization can be important.

Visualizations can have many values including:

- **-identifying major deficiencies in knowledge**
- **-highlighting the most important aspects of the structure or reaction system** which control reaction behavior, and those which are of relatively minor importance
- **-setting the stage for more quantitative tools** such as predictive kinetic models used in process optimization and control
- **-training**
- -as a **basis of comparison** between the composition of similar materials or the reactions of similar feedstocks
- **-to stimulate discussion** creating focus on controversial aspects of the knowledge.

Over the past 15 years, we have been utilizing visualizations to examine several complex reactions systems. In this paper, we provide a review of the process of creating quantitative reaction visualizations and review their use. We will use as examples the construction of models of coal and coal liquefaction and in a video model of catalytic naphtha reforming.

Making a Quantitative Visual Model - Model of Coal and Coal Liquefaction

The first step in assembling a visual model is to collect available information on composition and reactivity. In the case of coal structure, such information includes the proper distribution of elements, element groups, aliphatic and aromatic carbon species, functional groups (oxygen, sulfur and nitrogen), and reactive crosslinks. Knowledge of the reaction chemistry is critical in providing the glue which binds the structures together in a manner which may be used to simulate reaction behavior.

Quantitative reaction models require information on product yields and quality at many stages of reaction, so that the progressive steps in conversion can be illustrated. By assembling composition information on the feedstock and each of the intermediate products, one constructs structures which are consistent with this information at each severity level. The product distribution at the most mild reaction conditions may be used in conjunction with knowledge of the important reaction processes to feedback information to the necessary structures which must be present in the feed to explain the appearance of the products. In the case of mild coal liquefaction, the processes of aliphatic and etheric crosslink cleavage between aromatic centers, the hydrogenation/dehydrogenation and associated hydrogen transfer reactions, and functional group distribution changes (particularly dissappearance of reactive oxygen functional groups) have long be attributed to as the primary important reaction paths. A likely representation assumes that the original coal structure contains components similar to those in the products of

mild liquefaction, modified by hydrogen transfer and defunctionalization, and joined by certain reactive crosslinks. In a similar manner, the products and reactions from somewhat more severe processing may be used to imply the structures of the less severe products forming an iterative chain connecting the products of most severe treatment with the structure of the original feed.

To maintain a quantitative picture, the molar quantities of elements, functional groups, aromatics and aliphatics and the like are continuously accounted for throughout the transformation. Choosing the molecular size of the model is also critical - for coal the size of 10000 daltons proved a good compromise. This provided us with a model which was both large enough to represent the variations in product composition which are observed and to include sufficient quantities of crosslinks and functional groups to characterize the feed properly. Larger models required a far more complex task of construction and resulted in a loss of detail in the overall mass. Smaller models would not permit incorporation of product distribution detail and reactivity which are important in liquefaction behavior.

Figures 1 and 2 show models of a subbituminous and a bituminous coal produced in the manner described above. The models are quantitative in terms of the elemental distributions, aromatic and aliphatic components and functional groups as collected from composition and reaction data. The visualizations allow for a quick comparison between the two coals highlighting similarities and differences. Both illustrate a relatively low degree of aromatics condensation (in comparson to heavy crude oils, for instance) and although differences in the distribution of aromatics exist between the two, these features are relatively minor. The role of oxygen in the chemistry of both is apparent : oxygen is prevalent throughout the structure as crosslinks and ring substituents and multiple opportunities for hydrogen bond formation are seen, especially in the bituminous coal. Clearly any consideration of the reactions of these coals without including oxygen would be insufficient. At the time that these models were constructed, very little information was available on the detailed distribution of much of the oxygen, particularly the ether oxygen. Thus the percentage of ether oxygen present in important structural crosslinks, and the nature of non-crosslink ethers is seen as an important uncertainty in coal structure. For both of these coals, sulfur and nitrogen are seen to play relatively unimportant roles (with only a handful of each element in the 10000 dalton model), at least so far as their importance in the overall structure is concerned.

These models are presented in planar form with the intention of allowing for better visualization of the chemical connectivity. In reality, coal is a three-dimensional structure. Recent advances have allowed construction of more sophisticated models utilizing molecular dynamics to provide energy minimized three dimensional structures. Such models are far superior in representing the constraints imposed by spatial and energetic considerations and provide better tools for examination of three dimensional properties such as density and porosity.

Figures 3 and 4 show the progressive conversion of the bituminous coal via donor solvent liquefaction. The reactive crosslinks are disrupted and products of various functionalities, aromaticities and molecular sizes are generated. With more severe processing, both forward and reverse reactions occur leading to both smaller and larger products. Even at relatively severe conditions, these liquefaction products are substantial in molecular size and contain a significant amounts of heteroatom species (particularly oxygen). Figure 5 shows the products from two-stage liquefaction employing a thermal donor solvent stage and a catalytic hydrotreating stage in close sequence. The comparison of figures 4 and 5 provides a rapid visual sense of the advantages of two-stage technology. In contrast to the solvent products, the two-stage products are of far reduced molecular size and dramatically reduced heteroatom content.

Construction of a Model of Catalytic Naphtha Reforming

The process of catalytic naphtha reforming is an essential feature of the production of high quality gasoline components from crude oil. In reforming, a feedstock consisting entirely of hydrocarbons (no heteroatoms) of carbon numbers typically between C6 and C12 are processed over a catalyst (platinum-rhenium on alumina, for instance) to convert species having a low gasoline octane rating to species with improved octane values. The principal desired reactions involve the dehydrogenation of naphthenes and the dehydrocyclization of paraffins to produce aromatic species. Side reactions of cracking, hydrocracking, and isomerization occur with the desired reactions.

Modeling reforming reactions is complex because many species are reacting simultaneously via many potential reaction paths. Unlike liquefaction, the individual species in reforming can be largely identified using relatively straightforward techniques. The difficulty lies in understanding the balance of reactions occurring for each species, the relative contributions of the reactions for the different feed molecules, and in understanding how to control the reaction to provide the highest yields of desired products.

The process of producing a visualization of the reforming reactions involves many of the steps outlined in construction of the coal models: Namely, collecting detailed information on product composition at various levels of reaction severity and iterating back to the prior composition and reaction changes via information on the reaction matrix allow the transformation model to be constructed. Figures 6 and 7 show a quantitative represenation of the feed and products from the reforming of an Arabian naphtha. Even for the relatively mild reforming to a product octane of 81, there has been considerable production of aromatic species and conversion of most of the naphthenes. Heavy paraffins have also been converted, substantial hydrogen has been produced and some of the product has been converted to undesired light gases. Relatively few reactions are needed to explain the product distribution shifts, beyond the dominant roles of dehydrogenation, dehydrocyclization and cracking.

For the reforming visualization, we were interested in producing a tool to enhance the training of new operators and engineers involved in commercial reformer operation. We extended our visualization by creating individual 'snapshots' of the composition at various ranges of severity, taking the reactions one group at a time. These snapshots were then assembled using computer drawings and video tape and assembled into a video depicting the entire sequence of reactions. We have found this video visualization can provide an excellent overall feel for the process of reforming in a very short period of time.

Visualizing - the Future.

A number of emerging tools are permitting visualizations to be created with greater ease, high detail, greater accuracy, and with better ability to serve the valuable roles of visualizations outlined above. These tools include:

-Computational tools for representing molecular connectivity permitting construction of models on a computer platform.

-Use of molecular dynamics software to produce energy-minimized three-dimensional structures.

-Use of quantum mechanical simulations to predict reaction pathways from molecular energetics, reducing the need for experimental determinations of reaction paths and rates.

-Monte-Carlo approaches to assembling possible structures from component pieces and for displaying a full range of potential structures from multiple possibilities.

-Advances in compositional capability permitting models of greater molecular detail.

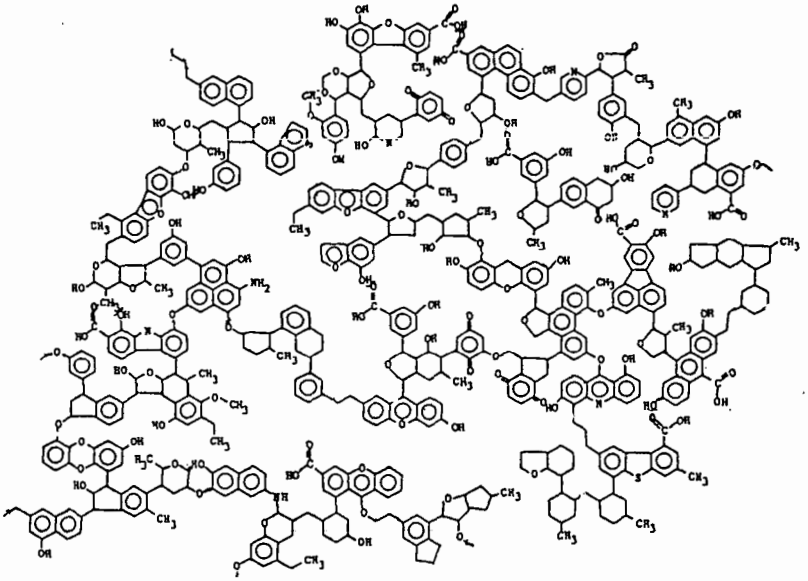

Figure 1. Model of Subbituminous Coal Structure

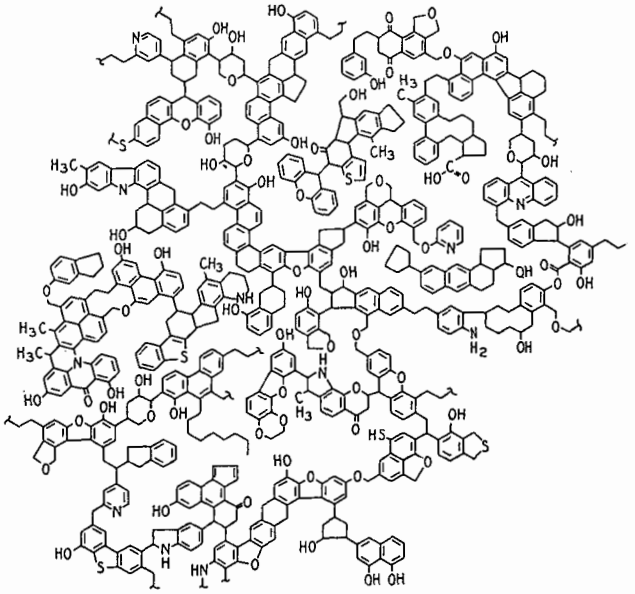

Figure 2. Model of Bituminous Coal Structure.

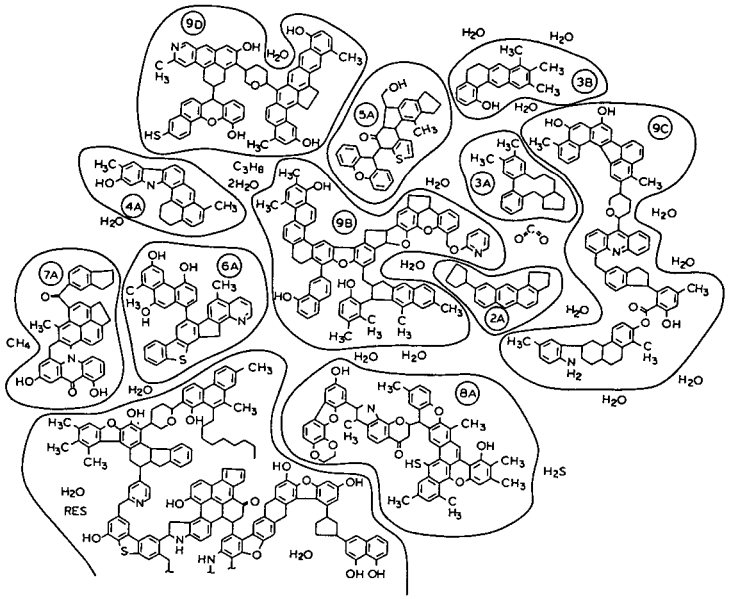

Figure 3. Model of Products from Mild Donor Solvent Liquefaction of Bituminous Coal

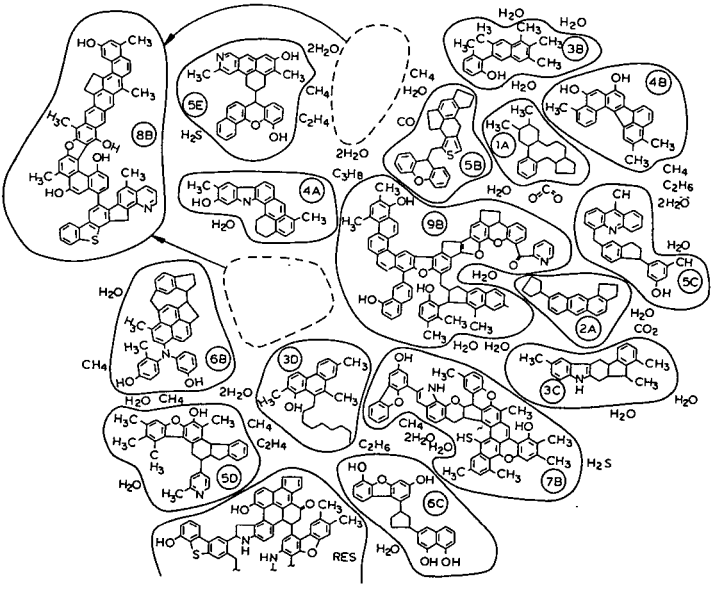

Figure 4. Model of Products from Severe Donor Solvent Liquefaction of Bituminous Coal

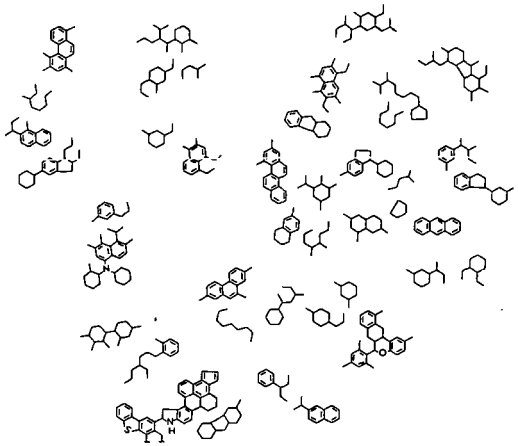

Figure 5. Model of Products from Two-Stage Liquefaction of Bituminous Coal

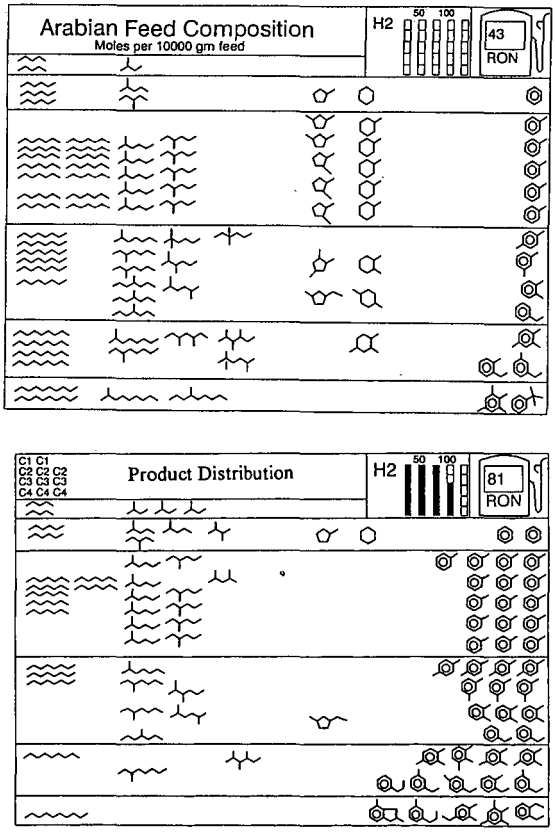

Figures 6 and 7. Feed and Products from Mild Reforming of an Arabian Naphtha.

Feasibility and Status of Coal Gasification Combined Cycle Plant in JAPAN

S. Uchida,O. Shinada,T.Furuya
Power Systems Headquaters
Mitsubishi Heavy Industries, Ltd.
3-1 Minatomirai 3 chome Nishi-ku Yokohama, JAPAN

Keywords:Coal gaifier,Combined cycle,Thermal efficiency

1.Introduction

Integrated Gasification Combined Cycle (IGCC) is regarded as the most powerful candidate for new coal firing power plant in the next generation, because of the following two points: it has a significantly high net thermal efficiency of 46-50+% which can be achieved by increasing the gas turbine inlet temperature, and it maintains superior environmental performance attained by means of a conversion process from "dirty" coal to "clean" purified gas and the disposal of glassy slag ash.

IGCC R&D in JAPAN is being carried out as a part of the "Sunshine Project", a national project concerned with promoting the use of new energies. The Ministry of International Trade and Industry(MITI) had started the IGCC R&D project in 1974 , to focus on a fluidized bed coal gasifiers. In 1986, MITI commissioned the New Energy and Industrial Technology Development Organization(NEDO) to restart an IGCC R&D project using an air blown entrained bed coal gasifier at the NAKOSO 200 ton/day pilot plant, the over all plant project schedule is shown in Figure 1.

This project, now in its final stage of the test operation, was in 1991 entrusted to the IGC Research Association by NEDO. The essential technologies for IGCC have been verified at this pilot plant through the achievement of a month of stable and continuous operation in March, 1995.

This air blown entrained bed gasification concept is more suitable for power generation as compared to the oxygen blown ones developed mainly for chemical plants in Europe and the USA, air blown ones do not require large amounts of the auxiliary power to produce oxygen (See Table 1). However, the air blown entrained bed gasification had several fault to its operation and was, therefore, never successful until our first success in April, 1995.
Due to its successful results, Mitsubishi has newly designed an IGCC system,"THE IGCC system ", which provides the highest net thermal plant efficiency and environmental benign in a cost-effective manner.

2. Results of the 200 ton/day air blown entrained bed coal gasification pilot plant operation

2.1 Outline of the 200 ton/day pilot plant

A schematic diagram of the pilot plant's system is shown in Figure 2. This plant, mainly consists of the air blown gasifier (gasifying 200 ton/day of coal), the hot and dry gas clean-up unit and the low calorie coal gas fired gas turbine (12.5MWe of capacity). The gas turbine can be tested and the performance, operational flexibility, reliability, and durability of the air blown IGCC technologies can be verified. Dry gas clean-up is composed of two parallel systems, one is a granular bed gas filter and fluidized bed desulfurization system, and the other is a candle ceramic filter and fixed bed honeycomb desulfurization system. MHI is in charge of supplying the air blown 200 ton/day gasifier, the fixed bed hot and dry gas clean-up unit and the testing stand for the full pressure and full scale gas turbine combustor.

MHI's fixed bed hot and dry gas clean-up unit is composed of a dust removal system made of a porous ceramic filter and honeycomb shaped stationary oxidized iron desulfurization unit. This system is of a significantly compact size and is completely water free. Its superior clean-up performance under high gas temperature conditions of 350~450℃ enables the effective use of sensitive heat from coal gas to be used as the gas turbine heat input. The handling system including valves, pipes and controls have been greatly simplified, as there are no moving materials, increasing system reliability and economy.
As of September 1995, the accumulative operating hours of the gasifier and the fixed bed clean-up exceeded 3800 hours and 1200 hours respectively, including the one month continuous operation of 789 hours.

It has successfully performed with the satisfactory results. The testing at the pilot plant will be completed by the end of March, 1996.

2.2 Results of the One Month Reliability Test

The 200 ton/day gasifier had achieved one month of continuous operation totaling 789 hours (about 33 days) from 3rd March to 5th April 1995. During this test period, the operation of the gasifier had been continuously stable, and the testing was completed according to the planned schedule. Table 2 shows the major operating parameters of the gasifier during this test.
It was confirmed that the gasifier can maintain sufficiently high heating values to produce coal gas for stable combustion in the gas turbine and also keep discharging continuously molten slag through the slag hole with 100% recycling of char.

Collected data shows superior performance of air blown gasification. 70% of cold gas efficiency, 99.9% of carbon conversion efficiency were obtained, and passes the highest net thermal plant efficiency at any demonstration plant. All of the ash in the coal fed to the gasifier is converted to non-leaching and compact glassy slag with negligible small unreacted carbon, thus enabling simple ash handling and economical ash disposal without fly ash, including unreacted carbon.

The fixed bed gas clean up test facility of a size of 20 ton/day had also achieved 765 hours of continuous operation during the same period of the long term reliability test operation as the 200 ton/day gasifier. This test shows 1~5 mg/Nm^3 of dust concentration and 20~50 ppm of sulfur content (H_2S,COS) at the outlet of the clean-up and the durability of the ceramic filter element, the oxidized iron desulfurization agent and the whole system.
Instead of elemental sulfur recovery system, gypsum recovery system under pressurized condition had been tested in the pilot plant.
Another advantage of this fixed bed clean-up equipment is the easiness to scale-up its capacity, because of the simple scale up criteria that requires that only the quantity of the element to be increased in accordance with the gas flow.

4. Mitsubishi IGCC system(THE IGCC system)

Based on the successful results of the 200 ton/day pilot plant, the base data for scaling-up to a 2000 ton/day class demonstration plant were able to be achieved.
The IGCC may be a more complicated system when compared to conventional fossil plants, so system integration and simplification is very important. Since MHI can supply all the key components of IGCC, MHI can drastically simplify the system based on an optimized integration among the interdependent main component and under a single responsibility.
The feasibility study on THE IGCC system has been executed, and details its superior performance and economical feasibility.

THE IGCC system is composed of the air blown two stage gasifier , the fixed bed dry gas

clean-up unit and the 1300℃ or 1500℃ class gas turbine, 701F or 701G (for 50 Hz use) and 501F or 501G (for 60 Hz use).

Adopting the fixed bed gas clean-up system, which is very compact in size and water-free, contributes to the simplicity of the whole plant system and a significant reduction of plant area. The small sized air separation unit (ASU) is installed in order to produce nitrogen as an inert gas for pressurized coal/char handling and seal gas at the gasifier. The remaining oxygen at ASU is mixed with air in the gasifier, so that the oxygen concentration in the gasifier will be 25 vol.%.
The predicted performance data is indicated in Table 3.

The net thermal efficiency of THE IGCC system is predicted to be 46~50+ LHV% It achieves a 20% reduction in the CO_2 gas emission with super critical steam condition compared with conventional pulverized coal firing power plants.
The SOx/NOx emission at the stack inlet is anticipated to be 10 ppm and the dust concentration is predicted to be less than 1 mg/Nm^3 at the inlet of the stack.
MHI is also ready to supply large capacity coal gas fired gas turbines. MHI has the proven technologies of the 1300℃ class natural gas fired gas turbines, the 1250 ℃ class blast furnace gas (BFG gas) fired gas turbines and is presently designing the 1500℃ class natural gas firing gas turbines.
MHI has also conducted coal gas firing test with the full pressure and full scale test stand of a gas turbine combustor at the 200 ton/day pilot plant. Its capacity corresponds to one can of the gas turbine for utility use. This test shows stable combustion at a low NOx conversion rate of 30~40 % (at 1000ppm of NH$_3$), which is required for the combustion of ammonia rich coal gas.
The gasifier and the gas clean-up unit can be arranged in a single steel structure. The required plant area per power output is reduced by 20% in comparison with conventional coal fired power plants.
The capital cost estimation of THE IGCC system executed at the feasibility study predicts 95% at the commercial phase when compared to conventional coal fired power plants. Consequently, THE IGCC system offers economical feasibility in the generation cost equivalent to that of the existing coal fired power plant.

5. Conclusion

The successful results of the R&D at the 200 ton/day pilot plant have verified the IGCC technologies of the air blown two stage coal gasifier and the fixed bed gas clean-up. The development of air blown IGCC has stepped up to the demonstration phase. The Mitsubishi IGCC system, composed of these technologies, is able to realize the highest net thermal efficiency and environmental benign in a cost-effective manner.

Reference :

[1] H. Ishikawa, T. Hamamatsu, H. Moritsuka, T. Toda ,S. Ishigami ,T.Furuya : *"Current Status of IGCC Development in Japan"*, VGB kraftwerkstechnik Vol. 72 No. 5 1992 p.405

[2] T. Toyoda, O. Shinada, S. Kaneko, K. Tokuda : *"Experience of 200 ton/day Coal Gasifier Operation"*, JSME/ASME International Conference on Power Generation '93 Vol. 2 1993 p. 538

[3] Takahata : *"Development of the 200 ton/day entrained coal gasification pilot plant"*, Proc. 4th The Japan Institute of Energy Congress No. 7 1995 p. 180

[4] S. Kaneko,T. Hashimoto,T. Huruya,S,Uchida,A,Hashimoto : *"Operation Experience with Air Blown 200ton/day Entrained Bed Coal Gasifier"* POWER GEN in 1996

TYPE	Gasifying Agent		Coal Feed		Gas Clean-up		Thermal Efficiency
	Air	Oxygen	Dry	Wet	Dry	Wet	
NEDO/IGC/MHI	○		○		○		High
Oxygen Blown Type A		○	○			○	Medium
Oxygen Blown Type B		○		○		○	Medium

Table 1 Comparison of IGCC System

	Unit	Plan	Result
Coal Gas Calorie (HHV)	kJ/m³N	4,150	4,200~4,600
Coal Gas Flow	T/hr	50.2(at 100%LOAD)	40(75%)~50(100%)
Sulfur Concentration (Inlet)	ppm	<1,500	570~670
Sulfur Concentration (Outlet)	ppm	<100	20~50
Dust Concentration (Inlet)	mg/ m³N	<3,000	180~230
Dust Concentration (Outlet)	mg/ m³N	<10	~1.1

Table 2 One Month Continuous Operation Data of the Pilot Plant

	Unit	Demonstration Plant		Commercial Plant	
Target	year	2000		2010	
Cycle	Hz	50	60	50	60
Gasifier	-	Air Blown Two Stage Entrained Bed Type			
Capacity	t/day	2,400	1,700	3,100	2,300
Dust Removal	-	Porous Ceramic Filter Type			
Desulfurization	-	Honeycomb Fixed Bed Type			
Gas Turbine	-	701F	501F	701G	501G
Gross Output	MW	400	275	546	408
Net Output	MW	368	255	510	380
Gross Efficiency	% LHV	46	46	50	50
SOx/NOx Emission	ppm	10/10			
Dust Emission	mg/m³N	1			

Table 3 Major Specification of THE IGCC system

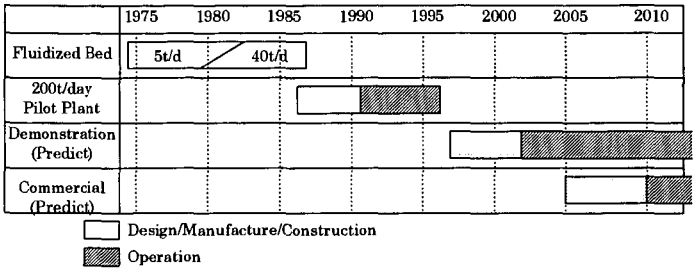

Figure 1 Master Schedule of IGCC Project in JAPAN

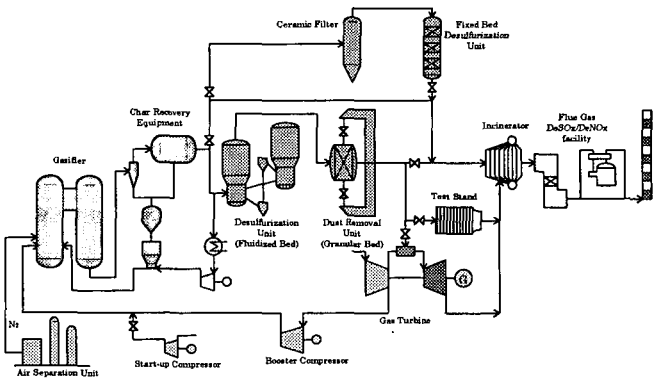

Figure 2 System Flow Diagram of 200ton/day pilot plant

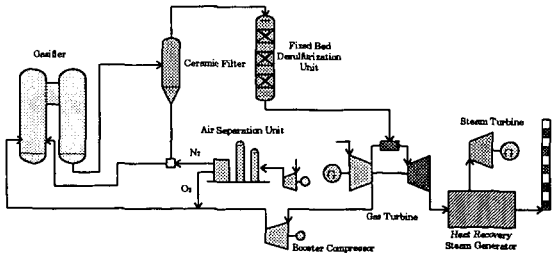

Figure 3 System Flow Diagram of THE IGCC plant

COKING PROBLEMS ASSOCIATED WITH HYDROCARBON CONVERSION PROCESSES

R. Terry K. Baker
Catalytic Materials Center, Materials Research Laboratory,
The Pennsylvania State University, University Park, PA 16802

Keywords: coke formation, coke mitigation, catalytic carbon, metal catalysts

ABSTRACT

The understanding of the factors controlling the deposition of carbonaceous solids resulting from the decomposition of hydrocarbons over hot metal surfaces has a considerable impact on a number of commercial processes including, catalytic steam reforming of methane, steam cracking of paraffinic feed stocks and systems involving carbon monoxide disproportionation reactions. The potential for carbon formation exists in any system in which hydrocarbons undergo thermal decomposition and it is well known that certain metals can increase the overall rate of this process by catalyzing the growth of filamentous and graphitic types of deposit. The highest catalytic activity for carbon deposition is exhibited by iron, cobalt and nickel, and alloys containing these metals. In this paper a review of the information obtained from the use of a combination of controlled atmosphere and high resolution transmission electron microscopy techniques to study the dynamics of carbon deposition arising from the metal catalyzed decomposition of hydrocarbons will be presented.

INTRODUCTION

A number of review articles have highlighted the complex nature of carbon deposits produced during hydrocarbon decomposition reactions [1-6]. The major constituents of a typical carbonaceous solid that might accumulate on a metal surface, either in the form of a tube or as a particle dispersed on a support medium, can be divided into three main classes: amorphous, filamentous and graphitic platelets. During a traditional routine analysis of a contaminated reactor vessel or a spent catalyst, these three forms of carbon would not be necessarily distinguished, but merely referred to collectively as "coke". Available evidence indicates that the amorphous carbon component is formed via condensation and polymerization reactions and this material originates from thermal processes. It is conceivable that a significant amount of hydrogen is incorporated in the deposit, however, as the temperature is raised dehydrogenation reactions will tend to reduce the hydrogen content. There is now a general consensus that the formation of the filamentous and graphitic forms of carbon require the participation of a catalytic entity that usually operates in a particulate form.

The mechanism commonly accepted to account for the observed characteristics of the steady-state growth of carbon filaments from the metal catalyzed decomposition of carbon-containing gases involves the following steps [7-9]:

(a) adsorption of reactant gas molecules at particular faces of the metal particle followed by decomposition to generate carbon species, and

(b) dissolution in and diffusion of carbon species through the metal particle to a different set of faces that favor precipitation of carbon in the form of a fibrous structure.

The latter set of faces control not only the degree of crystalline perfection of the deposited carbon filament, but also the conformational characteristics of the material. A consequence of this phenomenon is that certain metal faces will remain free of deposited carbon and therefore, available for continued reaction with the hydrocarbon.

While the rudiments of the formation of the graphite platelet deposit have not received the same attention as that devoted to the growth of filamentous carbon it is probable that many of the steps outlined above are also operative in the formation of this type of carbon. Nolan and coworkers [10] reported that graphite, in the form of a shell structure surrounding a metal particle core, was the exclusive type of deposit produced from a carbon monoxide reactant containing no added hydrogen. They observed that the limiting thickness of the graphite shells was about 30 layers, and that this parameter was dependent on the lifetime of the metal catalyst particles. Based on these findings, they argued that the growth of graphite layers did not occur via a mechanism that involved precipitation of carbon from the surface of the metal. These claims were in direct conflict those of earlier studies [11-13] that clearly demonstrated that precipitation was the key step in the formation of graphite.

CHARACTERIZATION OF CARBON DEPOSITS

Before proceeding further it is worthwhile to consider the relative rates of the formation of these three types of carbon as a function of reaction temperature and the plot, Figure 1 provides an indication of the typical composition of the "coke deposit" that one might

expect under various conditions from the interaction of a metal with a hydrocarbon environment. It can be seen that for reactions conducted between 400 to 650°C, the composition of the deposit will tend to consist of a large fraction of filamentous carbon and when such reactions are allowed to proceed for a prolonged period of time the fibrous structures will undergo a thickening process due the accumulation of an amorphous carbon coating. A further ramification of this sequence of events is that the growth of filamentous carbon on a reactor tube wall provides a high surface collection site for trapping the amorphous carbon constituent and this combination effectively produces a very strong composite material. At temperatures in excess of 750°C the contribution of carbon filaments to the overall deposit will tend to decline while that of amorphous carbon will exhibit a steady increase and the emergence of the graphite platelet constituent will become evident.

The details of the growth kinetic aspects of individual carbon filaments was elucidated a number of years ago from quantitative analysis of the dynamic events captured on video-tape from experiments performed in the controlled atmosphere electron microscope. From measurements of the rate of increase in length of similar width structures as a function of temperature it was possible to evaluate apparent activation energies for the growth of filaments from various metal catalysts. The important aspect to emerge from this exercise was that from the accumulated data Baker and coworkers [7] were able to develop a mechanism that accounted for several of the growth characteristics and also established that the rate controlling step in the process was carbon diffusion through the catalyst particle. In more recent years [14-17] it has been recognized that the structural perfection of the deposited carbon solid is a parameter that is governed by the nature and shape of the catalyst particle and crystallographic orientation of the precipitating faces as shown schematically in Figure 2a-2c. In addition, symmetrical diffusion of carbon species through the particle will give rise to a relatively straight structure. In contrast, when certain additives are present in the metal particle the diffusion characteristics are modified and this factor causes a non-balanced process that results in the formation of coiled structures.

METHODS OF INHIBITING CATALYTIC CARBON FORMATION

The realization that the chemical and physical nature of metal particles plays a key role in catalyzing the growth of the filamentous form of carbon and that this material is also responsible for providing a very efficient method of trapping other types of deposit has lead to a number of approaches designed to inhibit its formation. These methods have tended to fall into the categories of either coating treaunents of the metal surface with inert materials or the addition of selected compounds to the gas phase that might be expected to poison the activity of the metal towards catalytic carbon formation. From a consideration of the investigations that have been carried out, it is possible to establish a classification for the roles of various additives on the inhibition of filamentous carbon growth [18].

(a) There are some materials that merely provide a physical barrier towards hydrocarbon adsorption and subsequent decomposition on the metal surface, but during repeated temperature cycling tend to spall and the coating loses its effectiveness. e.g. Al_2O_3, B_2O_3

(b) Other additives reduce carbon solubility in the metal catalyst, but have no effect on the carbon diffusion characteristics through the particle, e.g. MoO_3, WO_3 and Ta_2O_5

(c) There are cases where an additive can reduce both the solubility of carbon and its diffusion through the metal particles, e.g. SiO_2, and finally,

(d) There certain electro-negative elements that when introduced into the either as a pre-treatment or on a continuous basis, effectively modify the chemistry of the metal surface so that it can no longer function as a catalyst to dissociatively chemisorb the carbon-containing gas molecules, e.g. sulfur, phosphorus and halides.

ISSUES THAT NEED TO BE ADDRESSED WITH REGARD TO CATALYTIC CARBON DEPOSITION

When one examines the ramifications of filamentous carbon formation under conditions where such structures are produced on either a metal tube surface or on isolated metal particles supported on a carrier material there are a number of questions that at point in time have not been satisfactorily answered. It is not clear whether these fibrous structures merely function as a high surface collection site or if they perform a catalytic function in being able to promote the formation of amorphous carbon from interaction with gas phase reactants. One might also offer a counter argument that an enhancement in the formation of the amorphous carbon component could effectively form a physically blockage of the metal surface, thereby inhibiting its catalytic action with respect to growth of filamentous carbon. A further factor could have a significant impact on the particular hydrocarbon conversion process is the possible impact of the fibrous material on the mass flow of reactants under either gas or liquid phase conditions.

Other potential problems center around the identity and fate of metal particles that perform the catalytic function. While we have established which metals are the most catalytically active for the growth of filamentous carbon there are still unsolved mysteries surrounding the precise influence of small amounts of a second metal. The addition of very small amounts of silver, tin, or copper to nickel, iron or cobalt can result in a dramatic increase in the ability of the ferromagnetic metal to catalyze the growth of filamentous carbon. Under a typical commercial reactor condition one must be aware that the likelihood of introducing impurity species into a host metal is extremely high and this behavior could have catastrophic effects on the carbon deposition process. Finally, it is imperative that we are able to determine the influence, if any, of the metallic inclusions in the deposit on the subsequent decoking step. It would be pertinent to ask whether such species function as catalysts for the removal of carbon and under these circumstances what is the fate of the metal particles following the gasification reaction. The ramifications of the difference in behavior of metal particles associated with filamentous carbon during reaction in oxygen is depicted in Figure 3. In the case where the metal facilitates the removal of carbon the particle returns to the original location on the support medium. In contrast, where gasification proceeds without the participation of the metal, then there is a high probability will eventually be swept out of the system by the reactant gas stream. In this context it might be worthwhile in certain reaction systems to consider introducing additives during the decoking cycle that are known to be good catalysts for the carbon gasification step and that are either benign towards carbon deposition or can easily be removed prior to re-introduction of the hydrocarbon feed.

SUMMARY

In conclusion, it is clear that significant improvements have been made over recent years with respect to controlling the rate of carbon deposition in a selected number of systems. There is, however, a strong case to be made for attention to be focused on some of the fundamental aspects of this problem so more effective treatments can be developed. One must be mindful that such treatments may not have universal application and it is necessary to be cognizant of a number of prevailing factors when one is attempting to design an inhibition package for a given system. These aspects include, the nature of the metal surfaces and the reactant molecules, the temperature at which contact between these components will occur and some knowledge of the identity and concentration of possible contaminants that may be present, particularly in the gas phase.

ACKNOWLEDGMENTS

A large fraction of the work reported here was carried out under a grant from the United States Department of Energy, Basic Energy Sciences, Grant DE-FG02-93ER14358.

REFERENCES

1. Hofer, L. J. E., in "Catalysis", Vol. 4 (P. H. Emmett.ed.) Reinhold Publishing Co., New York, 1956, p.373.
2. Palmer, H. B., and Cullis, C. F., in "Chemistry and Physics of Carbon", Vol. 1 (P. L. Walker, Jr. ed.), Marcel Dekker, New York, 1965, p. 265.
3. Rostrup-Nielsen, J. R., "Steam Reforming Catalysts", Tekorisk Forlay A/S, Danish Technical Press, Inc. 1975.
4. Trimm, D. L., Catal. Rev.-Sci. Eng. 16, 155 (1977).
5. Baker, R. T. K., and Harris, P. S., in "Chemistry and Physics of Carbon", Vol. 14,(P. L. Walker, Jr. and P. A. Thrower, eds.), Marcel Dekker, New York, 1978, p. 83.
6. Bartholomew, C. H., Catal. Rev.-Sci. Eng.24, 67 (1982).
7. Baker, R. T. K., Barber, M. A., Feates, F. S., Harris, P. S., and Waite, R. J., J. Catal. 26, 51 (1972.
8. Lobo, L. S., Trimm, D. L., and Figueiredo, J. L., in "Proc. 5th Intern. Congr. Catalysis, Palm Beach, 1972" (J. W. Hightower, ed.) Vol.2, North-Holland, Amsterdam, 1973, p.1125.
9. Alstrup, I., J. Catal. 109, 241 (1988).
10. Nolan, P. E., Lynch, D. C., and Cutler, A. H., Carbon 32, 477 (1994).
11. Presland, A. E. B., Roscoe, C., and Walker, P. L., Jr., 3rd.Conf. Ind. Carbon and Graphite, London, 1970.
12. Baker, R. T. K., Feates, F. S., and Harris, P. S., Carbon 10, 93 (1972).
13. Baker, R. T. K., Harris, P. S., Henderson, J., and Thomas, R. B., Carbon 13, 17 (1975).
14. Audier, M., Oberlin, A., Oberlin, M., Coulon, M., and Bonnetain, L., Carbon 19, 217 (1981).
15. Yang, R. T., and Chen, J. P., J. Catal. 115, 52 (1989).
16. Kim, M. S., Rodriguez, N. M., and Baker, R. T. K., J. Catal. 134, 253 (1992).
17. Rodriguez, N. M., Chambers, A., and Baker, R. T. K., Langmuir 11, 3862 (1995).
18. Baker, R. T. K., and Chludzinski, J. J., J. Catal. 64, 464 (1980).

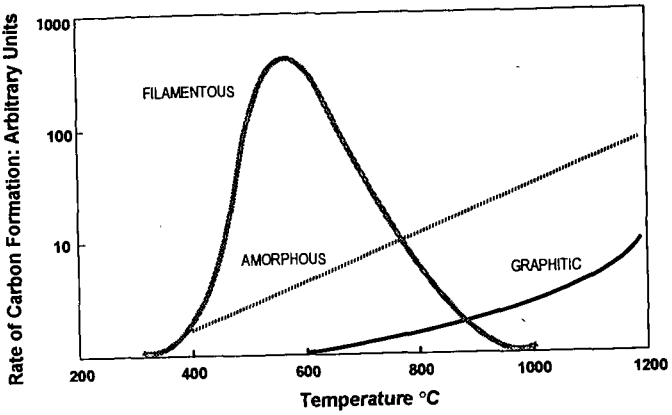

Figure 1. Relative rates of formation of the three types of carbon deposit as a function of reaction T.

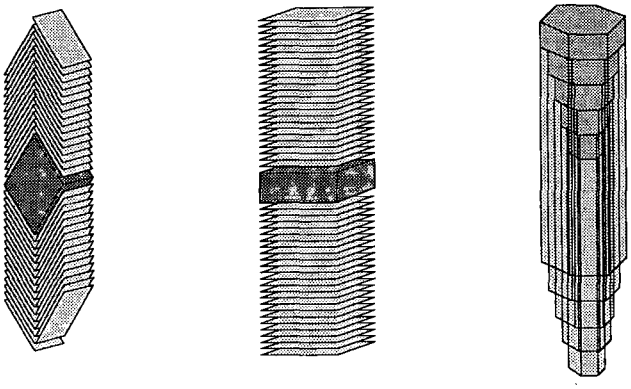

Figure 2. Schematic representation of different types of filamentous carbon structures

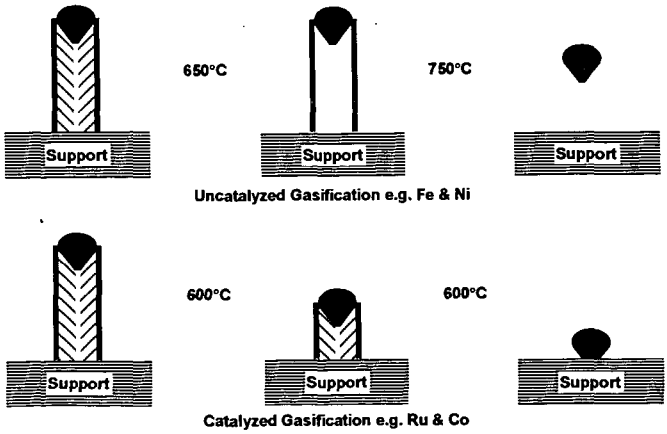

Figure 3. Fates of catalyst particles during gasification of filamentous carbon in O_2

Introduction to Hydrocarbon Conversion Science and Achievements of Professor Isao Mochida

Harry Marsh
Department of Inorganic Chemistry
University of Alicante, Apartado 99
E-03080-Alicante, SPAIN

Background to the studies of I. Mochida

Fossil fuels, such as coal, petroleum and natural gas (methane), although used dominantly as fuels, either by direct combustion, or to power engines, have other significant uses. Coal is carbonized, directly, to produce metallurgical coke and coal-tar from which is derived coal-tar pitch, this material being a precursor to several carbon artifacts. Further, coal can be 'liquefied' to produce acceptable fuels, although the economics for this, currently, are far from favorable. Each of these conversion processes has been studied extensively by Mochida, to produce industrially acceptable materials, and to be able to use, more effectively, raw materials or feedstocks with less and less acceptable specifications, and to improve the overall economy of the conversion processes.

Likewise, it is with petroleum. Crude petroleum is processed by thermal and vacuum distillation, including catalytic systems, to produce a variety of liquid fuels, for gasoline, diesel and aircraft engines, and for space heating. Not all of the barrel can be converted to such high value products. There exists a variety of 'pitch residues' from the conversion processes. Mid-century, these residues would be used either as a fuel, or would be converted to a solid in the so-called 'delayed cokers', the solid 'delayed coke' being itself used as a fuel or disposed of in land-fill operations. Mid-century onwards, after W.W. II, saw a tremendous increase in the use of petroleum, with associated increases in the tonnage of 'pitch residues' which required disposal. However, during this growth process it was realized that these 'pitch residues' could have commercial application, and that their status could be raised to that of a 'by-product'. Thus, the 'delayed coker' became more than a disposal unit, it became specialized equipment to produce the required 'sponge' (or 'regular') cokes and 'needle' cokes. Mochida undertook a massive programme of research into the workings of delayed cokers, and improvements in quality of delayed cokes. Delayed cokes find an irreplaceable use in the manufacture of carbon anodes which are used in the Hall-Héroult cells of the aluminum industry, and the large electrodes of the steel industry, used to transmit electrical energy into the crucibles of steel production.

Personal notes: I. Mochida

Professor Isao Mochida, born in 1944, took his B. Eng. in the University of Tokyo in 1963, with a M. Eng. also from the University of Tokyo, specializing in Linear Free Energy Relationships in Heterogeneous Catalysis. He joined the University of Kyushu in 1968, and currently has the title of Professor: Institute of Advanced Material Study. During these years in Kyushu, Professor Mochida has published 485 Technical Papers, has written 10 Books and has 25 Patents. He spent one year with Professor Harry Marsh, 1977-1978, in the University of Newcastle upon Tyne, U.K. The scientific community has recognized the massive contribution he has already made to the sciences associated with coal and petroleum, and their many derivatives, in the form of eight Awards from Societies both within Japan and abroad. Trained initially in catalysis, he has applied this discipline successfully in his studies associated with carbon science and with coal and petroleum refining. There is more. At the time when relation-

ships between Universities in Japan and Industry needed to be strengthened (and this was a world-wide problem) Mochida worked intensely to build-up a research school, and to relate the findings of this research to the problems which industry was experiencing. Further, this period of time saw a significant growth in the size of research teams from the occasional two or three, to numbers approaching about twenty. And other changes were taking place. These research teams were now including students from outside Japan, and students from Japan were being offered opportunities to study in Universities, worldwide. At the centre of these activities Mochida operated with an apparent limitless energy, with the welfare of his students very much at the fore-front of his thinking. So, simultaneously, massive contributions were made to the sciences of hydrocarbon conversions, and young people were being highly trained to take their place in industrial and academic societies.

New materials: I. Mochida

Mochida has the ability, also, to be extremely innovative. Taking a look at recent issues of the journal Carbon, *e.g.*, Carbon 1996, Mochida has, with his co-authors, studied the axial nano-scale microstructures in graphitized fibers inherited from liquid crystal mesophase. Limitations to thermal conductance, thermal capacity, tensile strength and Young's modulus of fibre materials, and hence limitations in applications, ultimately depend on the continuity of crystal alignments in such fibres. Such studies are to the fore-front of research into the applications of fibres and are both timely and relevant. Also, Mochida has recently looked at the carbonization properties of the fullerenes C_{60} and C_{70}. Further, in the area of new carbon forms, he has studied the mechanical properties of binderless carbon moulds prepared from heat-treated mesophase pitch of controlled grain size. A similar, but quite distinct problem is that of gas separations. Molecular sieve carbons, similar in behaviour to the microporous zeolites, have been known for some years now. Mochida has applied these approaches to the separation of carbon dioxide from coal-bed methane, a mixture of these two gases, usually heavily contaminated with water vapour. Such a separation requires not only a carbon with the appropriate microporosity, but with this contained between surfaces which are of a hydrophobic nature. The coal-bed methane needs to be of a suitable purity for use in homes and industry.

The mesophase story: I. Mochida

During his career, Mochida has applied his earlier training in catalysis to reactions associated with the formation of carbons, of diverse properties, from various original, aromatic feedstocks. Studies have been published of catalytic syntheses of 'mesophase' pitch from aromatic hydrocarbons, such processes allowing the molecular design of carbon precursors. Synthetic methods have been developed for the creation of pitches from pure aromatic hydrocarbons using such Lewis acids as HF/BF_3 or $AlCl_3$ as catalysts. The preparation of nitrogen-containing pitches, from quinoline and isoquinoline, is an attempt to understand how differences in locations of nitrogen atoms, within the ring structures of the graphene layer of graphitizable carbons, influences the carbonization properties of the starting materials and the properties of the derived carbons.

However, very significant contributions of Mochida are with the conversions of coal and petroleum to carbons and further derived materials. These two sources or feedstocks have two aspects in common. Both are very complex organic materials which require careful structural and chemical analyses, and both, on pyrolysis and carbonization, when in the fluid state, are able to form liquid-crystal systems, that is, the so-called mesophase. In simple terms, there are

many 'mesophases' which give the diverse structures to graphitizable carbons. Mesophases are generated from molecules (mesogens), size »1,000 u, formed during carbonizations of coals and pitches. Mesogens, themselves, possess a wide range of chemical reactivity, and it is this variation which results in liquid crystal formation of differing size and ability to coalesce. Herein lies another long story. It is the 'crystallinity' of these liquid-crystals which is carried over into the solid phase of the carbon or coke, and which imparts the associated properties of anisotropy and graphitizability. By way of comparison, if wood material or a phenolic resin is carbonized, without passing through a fluid phase, then the resultant carbon, although not amorphous, is of limited structural order, is isotropic, and certainly is non-graphitizable.

Coal carbonization: I. Mochida

As far as coal is concerned it has to be recognized that 'coal materials' exhibit a wide range of chemical and physical properties, called 'coal rank'. The youngest of coals, the lignites and brown coals, with their internal co-valent bonding, do not fuse on carbonization, but produce carbons (or chars) which are meso- and micro-porous and hence have the properties of an adsorbent. As the rank range is traversed, the co-valent bonding is progressively replaced by hydrogen bonding and Van der Waals bonding, this enabling the coals to fuse on carbonization. The structure of the coal also becomes progressively more aromatic in content. With a further increase in rank, it is found that this fusibility, or softening or plasticity reaches a maximum to descend to zero in the semi-anthracites and anthracites, where the weak hydrogen bonding is replaced by carbon to carbon co-valent bonding. It is the coals with descending fusibility which have coking ability. However, the making of metallurgical coke no longer depends upon the use of a single coal being fed to the coking ovens. Rather, quite often, more than ten coals are previously blended and it is the blend which is charged to the coke ovens to be subsequently carbonized. Each of the ten or more coals, on their own, would not make a metallurgical coke. Procedures involving co-carbonizations of the coal (coal blend) with additives of high solubility parameters and hydrogen transfer ability were developed. It is this theory of the carbonization process, the interactions within the mixed fused states, and the formation of liquid-crystal systems and the fusing of these liquid-crystals, which has enabled the technology of coke-making to advance in the way it has done.

Coal, essentially, and considering the vitrinite macerals, is an organic, macromolecular system, containing microporosity. The ability of the coal to fuse (depolymerize) is a function of the strength of bonding within the macromolecular networks. Pyrolysis of coal produces molecular degradation to form the plastic (liquid) system. Subsequent carbonization brings about dehydrogenative polymerization of the dominantly aromatic molecules within plastic coal such that when the molecular size is about 1,000 u, formation of liquid crystals occurs and coke structure is established. Depolymerization of higher activation energies is favoured at higher temperatures, with rapid heating to prevent the retrogressive reactions at lower temperatures. Rapid heating under pressure is favorable with the use of additives in co-carbonizations because they have an enhanced facility for dissolution in the coal and reaction at higher temperatures. Mochida has submitted a proposal to the Ministry of International Trade and Industry and Japanese Association of Iron and Steel Making, which outlines coke-making procedures to be adopted in the next decade. The proposal includes coal pretreatment, rapid heating to enhance the fusibility for coke strength, by lower temperature of calcination, and potential for anisotropic development, hot moulding, and carbonization at controlled heating rates. The application of such a scheme would widen the range of usable coals, would make coke making less energy intensive, improving quality and productivity, and suggesting the possibility of a continuous rather than a batch process of coke making.

Coal liquefaction: I. Mochida

A thorough understanding of the macromolecular structures of coal, of bondings within and between these macromolecules, as well as the microporosity (so enabling reactive molecules to enter into coal structure) has enabled Mochida to improve the process of coal liquefaction. Early on, he demonstrated the importance of coal liquefaction solvents in terms of their boiling range, their dissolving ability and capacity as well as the reactivity of hydrogen donating molecules. Hydrogen donors not only stabilize radicals from coal pyrolysis but also lead to bond fissure of the rather more stable bridges, so achieving larger extents of depolymerization and hence of oil yield. In the area of liquefaction catalysts, the contribution of Mochida is with the design, the recovery and regeneration of catalysts, proposing the use of TiO_2 and carbon. He has advanced integrated schemes which include coal pretreatment, coal dissolution using donors at high temperatures, with two or three steps for the catalytic upgrading, such as hydro-desulfurization and hydro-denitrification.

Activated cokes (carbons): I. Mochida

Professor Mochida applied his combined understanding of coal chemistry and structure, as well as surface chemistry and heterogeneous catalysis to the production of activated carbons from coal, with the viewpoint of efficient removal of oxides of nitrogen and sulfur from combustion gases. Using a bituminous coal, he produced an activated carbon of higher performance characteristics than that of Bergbau Forschung (now DMT). He found (a) that the activity of the carbon for NO_x reduction, using ammonia, is intimately related to the oxygen functionality associated with the oxidatively adsorbed SO_2, (b) that nitrogen functional groups introduced into the carbon, during the stage of the NH_3-NO reaction, enhance the NO_x reduction, and (c) that the regeneration of SO_2 adsorption activity, after SO_2 recovery, relates to extents of surface oxygen complexes contained on carbon surfaces. Removal of SO_x and NO_x using activated coke (from coal) is now commercialized in Japan. The same principles have been applied to activated carbon fibers from PAN (polyacrylonitrile).

TECHNOLOGICAL DEVELOPMENT IN THE COAL AND HEAVY PETROLEUM UP-GRADING TO FUTURE SOCIETY

Isao Mochida
Institute of Advanced Material Study, Kyushu University,
6-1 Kasugakoen, Kasuga, Fukuoka 816, Japan

INTRODUCTION

Energy basically obtained from the fossil carbonaceous resources on the earth will suffer the shortage of supply principally due to rapidly growing demand in the developing countries of large population. Huge consumption of the resources will bring about significant damages to the global environment. Hence, extensive up-grading of petroleum and coal at very high efficiency, energy saving, and environmental protection should be pursued at the same time. The correct structure of fossil resources, molecular transformation of their complete conversion and reforming by multi-stage scheme, catalysis and catalyst designs for the respective stage, molecular transformation into the carbon of high performances for energy saving and environmental protection are the targets of current research.

In the present paper, concepts and results in such areas that have been studied by the author for 20 years are overviewed.

Structural Understanding of Coal and Petroleum

Coal and petroleum are both complex mixtures of hydrocarbons. Their heaviest ends are targets of detail structural analyses.

Coal has been characterized by its maceral compositions and ranks, which tell us empirical but useful correlations on its properties. Recent approach is to clarify its structure on molecular basis. Basically heavy molecules in the coal are polynuclear polyaromatic hydrocarbons with heteroatoms and alkyl substituents. Sizes of molecule and aromatic ring, number of nuclei, bindings among nuclei, moiety of heteroatoms, number and length of alkyl substituents are primary factors of molecules. The distribution of the factors is concerned while the molecular weight is estimated around 1500. Such macromolecular chains are entangled each other to form colloid or micelle which occludes smaller molecules. The bridges among the chains can be covalent or non-covalent. Recent study indicates that non-covalent bonds among the chains are breakable rather easily by physical as well as chemical pretreatment at least in active macerals, providing high solubility and fusibility after the liberation. Non-covalent bridges are hydrogen bond, charge transfer interaction, aromatic ring stacking and metallic ion bridges. The author emphasized the carboxyl linkage and their coordination to divalent cations in lower ranking coals as shown in **Figure 1**. Although the complete picture of coal molecules is not disclosed yet, analysis based on such a profile of molecules gives us an image of its chemical nature.

The asphaltene is another target of structural study, while the molecules in naphtha, gas oil, vacuum gas oil and maltene are fairly clarified, their accuracy depending on their molecular size and type of structure. The asphaltene is soluble in benzene, but is believed to be present in the micelle or an entangled assembly, molecular weight of the component being beyond 10,000. Molecular assembly of the asphaltene in vacuum residue should be clarified at elevated and ambient temperatures. The present authors have hydrogenated 99% of hexane insoluble component into hexane soluble. Interestingly, solubilized asphaltene inherits the basic metal porphyrin structures. Structural change at this solubilization gives us some keys to elucidate the molecular assembly in the asphaltene.

Molecular Transformation of Coal and Heavy Petroleum

When coal and heavy fraction of asphaltene are heated, their molecular assembly is to be liberated to give a fused state from coal and solution from the asphaltene. Solvent present or added plays an important role to produce such a liquid state. In another situation without adequate solvent or with strong intermolecular linkages, condensation reactions of macromolecules can take place within the cage of molecular assembly, giving less soluble and less fusible component. Hence, the decoagulation of molecular assembly prior to the heating is claimed by the author very favorable to suppress such retrogressive reactions. The condensed product, thus produced, is called char or isotropic carbon with least stacking of aromatic planes. The author emphasizes the importance of hydrogen donor and dissolving activity of the solvent.

The polymeric substances in the liquid state can be depolymerized through the breakage of the weakest intermolecular linkages. Such breakage can be spontaneous, hydrogenation assisted, and hydrogenolysis as schematically illustrated in **Figure 2**. The fissured linkage can be capped with hydrogen to give smaller molecules, otherwise another type of condensation reaction takes place to give large molecule of more stability, leading to carbonaceous product. Such a process can be defined as carbonization or coking, being a principle pathway to produce carbon materials of functionality or process-troubles such as sludge, plugging and carbonaceous poisons as described later. Competitive reaction scheme is illustrated in **Figure 3**. Hydrogenation-assisted and hydrogenolysis breakages are performed with hydrogen donors at rather high temperature and rapid heating.

The limitation in such mechanisms of depolymerization is certainly present in the reactivities of acceptors and donors, limiting the extent of depolymerization. The catalyst can

perform further depolymerization through the hydrogenation, acidic and hydro-cracking to give distillates.

Catalysis and Catalyst Design for the Molecular Conversion

The catalysts can hydrogenate the aromatic ring and break the single C-C, C-S, C-N, C-O bonds due to their hydrogenation activity originating from transition metal components and their acidity. The hydrogenation produces hydrogen donor, caps the free radical, and saturates the double bonds to be fissured by acidity. The aromatic ring can be opened into chain molecule through the successive steps of hydrogenation and acidic bond fission. Alkylation and trans-alkylation modify the nature of aromatic species.

The hydrogenation can suppress the retrogressive and coking reactions though the control of condensation reactions and enhancing fusibility or solubility. On the other hand, acidity of the catalyst adsorbs strongly the polar molecules, trapping them on the surface for a long time while the condensation reaction take places consecutively, leading to the carbon or coke on the catalyst surface.

Demetallation, desulfurization, denitrogenation and deoxygenation are major catalytic reactions for up-grading the hydrocarbon fuels. The molecular conversions pathways involved in the reactions are now being schematically described, although the difficulty increases with increasing molecular size because of difficulty in their molecular identification.

Another important factor is the intermolecular interactions in the liquid phase and on the catalyst surface. In some combinations, such interaction enhances the reaction while retards the reaction in other cases. Desulfurization of gas oil has been described on molecular bases. Chemistry involved in the desulfurization of 4,6-dimethyldibenzothiophene has been clarified.

The catalysts of better performances such as longer life, easy recovery and regeneration as well as high activity and selectivity are continuously looked for. The catalytic species and support are combined to achieve high performance, their chemical as well as physical interactions being concerned. Carbon and titania are reported to provide non-polar surface of intimate interaction with the catalytic species. Very fine particles of carbon as photographed in **Figure 4** are well dispersed and recoverable from ash minerals. New materials and new combinations are examined to obtain multi-functions.

The catalysis schemes are designed to allow the best performances of the catalysts. Optimum conditions are present to the optimum feed on the respective catalyst. Multi-stage reaction scheme is thus appropriate for the complete and selective conversion of coal and heavy petroleum, selecting the best catalyst and conditions for the respective stage. Solvent plays an important role even in the catalytic reactions.

Molecular Conversion of Coal and Heavy Petroleum into Carbons of High Performances

Carbons produced from coal and heavy petroleum are very indispensable by their high performances in the modern industry. Blast furnace coke, needle coke, carbon fiber and a variety of carbon artifacts are the case. Majority of such carbons is graphitizable through the ordered stacking of aromatic planes which is built in the early stage of carbonization. The mesophase or discotic liquid crystal is the intermediate state and product, leading to such carbons.

It is emphasized that the condensation into large aromatic planes and their stacking are balanced by selecting the feed, additive, preparative conditions and even catalysts of easy separation to form the mesophase. The author particularly emphasized roles of additives of hydrogen donating and dissolving activity. Molecular structure and molecular assembly at micro-, meso- and macro-scopic levels have been analyzed, and their relation to their properties is established. **Figure 5** illustrates microscopic views of mesophase, its as-spun and carbonized fibers. Thus, the carbons of high performance are designed through the preparation of precursor, and control of carbonization, graphitization, and forming on chemical and physical bases.

Carbon Materials for Energy Saving and Environmental Protection

The energy saving and environmental protection are the key issues for the effective use of resources. Carbon can provide some of excellent devices for these purposes. High strength per weight, high thermal conductivity, rapid and large adsorption and desorption, catalytically active surface of carbon fiber and active carbon fibers are such cases. Detail structural control for aromatic molecules including substituents and heteroatoms, and their stacking is the base for the design of the mesophase pitch and hence its derived high performance carbons. Very high strength and thermal conductivity are now achieved from aromatic hydrocarbon derived mesophase pitches prepared with HF/BF_3.

The author proposed a novel scheme of SOx and NOx removal over activated carbon fibers of controlled surface as shown in **Figure 6**. The calcination after the activation was found very effective to increase the activity for SOx oxidation and NOx reduction.

The authors is very grateful to all of his colleagues and many students at Kyushu University, a number of friends in the academics and industries of international linkages for their significant cowork and helps, and expresses special thanks to Professors Kenjiro Takeshita, Tetsuro Seiyama, Yukio Yoneda, John C. Bailar Jr., and Harry Marsh for their continuous guidance and friendship for many years of his research.

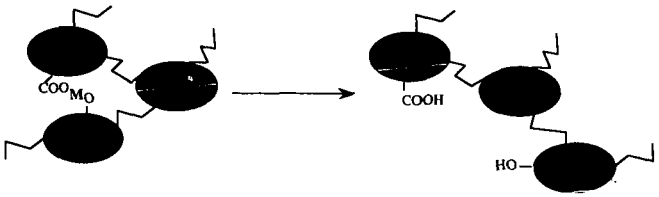

Figure 1 Coal Depolymerization Scheme through Decationing Treatment

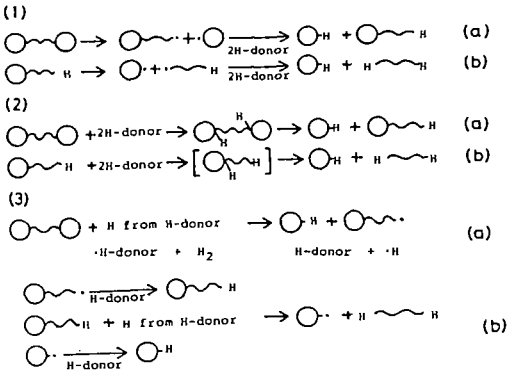

Fig.2 Hydrogen-transferring liquefaction mechanism
(1) Hydrogenative stabilization of fragmental radicals
(2) Hydrogenative bond-loosening
(3) Hydrogenative bond-dissociation
(molecular hydrogen participation)

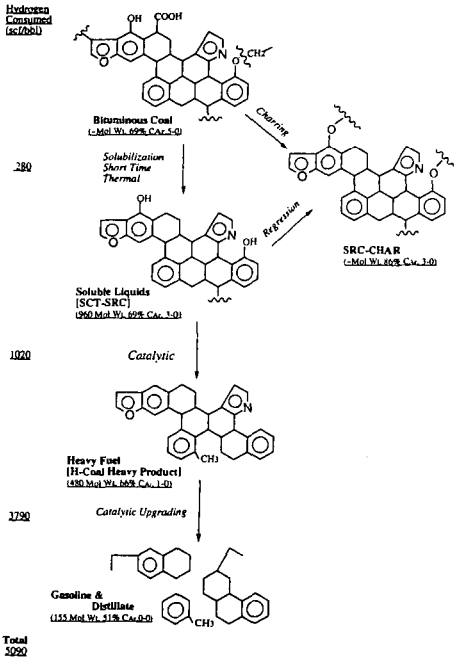

Figure 3 Structural Changes During Coal Liquefaction

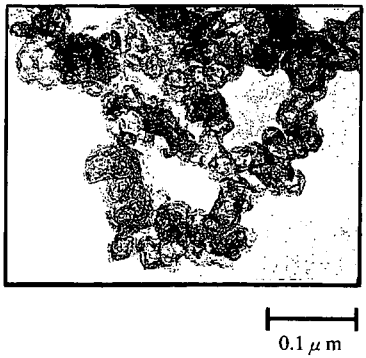

Figure 4 TEM photomicrograph of Ketjen Black

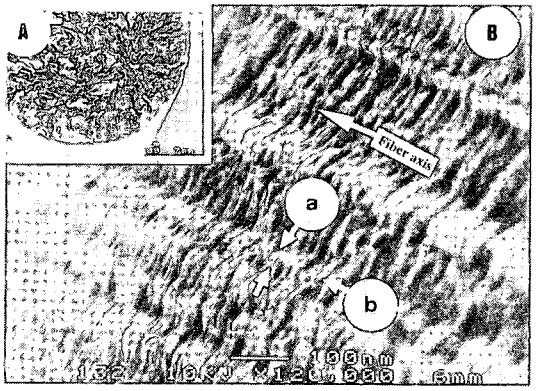

Figure 5 HR-SEM of mesophase pitch carbon fiber

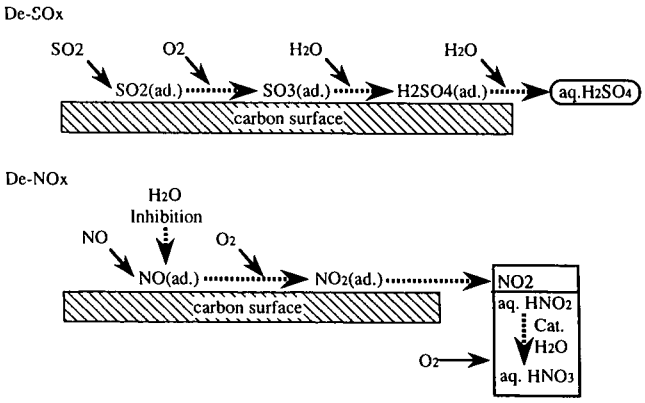

Figure 6 A Novel Scheme of SOx and NOx Removal over ACF

USE OF ILLINOIS BY-PRODUCT RESIDUES FOR PAVING MATERIALS

N. Ghafoori[1], L. Wang[2], S. Kassel[3]
Department of Civil Engineering
Southern Illinois University at Carbondale
Carbondale, Illinois 62901

Keywords: coal, combustion residue, and roller compacted concrete

ABSTRACT

Tests were conducted in a field demonstration project to determine if by-products of fluidized bed and pulverized coal combustions (FBC and PCC) can be used in production of surface wearing course pavements for secondary/county roads. Various proportions of pre-hydrated FBC spent bed, as a fine aggregate; PCC fly ash, as a primary cementitious binder, with or without low dosage of portland cement; and crushed limestone coarse aggregate were blended at their optimum moisture content to produce zero-slump concrete mixtures. Pavement slabs of 6 ft by 12 ft were constructed by compacting 10 in. loose fresh matrix into 8 in. final thickness, in two lifts, using a self-propelled steel vibratory roller. No other surface finish treatments were used.

Information gathered in this paper makes the user of roller compacted concrete (RCC) containing FBC/PCC by-product residues aware of the fact that excellent engineering characteristics can be attained even when little or no portland cement is used. After 18 months from the date of initial casting, the pavement sections are crack-free and remain in excellent surface condition.

BACKGROUND

In the United States, nearly 80% of the coal produced is used for electric power generation and about 15% of this amount is recovered as coal combustion by-products[1]. Currently, 90 million short tons of ash is produced annually and the level of production is expected to reach 200 million short tons by the year 2000[2,3,4]. The high cost of waste disposal, scarcity of disposal sites, and serious environmental damages associated with the disposal of coal combustion residues have encouraged innovative utilization strategies. Undoubtedly, the construction industry, with its already depleted natural resources and ability to assimilate large volumes of materials, is in a unique position to provide safe and economical solutions of by-product utilization in a variety of construction-related applications.

While past laboratory investigation had provided valuable scientific data on the engineering properties of various FBC/PCC concrete mixtures and identified a number of potentially viable applications, field feasibility studies were needed to bring the laboratory investigation a step closer to reality[5,6]. The paper presented herein reports on a field demonstration project aimed at evaluating the constructability and engineering performance of the experimental slabs utilizing FBC spent bed and PCC fly ash. A nearly 300 ft road, comprising of 25 different slab sections, was constructed at a site located in Carterville, Illinois. Both conventional (vibratory) and roller compacted concrete placement techniques were utilized. Once the pavement sections were placed and finished, a coat of chemical sealant was spread on the slab surface to maintain sufficient moisture for the hydration of cementitious binders. The road was seal-cured for nearly two weeks before it was opened to traffic.

The findings of the surface course roller compacted slabs are presented and discussed in the paragraphs to follow.

MATERIALS AND METHODS

The FBC spent bed was obtained from a coal-fired circulating fluidized bed combustor at a co-generation plant burning high-sulfur Illinois coal. Its physico-chemical properties are shown in Tables 1 and 2. In order to eliminate the excess heat of hydration and subsequent expansive phases, the FBC residues were pre-hydrated prior to blending with other concrete constituents[7]. The fly ash selected for the study, a by-product of pulverized coal combustion process, complied with the requirements of ASTM C 618[8]. The chemical and physical characteristics associated with this fly ash are documented in Tables 1 and 3, respectively. A low dosage of Type V portland cement (5% by mass of total dry solids), as a complimentary cementitious binder, was used in some slab sections. The crushed limestone coarse aggregate was obtained from a quarry in southern Illinois.

---

[1]Associate Professor, [2]Research Graduate Assistant, and [3]Research Undergraduate Assistant

The physical properties are shown in Table 4. The mixture designation, solid constituents and proportions, nominal moisture content, and air-dry density are listed in Table 5.
Cylindrical (4" x 8") and beam-shaped (4" x 4" x 14") specimens were cored at different ages. They were tested for strength (ASTM C 39, ASTM C 496, and ASTM C 78)[9], elasticity (ASTM C 469)[9], length change (ASTM C 157)[9], resistance to wear (ASTM C 779, Procedure C)[9] and freezing and thawing (ASTM C 666, Procedure A)[9].

DISCUSSION OF RESULTS

The influence of mixture proportion, curing age, and testing condition on compression behavior of roller compacted FBC/PCC surface course slabs were investigated; and the results are presented in Figures 1 and 2. Similar to conventional concrete, the FBC/PCC mixes continued to gain strength with age. An average increase of 23% and 35% in compressive strength was attained when concrete age was extended from 60 to 90 and from 90 to 180 days, respectively, under dry conditions. When tested under wet conditions, the improvement in strength was 36 and 49% for the aforementioned periods. The compression properties also improved as the FBC spent bed to PCC fly ash ratio decreased. The increase in strength was higher under wet conditions (an average of 33%) than that obtained under dry conditions (a mean value of 18%). However, the influence of moisture (wet or dry) on compressive strength reduced as concrete age increased. Slabs without portland cement displayed compressive strengths superior to those obtained for pavement sections containing cement (21% and 10% for dry and wet compressive strength, respectively).

Table 5 demonstrates the variation of splitting-tensile strength with respect to time for the FBC/PCC core specimens. Similar to the compressive strength, the splitting-tensile resistance is a function of mixture proportion and fly ash content of the matrix. Insofar as strength development is concerned, roughly 83% of 90-day strength was achieved after 60 days from the date of initial casting. An average increase in splitting tensile strength of 15% was observed as concrete age was extended from 90 to 180 days. While the addition of portland cement did not improve the compressive strength, it enhanced the tensile splitting of RCC slabs. The average ratios of splitting-tension to compression were typical of those expected for conventional concretes.

Young's modulus of elasticity for the RCC slabs was determined at various ages, and the results are shown in Table 6. Static modulus of elasticity varied from 2.51×10^6 to 4.17×10^6 psi. The FBC/PCC roller compacted concrete exhibited a lower elastic modulus than that of conventional concrete of the same strength level.

The progression of flexural strength with respect to cementitious content is illustrated in Table 7. Based on the results obtained, the flexural strength of all matrices displayed a similar trend to those of compressive and splitting-tensile strengths; the flexural capacity steadily improved as the fly ash content of the matrix increased. When a low dosage of portland cement was incorporated into FBC/PCC mixtures, a slight improvement in flexural strength was observed (an average value of 4.4%).

Figure 3 documents the linear expansion of the surface course FBC/PCC roller compacted concretes. The strain properties of the field slabs was stabilized after 2-4 weeks from the date of construction and, to date, remain insignificant. The addition of portland cement reduced, to some extent, the overall expansion strain of FBC/PCC slabs.

Figure 4 illustrates the abrasion resistance of roller compacted concrete mixes under wet surface conditions. In general, the depth of wear increased with abrasion time, and the rate of increase in expansion was fairly uniform as time of wear increased. A reduction in FBC spent bed to PCC fly ash ratio or addition of a low dosage portland cement enhanced abrasion resistance of RCC slabs (12.5% decrease in abrasion wear with addition of portland cement). This improvement is attributed to a stronger cementitious mortar of the concrete surface which displayed more resistance to wear.

Resistance to rapid freezing and thawing of the beam-shaped specimens cored from the non air-entrained experimental slabs is shown in Table 8. The addition of fly ash, and to a great extent portland cement, increased the resistance to freezing and thawing. After a year of exposure to the freezing and thawing cycles of the winter climate, no deterioration or surface scaling has been experienced by any of the FBC/PCC roller compacted concrete slabs.

CONCLUDING REMARKS

In general, test results for FBC/PCC roller compacted concrete slabs were extremely encouraging. Strength and elastic modulus followed the well-known patterns of conventional concrete, and

improved as cementitious content of the matrix increased. Expansion strains, based on internal sulfate attack, were minimal and virtually nonexistent. The slabs containing a low dosage of portland cement exhibited an improved tensile strength, linear expansion, abrasion wear, and freezing and thawing properties. Bi-weekly inspections of the paved surfaces indicated that, after 18 months from the date of initial casting, the sections are crack-free and remain in excellent surface condition.

ACKNOWLEDGEMENTS

This research was funded, in part, by grants made possible by the Illinois department of Energy and Natural Resources through its Coal Development Board and Illinois Clean Coal Institute, and by the U. S. Department of Energy (Grant number DE-FC22-92PC92521). However, any opinions, findings, conclusions, or recommendations expressed herein are those of the authors and do not necessarily reflect the views of IDENR, ICCI and the DOE.

Thanks are extended to a number of manufacturers who contributed materials used in this field project.

REFERENCES

1. Energy Information Administration "Cost and Quality of Fuels for Electric Utility Plants 1991", Office of Coal, Nuclear, Electric and Alternate Fuels, U.S. Department of Energy, Washington, DC 20585, August, 1992, 58 pp.
2. EPA report to Congress, "Wastes from the Combustion of Coal by Electric Utility Power Plants", United States Environmental Protection Agency, February, 1988, 45 pp.
3. Tyson, S.S., "Guidance for Coal Ash Use: Codes and Standard Activities for High-Volume Applications", Proceedings of 9th Annual International Pittsburgh Coal Conference, Pittsburgh, PA, 1992, pp. 815-817.
4. Coal Combustion Byproduct (CCB), "Production and Use: 1966-1993", Report for Coal Burning Utilities in the United States, American Coal Ash Association, Alexandria, VA 1995, 68 pp.
5. Ghafoori, N., "Engineering Characteristics and Durability of Roller Compacted Non-Cement FBC Mixes for Secondary Roads", Annual Report, Illinois Clean Coal Institute and Illinois Department of Natural Resources, September, 1994, 31 pp.
6. Ghafoori, N., "A Field Demonstration Project Utilizing FBC/PCC Residues for Paving Materials", Annual Report, Illinois Clean Coal Institute, September, 1995, 22 pp.
7. Ghafoori, N., and Sami, S., "A Simplified and Practical Approach for Effective Prehydration of Fluidized Bed Combustion Residues", Proceedings of the Coal, Energy and Environmental Conference, October 12-16, 1992, Ostrava, Czechoslovakia, Section IV, pp. 1-9.
8. Standard Specification for Fly Ash and Raw or Calcined Natural Pozzolan for Use as a Mineral Admixture in Portland Cement Concrete, ASTM C 618, American Society for Testing and Materials, Philadelphia, PA, 1987, 3 pp.
9. American Society for Testing and Materials, Annual Book of ASTM Standard, Part 14 and 19, Philadelphia, PA, 1989.
10. American Concrete Institute (ACI) Committee 226, "Fly Ash in Concrete", ACI Materials Journal, 1987, pp. 381-410.
11. Ghafoori, N., and Chang, W.F., "Roller Compacted Concrete Utilizing Dihydrate Phosphogypsum, Journal of Transportation Research Record, September, 1990, Vol. 1, No. 1301, pp. 139-148.
12. Helmuth, R., "Fly Ash in Cement and Concrete", Portland Cement Association, SP040-OIT, 1987, 203 pp.
13. Mindess, S., and Young, Y.F., "Concrete", Prentice-Hall Inc., Englewood Cliffs, NJ, 1981, 671 pp.
14. Neville, A.M., "Properties of Concrete", John Wiley and sons, New York, NY, 1981, 779 pp.
15. Sukandar, B.M., "Abrasion of Concrete Block Pavers", Master Thesis, Department of Civil Engineering and Mechanics, Southern Illinois University, Carbondale, IL, January, 1993, 165 pp.
16. Yoder, E.J., and Witczak, A., "Principles of Pavement Design, 2nd Edition, John Wiley and Sons, 1975, 711 pp.

Table 1: Chemical Test Data of FBC Spent Bed and PCC Fly Ash

Chemical Composition	"FBC" Spent Bed	"PCC" Fly Ash	Fly Ash Specifications (ASTM C 618)
Silicon Oxide (SiO_2)	9.70	49.10	----
Aluminum Oxide (Al_2O_3)	3.69	25.50	----
Iron Oxide (Fe_2O_3)	2.16	16.60	----
Total ($SiO_2+Al_2O_3+Fe_2O_3$)	15.55	91.20	50.0 Minimum, Class C 70.0 Minimum, Class F
Sulfur Trioxide (SO_3)	24.42	0.50	50.0 Maximum
Calcium Oxide (CaO)	53.10	1.56	Less than 10%, Class F More than 10%, Class C
Magnesium Oxide (MgO)	0.88	0.89	----
Loss on Ignition	0.80	0.38	6:0 Maximum
Free Moisture	0.0	0.16	3.0 Maximum
Water of Hydration	2.65	0.0	----
Total Na_2O	0.16	0.37	----
Available Alkalies as Na_2O	N/A	0.08	1.5 Maximum
Total K_2O	0.39	2.26	----
Others ($TiO_2+P_2O_5+BaO$)	2.04	2.60	----

Table 2: Physical Properties of FBC Spent Bed

Fineness Modulus	Specific Gravity (OD)	Specific Gravity (SSD)	Absorption (%)	Organic Impurities
1.80	1.92	2.19	14.60	None

Table 3: Physical Properties of PCC Fly Ash

#325 Sieve Fineness		Specific Gravity	Autoclaved Expansion		Water Requirement		7-Day Compressive Strength		
Actual	Limit		Actual	Limit			Actual	ASTM	AASHTO
22.60	Max. 34%	2.39	0.03	0.80%	93.30	Max. 105	85.40	Min. 75%	Min. 60%

Table 4: Physical Properties of Crushed Limestone Coarse Aggregate

Maximum Size (Max. Normal Size)	Specific Gravity (OD)	Specific Gravity (SSD)	Absorption (%)	Rodded Unit Weight (OD) (lb/ft^3)	Rodded Unit Weight (SSD) (lb/ft^3)	Void Ratio
1 (3/4)	2.64	2.67	0.75	93.50	94.20	43.75

Table 5: Mixture Proportion Details for FBC/PCC Roller Compacted Concrete Mixtures

Mix No.	FBC Spent Bed (%) *	Silicious Fine Aggregate (%)	PCC Fly Ash (%)	Portlaud Cement (%)	Limestone Coarse Aggregate (%)	Nominal Moisture Content (%)	Air-Dry Density (lb/ft^3)
C3	26.67	----	13.33	----	60.0	7.67	144.47
C5	20.0	----	20.0	----	60.0	7.74	145.12
C1P	29.5	----	5.5	5.0	60.0	8.27	140.66
C3P	24.17	----	10.83	5.0	60.0	7.95	144.43
C5P	17.5	----	17.5	5.0	60.0	7.62	142.43

* Note: All percentages are by mass of total dry solids

Table 6: Splitting-Tensile Strength and Static Modulus of Elasticity of FBC/PCC Roller Compacted Concrete Mixtures

Mix No.	Splitting-Tensile Strength (psi)			Splitting-Tension to Compression Ratio			Modulus of Elasticity (10^6 psi)		
	Curing Age (Days)			Curing Age (Days)			Curing Age (Days)		
	60	90	180	60	90	180	60	90	180
C3	323	406	476	0.078	0.098	0.087	3.54	3.80	4.06
C5	442	500	549	0.103	0.092	0.096	3.70	3.94	4.17
C1P	236	300	362	0.111	0.110	0.108	2.51	2.78	3.09
C3P	352	438	530	0.106	0.109	0.120	3.30	3.48	3.66
C5P	467	536	571	0.120	0.119	0.121	3.41	3.60	3.79

Table 7: 90-Day Flexural Strength of FBC/PCC Roller Compacted Concrete Mixtures

Mix. No.	Flexural Strength (psi)	Strength Ratio	
		Flex./Comp.	Flex./Split
C3	646.88	0.127	1.60
C5	701.25	0.128	1.40
C1P	486.3	0.189	1.62
C3P	665.35	0.165	1.52
C5P	743	0.165	1.39

Table 8: Freezing and Thawing of FBC/PCC Roller Compacted Concrete Mixtures (Mass Loss %)

Mix No.	Number of Freezing and Thawing Cycles								
	5	10	15	20	25	30	35	40	45
C3	0.43+	7.42#	17.1#	30.5#					
C5	0	0.41+	0.41+	1.03*	3.08#	44.8#			
C1P	0.44-	2.44+	22.6#	41.2#					
C3P	0.21-	0.42-	5*	15.2#	55.7#				
C5P	0	0	0.22-	0.43-	1.3+	4.11+	10.6#	29.2#	

- slight flaking; + slight chipping; * noticeable cracking in specimen; # severe flaking and chipping

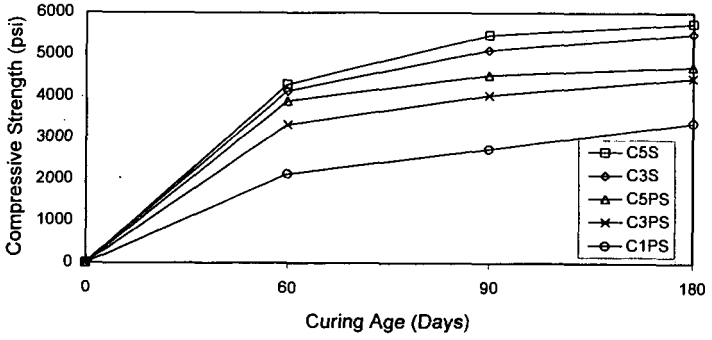

Figure 1: Field Air-Dry Compressive Strength of Surface Course FBC/PCC Roller Compacted Concrete Mixtures

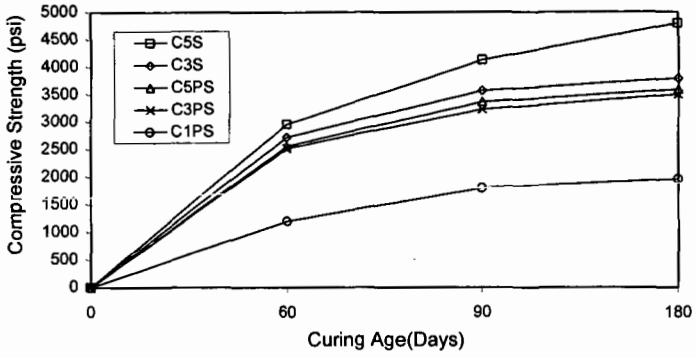

Figure 2: Field Soaked Compressive Strength of Surface Course FBC/PCC Roller Compacted Concrete Mixtures

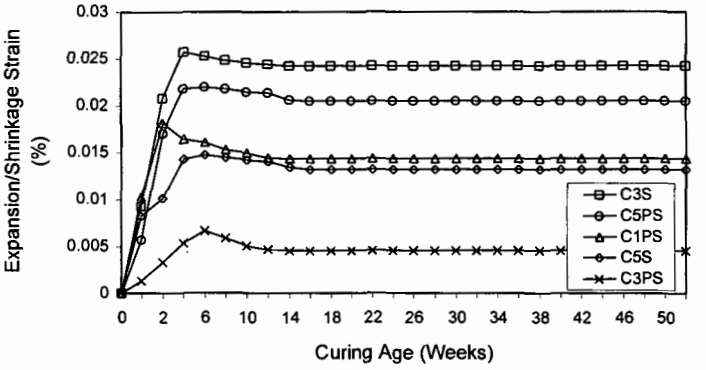

Figure 3: Field Expansion/Shrinkage of Surface Course FBC/PCC Roller Compacted Concrete Mixtures

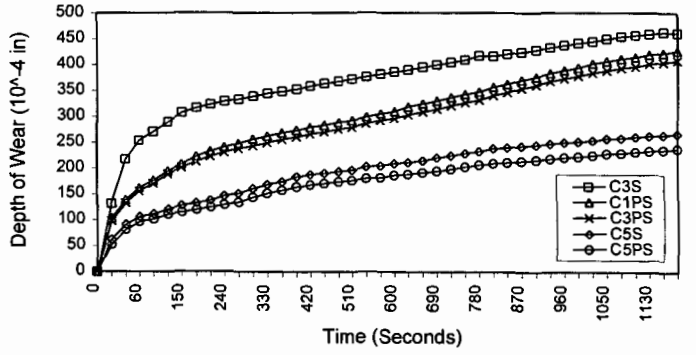

Figure 4: Field Abrasion Resistance of Surface Course FBC/PCC Roller Compacted Concrete Mixtures (Wet at Testing)

Roller Compacted Base Course Construction Using Lime Stabilized Fly Ash and Flue Gas Desulfurization Sludge By-Product

Joel H. Beeghly, Project Manager
Dravo Lime Company Research Center
3600 Neville Road
Pittsburgh, Pennsylvania 15225

Keywords: lime, stabilization, flue gas desulfurization

ABSTRACT

Dewatered calcium sulfite and calcium sulfate sludges from unoxidized flue gas desulfurization (FGD) processes at coal fired power plants can be mixed with coal fly ash and lime to cause a cementitious chemical reaction used to construct a roller compacted base course (RCFGD) or an impermeable pond liner. The chemical reaction is described as lime reacting with alumina from the fly ash which in turn reacts with the calcium sulfite and sulfate FGD waste to form calcium sulfo-aluminate compounds. Leachate data is similar to primary drinking water quality standards. Two field demonstrations of RCFGD and a proposed mix design procedure are described. Factors that affect strength gain and freeze-thaw durability such as optimum moisture content, fly ash to FGD ratio, and age of FGD are discussed. Better understanding is needed on how to predict long term strength performance and expansive potential given the nature of long term hydration forming ettringite compounds and the vulnerability to destructive freeze-thaw cycles.

INTRODUCTION

Lime is commonly used as a reagent to remove SO_2 from power plant emission burning medium and high sulfur bituminous coal. A leading supplier of lime products for flue gas treatment applications, the Dravo Lime Company is also extensively involved in the development of lime-based environmental technologies, including ways to better manage the large volume of waste product resulting from these efforts to clean the stack gases from large coal-fired publicly owned utilities. In the United States alone, over 68 million tons of coal ash materials and 20 million tons of flue gas desulfurization (FGD) materials must be handled. Most of the ash and nearly all of the FGD by-products must be disposed in landfills.[1] This huge volume of waste material disposal applies to unoxidized FGD systems that use either lime or limestone as the alkaline sorbent.

A common practice for landfill disposal with twenty years experience is a sludge fixation process whereby the FGD sludge is dewatered by vacuum filtration or centrifuges, and the cake solids are mixed with the plant's fly ash that was collected separately and some pulverized quicklime. This mixture is referred to as fixated scrubber sludge solids (FSSS). As it is being placed and compacted in a landfill disposal cell, chemical reactions begin causing the material to harden.

The Dravo Lime Company (DLC) serves 14 power stations in the Ohio River Valley generating about 13,500 MW of power. Twelve of these stations practice the above lime-fly ash stabilization process, often called by the original process tradename, POZ-O-TEC. The strength of FSSS for landfill disposal is not high enough at 200 psi @ 28 days curing or durable enough for heavy traffic and freeze-thaw conditions. However, when compared to natural soils, fixated FGD scrubber sludge solids have been shown to have high natural strength and low permeability.[2] Although important, permeability testing and results will not be covered in this paper.

This paper will discuss the progress of on-going research at Dravo Lime Company on how this fixated scrubber sludge solids (FSSS) mixture can be upgraded in terms of strength gain and durability and be used as a roadbase pavement or structural fill material that would be applied by placing it using construction techniques similar to those for roller compacted concrete (RCC).

ROLLER COMPACTED CONCRETE OR STABILIZED BASE COURSE

Conventional RCC is a dry and stable mix of aggregate, portland cement or lime, and water. It is also similar to lime stabilization of soil or aggregate base course which is widely used to improve the strength and durability of soils by ion exchange and cementitious reactions, enabling their use as engineering materials in the construction of pavements and structural fills. RCC is typically laid by modified asphalt pavers or a road grader and compacted by rollers that follow close behind. The material should show tremendous stability in the fresh state. As the FGD-fly ash-lime mixture hydrates, the material acquires strength but not likely as much strength as

conventional portland cement concrete. Adequate strength for stabilized base course is about 400 psi in 28 days curing for most applications. It is believed the FSSS mixture using additional lime and coal ash material can be designed to attain 400 psi. It will be called roller compacted FGD stabilized base material (RCFGD).

However, the RCC made from FSSS is not suited to perform as a highway wearing cause pavement because of low abrasion resistance. Some experience suggests it can exhibit suitable durability in terms of freeze-thaw resistance but more proof is needed to define the durability limitations which is discussed further.

CHARACTERIZATION OF FSSS COMPONENTS

Fixated scrubber sludge solids (FSSS) is the term to apply to the mixture of sludge cake, fly ash, and lime to allow stabilization of the sludge cake for landfill disposal. The term for upgraded FSSS for use as roller compacted base course will be labeled roller compacted FGD (RCFGD). The FGD scrubber solids mineralogical composition from a lime scrubber, most of which are based on the Dravo Lime magnesium enhanced lime Thiosorbic process and some inhibited oxidation limestone scrubbers, is mostly calcium sulfite hemi-hydrate ($CaSO_3 \cdot \frac{1}{2}H_2O$) ranging 75-85% and some calcium sulfate dihydrate ($CaSO_4 \cdot 2H_2O$) ranging 10-20% with minor amount of calcium carbonate ($CaCO_3$) ranging 5-15% and minor amounts fly ash minerals. Coal fly ash is mostly clay like minerals composed of alumina, silica, and iron oxide. A geochemical oxide or elemental form analysis is listed in Table 1. Also listed in the composition of the quicklime component which is closer to a unhydrated calcitic quicklime than a dolomitic lime.

One method to evaluate pavement performance is the unconfined compression test (ASTM D2166). In this procedure strengths of specimens compacted to a known density and water content according to ASTM D698 (Standard Procter Test) are evaluated after different curing periods and conditions.[3]

MIX PROPORTION FOR LANDFILL DISPOSAL

The proportion of the components as they are mixed to stabilize the FGD sludge for landfill disposal varies somewhat from plant to plant and from day to day depending on the percent solids of the dewatered sludge cake and the availability of the fly ash. The objective is do make a mixture that can be compacted to a density required by the solid waste regulatory authority. Generally, the ratio of fly ash to scrubber solids is 0.75 or less for every 1.0 on a dry weight basis. The predominately calcium sulfite sludge comes from large diameter thickeners and then is dewatered by drum vacuum filters or centrifuges to about 40% solids based on the total wet weight. The cake is mixed with the fly ash and 2-3% pulverized quicklime (CaO) in a pug mill. Only enough lime is added to cause enough hardening to stabilize the sludge and prevent leachate by adequate strength development and resultant clay-like impermeability. The approximately 35-42% FGD sludge solids is increased to about 60-65% solids in the FSSS. Smith presents a good description of the FSSS process.[4] The mixture is conveyed to a stockpile area to cure for a few days and stiffen to facilitate placement and compaction in the landfill. The state EPA regulatory operating permit will specify for landfill disposal the density and permeability of the compacted solids, thereby governing the amount of compaction effort.

ENVIRONMENTAL WATER QUALITY IMPACT

From combustion of bituminous coal, the FGD solids and fly ash are classified by the USEPA as non-hazardous. Presented in August, 1993, their final regulatory decision on wet FGD emission control waste stated that these materials are not regulated as hazardous wastes under CERCLA Subtitle C and officially placed them under Subtitle D as solid wastes under the jurisdiction of individual states. Classified as a residual solid waste, the State of Ohio EPA program encourages beneficial reuse of FSSS as long as water quality of the surrounding area is not affected. They require each specific project submit a proposal and description for beneficial use status. However, the process of mixing a FSSS with additional fly ash and lime makes the roller compacted mix a product and thus exempt from requiring Ohio EPA approval. However, correspondence with local and state regulatory officials is prudent to foster understanding of the technology and minimal environmental impact of beneficial uses of RCFGD.

The Ohio EPA judges from leachate water quality testing any potential risk. As shown in Table 2 the leachate from one FSSS and fly ash source being utilized are one example showing concentrations of heavy metal elements very much below concentrations considered hazardous (RCRA limits)and actually similar to primary drinking water standards. As permitted by Ohio EPA, the ASTM leachate procedure 3987-85 using distilled water was used instead of the TCLP method that uses acid. The levels are well below Ohio EPA residual waste Class III limits. Leachate concentration for elements other than the TCLP metals are shown.

CEMENTITIOUS POZZOLANIC AND SULFO-POZZOLANIC REACTIONS

There are two basic but related types of chemical reactions that are responsible for the hardening process. Both are a type of pozzolanic reactivity commonly used in stabilization and solidification of waste materials. The first hardening reaction is the more understood pozzolanic reaction where the high pH lime (CaO) solubilizes the silica (SiO_2), glassy amorphous alumina (Al_2O_3), and aluminosiliceous glass from the fly ash component in the presence of high pH and water. These reactions are similar to the hydration of portland cement. This relatively slow reaction solidification is noticeable in about four hours by the stiffening to a mortar or stiff paste like consistency. If compacted, this consumption of free moisture in the FSSS cake material will cause the sludge cake to harden and gain bearing strength. Calcium silicate hydrates ($xCaO - ySiO_2 - zH_2O$), calcium aluminate hydrates ($xCaO - yAl_2O_3 - zH_2O$), calcium silica-alumina hydrates ($wCaO - xAl_2O_3 - ySiO_2 - zH_2O$) and calcium alumina-ferro hydrates ($wCaO - xAl_2O_3 - yFe_2O_3 - zH_2O$) are the reaction products.

A secondary reaction begins once the calcium aluminate hydrates are formed. Often called sulfo-pozzolanic, calcium aluminate at high pH reacts with calcium sulfite and calcium sulfate react to form a class of compounds called calcium sulfo-aluminate or calcium aluminosulfate minerals. This type of chemical compound, called ettringite, is represented by the following reaction.

$$2Ca(OH)_2 + 3CaSO_4 \cdot 2H_2O + CaO \cdot Al_2O_3 + 3OH_2O \rightarrow (CaO)_6\ Al_2(SO_4)_3 \cdot 32H_2O$$

Another molecular formula for ettringite is written as $3CaO \cdot Al_2O_3 - CaSO_4 \cdot 32H_2O$. This reaction continues to occur for more than one year. It utilizes 32 moles of water for every 3 moles of available CaO and 3 moles of $CaSO_4$ consumed, and thus ettringite is a big contributor to long term development of compressive strength. However, as noted later, its long term stability is questioned. McCarthy and Tishmack express the reaction differently as follows:

$$6\ Ca^{2+} + 2\ Al(OH)_4^- + 3\ SO_4^{2-} + 4(OH)^- + 26\ H_2O \rightarrow Ca_6\ Al_2(SO_4)_3\ (OH)_{12} \cdot 26H_2O$$

They state the actual phase is more complex, with some carbonate substitution for sulfate and variable H_2O content. Also, Si can substitute for Al, forming solid solutions with thaumasite, $Ca_6\ Si_2\ (SO_4)_2\ (CO_3)_2\ (OH)_{12} \cdot 24H_2O$. [5]

PRODUCTION OF RCFGD: TWO CASE HISTORIES

FSSS that is produced for landfill disposal on any given day may not be suitable for beneficial uses such as structural fill, road base, or pond liner. A more controlled and batch type mixing process is preferable where quality and productivity are more assured. A quality control / quality assurance program can be more effective if there is a smaller or secondary pug mill to mix the FSSS containing extra fly ash with additional lime or lime related materials, i.e., lime kiln dust, and additional ash by-products i.e. bottom ash. The addition of both can offer a good means to help the FSSS achieve both more pozzolanic reactivity and a higher percent solids and therefore be closer to its optimum dry density necessary for facilitate the compaction effort. Otherwise, excessive levels of moisture or variations in the amount of fly ash in the FSSS component would prevent a uniform mix and hinder product quality control.

A process for developing RC base course mixes that will satisfy mix design criteria, i.e. 400 psi at 28 days, is being researched by DLC in cooperation with other organizations namely American Electric Power Service Corporation (AEP), VFL Technology Corporation (VFL), and The Ohio State University (OSU).

1993 OSU Cattle Feedlot Pavement: In 1993 DLC and OSU, Department of Civil Engineering performed laboratory studies that showed adequate RCFGD strengths could be made for a base course pavement at a cattle feedlot. In cooperation with the American Electric Power Service Corporation, FSSS from their Conesville plant was converted into RCFGD for a pavement to keep cattle out of the mud during the winter at the feedlot and a storage area for large round hay bales. As shown in Table 3, the ratio of fly ash to FGD was doubled from 0.8:1.0 for the FSSS control (landfill product) to 1.6:1.0 for the RCFGD product. Also, the lime content was increased from 2.0% in the FSSS to 6.5% for two test sections and 11.5% in a third section. Samples of each material were taken to lab and allowed to cure. The 28 day strength increased from 45 psi for the FSSS mix to 190-260 psi for the RCFGD mixes at 6.5% CaO. The 90 day strengths increased likewise from 100 psi to 480-580 psi. A third test at 11.5% lime did not increase strengths at the higher amount. A block of pavement was cut out and removed after

the first winter at 9 months age. A strength of 400 psi was found. More detail on this first RCFGD project has been previously reported.[2]

1995 Bob Evans Farm Cattle Feedlot Pavement: In the summer of 1995, an opportunity arose to use a portable pug mill to make lime activated RCFGD, operated by VFL Technology and in cooperation with American Electric Power Gavin Plant personnel. This means of secondary mixing provides a way to add extra ash, i.e., bottom ash or boiler slag, and extra lime bearing material into the FSSS in order to maintain better quality of the RCFGD mix by controlling the percent solids and cementitious reagent. The FSSS was specified to have minimum 1:1 FA to FGD. The pug mill has two variable speed feed hoppers. One is for the FSSS and one for additional bottom ash. A silo will store and feed the cementitious reagent. It produces continuous quantities upon demand much like an asphalt hot mix or ready mix concrete plant at a rate of about 120-150 tons per hour.

One of project objectives was to compare the extra lime fines to the use of lime kiln dust, which is generally 20% ± 5% quicklime and 75% pulverized limestone. Therefore, more is required. The dosages compared in the plant mixes described in Table 4 are 8% lime fines and 20% lime kiln dust (LKD). More research will determine the optimum dosage of each. Table 4 also shows a lab mix of 8% LKD. Unconfined compressive strengths with 8 and 20% LKD tests surpassed the 400 psi at 28 days age criteria. These strength and densities agreed closely with similar lab mixes performed earlier by American Electric Power's Civil Engineering Laboratory.[6] Details of results including costs and durability tests i.e. freeze-thaw resistance, will be the subject of a future report.

MIX DESIGN PROCEDURE TO MAKE RCFGD FROM FSSS

A proposed procedure is outlined for designing and confirming a mix design to meet the design strength for RCFGD and can be summarized in four steps:

Step 1 - Specification for FSSS: The first stage is to develop a specification or criteria for the fixated scrubber sludge solids (FSSS) that is to be the main component in the RCFGD mix. When placing an order for RCFGD, a separate stockpile of "high grade" FSSS can be segregated on the concrete storage pad. To start with, the filter cake solids should be maximized or have a minimum of 40% solids (wet weight basis). The amount of fly ash and lime added to make FSSS should be mixed to increase the percent solids to about 66% or more (a 66% solids wet weight basis equals to 51.5% on a dry weight basis). The ratio of fly ash to filter cake solids on a dry weight basis should approximate 1:1. More fly ash if available up to 1.6:1.0 may be better for more moisture control. At least 2-3% pulverized quicklime should be added to initiate the chemical reaction. Experience has shown the FSSS should cure at least one day in a stockpile before using it to make RCFGD but not more than 3 days. Over four days, the strength gain in the FSSS mix alone would be destroyed when re-mixing for RCFGD.

Step 2 - Develop procedure to design RCFGD: The second stage is to determine the optimum moisture content (OMC) so as to determine the amount of additional extra dry pozzolanic and cementitious material to increase the strength of RCFGD. Excessive water contents would prevent optimum compaction or maximum dry density. However, 2-5% of extra moisture is desirable to hydrate the extra lime required (~5% CaO as free, available and pulverized quicklime or equivalent).

a) The amount of free moisture that achieves a compacted base course of maximum dry density is determined by constructing / generating a OMC curve according to ASTM D-698[3]. It is reported on a dry weight basis i.e. weight of moisture divided by the weight of dry solids. An example is shown in Table 5.

b) The optimum moisture content is apt to be much lower than the moisture content of the FSSS. Additional ash and/or lime based cementitious fines, i.e. pulverize quicklime or lime kiln dust, needs to be added in a second mixing operation like that described at the VFL pugmill to closely approach the OMC. The amount of additional ash material needed can be represented by the following formula:

$$\text{OMC} = \frac{\text{water content present in FSSS}}{\text{solids in FSSS + additional solids needed}} \times 100$$

Example: Assume an OMC is found to be about 35% on a dry weight basis. Assume the FSSS is 66% solids on the wet basis. It contains 34% water. The amount of additional

ash required calculates to 0.31 lb for every 1.0 lb of FSSS. The added ash is assumed here to be dry. Variable speed settings of each hopper feeder can be set accordingly.

$$35\%\ \text{OMC} = \frac{0.34\ \text{water}}{0.66\ \text{FSSS} + 0.31\ \text{added ash}} \times 100$$

c) Strength gain should be confirmed. In this phase of Step 2, one is to mold specimens to determine unconfined compression strength (UCS) of the OMC mix. This should be done in conjunction with checking levels of extra cementitious reagent in order to confirm strength gain from at least 7 to 28 days but as early as 4 days curing. UCS should be determined according to ASTM D-2166-85. Dry and wet density would be calculated. The water content of the broken procter cylinders for strength should be determined and recorded.

Step 3 - Field Demonstration Mix and Conformation, Field Sampling for UCS, Water Content, and Density: Once placed and compacted in the field in place densities and water content should be determined and compared to that designed. Molded samples for UCS should be made to cure and break for strength gain confirmation.

FIELD SAMPLING FOR UNCONFINED COMPRESSIVE STRENGTH, MOISTURE, AND DENSITY

The specimens would be extruded on site, kept moist, and transported safely to a laboratory curing chamber. Unconfined compressive strength is determined at 7, 14, 28, and 60 days. Two specimens are broken on at least two of the days to check for repetition/consistency. Each molded sample should be weighed and checked for wet density. After compaction and extrusion of the specimen, only a small amount of water should be observed on the base of the mold. Surfaces of the specimens should appear damp. The dry density can be determined after determining the free moisture of the uncompacted material assuming very little if any water was compacted out of the specimen during the molding process. Extra specimens for durability testing such as wet-dry or freeze-thaw resistance would also have to be made.

In place density measurements using the sand cone volumetric displacement procedure (ASTM D4914) or a Troxler nuclear densionmeter should be taken for comparison to the procter mold densities. The free moisture should be a few percentage points in excess of the OMC content to account for quicklime hydration.

RCFGD BENEFICIAL USE - NEED FOR CAUTION, PROOF OF DURABILITY

Road base construction using RCFGD in the thousands of tons have been applied in Florida and Texas.[7,8,9] Both lime and portland cement has been used as the stabilizing agent, and other sources than coal FGD wet sludge have been used. In the Ohio River Valley, power plants that scrub are more interested in learning how to design and construct beneficial use applications such as roller compacted pavement or structural fill. One of the major concerns for successful long term applications of this cementitious reaction in the more northern climate is the long term durability, most specifically resistance to degradation from freeze-thaw cycles.

The first record of attempting FSSS for roadbase construction in the Ohio Valley region was near Pittsburgh, PA, in 1977.[10] Cores of the road base were taken after 3 and 7 years for freeze-thaw testing by the vacuum saturation method as stipulated in ASTM C-593.[11] Strengths were not decreased as one might expect by this severe test.

The only recent work has been reported by researchers at OSU, AEP and VFL. They all used ASTM D 560 method titled "Freezing and Thawing Compacted Soil-Cement Mixtures."[3] However, Wolfe, Chen, and Hargroves at OSU [12,13] modified the procedure to gauge results by testing UCS rather than measuring weight loss after each freeze-thaw cycle. VFL and AEP are researching a pass-fail criteria based on volume change and strength as opposed to the conventional practice of measuring weight loss per ASTM D560.[6] More research needs to confirm if this criteria can be met for RCFGD using extra lime and fly ash at the respective OMC.

Chen and Wolfe of OSU found good strengths under freeze-thaw conditions provided 5% extra lime was added to the FSSS before compaction and the time from compaction to first freeze was at least 60 days. Also, they showed that water contents above 40% (dry weight) exhibited low strength after 12 cycles of freeze-thaw.[12] Hargroves of OSU showed that after 60 days curing the 12 cycles of freeze-thaw lowered compressive stengths from about 600 psi to 300-

500 psi..[13] More research must confirm if this loss in strength is acceptable. In general, more experience by various researchers is needed before a consensus can be found on how to perform freeze-thaw testing and what criteria and parameters to judge user acceptance.

Another major need for answers to questions from highway construction design engineers is the potential for swelling reactions like those reportedly caused by other types of compacted FGD by-product materials. Specifically, dry FGD by-products from fluid bed combustion and duct injection systems have similar chemical and mineralogical composition and cementitious strength gaining reactions when conditioned with water and then compacted. Studies have reported dry FGD by-products have swelling characteristics due to the slow hydration and formation of ettringite.[14] Swelling has been known to occur after clay soils high in sulfate content were stabilized with lime in order to construct a road.[15] Graham et.al. reported that under a confining pressure, ettringite formed preferentially inside available pore space, indicating that the formation mechanism may be regulated by a surcharge.[16] Others fear the subsequent formation of thaumosite ($Ca_6Si_{12}(CO_3)_2(SO_4)_2(OH)_{12}\cdot 24H_2O$) may further degrade performance.[5,17] Still others have reported studies where the addition of extra pulverized fly ash improved durability of the dry FGD mixtures for structural fill or pelletized for use as construction aggregates.[18] Papers on FSSS by the noted author Charles Smith of Conversion Systems, Inc. have never mentioned potential swelling or descriptive tests to predict same.[4,5,8] Saylak et.al. states ettringite is stable if there is ample supply of sulfate available.[6] They recommend using low alumina content portland cement as the cementitious stabilizing agent. Long term swelling tests need to be conducted using ASTM method D4546.[2]

ASTM SUB-COMMITTEE 50.03

The ASTM E50.03 coal ash task group recently published a standard ASTM P5 23-95 "Guide for the Use of Coal Combustion Fly Ash Structural Fills".[19] This provisional guide covers the design and construction procedures for consideration of engineering, economics, and environmental factors in the development of fly ash structural fills. Committee E-50 covers environmental risk assessment. The sub-committee E50.03 is responsible for pollution prevention, reuse, recycling, and environmental efficiency. Utilization of coal combustion fly ash conserves land, natural resources, and energy. A similar effort in creating guidelines should be considered for RCFGD for use as a stabilized base and structural fill.

SUMMARY AND CONCLUSIONS

Roller compacted stabilized base course for construction projects required to withstand heavy weight traffic is a potential high volume beneficial use for fixated FGD scrubber sludge solids (FSSS) that are enhanced by the addition of extra fly ash/bottom ash and quicklime in order to efficiently compact to maximum density and thereby attain higher compressive strength and long-term durability.

The chemical composition of the mix components and cementitious chemical reactions that cause increases in bearing strength are discussed. The common practice of producing FSSS for landfill disposal is compared to the advanced mixing process to obtain higher strengths for beneficial use applications in land construction. Leachate water quality of FSSS is non-toxic and similar to primary drinking water standards. State of Ohio regulatory policy encourages large scale demonstrations of beneficial use. Processing to enhance the FGD by-products for beneficial use eliminates the requirement for regulatory approval, but the EPA authorities still need information for better understanding and public support.

Two case histories and a procedure for designing a mix to have optimum moisture content (OMC) were discussed. One recent case used a portable pug mill to obtain OMC and increased strength by addition of extra coal ash and lime. Twenty percent lime kiln dust was successfully used as a substitute for 8% pulverized quicklime. Adequate strength of 400 psi can be achieved.

Concerns about long term durability are discussed. There is not enough field demonstration evidence that satisfactory long term durability can be attained under freeze-thaw conditions. Better consensus is needed on how to test for durability. The risk of potential swelling from expansive long term hydration reactions of ettringite formation must be clarified. ASTM E-50 committee on environmental risk assessment using recycled products offers a means to write a specification for designing roller compacted base course using FGD and coal ash by-products. Efforts to develop beneficial uses of these materials should be enhanced by the growing public interest in concepts and the example of environmental sustainability.

REFERENCES

1. American Coal Ash Association, 1995, "1993 Coal Combustion By-Product Production and Use," Alexandria, VA.

2. Wolfe, W.E, and Cline, J.H., 1995, "A Field Demonstration of the Use of Wet and Dry Scrubber Sludges in Engineered Structures," Proceedings: Eleventh International Symposium on Use and Management of Coal Combustion By-Products, American Coal Ash Association, Alexandria, VA, Paper No. 7.

3. American Society Testing & Materials, 1989, Annual Book of ASTM Standards, Vol. 4.08, Philadelphia, PA.

4. Smith, C.L., 1985, "Lime-Based Fixation of Flue Gas Desulfurization Wastes," ASTM Symposium STP 931, Lime for Environmental Uses, Philadelphia, PA, June, pp 52-68.

5. McCarthy, G.J. and Solem-Tishmack, J.K., 1994, "Hydration Mineralogy of Cementitious Coal Combustion By-Products," Advances in Cement and Concrete Materials Engrg. Div./ASCE, NY, NY, Proceedings: 87th Annual Meeting Air & Waste Management Association, Cincinnati, Ohio, June 19-24, 1994.

6. Personal Communications with R.J. Collins of VFL Technology and P. Amanya and E. Booth of American Electric Power, November 15, 1995.

7. Smith, C.L., 1993, "15 Million Tons of Fly Ash Yearly in FGD Sludge Fixation," Proceedings: Tenth International Symposium on Coal Ash Utilization, American Coal Ash Association, Alexandria, VA, Paper No. 2.

8. Saylak, D., Sorensen, G., and Golden, D.M., 1994, "Construction Applications for FGD By-Products," Proceedings: 87th Annual Meeting Air & Waste Management Association, Cincinnati, Ohio, June 19-24, 1994.

9. Prusinski, J.R., et al., 1995, "Development and Construction of Road Bases from Flue Gas Desulfurization Material Blends," Proceedings: Eleventh International Symposium on Use and Management of Coal Combustion By-Products, American Coal Ash Association, Alexandria, VA, Paper No. 22.

10. Smith, C.L., 1989, "Fixated FGD Scrubber Solids," Proceedings: Power-Gen, 1989, New Orleans, LA, December, 1989, pp 312-325.

11. American Society for Testing & Materials, 1993, Annual Book of ASTM Standards, Vol. 4.01, Philadelphia, PA.

12. Chen, X. and Wolfe, W.E., 1995, "The Durability of Stabilized Flue Gas Desulfurization Sludge," Proceedings: University of Kentucky Ash Utilization Conference, Lexington, KY, October 23-25, 1995.

13. Hargroves, M.D., 1994, "The effect of Freeze-Thaw Cycles on the Strength of Flue Gas Desulfurization Sludge," Master Thesis, The Ohio State University, Department of Civil Engineering.

14. Adams, D.A. and Wolfe, W.E., 1993, "The Potential for Swelling in Samples of Compacted Flue Gas Desulfurized By-Product," Proceedings: Tenth Ash Use Symposium, American Coal Ash Association, Alexandria, VA, Vol. 2, Paper No. 61.

15. Mitchell, J.K. and Dermatas, D., 1992, "Clay Soil Heave Caused by Lime-Sulfate Reactions," Innovations and Uses for Lime, ASTM STP 1135, American Society for Testing and Materials, Philadelphia, PA, pp 41-64.

16. Graham, V.M., et al., 1993, "Mineralogical Transformations of Ettringite in Concrete Derived from Dry FGD By-Products," Proceedings: Pittsburgh Coal Conference, University of Pittsburgh, School of Engineering, Pittsburgh, PA, pp 864-868.

17. Weinberg, A. and Hemmings, R.T., 1995, "Results from Continued Monitoring of Advanced Coal Combustion By-Products: The Effects of Mineral Transformations on Material Properties," Proceedings: University of Kentucky Ash Utilization Conference, Lexington, KY, October 23-25, 1995.

18. Wu, M.M., et.al, 1995, "Composition Effects on Durability of Aggregates made from Coal Combustion By-Products," Proceedings: University of Kentucky Ash Utilization Conference, Lexington, KY, October 23-25, 1995.

19. American Society Testing Materials, 1995, "Provisional Standard Guide for Use of Coal Combustion Fly Ash in Structural Fills," designation PS 23-95, Philadelphia, PA

Table 1

Chemical Composition of RCFGD Components

	Range, % by weight		
	Conesville FGD Solids	Fly Ash	Quick Lime
CaO	29 - 35	1 - 3	87 - 95
MgO	1.3 - 1.5	0.5 - 1.0	3 - 6
SiO_2	10 - 17	33 - 45	1.8 - 2.9
Al_2O_3	5 - 10	17 - 22	0.5 - 0.7
Fe_2O_3	5 - 10	20 - 34	0.2 - 0.3
Na_2O	<0.2	0.2 - 0.6	trace
K_2O	0.2 - 0.8	1.3 - 2.2	trace
SO_3	26 - 33	1.0 - 2.4	<0.20
LOI	10 - 13	1 - 6	0.4 - 1.5

Table 2

Leachate Tests of Conesville FSSS and Fly Ash
ASTM Distilled Water Extraction (18 hr., 20:1 water : solid)

units: mg/l	FSSS Conesville	Fly Ash Conesville	Class III Residual Waste	RCRA Limits	Primary Drinking Water Standards
Parameters - toxic metals:					
As	0.008	0.15	1	5	0.05
Ba	0.22	0.13	30	100	1
Cd	<0.005	0.01	0.2	1	0.01
Cr	<0.002	0.02	1	5	0.05
Pb	<0.002	<0.002	1	5	0.05
Hg	<0.0002	<0.0002	0.04	0.2	0.002
Se	0.007	<0.005	0.2	1	0.01
Ag	<0.005	<0.003	1	5	0.05
Other Trace Elements :					
B	0.36	–	–		
Cu	0.001	0.27	–		
Cl	61	2	7,500		
F	0.8	0	120		
Fe	<0.01	5	9		
Mn	<0.01	0	9		
SO_4	36	650	7,500		
Na	7.4	10.5	7,500		
TDS	560	940	10,000		
pH	10.5	4.1			
alkalinity	260	<1			
acidity	<1	202			

Table 3

RCFGD at OSU Feedlot made from Conesville Plant FGD Solids (FSSS) plus extra Fly Ash and Lime, September, 1993

	Control Mix (FSSS)	Extra Lime Added at OSU Feedlot	Extra Lime Added at Conesville	Extra Lime, Conesville and OSU
FA:FGD (dry)	1.0 : 1.0	1.6 : 1.0	1.6 : 1.0	1.6 : 1.0
Total Lime Added, %	2	6.5	6.5	11.5
Per Cent Solids	52.6	61.7	63.1	62.8
Wet Density, lbs./cu.ft.	101.5	97.2	99.8	99.1
Dry Density, lbs./cu.ft.	68.8	70.3	72.9	72.2
Unconfined Compressive Strength, psi :				
28 day	45	190	260	220
90 day	100	580	480	310

Table 4

Roller Compacted FGD Base Course made at Bob Evans Feedlot and mixed at Gavin AEP - VFL Pug Mill, August, 1995

	Plant Mix	Plant Mix	Lab Mix
Extra Lime:	8% Lime Fines	20% Lime Kiln Dust	8% Lime Kiln Dust
Mix Design:			
FA:FGD (1)	1.0:1.0	1.0:1.0	
FSSS (2)	80%	80%	100%
BA (3)	20%	20%	0%
Results:			
Moisture	29%	32%	34%
Wet Density: lbs./cu.ft.	107.2	110.1	103.8
Dry Density: lbs./cu.ft.	83.2	83.6	85.0
Unconfined Compressive Strength: psi			
7 day	90	100	114
14 day	190	220	270
28 day	350	470	400
60 day	520	790	510 (87 day)

Notes: 1) FA = Gavin flyash; FA:FGD ratio is on dry weight basis to make FSSS.
2) FSSS is the FA:FGD mixture plus 2% quicklime mixed at Gavin pugmill.
3) BA is the bottom ash mixed along with extra lime at VFL pug mill.

Table 5

Moisture-Density Relationship for Gavin FSSS + 20% Lime Kiln Dust

Proportions adjusted to meet the criteria for the 4 different WC ratios.

SAMPLE	WC2	WC3	WC4	WC5
WT MOLD + WS (lb.)	13.96	14.06	14.12	14.16
WT MOLD (lb.)	10.42	10.42	10.42	10.42
VOL MOLD (cu. ft.)	0.0333	0.0333	0.0333	0.0333
WET DENSITY (lb./cu.ft.)	106.3	109.3	111	112.3
WT TARE + WS (g)	232.9	234.7	242.2	224.3
WT TARE + DS (g)	197.9	194.8	198.2	178.6
WT TARE (g)	21.9	21.9	21.9	21.9
WT DS (g)	176	172.9	176.3	156.7
WT WATER (g)	35	39.9	44	45.7
WATER CONTENT %	0.20	0.23	0.25	0.29
DRY DENSITY (lb./cu.ft.)	88.67	88.86	88.8	87.05

(legend: WT = weight, WS = wet solids, DS = dry solids)

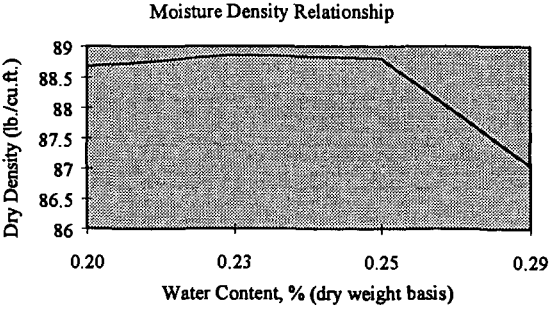

ACKNOWLEDGMENTS

The author wishes to thank Professor Wm. Wolfe of The Ohio State University, Department of Civil Engineering, and Mr. Pedro Amanya and Mr. Greg Keenan of the American Electric Power Service Corporation for their advice and information in preparing this paper.

THE EFFECT OF CARBONATION REACTIONS ON THE LONG TERM STABILITY OF PRODUCTS MADE FROM DRY FGD MATERIALS.

T.L. Robl[1]; U.M. Graham[1]; D.N. Taulbee[1] and W. Giles[2], 1. University of Kentucky, Center for Applied Energy Research, 3572 Iron Works Pike, Lexington, KY 40511, 2. Freeman United Coal Mining Co., Crown Complex, P.O. Box 259 Farmersville, IL 62533

Keywords: Ettringite, Carbonation, FGD-Material Stability

ABSTRACT

Flue gas desulfurization (FGD) technologies such as spray dryers and fluidized bed combustors produce a dry by-product which often has substantial quantities of unreacted lime or hydrated lime. The reactivity of the lime with the other constituents upon hydration, imparts a cementitious property. The major early hydration reactions include: the hydration of calcium sulfate to gypsum, the formation of the cementitious mineral ettringite, a calcium sulfo-aluminate-hydrate and the formation of CAS gels. Weathering is found to decrease the strength and integrity of these materials. Field studies, based on soil gas analysis, indicate that these materials rapidly absorb CO_2. Studies of the mineralogic transformation which take place upon hydration and subsequent weathering indicate that carbonation reactions result in extensive calcium carbonate formation over time. However, carbonate formation takes place at the expense of gypsum, not ettringite as suggested by laboratory studies. Based on field evidence and X-ray data, ettringite appears to be relatively stable.

INTRODUCTION

Dry lime and limestone based flue gas desulfurization methods, such as fluidized bed combustion and spray dryer technologies, produce a dry product which typically contains free lime in a hydrated or unhydrated form. Free lime along with water, the products of sulfation, typically anhydrite $CaSO_4$, or hemi-hydrate ($CASO_4.1/2H_2O$), and the decrystalized alumino-silicate mineral matter from the coal readily react to form a hardened mass. Because of this cementitious characterization many uses for these materials have been proposed such as structural fill in mines, road base stabilization, grouts and, in a pelletized form, artificial aggregates for concrete and asphalt application. The use of this material is dependent in most cases on the material's strength, durability and long term stability.

However, the principal cementitious mineral, ettringite, has long been known to be susceptible to attack and degradation from carbonation. Laboratory experiments have determined that ettringite can be readily broken down with high concentrations of CO_2 under hydrous conditions to more fundamental compounds.[1,2] This results in a loss of strength and material integrity.

STUDY OBJECTIVES, METHODS AND MATERIALS

The objective of this work is to determine how important carbonation reactions are and their effect on the nature of the materials. Studies are being conducted of CO_2 uptake in field lysimeters filled with materials from the U.S. Department of Energy and U.S. the Environmental Protection Agency sponsored demonstration of the Coolside technology at Ohio Edison's Edgewater Power Plant (Coolside #2).[3] The Coolside demonstration material was placed in three large (3x3x3.5 m deep) field lysimeter cells. These lysimeters were packed at densities within 5% of 1,100 Kg/m^3 (cell L3), 1,040 Kg/m^3(L2), and 720 K/m^3(L1). The cells were monitored for their mineralogical changes after having been exposed for three seasonal cycles. Drill cores were prepared from the upper 0.5 meters of the three lysimeters and the cored material was analyzed for ettringite formation using X-ray diffraction and scanning electron microscopic analyses. Ettringite was observed to have formed in all lysimeters upon reaction of the FGD waste material with the downward penetrating rain water. In April of 1994 the lysimeters were equipped with gas monitoring wells at 20, 40 and 76 cm of depth (Table I). The wells consist of glass tubes, which are open at one end to a given depth and capped with a septum to allow gas to be withdrawn for analysis. In April of 1995, wells at 107 cm of depth were added.

The impact of weathering on the mineralogy of the materials was conducted on samples collected at the Freeman United Coal Company's Crown III Mine, located in central Illinois. The company has pioneered fluidized bed combustion backhaul and disposal methods at this site which was open in 1991. Circulating fluidized bed combustion (CFBC) fly ash is hauled in semi-trailer dump trucks to the mine. The ash is dumped into a hopper and metered out with screw feeders and mixed with water before being pumped to the disposal site. The solids are settled from the slurry and the water returned to the mixer. The solids settle into a mud-like paste that typically hardens within days. In addition to the fly ash materials, coarser bottom ash representing about 20% of the total material received is also handled at the mine. It is disposed of dry in the landfill area and

then wetted.

EARLY HYDRATION AND CEMENTITIOUS REACTIONS

The comparison of the dry fluidized bed combustion materials varies but generally the materials consist of anhydrite ($CaSO_4$), lime (CaO), quartz (SiO_2), minor calcite ($CaCO_3$) and glassy silicious ash particles. In spray dryer and duct injection materials the lime and anhydrite may be partially or fully hydrated. The important early hydration reactions consist of the hydration of the lime to portlandite $Ca(OH)_2$, and its partial dissolution to form a highly alkaline solution, or

(1) $CaO + H_2O \rightarrow Ca(OH)_2 \approx Ca^{2+} + 2OH^-$

and the hydration of anhydrite to gypsum ($CaSO_4 \cdot 2H_2O$), or

(2) $CaSO_4 \rightarrow Ca^{2+} + SO_4^{2-} + 2H_2O \approx CaSO_4 \cdot 2H_2O$

Anhydrite is an orthorhombic mineral and is much denser (2.98 g/cm^3) and more soluble ($K_s = 4.2 \times 10^{-5}$) than monoclinic gypsum (2.32 g/cm^3 and $K_s = 2.4 \times 10^{-5}$). The anhydrite-gypsum transition probably does not occur in the solid state, but rather through a dissolution-precipitation mechnanism. Another very important reaction which takes place rapidly upon hydration is the formation of ettringite ($Ca_6Al_2(SO_4)_3(OH)_{12} \cdot 26H_2O$),

(3) $6\ Ca^{2+} + 2\ Al(OH)_4^- + 3\ SO_4^{2-} + 4\ OH^- + 26\ H_2O \rightarrow Ca_6Al_2(SO_4)_3(OH)_{12} \cdot 26H_2O$

The formation of ettringite is a competing reaction to that of gypsum. However, it also requires alumina and hydroxide ions and is typically found on, or near, coal ash particles, its source of alumina.

The ideal form of ettringite is $Ca_6Al_2(SO_4)_3(OH)_{12} \cdot 26H_2O$. Stoichiometric ettringite, however, is an artifact of the laboratory, and in nature it is variable in composition. Another important member of the ettringite family is thaumasite, $Ca_6Si_2(SO_4)_2(CO_3)_2(OH)_{12} \cdot 24H_2O$ which contains silica in substitution for some of the alumina and carbonate for some of the sulfate. It is now believed by some that thaumasite and ettringite form a solid solution series.[4]

The structure of ettringite is complex. Work by Moore and Taylor determined that ettringite had a trigonal hexagonal unit cell which consists of columns which have the composition $(Ca_6[Al(OH)_6]_2 \cdot 24H_2O)^{6+}$ which are aligned along the crystallographic c-axis (Al^{+3} ions are octahedral coordinated by $(OH)^-$) and are accompanied by channels of the composition $((SO_4)_3 H_2O)^{6-}$.[5]

CARBONATION REACTIONS

The rapid reaction of carbon dioxide with fresh CFBC material, where ettringite had not yet formed, was measured in our own laboratory experiments and presented previously. We found that the rate of uptake and quantity of gas absorbed was highly dependent upon the degree of hydration.[6] Dry samples of ettringite also do not react significantly with CO_2. Hydrated samples of ettringite rapidly reacted with CO_2 and decomposed to form gypsum, aluminum hydroxide and calcite.

The reactivity of CO_2 with synthetic ettringite in the laboratory is not directly relatable to complex mineral assemblages under field conditions. As part of our field study of the leaching potential of the materials generated by the Coolside process, we measured the concentration of CO_2 in both the soil gas and the gas in the Coolside FGD materials. Concentrations of CO_2 as high as 3% were measured in the soil gases overlying the Coolside materials but were either near the limits of detection or unmeasurable in the gases within the materials themselves or near the soil-FGD material boundary (Table I). Thus, field observations confirmed the absorption of CO_2 by the FGD materials found in the laboratory experiments.

MINERALOGIC TRANSFORMATIONS

The mineralogic transformations which take place during weathering was studied in samples collected from the Freeman United FDG disposal area. A suite of 19 samples were collected, ranging in age from fresh unhydrated materials to severely weathered samples which were approximately 3 years old.

The fresh unhydrated samples were composed of anhydrite, lime and glassy silicious material derived from the coal. Ettringite was found to form rapidly, as it is an important mineral in the 1 day and 1 month old samples and was the dominant mineral phase present in some of the more aluminum rich samples (Figure 1). The total amount of ettringite formed correlated strongly with the amount of alumina in the samples, suggesting that its formation was limited by the availability of this component.

The older samples collected strongly showed the effects of carbonation. They were in general weak and friable compared to the freshly hydrated samples. The amount of calcite present in the older samples was found to be much higher. The hydrated fly ash samples had an average of 6.7.% CO_2 versus 16.7% in the fly ash samples older than one year. Thus atmospheric CO_2 is a major reactant in the system.

At very high pHs, i.e. ~12, such as developed by a solution saturated with $Ca(OH)_2$, CO_2 is readily absorbed, reacts directly with the hydroxide and disassociates to the carbonate ion,
(3) $CO_2 + OH^- \rightarrow HCO_3^- \leftrightarrows H^+ + CO_3^{2-}$

The carbonate and calcium ions form calcium carbonate, which is highly insoluble at an elevated pH.

The concentration of sulfate in the samples was found to decrease in older samples by about 25%. This was concomitant with the increase in carbonate, which suggests that, in the longer term, calcite is replacing gypsum,
(4) $CO_3^{2-} + CaSO_4 \cdot 2H_2O \rightarrow CaCO_3 + SO_4^{2-} + 2H_2O$

Gypsum all but disappeared in the older samples. This is not unexpected, as calcite has a lower solubility product than gypsum (pK_s~ 8.4 for calcite vs pK_s~4.6 for gypsum at 25 °C), and is much less soluble under alkaline conditions.

In general the field study indicated that ettringite is highly stable in the weathering environment, as the X-ray diffraction results indicated its presence in abundance in all of the older samples (Figure 1). The most severely weathered sample contained no gypsum and did show some attenuation of the ettringite peaks relative to the other samples, and the ettringite in this sample may have undergone some weathering induced decay. However, in general the ettringite in the samples was found to be highly stable relative to other neoformed hydrous minerals such as gypsum and portlandite.

SUMMARY

The field studies fully confirmed the laboratory measurements indicating the highly reactive nature of the dry FGD materials with respect to CO_2. However, direct carbonation of ettringite was not found. The primary carbonation reaction is the replacement of gypsum by calcite and the presumable loss of sulfate from the system. Only when the gypsum was exhausted was evidence found for the carbonation of ettringite. McCarthy et al. found thaumasite forming in weathered AFBC and LIMBs materials which they studied and noted that the samples lost strength when thaumasite appeared.[7] No Thaumasite was detected in any of the weathering products for these materials. The loss of competency and strength in these samples appeared to be a function of the breakdown of matrix minerals other than ettringite, such as gypsum and calcite.

ACKNOWLEDGEMENTS

This work was supported in part with funds provided by the United States Department of Energy Through Cooperative Agreement No.DE-FC21-93MC30251.

REFERENCES

1. Grounds, T. H.G. Midgley and D.V. Nowell, 1988, Carbonation of Ettringite by Atmospheric Carbon Dioxide. *Thermochimica Acta*, **V 135**, p. 347-352.
2. Ghorab, H.Y., D. Heinz, U. Ludwig, T. Meskendahl and A. Wolter, 1980, On the Stability of Calcium Aluminate Sulfate Hydrates in Pure Systems and in Cements. *7th International Congress on the Chemistry of Cement*, **V IV**, Paris, France, p. 497-502.
3. Kanary, D.A., R.M. Statnick, H.Yoon, D.C McCoy, J.A. Withum and G.A. Kudlac, 1990, Coolside Process Demonstration at the Ohio Edison Company Edgewater Plant Unit 4 - Boiler 13. *Proceedings, 1990 SO_2 Control Symposium,* EPRI and U.S. EPA, Ses.7A, **V 3**, 19p.
4. McCarthy, G.J. and J.K. Solem-Tishmack, 1994, Hydration Mineralogy of Cements Coal Combustion By-Products, Proceedings of an Engineering Foundation Conference, *Advances in Cement and Concrete*, p. 103-121.
5. Moore, A.E. and Taylor, 1968, *Nature*, **V 268,** p.1085.
6. Taulbee, D., U.M. Graham, R..F. Rathbone and T.L. Robl, 1995, Investigation of the CO_2 Absorption Capacity of Dry FGD Wastes. *Preprints, Division of Fuel Chemisty, ACS*, **V 40,** p.858-862.
7. McCarthy, G.J. D.G. Grier, J.A. Parks, S.D. Adamek, 1995, Long Term Stability of Disposed Cementitious Coal Combustion By-Products. *Proceedings, 1995 International Ash Utilization Symposium*, University of Kentucky, CAER, Lexington, KY, 6p.

Lysimeter	Material	Depth	N	Avg %CO_2	Std Dev	Max	Min
L1-Coolside	Soil	20	39	0.531	0.392	1.9	0.05
	Soil	46	38	0.152	0.100	0.4	dl
	Soil/FGD	76	38	0.008	0.033	0.2	dl
	FGD	107	14	0.002	0.005	0.015	dl
L2-Coolside	Soil	20	39	0.486	0.314	1.4	0.05
	Soil	46	39	0.115	0.114	0.63	dl
	Soil/FGD	76	39	0.013	0.031	0.15	dl
	FGD	107	14	0.001	0.003	0.01	dl
L3-Coolside	Soil	20	30	0.693	0.620	2.8	dl
	Soil	46	29	0.992	0.892	3.2	0.02
	Soil/FGD	76	31	0.098	0.351	2	dl
	FGD	107	10	0.007	0.007	0.015	dl
L4-PCC FA	Soil	20	39	0.218	0.221	0.8	dl
	Soil	46	38	0.084	0.068	0.3	dl
	Soil/FA	76	39	0.223	0.214	0.84	dl
	Fly Ash	107	14	0.313	0.280	1	0.04

Table I. CO_2 Concentration Measured in Gas Wells Located Above and in Lysimeter Field Cells Filled with Coolside FGD Materials. Control Cell L4 is Filled with Conventional Fly Ash. CO_2 is in Percent Volume. Atmospheric CO_2 Concentration is Approximately 0.036% (360 ppm) at This Site, Detection Limit (dl) is ~0.0150% (150 ppm).

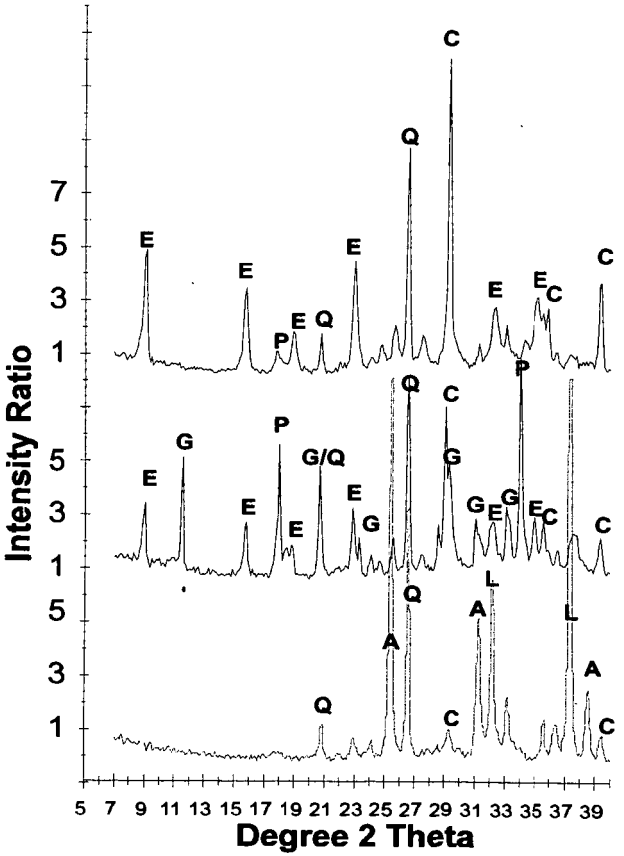

Figure 1. Xray Diffraction Spectra for As-Received dry FGD Material (Lower, Dotted Trace), Recently Hydrated Material (1 Week Old) and Highly Weathered Material (Upper, Approximately 2.2 years Old). Peaks for Calcite (C), Gypsum (G) Anhydrite (A) Ettringite (E), Portlandite (P), Quartz (Q), Lime (L) are Indicated.

CHARACTERISTICS OF PNEUMATICALLY-EMPLACED DRY FLUE GAS DESULFURIZATION MATERIALS

S.D. Carter, R.F. Rathbone, U.M. Graham, and T.L. Robl
Center for Applied Energy Research
University of Kentucky
3572 Iron Works Pike, Lexington, KY 40511

K.G. Sutterer
Department of Civil Engineering
University of Kentucky
Lexington, KY 40506

Keywords: Dry flue gas desulfurization material, pneumatic emplacement, mineralogy

ABSTRACT

The University of Kentucky in collaboration with the Department of Energy, Addington, Inc. and Costain Coal is currently developing a commercial concept for the haul back of dry flue gas desulfurization materials (FGDM) into highwall mine adits. The University's Center for Applied Energy Research (CAER) is investigating emplacement systems for a mine demonstration which is planned for the third quarter of 1996. A laboratory-scale transport system has been built at the CAER to evaluate the potential of pneumatic transport for FGDM emplacement. The system is modeled after shotcreting systems in which water is mixed with cement (FGDM) in a nozzle at the end of the pneumatic pipe. Solids travel approximately 70 ft in the lab-scale system at a rate of up to 6 lb FGDM/minute prior to impingement onto a sample collector. Prehydrated FGDM from a circulating fluidized bed combustor has been successfully emplaced onto vertically positioned sample surfaces without excessive dust liberation. The test program is focussed on determining the pneumatic conditions necessary to maximize the strength of the emplaced FGDM under anticipated mine curing conditions while minimizing dust formation. The mineralogy and strength of a pneumatically created sample are described following curing for 60 days.

INTRODUCTION

An important potential advantage of the FGDM haul-back concept for a highwall mining company is that 100% coal recovery is possible. Current highwall techniques must leave behind a structural web of coal, recovering approximately 65 to 75% of the resource. By leaving coal webs equivalent to the width of the mining head, it is possible with the haul-back scheme to fill the empty adits with FGDM and then mine the remaining coal web by using the hardened FGDM for structural support. This concept requires that the emplaced FGDM be sufficiently strong to provide support during the second phase of coal mining. The overall strength of the emplaced FGDM depends not only on its physical properties but also on the efficiency of emplacement. A relatively strong material is useless in this application if only, say, 75% of the adit is filled. Therefore, an essential characteristic of the emplacement technology for this haul-back concept is high fill efficiency. Another essential feature is that the material must be emplaced remotely because no worker should ever be required to enter a highwall mine with an unbolted roof. It is almost certain that roof bolting, accompanied by some amount of manual emplacement, would not be economically feasible.

A pneumatically-based system was chosen for initial consideration in this project because of the potential of shotcrete technology to completely fill the mine adit without forms. Hydraulic backfill of highwall adits is difficult because the adits are normally horizontal and slump prevents fill to the ceiling. With pneumatically-based (shotcrete) technology, however, concrete can be applied to vertical and even overhead surfaces, making it ideal for underground tunnel support. A prime example is its use in portions of the Metro subway system in Washington, D.C. For underground mining environments, Krantz found that shotcreting was successful in sealing, preventing spalling, and providing roof stability.[1] The ability to remotely line tunnels and shafts using shotcrete technology has also been demonstrated.[2,3] A disadvantage of shotcrete technology is that its production rates are relatively low compared to hydraulic concrete emplacement methods. Shotcreting has been primarily used for lining applications and not for bulk filling. However, it has been reported that a hybrid shotcreting system, the "Blastmixer," is capable of placing 50 tons of concrete per hour using large volumes of low-pressure air.[4]

EXPERIMENTAL

System Description. The source of pneumatic air for the emplacement test unit (ETU), Figure 1, is a vortex blower with a capacity of 220 ft^3/min @ 0 psig and 50 ft^3/min @ 7.9 psig. Therefore, the system is limited to low pressure operation. A pitot tube is used to measure the air flowrate at the inlet of the blower. A metered stream of water can be added at the

inlet of the blower to create a mist of water, if desired. The air flowrate is controlled by a gate valve downstream of the blower. The tstream of the blower. The temperature and pressure are mea outlet of the blower to provide a secondary measure of the air flowrate from performance curves provided by the blower manufacturer. Pressure is measured just downstream of the controlling gate valve to monitor the system for blockages.

Solids are injected into the two-inch schedule-40 steel pipe by a rotary valve. The valve can deliver FGDM at a rate of up to 6 lb/minute. A sealable hopper with a volume of 0.86 ft^3 supplies solids to the valve. Purge air is injected into the bin at three points to fluidize the solids and facilitate the feeding of the solids through the valve. An electric vibrator is mounted on the bin to alleviate problems with solids flow in the hopper. Addition of solids to the hopper during operation is not possible with the system in this configuration.

Solids are pneumatically transferred over a distance of 70 ft within 2-inch schedule-40 steel pipe which is covered by 0.5 inches of foam insulation. The pipe is insulated so that the extent of hydration reactions involving free lime (CaO) may be estimated when water is present during pneumatic conveyance. Thermocouples are located at 20-ft intervals to monitor any increase in temperature caused by hydration reactions. The pressure drop across the straight run of pipe is measured to monitor the air and solid flowrates.

The flexible metal hose connecting the last pipe section to the main run of pipe serves to permit the manual positioning of the nozzle. The nozzle must be maneuvered so that the FGDM shotcrete is evenly distributed over the sample panel. A thermocouple is placed through the bottom of the sample panel at its mid point so that it minimally intrudes in the path of the shotcrete jet. The nozzle is constructed of 1.5-inch schedule-40 PVC pipe and fittings (1.61-inch inside diameter). Water is injected radially inward through a ring of 24 holes (each 0.0145 inches in diameter) in the pipe.

Testing Objectives. The basic goal of the experimental plan is to evaluate the performance of FGDM as a function shotcreting parameters so that the requirements for the mine demonstration technology can be specified. Once the important shotcreting parameters are determined for the FGDM, a robotic vehicle based on state-of-the-art mining technology can be fitted with a shotcrete nozzle for remote emplacement. While any new material to be considered for shotcrete emplacement must be experimentally evaluated, the high free lime (CaO) content of many types of FGDM makes testing doubly important. Substantial amounts of heat are generated during the hydration of CaO to form $Ca(OH)_2$, promoting concerns about ignition of the coal seam and about possible steam explosions during emplacement. In addition, hydration of FGDM containing free lime in excess water has been shown to decrease the strength of sample pellets.[5] By prehydrating the FGD material with only enough water to hydrate the CaO, the strength of sample pellets following subsequent hydration was increased. The experimental plan addresses several scenarios regarding CaO hydration sequences, including the addition of water mist to the pneumatic transport pipe. The potential advantages of pre-wetting the FGDM during pneumatic transport are that the solids can be cooled by external heat exchange prior to emplacement and that the nozzle performance will be improved (i.e. less dust liberation). For this paper, the FGDM was prehydrated prior to pneumatic transport. While a fundamental goal of this effort is to optimize the workability of the material during emplacement, another important objective is to characterize the establishment of strength as a function of time. This paper examines the chemical and physical characteristics of a shotcrete sample produced from prehydrated FGDM after curing for 60 days.

X-Ray Diffraction Analyses. X-ray diffraction (XRD) analyses were performed on the prehydrated feedstock and on three samples of the cured FGDM slab 60 days after emplacement. Cu Kα radiation from 7° to 40° (63° for the feedstock) 2θ at 0.1° increments was utilized. Crystalline phases were identified using the JCPDS file on CD-rom. Samples were ground with a mortar and pestle prior to analysis.

Material Studied. Fly ash from the Archer Daniel Midland (ADM) co-generation plant in Decatur, Il. was used in this study. The plant utilizes circulating fluidized bed combustion (CFBC). Freeman United Mining Co. disposes of the FGDM at its Crown III facility in Farmersville, Il. The sample was collected in air-tight plastic drums upon arrival at the Freeman United facility. The FGDM was prehydrated at a weight ratio of 1 part water to 10 parts FGDM. This ratio was determined from previous work to slake the free lime without initiating cementitious reactions. The following minerals comprised the majority of the crystalline phases of the prehydrated FGDM as determined by XRD: anhydrite ($CaSO_4$), portlandite ($Ca(OH)_2$), quartz (SiO_2), hematite (Fe_2O_3), magnetite (Fe_3O_4), calcite ($CaCO_3$), periclase (MgO), and lime. In addition to these major minerals, ettringite ($Ca_6Al_2(SO_4)_3(OH)_{12}\cdot 26H_2O$) and gypsum ($CaSO_4\cdot 2H_2O$) were identified in minor amounts.

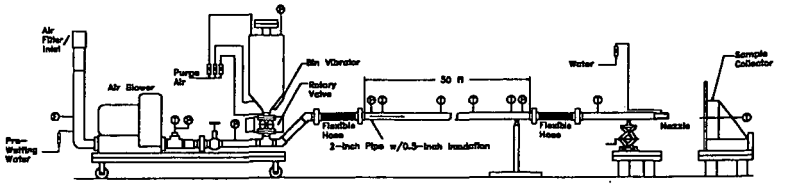

Figure 1. Schematic diagram of the pneumatic laboratory-scale emplacement test unit (ETU).

From this analysis it was determined that the free lime was almost completely converted and that cementitious reactions had not occurred to a significant degree. Therefore, it was confirmed that an optimal quantity of prehydrating water had been utilized.

RESULTS AND DISCUSSION

Nozzle Optimization. Shotcreting involves the creation of a turbulent jet of air that contains a mixture of solids and water mist. Ideally, the jet impinges on a surface, and particle-free air exits parallel to the surface, leaving the water and solids behind. In reality, however, a significant amount of water and solid particles remain airborne. A study was performed to determine the amount of mist loss as a function of air velocity and distance of the nozzle to the collection surface. While these water-only experiments may not be truly representative of the solid-water mix that remains airborne, it should at least indicate the trends that can be expected for these parameters. During these experiments, water at a rate of 15 gal/hr was injected into the nozzle. The air/water jet then impinged onto a flat plywood surface mounted vertically so that all the water that adhered to the surface would drain into a container and could be measured. The best results, approximately 80% retention efficiency, were obtained for the higher air velocity runs (362 ft/sec) at a distance of 4 ft between the collector and the nozzle. These conditions were used for the production of the shotcrete sample studied in this paper.

Production of FGDM Shotcrete Samples. For each test, a full hopper (0.86 ft^3) of dry FGDM is used. Complete mass balances are impossible to achieve because the system is not closed, permitting the escape of dust and mist. However, as discussed previously, it is estimated that 80% of the particles and droplets in the air jet are retained on the sample collector under the conditions of this study. Several slabs of FGDM shotcrete, approximately 3 inches in thickness and 1 foot in diameter, have been successfully prepared to-date. The pneumatically emplaced FGDM adhered to the vertically positioned plywood without slumping. The FGDM/water mixture exhibited stiffness immediately upon deposition suggesting a consistency that, in larger volumes, would be advantageous for bulk fill applications without the need for forms. For the FGDM shotcrete sample that is the focus of this paper, a water/FGDM ratio of 0.45 was utilized. This ratio was chosen because it was shown during previous tests to provide the best emplacement results. A relatively high water addition rate is beneficial because it reduces dust formation and it gives the material good workability for even deposition. Excessive water is squeezed out of the sample because of the force of the impingement. Therefore, the moisture content of the sample immediately after emplacement was likely lower than the 0.45 water/FGDM ratio that was produced in the nozzle. Moreover, the water content of freshly deposited shotcrete is not a highly variable parameter because the water content tends to be self regulating for the range of water addition rates that produce good shotcrete consistency.

Immediately after formation, the sample slab was covered with damp cloth and then with plastic to prevent moisture evaporation without providing excessive water. For strength tests, 2-inch-long 1.4-inch-diameter cores were produced using a carbide-steel-tipped hole saw. The cores were then kept moist prior to testing.

Strength Development During Curing. Unconfined compression tests were performed on core samples at 20 and 50 days following emplacement. The 20 day strength was 200 psi, and the

apparent density of the core sample was determined to be 1.47 g/cm^3. The strength at 50 days was determined to be greater than 650 psi. A more precise measure of the compressive strength at 50 days was not obtained because the testing apparatus was not set up for stresses greater than 1000 lb to be placed on the sample. An uncompressive strength of at least 500 psi will be necessary for the emplaced FGDM to prevent subsidence when the structural web of coal is removed during the second phase of mining. Previous work has shown that compressive strengths greater than 1000 psi are possible with these materials when the samples are formed and cured within a rigid container.[5] The present study has now confirmed that pneumatically emplaced FGDM will be able to develop sufficient strength for this backhaul concept.

Mineralogy of Cured FGD Shotcrete. A highwall coal mine adit can contain essentially no water, or it can be completely filled with water. Therefore, the amount of excess water that is available to the emplaced FGDM during curing can be quite variable. Curing of the slab of shotcrete was performed under conditions most closely related to a dry mine environment. This sample will be subsequently referred to as 'dry-cured' for simplicity, even though it was stored with some moisture present. A subsample of the main slab was removed after 7 days and completely immersed in water to simulate a water-saturated mine. Samples of the dry-cured and the water-immersed shotcrete were analyzed by XRD 60 days after pneumatic emplacement. To observe the change in mineral forms as a result of the hydration of the feedstock and the different curing environments, selected mineral peaks were standardized to the quartz {101} peak (Figure 2). By doing so, it is assumed that quartz remained unaffected by the curing condition and that quartz was not selectively eliminated or concentrated in the shotcrete during emplacement.

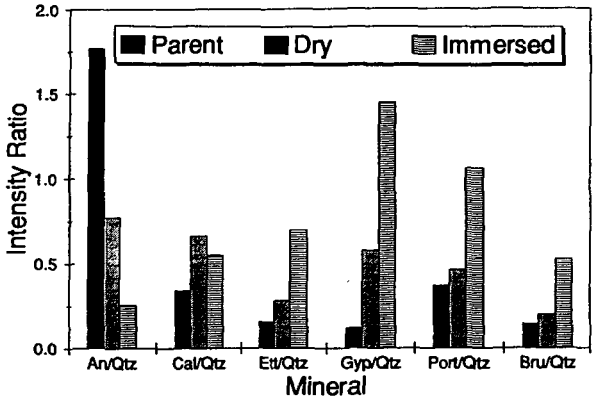

Figure 2. Comparison of major XRD peak intensities, normalized by quartz {101}, for the feedstock, dry-cured shotcrete, and water-immersed shotcrete samples.

The decreased abundance of anhydrite and corresponding increase in gypsum for the dry-cured sample compared to the feedstock (Figure 2) illustrates a major hydration reaction for this material. Other hydration reactions include the additional formation of ettringite, portlandite, and brucite ($Mg(OH)_2$). The formation of ettringite and gypsum are responsible for the strength that was shown to develop for the dry-cured slab. The amount of calcite was highest for the dry-cured sample because of contact with atmospheric CO_2. Continued hydration reactions were observed for immersed sample as illustrated by increased quantities of ettringite, gypsum, portlandite, and brucite. While the formation of additional ettringite can promote extra strength, the continued formation of gypsum from anhydrite by reaction with water that is diffusing back into the solid can reduce strength. Ettringite needles tend to fill pores which increase the density and strength of the FGDM cement. Gypsum also fills pores, but it can swell sufficiently to create cracks and decrease the strength of the solid. While no strength tests were performed for the immersed sample, it was obvious during sample preparation for XRD that the strength of the sample was diminished compared to the dry-cured sample. The formation of additional gypsum in the immersed sample may have been responsible for its reduced strength.

SUMMARY

Prehydrated FGDM from a CFBC was successfully emplaced onto a vertical surface by shotcrete technology. The strength developed by the dry-cured sample after 50 days was determined to be greater than 650 psi which is sufficient to support the mine roof during

mining of the structural web of coal. The levels of ettringite and gypsum in the dry-cured sample were consistent with the strength which had developed. It appears that some decrease in strength can be expected for these materials if subjected to excess water during curing in an unconfined environment.

ACKNOWLEDGMENTS

This work was supported by the U.S. Department of Energy under Cooperative Agreement No.: DE-FC21-93MC30251 (such support does not constitute an endorsement by the USDOE of the views expressed in this article). The authors would like to thank E. Coffey, M. Yewell and D. Taulbee of the CAER for assistance with this work. Also, W. Giles of Freeman United is acknowledged for providing FGDM to the project.

REFERENCES

1. Krantz, Gary W., *Information Circular 8994*, 1984, US Bureau of Mines.

2. Goff, James S., *Use of Shotcrete for Underground Structural Support*, Engineering Foundation Conference, 1974, ACI Pub. SP-45, pp. 405-417.

3. Monaghan, David A., Hoadley, David J. and Anderson, Grant L., *Shotcrete for Ground Support*, Engineering Foundation Conference, 1977, ACI Pub. SP-54, pp. 225-240

4. Ryan, T.F., *Gunite: A Handbook for Engineers*, 1973, Cement and Concrete Association, London, p. 26

5. Graham, U.M., Rathbone, R.F., Sutterer, K.G., and Robl, T.L., *1995 International Ash Utilization Symposium*, University of Kentucky, Center for Applied Energy Research, Oct. 23-25, Lexington.

STABILIZATION OF METAL-LADEN HAZARDOUS WASTES USING LIME-CONTAINING ASH FROM TWO FBC's AND A SPRAY-DRIER

J. Cobb, R. D. Neufeld, J. Pritts and V. Clifford
School of Engineering, University of Pittsburgh, Pittsburgh, PA 15261
C. Bender, Mill Service Co.; J. Beeghly, Dravo Lime Company., Pittsburgh, PA

Keywords: clean coal technology by-product reclamation, hazardous waste management, chemical stabilization

ABSTRACT

Clean coal technology by-products, collected from commercial operations under steady state conditions, are reacted at bench-scale with metal-laden hazardous wastes. Reaction conditions involve mixing calibrated weight ratios of by-product to hazardous waste with attention to minimizing added moisture. Of the 15 heavy metals monitored, lead appeared to be the element of greatest concern both from a leaching and a regulatory point of view. While leaching information is focused on lead stabilization, similar information exists for other metals as well. Stabilized solid products of reactions are sampled for TCLP evaluations. For samples showing evidence of metal stabilization, further experimentation was conducted evaluating optimum moisture content and development of physical strength (measured as compressive strength) over time of curing. Results show that certain hazardous wastes are highly amenable to chemical stabilization, while others are not; certain by-products provided superior stabilization, but did not allow for strength generation over time.

INTRODUCTION

The general objective this two-year project (*which has just completed the first year*) is to provide useful information and data on the ability of new and emerging sources of chemical treatment substances, in this case by-products from advanced clean coal technologies, to be used by the hazardous waste management community. These studies fall into two categories: (i) characterization of selected critical properties of by-products and (ii) observation of their ability to stabilize and solidify characteristic metal-laden solid hazardous wastes. A more commercial objective of the project is to link the producers of by-product with operators of hazardous waste treatment facilities in a mutually profitable manner. From the treatment facility operators' point of view, new sources of treatment material with abilities to stabilize and solidify their feed wastes can be added to their material source list. From the producers' point of view, new uses for by-products of their advanced coal combustors and desulfurizers will be developed and demonstrated. These producers have implemented various emission control technologies at coal-fired (and coal waste fired) electric power plants and are studying a number of others. The technologies currently in use generate significant amounts of by-products with limited commercial value. Consequently, much of the by-products are disposed as solid wastes. In particular, companies employing wet scrubber technologies for the desulfurization of flue gases have found few alternatives to disposal for the sludges generated in the processes due to the excess moisture present in the by-product. On the other hand, the contemporary development of dry desulfurization technologies offers great promise that these process by-products may have beneficial commercial application, such as those studied as part of this project.

Background: The project focuses on characteristic metal-laden hazardous waste. Federal regulations and many state regulations require generators of solid wastes to determine if the wastes they produce are hazardous. The determination process requires the generators to analyze leachates produced when the wastes are mixed with an extraction fluid and compare the results of that analysis to a published list that defines which parameters are of concern and the extract concentrations at which a waste containing those parameters is considered hazardous. Wastes that contain extract constituents on the list at concentrations that equal or exceed the published concentrations are considered to be characteristically hazardous (unless they are specifically excluded) and said to exhibit the "toxicity characteristic". Among the parameters included on the toxicity characteristic list published in the Federal regulations[1] are eight metals; the

[1] See 40 CFR 261.24.

concentrations at which a waste extract containing them is considered hazardous, are:

Metal Parameter	Hazardous Concentration in Leachate (mg/l)
Arsenic (As)	5.0
Barium (Ba)	100.0
Cadmium (Cd)	1.0
Chromium (Cr)	5.0
Lead (Pb)	5.0
Mercury (Hg)	0.2
Selenium (Se)	1.0
Silver (Ag)	5.0

Once a waste is determined to be hazardous, generators are restricted from directly disposing that waste anywhere in the United States. Prior to disposal, the waste must be treated to an extent that renders the resulting waste non-hazardous. The purpose of the treatment prior to disposal is to reduce the likelihood of migration of hazardous waste constituents from the waste. Wastes that are treated to meet the established standards can be disposed.

For purposes of this first-year research, toxic metal-laden wastes were treated at bench-scale by stabilization and solidification methods. Stabilization/solidification is a treatment technology used to reduce the hazard potential of a waste by converting the contaminants into their least soluble, mobile, or toxic form. Solidification refers to techniques that encapsulate the waste in a monolithic solid of high structural integrity. Solidification does not necessarily involve a chemical interaction between the wastes and the solidifying reagents but may mechanically bind the waste into the monolith. Similarly, stabilization does not necessarily involve solidification, since precipitation and complexation are also mechanisms of stabilization.

BY-PRODUCTS

The Clean Coal Technology (CCT) Program is a cooperative effort to demonstrate a new generation of innovative coal processes, which are environmentally cleaner and more efficient than conventional coal-burning processes [US DOE, 1991]. In dry CCT systems, a calcium-based sorbent (usually slaked lime, limestone, or dolomite) is injected directly into a furnace, ductwork, precipitator, or scrubber vessel that produces powdered or granular by-products, as opposed to the slurries associated with traditional wet scrubber systems. All these processes produce a by-product which is removed in the particulate control equipment. Dry by-products from lime or limestone injected into the furnace, such as in FBC systems, have neutralizing, sorptive, and cementitious properties that make them interesting as potential reagents for hazardous waste stabilization because of their high free quicklime (CaO) and anhydrous calcium sulfate ($CaSO_4$) contents. The specific composition of a particular type of by-product may vary widely depending upon the CCT process employed, the coal and sorbent composition, and the plant operating conditions. Since the chemical, physical, and engineering properties of dry CCT by-products are directly related to their history of use within the system and specific mineralogy, it is essential to accurately determine the mineralogical composition of these wastes and process configurations if safe and economical uses are to be defined.

Four clean-coal technology by-products were originally identified, but only the first three were used in this research.

1- Dry Scrubber Residue, supplied by CONSOL Inc. This material is from a spray drier at the outlet of a pulverized coal boiler burning high-sulfur eastern coal. Within the process, ash laden flue gas enters the bottom of the spray drier and all of the sulfur-capture residue rises through the upper port with the fly ash. The residue contains 45% fly ash, 36% $CaSO_3/CaSO_4$, 10% $Ca(OH)_2$, 2% $CaCO_3$, and 7% other inert material with moisture content of 2% or less.

2- Residue from a Coal-Fired Pressurized Fluid Bed Combustor (PFBC) at the Tidd Station of Ohio Power Company. This demonstration facility was constructed and is operated in cooperation with the U.S. Department of Energy in Round I of the Clean Coal Technology Program. The sorbent fed to the plant, rather than lime or limestone, is dolomite. Dolomite is used at the Tidd Station because it is both more porous (and thus more reactive) and easier to handle without bridging in the piping system. By operating

at high pressure, little of the dolomite in the residue is in the oxide form - most is present as carbonate. The dolomitic character of the sorbent yields a residue that is lower in pH than that produced from lime-based sorbents. This characteristic is particularly advantageous in stabilizing arsenic-laden waste solids. As this by-product contains magnesium, it will buffer the stronger lime alkalinity. The chemical composition of the residue is 50-60% equivalent $CaCO_3$ and 1-2% available (free or uncombined) CaO.

3- Residue from a Coal-Waste-Fired CFBC operated by the Ebensburg Power Company. Approximately 200,000 tons/year of this material is trucked back to the mines from which the coal wastes are derived. Some or all of this by-product could be diverted to nearby sites for beneficial use if they could be identified. The coal waste fed to the boiler has a sulfur content between 1.4 and 2.0 percent. The limestone is 83% $CaCO_3$. It is sized at 12 mesh x 0 and contains between 5 and 10 percent through 140 mesh. The fly ash is removed in a ten-segment baghouse and conveyed to a silo. Approximately 70% of the by-product in the silo is baghouse ash; 30% is bottom ash. Thus, the by-product is a relatively coarse material containing 82% ash, 12.5% limestone equivalent and 5.5% $CaSO_3/CaSO_4$.

4- Residue from a Coal-Fired Circulating Fluid Bed Combustor (CFBC), supplied by Anker Energy Corporation. This material is produced by the cogeneration project of Applied Energy Service at its Thames River Plant near Uncasville, Connecticut. Anker Energy Corporation supplies the coal used in the plant and through early 1995 had to backhaul the residue to its mines in West Virginia. It was anticipated that some or all of the approximately 100,000 tons/year of this by-product could be easily diverted to hazardous waste treatment plants along the general rail route from Connecticut to West Virginia. The AES Thames River Plant is base-loaded, operating at 95-96 percent of capacity constantly, thus the ash from it is very uniform. The residue is a relatively coarse material, as it contains both bottom and fly ash from the boiler, and contains 45% limestone equivalent, 28% ash and 27% $CaSO_3/CaSO_4$. Dravo Lime Company provided assistance in obtaining and transporting multiple representative samples from each clean coal technology site in accordance with ASTM-C-311. Samples were split for analysis and use at the University of Pittsburgh and the Dravo Lime Company.

HAZARDOUS WASTES

Six different hazardous wastes have been selected for examination by Mill Service, Inc., a regional centralized hazardous waste treater, from among the materials processed commercially at their facility. The table below outlines significant properties of each hazardous waste: note that lead is the contaminant of primary concern since it is the TCLP lead levels that exceed appropriate limits.

HAZARDOUS WASTES STABILIZED

Hazardous Waste Source	Hazardous Constituents of Concern	Total Concentration (mg/kg solids)	TCLP Concentration (mg/l)	TCLP Regulatory Limit (mg/l)
Sludge from Lead-Acid Storage Battery Production	Lead	3,000	20	5.0
	Cadmium	3	0.19	1.0
	Chromium	12	—	5.0
Contaminated Soil from a Munitions Depot	Lead	1,200	26	5.0
	Cadmium	4.8	—	1.0
	Chromium	59	—	5.0
	Copper	210	1.6	—
	Zinc	580	8.2	—
Contaminated Soil from a Multi-Use Industrial Site	Lead	5,000	80	5.0
	Cadmium	5.4	—	1.0
	Chromium	22	—	5.0
	Copper	260	—	—
	Zinc	660	17	—

Baghouse Dust from Basic Oxygen Furnace (BOF) Steelmaking	Lead	1,400	14	5.0
	Cadmium	55	—	1.0
	Chromium	260	—	5.0
	Copper	57	—	—
	Nickel	130	—	—
	Vanadium	76	—	—
	Zinc	41,000	4.4	—
Ash from a Municipal Solid Waste Incinerator	Lead	5,700	20	5.0
	Barium	550	—	100
	Cadmium	630	—	1.0
	Chromium	130	—	5.0
	Copper	1,300	—	—
	Zinc	23,000	2.1	—
Contaminated Soil from a Former Waste Water Treatment Plant	Lead	750	7.8	5.0

RESULTS & CONCLUSIONS

Bench-scale stabilization experiments consisted of mixing by-products with hazardous wastes at weight ratios ranging from 0 to 1:2 with minimal moisture addition. Sampling of the stabilized mass was done immediately after treatment for evaluation of TCLP leachate compositions. As may be expected, some combinations of by-product/wastes exhibited stabilization more consistently than others. Figures 1 and 2 provide contrasting resultant information for two representative sets of stabilization experiments: figure 1 shows information illustrating lead stabilization while figure 2 shows failure to stabilize lead.

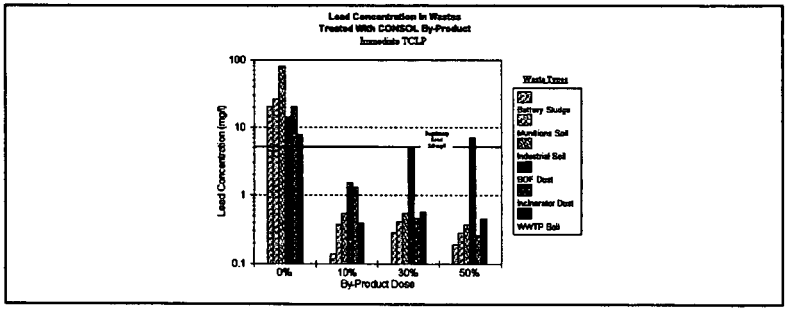

Figure 1
Successful Lead Stabilization

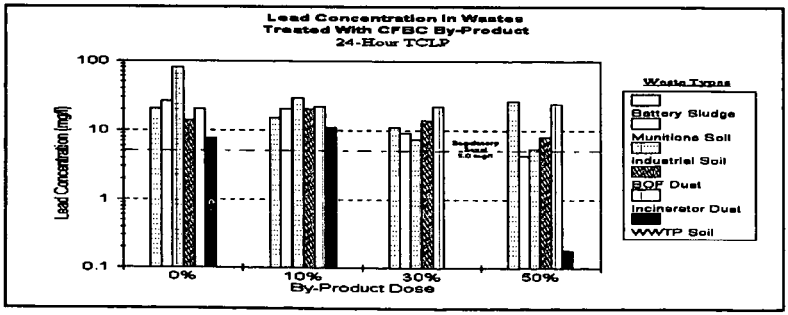

Figure 2
Unsuccessful Lead Stabilization

Solidification/Strength Development: In addition to chemical stabilization, aliquots of hazardous waste and by-products were evaluated for development of strength over time when prepared at optimal moisture contents. Optimal moisture values were determined to be that at which the "stiffened" mass would produce a "slump" in the neighborhood of 1 inch to 2 inches when tested in accordance with standard concrete testing procedures. Figure 3, a representative plot of compressive strength development over time, indicates that for some samples, strength development is considerable while little strength development is achieved for others.

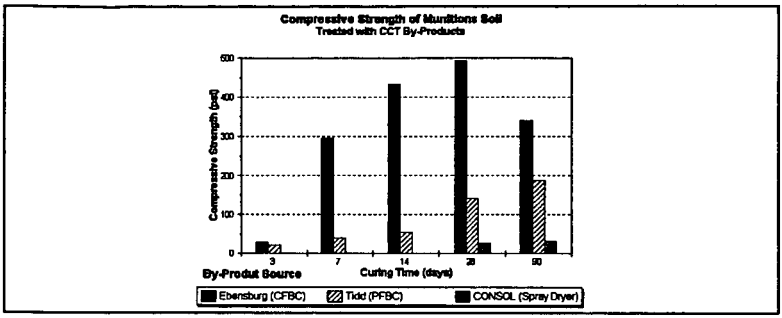

Figure 3
Strength Development over Time

SUMMARY

- Clean Coal Technology by-products may be used for heavy metal stabilization of a number of hazardous waste sources, however laboratory evaluations must be conducted to assure final product quality.
- Pozzolanic properties of clean coal technology by-products are useful in making a hardened product for reuse or disposal.
- By-products producing a highly stabilized materials do not often produce the strongest product. Thus, evaluation of final product use and/or disposal options must be made on a case-by-case basis.
- Commercial-scale stabilization testing will be undertaken during the second year of this project in conjunction with developing an understanding of underlying principles governing the behavior of these new treatment chemicals.

REFERENCES:

"Clean Coal Technology - The New Coal Era", Washington, DC: U.S. Department of Energy, Assistant Secretary for Fossil Energy, January, 1991.

ACKNOWLEDGMENT:

This paper was prepared with the support of the U.S. Department of Energy, under Cooperative Agreement No. DE-FC21-94MC3117. However, any opinions, finding, conclusions, or recommendations expressed herein are those of the authors and do not necessarily reflect the views of the DOE.

THE USE OF FLUIDIZED BED COMBUSTER ASH IN THE SOLIDIFICATION OF HIGH OIL AND GREASE SEDIMENTS

R. Gregory Bennett and Ernest F. Stine Jr., Ph.D
IT Corporation, 312 Directors Drive, Knoxville, TN 37923

Keywords: Fluidized bed combuster ash; High oil and grease sediment; Treatability study

INTRODUCTION and BACKROUND

It has been common practice at petroleum refineries to dispose of oil sludges (containing oil, grease solids and water) in onsite pits. Remediation of these pits has typically involved in-situ solidification of the sludges using mixtures of Portland cement and fly ash. While this leaves the oily material in place, the resulting form is less permeable than the resulting sludge and has significant strength to support a cap. The supported cap reduces the infiltration rate of water to contact the solidified sludges. Due to the cumulative impact of the solidification and capping process the mobility of these materials is therefore reduced.

Since 1991 an oil refinery has been investigating the closure of several large storm water impoundment ponds. These ponds contain sediments that are high in oil and grease and mostly low in solids. Oil and grease content ranges from 1.5 to 20% by EPA Method 9071[1]. Consistencies and liquid content of the sediments vary from a very wet free flowing emulsion to a congealed sludge with about 70% solids. The primary concern of closure was to solidify the residues while still maintaining the low leachability and mobility of both metals and volatile organic hydrocarbons (VOCs).

During the project evaluation phase, a consulting engineering firm conducted a treatability study that evaluated Portland cement, cement kiln dust, Class C fly ash and pulverized quicklime for solidification of various pond sediment samples. The goal of this study was to develop formulations that would reduce the leachability of metals and VOCs below regulatory limits and obtain unconfined compressive strengths greater than 0.98 kilograms/sq.cm (Kg/sq.cm). The study's recommendations ranged from formulations with 20% Portland cement and 10% fly ash blend to formulations using 30 to 35% Portland cement. At these recommended cement loadings, the cost of the remediation was unacceptably very high. IT-Davy, a joint venture between IT Corporation and Davy Environmental, was hired to provide final engineering design and investigate lower cost solidification formulations. IT-Davy successfully demonstrated the use of by-product blends through field studies, a laboratory bench-scale confirmation study and a full-scale pilot demonstration.

Preliminary Field Screening Studies

Two stages of testing were performed in the field as a screening of reagents for later laboratory work. The first stage consisted of testing single reagents and blended reagents for strength development, rate of hardening, heat generation, and water absorption after hydration. Experiments consisted of testing 12 single reagents and 30 blends of these reagents. Reagents included four Class C fly ashes, five fluidized bed combuster ashes , two cement kiln dusts and Type I Portland cement.

The second screening stage consisted of mixing different single reagents and reagent blends that harden on hydration with a sediment sample (composited from several lagoons on the site) to achieve the highest strength. Seven of the more promising single reagents from the first stage that had good water adsorption, possible strength formation and low heats of reaction were mixed with a composite sediment sample in various dosages and measured for strength using development. Strength was measured by penetration resistance using a pocket penetrometer at seven days of cure. Various blended combinations of these reagents were then compared for strength using penetration resistance as measured by pocket penetrometer at seven days. These blends included cement/fly ash, cement kiln dust/fly ash, cement/fluidized bed combuster ash and mixtures of other by-products. Ratios of blend components were changed in increments of 20% to find the optimum mixture of reagents for the blend. The dosage of reagent blends was compared for formulations that met >1.0 Kg/sq.cm penetration resistance. Additional field screening was performed to optimize the reagent dosages of cement only and fly ash /fluidized bed combuster ash (FA/FBCA) blends.

Results showed that strengths could be achieved using cement or blends of fly ash and fluidized bed combuster ash at high dosages. Further testing was done on individual samples from each of the six lagoons on site (A, B, C, D, E, F). The percent solids and oil and grease content of these lagoons are found in Table 1. To increase the strength and lower the dosages, an absorptive soil was added to formulations with cement and FA/FBCA blend. The soil absorbed free water and thickened low solid sediments. With the addition of the soil, the strength criterion was increased to >3.0 Kg/sq. cm at seven days of cure increasing the oil retention of the formulations.

Bench-Scale Confirmation Testing

Four of the six lagoons were sampled and sediments were sent to IT's Environmental Technology Development Center in Oak Ridge, Tennessee for bench-scale testing. Sediment samples were designated A, B, C, D to identify the lagoon that they were taken. Using the results from the field screening, the

potential formulations shown in Table 2 were chosen for a bench-scale verification test. Two or three formulations were selected for each of four lagoon sample locations, labeled A, B, C, and D. Each location had varying amounts of solids, moisture, and oil and grease content. Percent solids and oil and grease are shown for all six lagoons are shown in Table 1. In most of the mixes, adsorptive soil was added to increase the solids content of the sediments. At all of the sample locations, formulations were tested using cement (as a control reagent for comparison) and the FA/FBCA blend. For samples A and B the formulations from the previous treatability study that used cement only or cement/fly ash blend without soil were made for comparison. Formulations were tested for the following:

- Unconfined compressive strength (UCS) at 3, 7, 28, 90 days measured by ASTM D2166-91[2]
- Permeability at seven days measured by ASTM D5084[3]
- Oil retention at seven days measured by liquid loss at 42 psi of compression for five minutes
- Sample cohesiveness in water after 14 days
- Volume increases
- Compliance with Toxicity Characteristic (TC) regulatory limits by analyzing the material using the Toxicity Characteristic Leachate Procedure (TCLP)[4]

Full-scale Demonstration

Successful FA/FBCA blend mix formulations were used in a full-scale in-situ pilot demonstration. A large area of a sediment pond was diked for this demonstration. Free standing water and oil were removed before the addition of fill soil and reagent. Various mixing and reagent addition techniques were explored. The optimized laboratory formulations were tested against various reduced reagent formulations to confirm dosage rates. Samples were taken to measure the success of the remediation. The goal was to confirm the strength of 1.4 Kg/sq.cm and permeability less than 1×10^{-5} cm/sec achieved during laboratory investigations. Test samples were made in 7.6 x 15.2 cm cylinders during daily production. Each was tested for UCS at 3, 7, and 28 days of cure. Permeability was tested at seven days.

RESULTS and DISCUSSION

Preliminary Field Screening Studies

The first stage of field reagent screening began by testing various possible cement substitutes for cement like properties of hardening, heat evolution, and water absorbtion. Water was added to various Class C fly ashes, fluidized bed combuster ashes and cement kiln dust. Portland cement was hydrated for comparison. Test results identified potential reagents from each group, but showed that the Class C ashes as a group performed most like cement.

Sediment formulations were then prepared using reagent dosages of 40 to 60 g per 100 g of sediment. Strength development was tested at seven days by penetration resistance. Of the 11 reagents, only one Class C fly ash and two FBCAs showed strengths over 1 Kg/sq.cm at seven days. However, at 40 to 60% loadings these could not compare favorably to cement loadings of 20%.

Cement and Class C fly ash blends from the earlier study were reevaluated. Ratios of cement to fly ash were varied in 20% increments. In all cases 7-day strength decreased as cement was replaced with fly ash. This test was repeated using FA/FBCA blends and gave similar results. In an attempt to eliminate the need for cement, cement kiln dust were blended with various Class C fly ash mixes using loadings up to 45%. None met the desired strength after seven days. The by-product blends were then evaluated using various fluidized bed comuster ashes with Class C fly ash. At specific ratios, these blends exhibited strengths almost equal to cement mixtures. The mix ratios of reagents were unique for each specific combination of by-products (ashes). Since the cost of the coal burner by-products was very low compared to cement, higher ratios of reagents could be used at a significant cost savings.

Similar formulations were made using fill soil as an absorbent and to increase the solids content of the mixture. Results revealed that reductions could be made in the loading of both single and blended reagents. The addition of soil allowed some previously unsuccessful blend combinations to show strengths above 3 Kg/sq.cm with greater oil retention. Even with the soil addition the use of cement kiln dust was not effective.

The reagents with the most potential were then tested at different soil to sediment and reagent loadings. Results are in Table 3.

These results confirmed that the addition of soil to absorb the excess oil and water and increase the solid content of the sediment would reduce the dosage rate for cement. Results also showed that when using an optimum soil to sediment ratio of 1 to 0.75 that the FA/FBCA performed as well as cement alone. Not only was the performance equal, but the reagent cost was reduced by 40% when using the FA/FBCA blend even at slightly higher dosages.

Final field treatability testing was performed using sediment samples from all six lagoons, bracketing the range of conditions on the site. Final mixes were made using two ratios of FA/FBCA in the dry blend that was mixed with the sediment.

The final field tests confirmed the previous test results. As a general trend using the reagent FA/FBCA blend at a high mix ratio, significant strength formed at lower dosages a lower blend ratio. Soil to sediment comparisons showed that the ratio of soil to sediment to get an acceptable compressive strength are dependent on the sample location. Since a lower ratio would reduce the bulking factor, the lowest ratio of soil to sediment was preferred. At the optimum soil ratio of 1:0.75 and at a high blend mix ratio a reagent dosage of 25% met strengths of >3 Kg/sq.cm for all sediment locations. These mix formulations were selected for the next phase, a controlled bench-scale verification study. These formulations are the subject of a patent application.

Bench-scale Verification Study

Sample formulations were made in two to three kilogram batches. Mixes were made using a Hobart mixer, with a spade shaped blade. The mix was placed into 5.1 x 10.2 cm cylindrical molds. Molds were allowed to cure in sealed containers at room temperature on the bench top. Bulk density was determined on the uncured mix by weighing the filled molds. No significant changes in volume of the mix occurred as the samples cured. Raw sample bulk densities varied from 1.07 g/cm^3 for the four sample locations. Grout mix densities for these sample varied from 1.2 to 1.6 g/cm^3.

Unconfined compressive strengths were tested by ASTM Method D2166 at 3, 7, 28, and 90 days. The passing criterion was >1.4 Kg/sq.cm at seven days of cure, which is based on developing enough strength to support construction equipment during the remediation phase of the project. No other specific criteria were established, but the total strength at 28 days of each sample were compared. See Table 4 for the UCS data. All the formulations using the FA/FBCA blend met the desired strengths. The cement formulations using soil were lower than the desired strength and the cement only formulations were much lower than the desired strength.

Sample molds were tested for permeability at seven days of cure by ASTM method D5084. Passing criteria was to have lower permeability than the permeability of the surrounding basin. The closure plan established 1 x 10^{-5} cm/sec as the passing goal. All of the tested formulations met this requirement.

Liquid retention capacity was tested at seven days of cure. Samples used to measure unconfined compressive strength were crushed and reworked by hand. This material was placed into a 3.6 cm diameter stainless steel Carver mold. The mold was configured with a porous bottom plate that was covered with a filter paper to separate the sample from the plate. The mold was filled with sample, manually compacted and a 3.0 Kg/sq.cm load was applied for 5 min. Liquid retention was measured as a percentage of the weight retained. All of the samples retained betwwen 89 and 96.6 % of thier total liquid content. The FA/FBCA blend formulations all retained over 95% of their weights. Values for the cement mixes were generally 5% lower. When the percent liquid retention wasgraphed against the unconfined compressive strength, the graph showed that retention values improve with increasing strength up to 1.8Kg/sq.cm.

The durability of 14 day cure samples was tested by submerging them in water. Blocks of solidified samples were immersed in beakers of water. Covers were placed on top to prevent evaporation. Results were recorded as visual observations. Cohesiveness, precipitation and oil sheen were noted. Observations were recorded over 90 days. These results show that slight oil sheens are present on all sample surfaces. In all cases the cement formulations exhibited more sheen than the FA/FBCA blend mixes. After two days the sheen was reduced in all beakers. White precipitate formed in cement mixes at two hours. At later time a smaller quantity of similar precipitate also formed in the by-product blend mixes. This precipitate is thought to be calcium hydroxide or calcium sulfate, by-products of cement hydration. No evidence of physical deterioration was seen in any of the samples. No changes occurred between nine and ninety days.

Samples were extracted at seven days using the TCLP method . The extracts were analyzed for semi-volatiles, volatiles and metals. No concentrations were expected above regulatory requirements because the original materials were within passing criteria. The leachability of the treated materials were all less than or equal to the leachabilities of the untreated sediments, and therefore below the TC regulatory criteria for these compounds.

The following recommendations were made from the bench-scale verification results:

- The FA/FBCA blend is an effective and economical replacement for cement in the stabilization of oily sediment.
- Absorbent fill soil is suitable for reducing reagent loading, while maintaining high strength, durability and low permeability.
- Controlling solids content is critical to effective solidification.
- Oil and grease in concentrations < 20% has little effect on the reagent dosages in the proposed mix designs.

The recommend mix designs are: 1) Removal of free water before solidification; 2) Use absorbent fill soil to obtain 55 to 60% solids content; and 3) Add 25 to 30% FA/FBCA blend.

Recommendations from bench-scale verification were used to design a full-scale in-situ pilot demonstration.

Full-scale In-situ Demonstration

The purpose of the pilot demonstration was to test the ability to use the laboratory designs in the field. Many operational performance goals were addressed in this study that are beyond the scope of this paper. The technical goals of strength, mixing and permeability will be addressed.

Before stabilization a large sediment basin was divided using several dikes. The demonstration area was then dewatered by pumping free liquid from above the sediment. Solids content was increased to between 55 and 60% using fill soil. A long-stick trackhoe was used to mix soil into the sediment. Blending took place over several days so that the moisture could be absorbed by the soil. Additional soil was added as determined by field moisture determinations. Reagents were added to the mixture by delivery using a pneumatic tanker. Mixing was by three different techniques: 1) Long-stick trackhoe blending; 2) In-situ rotary mixer blending; and 3) Bulldozer blending.

The first two methods were done in-situ while the bulldozer blending was done on a pad. Both the bulldozer and the trackhoe mix were of a satisfactory consistency. Rotary mixer blending was unsatisfactory due to entanglements of debris with the mixer and the consistency of the mixes.

Variations in mix formulations were made to test the criticality of percent solids and reagent dosages. Samples were taken during mixing to be tested for compressive strength and permeability. Samples were aged in sealed containers on laboratory bench top separate from the remediation areas. Table 5 contains soil sediment ratios, percent reagents, final percent solids, compressive strengths, and permeabilities. Mixes with above 55% solids before adding the by-product blend gave acceptable strengths above 1.4 Kg/sq.cm at seven days. Permeabilities for all mixes were below 1×10^{-5} cm/sec which is ten times greater than the permeability of the surrounding soil. These data show that field results are consistent with earlier field screening and bench scale verification data.

CONCLUSIONS

IT-Davy demonstrated that an alternative solidification reagent is available to stabilize sediment with oil and grease contents below 20%. When used at the proper solids content a FA/FBCA blend gave equal or better strength and permeability compared to Portland cement. Because the cost of these combined reagents is lower than cement, larger dosages can be used at a lower cost. The practicality of these reagents has been demonstrated by field screening, bench-scale verification and a full-scale in-situ demonstration.

REFERENCES

1 EPA Method 9071, "Oil and Grease Extraction Method for Sludge and Sediment Samples", Test Methods for Evaluating Solid Waste Physical/Chemical Methods SW 846, 3rd Ed. Vol 1C

2 ASTM D2166, "Test Method for Unconfined Compressive Strength of Cohesive Soils", American Society of Testing and Materials, 1991. Vol. 04.08

3 ASTM D5084, "Test Method for Measurement of Hydraulic Conductivity of Saturated Porous Materials Using a Flexible Wall Permeameter", American Society of Testing and Materials, 1991. Vol. 04.08

4 EPA Method 1311, "Toxicity Characterization Leaching Procedure", Test Methods for Evaluating Solid Waste Physical/Chemical Methods SW 846, 3rd Ed. Vol 1C

TABLE 1. PERCENT SOLIDS AND OIL AND GREASE FOR ALL SIX LAGOON SITES

SAMPLE LOCATION	% SOLIDS	% OIL and GREASE
A	20	6
B	35	12
C	29	11
D	20	11
E	46	11
F	67	20

TABLE 2. BENCH-SCALE VERIFICATION TEST FORMULATIONS

SAMPLE LOCATION	REAGENT	DOSAGE PER 100 g OF SEDIMENT	ABSORPTIVE SOIL PER 100 g OF SEDIMENT
A	PORTLAND CEMENT FA/FBCA BLEND PORTLAND CEMENT	17 30 25	125 125 0
B	PORTLAND CEMENT FA/FBCA BLEND CEMENT/FLY ASH BLEND	17 20 25	75 75 0
C	PORTLAND CEMENT FA/FBCA BLEND	22 30	75 75
D	PORTLAND CEMENT FA/FBCA BLEND	17 20	75 75

TABLE 3. PENETRATION RESISTANCE AT 7 DAYS (Kg/sq.cm)

SOIL/SEDIMENT (w/w)	DOSAGE PER 100 g OF SEDIMENT	PENETRATION RESISTANCE USING EACH REAGENT		
		TYPE I PORTLAND CEMENT	CLASS C FLY ASH	FA/FBCA BLEND (MID-LEVEL RATIO)*
1/1	10	1.6	-	0.4
1/1	15	4.0	0.1	1.5
1/1	20	-	0.2	2.5
1/0.75	15	3.0	-	3.1
1/0.75	20	3.5	-	4.2
1/0.75	25	-	0.5	>4.5
1/0.5	15	1.2	-	-
1/0.5	20	3.0	-	2.6
1/0.5	25	>4.5	0.3	3.4
1/0.5	30	-	1.3	>4.5

* Multiple ratios of FA/FBCA were investigated. These results are for the mid-level ratio blend of FA/FBCA.

TABLE 4. UNCONFINED COMPRESSIVE STRENGTH

SEDIMENT SAMPLE	MIX FORMULATION	UCS (kg/sq.cm)			
		3 DAYS	7 DAYS	28 DAYS	90 DAYS
A	Sed:Soil:Cement (100g:125g:17g)	0.35	0.42	0.84	0.98
	Sed:Soil:FA/FBCA Blend (100g:125g:30g)	1.62	3.52	4.29	4.71
	Sed:Cement (100g:25g)	ND	1.12	2.04	ND
B	Sed:Soil:Cement (100g:75g:17g)	0.84	1.34	1.90	2.81
	Sed:Soil:FA/FBCA Blend (100g:75g:20g)	0.56	1.62	1.97	2.53
	Sed:Cement/Fly ash (100g:25g)	ND	0.63	1.20	ND
C	Sed:Soil:Cement (100g:75g:22g)	0.14	0.14	0.21	0.28
	Sed:Soil:FA/FBCA Blend (100g:75g:30g)	0.77	2.95	4.22	4.71
D	Sed:Soil:Cement (100g:75g:17g)	1.12	1.62	2.39	2.95
	Sed:Soil:FA/FBCA Blend (100g:75g:20g)	0.63	1.76	2.25	2.53

TABLE 5. FULL-SCALE IN-SITU DEMONSTRATION DATA

	ISOLATION DIKE AREA		SOUTH DEMONSTRATION AREA				DOZER MIX AREA
	Cell No. 1	Cell No. 2	Cell No. 1	Cell No. 2	Cell No. 3	Cell No. 4	
Sediment to Soil Ratio	1:2.8	1:2.1	1:2.5	1:1.4	1:0.9	1:0.7	1:0.75
Percent Solids, Sediment and Soil	68%	65%	54%	53%	48%	45%	54%
Percent FA/FBCA Blend, by Wet Weight							
- Of Sediment	55%	42%	39%	29%	17%	14%	25%
- Of Sediment/Soil	14%	14%	16%	12%	9%	8%	17%
Final Mix, Percent Solids	72%	69%	60%	58%	52%	49%	60%
-Density, Kg/sq.cm	7.45	7.38	6.61	6.19	--	--	6.75
Compressive Strength, Kg/sq.cm							
- 3 days	0.70	0.70	0.42	0.28	Soft	Soft	Soft
- 7 days (ave. of 2)	1.69	2.04	1.27	0.28	Soft	Soft	--
- 28 days	4.50	3.30	2.18	1.41	Soft	Soft	--
Permeability, cm/sec x 10^{-7}							
- 7 days	—	1.6	1.7	1.6	—	—	5.7

CHARACTERIZING SYNTHETIC GYPSUM FOR WALLBOARD MANUFACTURE

P. J. Henkels
USG Corporation Research Center
700 N. Highway 45
Libertyville, IL 60048

J.C. Gaynor
United States Gypsum Company
125 S. Franklin
Chicago, IL 60606

Keywords: FGD Synthetic Gypsum, Gypsum Wallboard, Test Methods

INTRODUCTION

United States Gypsum Company (USGC) has developed specifications and guidelines covering the chemical and physical aspects of synthetic gypsum to help predict end use acceptability in wallboard manufacture. These guidelines are based in part on past experiences with natural and synthetic gypsum. Similarly, most wallboard manufacturers in North America have developed their own guidelines based in part on its unique history and particular experiences with synthetic gypsum. While there are similarities between manufacturers' guidelines, differences do exist.

This paper discusses the importance of selected parameters contained in the FGD gypsum guidelines. In most cases, the parameters are equally relevant to other synthetic gypsums and the naturally occurring gypsum mineral as well.

USGC's general guidelines of FGD gypsum along with guidelines from the German Gypsum Association are listed in Table One. The guidelines are not an all inclusive list of every gypsum property important to the wallboard manufacturer. The guidelines serve as a starting point in negotiating sales agreements between the wallboard manufacturer and synthetic gypsum supplier. The product specification agreement at USGC is tailored to each individual source depending in large part to the percent usage at the wallboard facility, type of synthetic gypsum and capabilities of the supplier.

GYPSUM CHARACTERIZATION

Gypsum Purity. Obviously, gypsum ($CaSO_4 \cdot 2H_2O$) purity is an important attribute. Purity is key in manufacturing wallboard. Purity of mined natural rock varies widely usually from 80 - 96%. High purity is desired because lower weight gypsum board may be produced. Generally, a higher purity is desired for synthetic gypsum compared to natural rock in wallboard manufacture. Usually, high purity synthetic gypsum can be reasonably obtained by the supplier. Therefore, a higher purity synthetic gypsum will have increased value.

Impurities found in synthetic as well as natural gypsum can be quite detrimental to the wallboard produced. The higher purity reduces the chance of deleterious effects from these impurities.

Purity can be determined by several test methods including Differential Scanning Calorimetry/Thermal Gravimetry (DSC/TGA), X-Ray Fluorescence Spectroscopy (XRF) and SO_3 analysis.

Free Moisture. Many synthetic gypsums discharged from by-product manufacturers are in the form of a wet cake. The free or surface moisture of the cake is usually in the range of 6 - 25%. Natural mined rock will vary from 0 - 3% moisture. Often, the amount of synthetic gypsum that a wallboard plant can blend in with the natural rock will be dictated by the thermal capacity of the rock drying system. High moisture reduces the amount of synthetic gypsum that can be blended. This reduces its value.

Often a wallboard manufacturer will enter a sales agreement with a supplier prior to the availability of the synthetic gypsum. When the actual free moisture is significantly greater than contracted, processing capacity problems will arise. This could be due to both thermal drying limits and because of the more challenging handling characteristics of high moisture gypsum. High moisture gypsum has a greater tendency to stick and build up on conveying equipment.

Free moisture of natural and synthetic gypsum materials are determined using a simple oven weight loss method per ASTM C471. In addition, heat and moisture determining balances are used.

Impurities. The type and quantity of impurities have the greatest impact on qualifying the use of a synthetic and natural gypsum. The guidelines list the predominant impurities found in FGD gypsum. Discussion of selected impurities follow.

Residual Carbonates. Unreacted limestone ($Ca/MgCO_3$) is the predominant impurity found in many synthetic gypsum sources. Limestone is a common impurity in natural gypsum as well. Fortunately, limestone remains chemically inert through the board conversion process. However, increased wear on processing equipment results when encountering high amounts of limestone (Mohs value 3 - 4) since it is a harder substance than gypsum (Mohs value 1.6 - 2).

Limestone quantity can be determined through XRF oxide analysis of calcium and magnesium in conjunction with carbon dioxide (CO_2) analysis by coulometric titrimetry. Alternatively, CO_2 can be quantified through DSC scans.

Flyash. One concern with flyash in FGD gypsum is the chemical variability associated with burning different fuel sources (e.g. various coals and Orimulsion™). Flyash can affect paper to core bond during wallboard manufacture. The variability can cause intolerable problems in wallboard conversion. Also, flyash laden with silica and iron causes increased wear on process equipment.

An important concern with flyash is the amount of trace elements that may accompany it. This can raise serious industrial hygiene issues. Trace elements and the analysis will be discussed in a later section.

Flyash is easily detected using a scanning electron microscope (SEM). By using image analysis, an estimate of the amount of flyash present can be established. Fly ash can also be calculated by determining the mass balance around the scrubber and dust collection system. Figure One is an SEM photo of flyash impurity in a FGD gypsum sample.

Silica (SiO_2). Silicon dioxide is an important impurity from an industrial hygiene perspective and a process issue for all mineral industries. Silica is common in both natural and synthetic gypsums. It can be part of a clay, flyash or quartz impurity.

High quantities of respirable (0 - 4 microns) silica could present an industrial hygiene issue.

Crystalline silica or quartz is a very hard substance (Mohs value 7). Even low amounts (1-2%) can cause dramatic accelerated wear on gypsum processing equipment.

Amorphous silica is also contained in a variety of clays. Clays negatively impact the amount of water required to form a fluid slurry and thus, create a higher thermal demand to drive off the excess water in the board conversion process.

Silica can be quantified using XRF. X-Ray diffraction (XRD) is used to identify whether the SiO_2 present is amorphous or crystalline in nature. In addition, ASTM C-471 describes a wet chemistry method to determine SiO_2 and insoluble matter.

Calcium Sulfite ($CaSO_3 \cdot 1/2H_20$). FGD systems may be designed to produce unoxidized gypsum or calcium sulfite instead of calcium sulfate dihydrate. This material is always landfilled. Sulfite impurities are a much greater concern at the gypsum producing FGD systems because they lead to scaling and other processing problems. The fine particle size of sulfite will cause cake washing and dewatering problems. Calcium sulfite is an unwanted impurity in any gypsum.

Thermal analysis and XRF will detect sulfite above 0.1%. Titration procedures are considered a better method to determine sulfite. A titration procedure is listed in EPRI-Method 40 (EPRI CS-3612. Project 1031-4. Final Report dated July, 1984).

Soluble Salts. Soluble salt impurities are one of the most important parameters affecting the physical properties of gypsum wallboard. Salts are a common impurity in natural and several different types of synthetic gypsums. It is common practice to mine around natural gypsum rock seams high in salt content. Chloride salts are common in natural and some synthetic gypsums. In addition, high amounts of magnesium salts can end up in some synthetic gypsums. Magnesium can originate from limestone sources used to neutralize waste acid and in desulfurization systems.

Salts readily go into solution when the calcined gypsum (stucco) is mixed with water and other additives in the board mixer. During the drying of the gypsum board in the kiln the salts migrate to the paper - core interface and interrupt the paper to core bond. Salts are very hydroscopic and cause moisture to deposit in the critical bond area of the board. On exposure to high moisture from joint finishing and wallpaper products the drywall paper can detach itself from the core.

The four soluble salt ions typically monitored are magnesium (Mg^{2+}), potassium (K^{+}), sodium (Na^{+}), and chloride (Cl^{-}). Soluble salts are analyzed by several different methods. Atomic absorption is used for the determination of magnesium. Atomic emission is used for the determination of potassium and sodium. Ion-selective electrode (ISE) is used for the determination of chloride. ISE can also be used for sodium and potassium determinations.

Table Two shows a typical soluble salt analysis for a synthetic gypsum sample. Total salts are based on a mathematical reconstruction. This mathematical reconstruction is based on the theoretical solubility of the ions.

Trace Elements. Trace elements and pH are evaluated on all natural and synthetic gypsum sources for industrial hygiene purposes. Trace elements normally evaluated are shown in Table Three. Trace elements are unwanted impurities. They arise from flyash contamination and increase process equipment wear. Also, trace elements are commonly found in most naturally occurring minerals including gypsum and limestone.

Trace elements can be determined through several methods including Atomic Absorption/Emission (AA) with a graphite furnace option, wet chemistry methods, Inductive Coupled Plasma (ICP) and XRF.

Organic impurities. Although not listed in the FGD guidelines, organic impurities even at trace (ppm) levels can have a dramatic effect on gypsum board operations. Organics are unwanted impurities in gypsum. The effects of organics found in natural and synthetic sources are observed during gypsum rehydration in the board conversion process. They can easily cause the rehydration time to dramatically lengthen and cause the board line to slow down and reduce production. Organics adversely affect crystal growth and reduce strength development of the gypsum core.

Residual organic impurities in synthetic gypsum from waste acid neutralization processes such as citric and lactic acid production can strongly retard the hydration of gypsum stucco.

Organic impurities can be identified through several methods including coulometric titrimetry, Infrared Spectroscopy (IR), Nuclear Magnetic Resonance (NMR) and High Performance Liquid Chromatography (HPLC).

Physical Properties. Although chemically the same, there can be significant physical property differences between natural and synthetic gypsums. It is well publicized that there are significant differences in particle size and shape between natural roller milled ground gypsum rock (land plaster) and most synthetic gypsums.

Particle Size. Most synthetic gypsums are formed in a solution environment supersaturated with respect to gypsum and accompanied with vigorous agitation. Under these conditions, the gypsum particles precipitate fairly uniformly in particle size and shape. The particular size and shape depends on the process conditions of the unit operations. USGC FGD guidelines list a 20 micron minimum median particle size. More commonly, synthetic gypsums have median particle size is in the 35 - 45 micron range.

Many synthetic gypsums have narrow or monolithic particle size distributions. Typical roller milled natural gypsum has a much broader particle size distribution. Figure Two shows SEM photomicrographs of natural and FGD gypsum. Figure Three shows a comparative particle size histogram between natural and a FGD gypsum.

A monolithic particle size distribution with a large mean particle size (40 - 60 microns median) for synthetic gypsum is preferred even though it creates processing challenges at the wallboard facility. Large particles (low surface area) will readily dewater. Low free moisture is a desired quality because of lower drying costs. Also, as free moisture is reduced through dewatering, the quantity of water soluble impurities will be reduced.

In general, synthetic gypsums that have poor dewatering characteristics also have high surface moisture and high surface area. In addition, the material has more challenging material handling properties and causes increased amounts of process water to be used during the continuous casting of gypsum board. The later point causes a higher thermal demand in drying the gypsum board.

Therefore, it is preferred that the gypsum supplier design the synthetic gypsum system to produce gypsum particles that will readily dewater. Despite engineering design challenges at the wallboard plant, synthetic gypsums with large particles are desired because they impart good dewatering properties.

Particle size is measured using laser scattering or sedimentation technique. The two methods do not always yield the same results. Figure Five shows particle size distribution for natural and synthetic gypsums using laser light scattering and sedimentation. Note that for both samples the laser technique yields a higher mean particle size then sedimentation.

Surface area is another method to measure particle fineness. The Blaine surface area technique is a common measuring method used for powders. The Fisher™ subsieve sizer is used as well. The surface area of natural roller milled gypsum is typically 2000 - 3000 cm^2/gram. Wallboard grade FGD gypsum is commonly below 1000 cm^2/gram.

Aspect Ratio. Some wallboard manufacturers will include an aspect ratio guideline (usually 10:1:1 - 20:1:1 maximum) on particle shape. The aspect ratio guideline is usually put into product specifications to insure against contending with problems associated with needle-like gypsum crystals in processing, calcining and wallboard manufacture. Since gypsum particles retain their shape after calcination, high aspect ratio particles can cause an increase in water demand during board conversion.

The synthetic gypsum producer needs to concern itself with aspect ratio because of its influence on internal processing issues. Needle shaped gypsum particles are more difficult to dewater than large blocky shaped crystals. Thus, under the same processing conditions, gypsum with a high aspect ratio will contain higher surface free moisture and water soluble impurities. It may also be more expensive to process in order to meet finished product guidelines. Hence, the material will have reduced value.

The aspect ratio of natural gypsum is generally 1: 1. The particle shape of gypsum can easily be determined using the SEM.

Bulk Density. Large monosized gypsum particles of many FGD gypsums tend to exhibit a high bulk density. Often, the synthetic gypsum is to be purchased sight unseen by the gypsum company. This can present engineering and process challenges to the wallboard manufacturer in designing suitable material handling systems due to the high bulk density. Loose bulk density of natural gypsum is about 50 pcf. The bulk density of synthetic gypsums can vary widely from less than 40 pcf to over 70 pcf. Table Four lists bulk densities of selected natural and synthetic gypsums used by USGC. Bulk density is easily measured through the weighing of a known volume of material.

SUMMARY

Over the years of using natural and synthetic gypsums, USGC has developed and employed several methods of characterizing natural and synthetic gypsum. Synthetic and natural gypsum are chemically the same. The kind and amount of impurities will vary from source to source for both natural and synthetic gypsums. Chemical and physical property testing techniques are the same for natural and synthetic gypsum. It is the physical properties that commonly distinguish synthetic from natural gypsum.

In general, synthetic gypsum has a narrow particle size distribution. Natural gypsums are ground and have a much broader particle size distribution. Other physical properties differences such as surface area, bulk density and aspect ratio are related to the narrow particle size distribution of synthetic gypsum.

Synthetic gypsum is received at the wallboard plant in a wet cake form. It is important to the wallboard manufacturer that the gypsum be as low as possible in free moisture within the capability of the supplier. Lower free moisture reduces wallboard manufacturing costs.

REFERENCES

1. P. J. Henkels and J.C. Gaynor, "Characterization of Synthetic Gypsum", The Fourth International Conference on FGD and Other Synthetic Gypsum, May 1995.

2. J. W. Barber, B. A. Hudgens, C. D. Byers and V. R. Nathan, "Characterization of Synthetic Gypsum", The Second International Conference of FGD and Chemical Gypsum, May 1991.

TABLE ONE **FGD GYPSUM GUIDELINES**

	USG	German Gypsum Association
Purity ($CaSO_4 \cdot 2H_2O$) (%, min)	95	95
SO_3 (%, min.)	44.2	—
Free Moisture (%, max.)	10	10
Flyash (%, max.)	1.0	---
SiO_2 (%, max.)	1.0	---
Calcium Sulfite (%, max.)	1.0	0.25
Chloride (max. ppm)	120	100
Total Water Soluble Salts (max. ppm)	600	---
Average Particle Size (min. microns)	20	---
Surface Area (cm^2/gram)	3500 max.	---
pH	6 - 8	5 - 9

TABLE TWO **SAMPLE SOLUBLE SALT ASSAY**

Soluble Salts:	**Synthetic (ppm)**		**Natural (ppm)**
Potassium (K)	1		13
Sodium (Na)	7		15
Magnesium (Mg)	26		29
Chloride (Cl)	32		23
Reconstruction			
KCl	2		24
NaCl	17		19
Mg(Cl)2	27		0
Ca(Cl)2	0		0
K2SO4	0		0
Na2SO4	0		23
Mg2SO4	94		143
Total	141		209
Equivalent lbs/ton	0.28		0.42

TABLE THREE **TRACE ELEMENTS**

Zinc
Cadmium
Chromium
Nickel
Cobalt
Copper
Lead
Tin
Molybdenum
Fluorine
Arsenic
Antimony
Mercury
Selenium
Vanadium
pH

TABLE FOUR **BULK DENSITY**

	Loose Bulk Density
Natural Gypsum	50 pcf
Synthetic Gypsum #1	75 pcf
Synthetic Gypsum #2	45 pcf
Synthetic Gypsum #3	53 pcf
Synthetic Gypsum #4	62 pcf

FIGURE ONE **SEM Photograph of Flyash Impurity in Synthetic Gypsum**

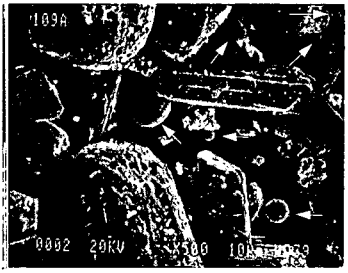

FIGURE TWO **SEM Photographs of FGD and Natural Gypsum**

FGD GYPSUM

Natural Gypsum

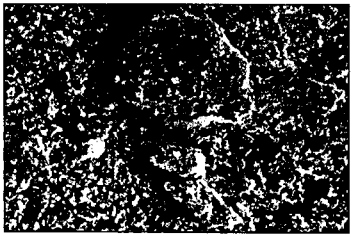

FIGURE THREE

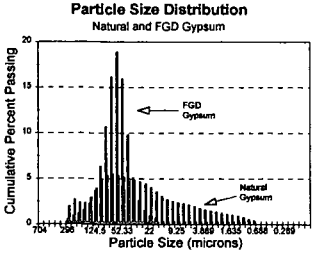

FIGURE FOUR

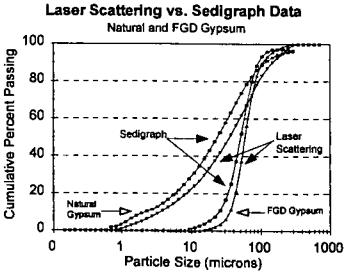

BIOMASS PRODUCTION AND WATER QUALITY IN AN ACIDIC SPOIL AMENDED WITH Mg(OH)2-ENRICHED BY-PRODUCT GYPSUM

Humberto Yibirin, R.C. Stehouwer, J. Bigham, and P. Sutton.
OARDC/School of Natural Resources, Williams Hall
Wooster, OH 44691

Keywords: GYPSUM, MAGNESIUM, SPOIL, LAND RECLAMATION

Gypsum (G) and $Mg(OH)_2$ (FGD-Mg) are recovered from the thickener overflow of an experimental wet FGD scrubber in the Zimmer power plant of CINergy (Cincinnati Gas and Electric Company). The purity of recovered G ranges from almost 100 to 92%, with impurities occurring mainly as $Mg(OH)_2$. Gypsum contaminated with $Mg(OH)_2$ is referred to as $Mg(OH)_2$-enriched by-product gypsum (Mg-G).

Because of its $Mg(OH)_2$ content, Mg-G can potentially be used as a source of both Ca and Mg for green plants growing on soils and spoils with low levels of available Ca and Mg. In addition, the presence of $Mg(OH)_2$ should allow Mg-G to be used as an alkaline amendment for the reclamation of hyper-acid spoils. The total abandoned surface coal mined land needing reclamation in eastern USA has been estimated to be more than 0.5 million ha (Sutton and Dick, 1987). Gypsum can reduce Al toxicity by: (1)increased ratio of Ca to Al in the soil solution (Kinraide et al., 1992), and (2) physical removal of Al from the soil profile through Ca exchange (Wendell and Ritchey, 1993). The $Mg(OH)_2$ in Mg-G may enhance the effectiveness of these mechanisms for amelioration of phytotoxic conditions below the zone of incorporation. The presence of Mg and sulfate increases the potential for salt loading (Stehouwer et al., 1995), which may enhance downward movement of Ca and Al.

The purpose of this greenhouse study was to investigate the effects of G and Mg-G, at three application rates, on spoil and leachate pH and electrical conductivity (EC), and movement of major and trace elements. Preliminary observations on plant growth are also reported.

MATERIALS AND METHODS

Acidic minespoil was sampled from the upper 20 cm of an abandoned mineland (AML) site located at the Eastern Ohio Resource Development Center (EORDC). The samples were air-dried and passed through a 12.7-mm sieve. Initial Bray #1 P was 25 mg kg^{-1}; NH_4-acetate extractable Ca, K, Mg, and Al were 225, 54, 37, and 601 mg kg^{-1} respectively; CEC was 30 $cmol_c$ kg^{-1}, and pH was 2.9.

Three by-product materials were used: G (98% gypsum), and two Mg-G blends (4%Mg-G, and 8% Mg-G) which contained 4 and 8% (w/w) $Mg(OH)_2$ equivalent. Reagent grade $Ca(OH)_2$ was also mixed with G to produce two mixtures (4%Ca-G, and 8%Ca-G) with neutralizing potentials equal to 4%Mg-G and 8% Mg-G respectively.

Spoil material (8 kg) was poured into PVC columns (60 cm tall, 15 cm diam.) to a height of 36 cm forming an untreated sub-surface layer. A 15-cm surface layer of spoil (3.4 kg) was then thoroughly mixed with the various treatments and placed over the untreated spoil. The columns were mounted on flat PVC plates with a nipple in the center to allow for leachate collection.

Treatments consisted of G, 4%Mg-G, 8%Mg-G, 4%Ca-G, or 8%Ca-G applied at rates equivalent to 145, 290, and 580 Mg ha^{-1} . These rates were calculated to supply Ca from G in amounts equal to 2.5, 5.0, and 10.0 times the spoil CEC in the treated layer. Control treatments included unamended spoil and spoil amended to pH 7.0 with limestone (112 Mg ha^{-1}). Treatments were arranged in randomized complete blocks with three replications. Fertilizers were applied together with the treatments in amounts of 0.5 g NH_4NO_3, 0.4 g triple superphosphate, and 2 g KCl.

Columns were then leached with 2.5 L of deionized water and the first leachates (150-200 ml) were collected. Following this first leaching, 5 g of soil was collected from the surface 5-cm depth of each column for pH and EC measurements, and each column was planted with 30 seeds of Orchardgrass (*Dactylis glomerata* L.). After an initial 80-d growing period, orchardgrass was harvested monthly for a total of 4 harvests. Leachates were also collected at the end of the study. Columns were watered daily with deionized water such that the amount of water applied during the study was equivalent to the average annual rainfall for SE Ohio (≈1000 mm).

Leachates were analyzed for pH, EC, and for As, B, Ba, Be, Ca, Cd, Co, Cr, Cu, Fe, K, Li, Mg, Mn, Mo, Na, Ni, P, Pb, S, Sb, Se, Si, and Zn by inductively coupled plasma emission spectrometry. Data analysis was conducted using analysis of variance procedures, and single degree of freedom orthogonal contrasts.

RESULTS AND DISCUSSION

The Mg-G and Ca-G amendments were equally effective at increasing the pH of the acidic minespoil in the treated layer (Table 1). None of the amendments used, however, increased the pH of the first or final leachates compared to the untreated spoil. Increases in spoil pH led to increased growth of orchardgrass, however, the largest application rates of 4% and 8% Mg-G suppressed yield in the first two harvests. This initial yield suppression was associated with large increases in EC.

Mg-G increased spoil and leachate EC more than any other treatment (Table 1). The use of 4%Mg-G increased spoil EC 1.23 times compared to 4%Ca-G, 8%Ca-G, or gypsum, and 3.4 times compared to either the untreated or limed spoil. These differences were larger when the spoil was amended with 8%Mg-G. Leaching of salts out of the column during the course of the study reduced the EC in the final leachates, but Mg-G effects on EC were still present. Stehouwer et al. (1995) showed that the solubility of Mg in a spoil amended with materials containing $CaSO_4$ and $Mg(OH)_2$ may be controlled by epsomite ($MgSO_4.6H_2O$) which is ≈ 300 times more soluble than gypsum. Enrichment of gypsum with Mg, therefore, increased the potential for salt loading. Gypsum-containing treatments increased the leachate concentrations of Ca, Mg, Al, Fe, Mn, and S (Table 2), and of Cd, Cr, Pb, Cu, and B (Table 3) relative to the control treatments. The largest increase occurred with Mg-G. Most cations were much less mobile with limestone and Ca-G treatments. The use of G alone increased the movement of Al, S, Fe, Mn, Cr, and B compared to Ca-G. The $Ca(OH)_2$ in Ca-G reduced the movement of metal cations in the spoil compared to G alone, thus making Ca-G behave more like limestone than G. By contrast, the $Mg(OH)_2$ in Mg-G increased the movement of metal cations in the spoil compared to G alone, limestone, or Ca-G. Effects of Mg-G on cation movement were most likely not due to pH differences since Mg-G and Ca-G had similar effects on pH. The increased transport of these metals with Mg-G appeared to be due to large concentrations of Mg^{2+} in solution. We believe the increases in metals in the leachates were due to mobilization of metals present in the spoil. These were brought into solution through exchange reactions with Mg^{2+} and then transported downward.

Amendment with Mg-G increased pH, thus allowing revegetation of otherwise phytotoxic spoils. In addition to being a source of Ca and Mg, Mg-G enhanced downward movement of Al, and Fe which may promote root penetration in untreated subsurface layers, and improve the chances of reclamation success. Amendment applications, however, should be limited to rates that will not cause phytotoxic salt concentrations, excessively high pH, or increase the concentrations of heavy metals in water to harmful levels.

Table 1. Initial and final electrical conductivity (EC) and pH in the spoil and leachate, averaged across rates, as affected by wet FGD $Mg(OH)_2$-enriched gypsum, gypsum, $Ca(OH)_2$-enriched gypsum, and calcitic limestone*.

	Spoil Init	Leach First	Leach Final	Spoil Init	Leach First	Leach Final
	------ pH ------			-----EC, S m^{-1} -----		
4%Mg-G	5.60	2.27	2.58	0.27	0.64	0.32
8% Mg-G	7.31	2.26	2.67	0.32	0.64	0.29
4%Ca-G	5.82	2.27	2.55	0.23	0.44	0.24
8%Ca-G	7.23	2.26	2.55	0.21	0.47	0.21
Gypsum	3.09	2.26	2.60	0.22	0.53	0.28
Untreated	2.87	2.33	2.78	0.07	0.30	0.09
Limestone	7.09	2.33	2.71	0.09	0.30	0.10
avg.	5.71	2.27	2.61	0.23	0.52	0.25
lsd 0.05†	0.31	NS	0.05	0.03	0.09	0.04

† lsd = least significant difference.
* leachate and initial are abbreviated as leach and init.

Table 2. Major element composition of first leachate, averaged across rates, as affected by wet FGD $Mg(OH)_2$-enriched gypsum, gypsum, $Ca(OH)_2$-enriched gypsum, and calcitic limestone.

	Ca	Mg	Al	Fe	Mn	S
	---------- mg L^{-1} ----------					
4%Mg-G	124	301	866	142	3	1821
8% Mg-G	105	249	950	150	3	1903
4%Ca-G	64	53	418	72	2	646
8%Ca-G	69	56	432	76	2	617
Gypsum	78	108	700	114	3	1201
Untreated	40	35	227	48	1	440
Limestone	36	37	246	53	1	479
avg.	82	139	622	104	2	1146
lsd† 0.05	22	57	170	22	1	258

† lsd = least significant difference.

Table 3. Trace element composition of first leachate, averaged across rates, as affected by wet FGD $Mg(OH)_2$-enriched gypsum, gypsum, $Ca(OH)_2$-enriched gypsum, and calcitic limestone.

	As	Cd	Cr	Pb	Cu	B
	---------- mg L^{-1} ----------					
4%Mg-G	<0.04	0.05	0.28	0.22	0.64	4.41
8% Mg-G	<0.04	0.05	0.30	0.21	0.65	3.91
4%Ca-G	<0.04	0.04	0.14	0.11	0.50	0.40
8%Ca-G	<0.04	0.04	0.15	0.09	0.52	0.35
Gypsum	<0.04	0.05	0.24	0.18	0.63	1.30
Untreated	<0.04	0.03	0.09	0.08	0.35	0.27
Limestone	<0.04	0.03	0.08	0.19	0.32	0.23
avg.	<0.04	0.05	0.21	0.16	0.56	1.86
lsd† 0.05	NS	0.01	0.05	0.08	0.1	0.7

† lsd = least significant difference.

ACKNOWLEDGMENT

This study is part of an ongoing research program conducted at The Ohio State University. Support for this research was provided by The Ohio Coal Development Office, CINergy (Cincinnati Gas & Electric Co.), and Dravo Lime Company.

LITERATURE CITED

Kinraide, T.B., P.R. Ryan, and L.V. Kochian. 1992. Interactive effects of Al^{+3}, H^{+}, and other cations on root elongation considered in terms of cell-surface electrical potential . Plant Physiol. 99:1461-1468.

Stehouwer, R.C, P. Sutton, R.K. Fowler, and W.A. Dick. 1995. Minespoil amendment with dry flue gas desulfurization by-products:Element solubility and mobility. J. Environ. Qual. 24:164-174.

Sutton, P., and W.A. Dick. 1987. Reclamation of acidic mined lands in humid areas. Adv. Agron. 41:377-405.

Wendell, R.R., and K.D. Ritchey. 1993. Use of high-gypsum flue gas desulfurization by-products in agriculture, p. 40-45. *In* Shiao-Hung (ed.), Proceedings of the Tenth Annual International Pittsburgh Coal Conference. September 20-24, 1993. Pittsburgh, PA.

This page left intentionally blank.

MANUFACTURE OF AMMONIUM SULFATE FERTILIZER FROM GYPSUM-RICH BYPRODUCT OF FLUE GAS DESULFURIZATION - A Prefeasibility Cost Estimate

M.-I. M. Chou, M. Rostam-Abadi, and J.M. Lytle
Illinois State Geological Survey
615 E. Peabody Dr.
Champaign, IL 61820

F.P. Achorn,
Southeast Marketing Chem. Process Inc.
Suite 404, Florence, AL 35631

KEYWORDS: ammonium sulfate, gypsum, desulfurization

ABSTRACT

Costs for constructing and operating a conceptual plant based on a proposed process that converts flue gas desulfurization (FGD)-gypsum to ammonium sulfate fertilizer has been calculated and used to estimate a market price for the product. The average market price of granular ammonium sulfate ($138/ton) exceeds the rough estimated cost of ammonium sulfate from the proposed process ($111/ton), by 25 percent, if granular size ammonium sulfate crystals of 1.2 to 3.3 millimeters in diameters can be produced by the proposed process. However, there was at least ±30% margin in the cost estimate calculations. The additional costs for compaction, if needed to create granules of the required size, would make the process uneconomical unless considerable efficiency gains are achieved to balance the additional costs. This study suggests the need both to refine the crystallization process and to find potential markets for the calcium carbonate produced by the process.

INTRODUCTION AND BACKGROUND

The 1990 amendments to the Clean Air Act mandate a 2-stage 10-million ton reduction in sulfur dioxide emissions in the United States. Emission controls using flue gas desulfurization (FGD) technologies have been commercially demonstrated. However, in addition to capital costs for equipment and operating expenses, plants burning high sulfur coal and using FGD technologies must also bear increasingly expensive landfill disposal costs for the solid waste produced. FGD technologies would be much less of a financial burden if successful commercial uses were developed for the gypsum-rich byproducts of wet limestone scrubbing.

A process for converting FGD-gypsum to calcium carbonate and ammonium sulfate by allowing it to react with CO_2 and ammonia or by allowing it to react with ammonium carbonate was studied at the ISGS. A variation of this process could provide electric utilities a means converting the CO_2 and SO_2 in their flue gas to useful commercial products. The fertilizer industry would also be provided with an abundant source of ammonium sulfate to supply sulfur nutrient in NPK fertilizer blends. If successful, the results of this project could provide a solution, from both the environmental and economic standpoints, to the problem of disposing of large quantities of by-products from FGD processes. The technical feasibility of producing fertilizer-grade ammonium sulfate from FGD-gypsum has been assessed (Chou et al., 1995). It is important, therefore, to assess the economic feasibility of producing commercial-grade ammonium sulfate fertilizer from FGD-gypsum The preliminary process flow diagram and the rough cost estimates of the process are presented in this paper.

PROCESS FLOW DIAGRAM

The proposed process is similar to the one used in Europe and India in the 1960s to produce large quantities of ammonium sulfate from natural gypsum (Sauchelli, 1964). Some modifications were made on the gypsum conversion reactor based on pilot plant tests by the TVA (Meline et al., 1971).

Figure 1 shows the proposed flow diagram for the conversion of gypsum to ammonium sulfate fertilizer and calcium carbonate. The flow diagram contains four major units: 1) absorption tower, 2) gypsum converter, 3) concentrator-crystallizer, and 4) solid handling system .

In an absorption tower, ammonium carbonate, a major reactant, is formed by reacting carbon dioxide and ammonia in aqueous solution. The ammonium carbonate solution is then mixed with gypsum ($CaSO_4 \cdot 2H_2O$) and delivered to a gypsum conversion unit .

In the gypsum converter, the mixture is converted to ammonium sulfate solution and calcium carbonate by the following reaction:

$(NH_4)_2CO_3 + CaSO_4 \cdot 2H_2O \rightarrow (NH_4)_2SO_4 + CaCO_3 + 2H_2O$

The overflow from the gypsum converter, containing all of the $(NH_4)_2SO_4$ produced, will give a solution of 35% ammonium sulfate. The solution will be concentrated from 35 to about 42 to 45% in a standard Swenson vacuum-type concentrator with forced circulation. A vacuum crystallizer equipped with a heat exchanger (evaporator-crystallizer) designed to control the conditions for crystal formation is used. The ammonium sulfate solution should be supersaturated within a metastable field during the process of crystallization, in order to produce the larger crystals (particle size 1.2 to 3.3 millimeters with average 2.4 millimeters) required for fertilizer application. Two medium-sized crystallizers are used to provide a shorter retention time during crystallization.

The slurry with crystals from the crystallizer is centrifuged and the crystals are washed with dilute aqueous ammonia. The solution from the centrifuge is used to dissolve fines from screening the product. The $(NH_4)_2SO_4$ crystals are first dried then cooled in rotary type equipment. Material from the cooler is screened on double deck vibrating screens. Oversized and undersized crystals from the screens are directed to the dissolution tank. Suitable size crystals (1.2 to 3.3mm) are delivered to bulk storage.

ASSUMPTIONS FOR RAW MATERIALS ESTIMATION

Gypsum - The yearly production of FGD-gypsum from a 550 Mw electrical generating plant was calculated based on data (Hillenbrenner, 1995) from the City Water Light and Power Utility of Springfield, IL. This company uses a limestone scrubbing process to remove sulfur dioxide from the exhaust gases by converting it to gypsum ($CaSO_4 \cdot 2H_2O$). The plant consumes coal at a rate of 0.96 pounds per kwh and the sulfur content of the coal is about 3%. Based on a load factor of 65% for 300 days per year of operation, the plant produces 200,000 tons gypsum per year.

Ammonia gas - Assuming 98% recovery, one ton of gypsum could produce 0.752 tons of ammonium sulfate. This requires 0.22 tons of ammonia gas (10% excess) consumption per ton of gypsum (Bennett, 1962; Hillenbrenner, 1995) or 0.292 tons of ammonium gas consumption per ton of ammonium sulfate. The proposed plant will require about 123.4 tons of ammonia gas per day (or 43,800 tons per year to produce 150,000 tons of ammonium sulfate per year.

Carbon dioxide - The proposed plant would be built near a utility or a lime producing plant that could supply the carbon dioxide. It was assumed, for this estimate, that the CO_2 would be obtained from the utility or a lime producing plant at no cost.

It is assumed that the 0.581 tons of $CaCO_3$ produced per ton of gypsum processed (or 0.773 tons of $CaCO_3$ per ton of ammonium sulfate) will be recycled to the scrubber. This will result in recycling 325.9 tons of $CaCO_3$ per day.

EQUIPMENT AND COST ESTIMATIONS

The cost estimates are based on the assumption that a linear projection of the TVA pilot plant equipment (Meline et al, 1971) to a commercial scale plant will result in at least a 30 percent increase in production capacity and allow for usual plant down-time while producing 150,000 tons of ammonium sulfate per year. All cost estimates are for a conceptual plant design. Additional references used in the calculation include the sixth edition of the Chemical Engineer's Handbook by Perry & Green and economics factors for 1993 and 1994 found in the chemical engineering journals. See Tables 1 to 3 for the cost summary.

COMPACTION ALTERNATIVE

A specific size of ammonium sulfate is demanded by the fertilizer and chemical industries. If sufficiently large crystals of ammonium sulfate can not be produced, an alternative is to compact the smaller crystals. Based on available literature information (Compaction, 1983), a process for compacting the smaller size product was developed and used to estimate the additional costs.

For the compaction process, the smaller size ammonium sulfate is delivered to a fresh feed hopper. The crystals are weighed and then delivered to the compactors, which are two rolls that are

hydraulically operated so that the materials passing between the rolls are compressed into flakes. The flakes are broken to desired sizes by a specially designed coarse crusher. Materials from the crusher are screened to extract the desired particle size. Oversize materials from the screens are returned to the crusher, fines from the screens are recirculated to the compactor. The sized product is usually passed through a rotary drum to remove the rough edges from the product.

RESULTS AND DISCUSSION

The total cost and individual unit costs for the installed equipment for the basic process are shown in Table 1. The fixed capital and working capital investments are shown in Table 2. Table 3 lists the costs for raw material, operating cost, other cost, in-plant (transfer) cost and the ex-gate cost. These estimates assume the cost of ammonia in Illinois is $200 per ton (Green Markets, March '95) and the total material cost is to be $58.40 per ton of product. The operating cost was calculated to be $26.14 per ton (Table 3). Since the calcium carbonate will be recycled, the process receives a credit for the cost of the limestone that is replaced (based on $15 per ton for limestone). The calculations show this credit should be $11.60 per ton of ammonium sulfate. The net production cost of the ammonium sulfate without considering capital cost is $72.94 per ton. The capital costs shown in Table 2, were used to determine the cost of depreciation, taxes, and insurance. With these costs the subtotal cost was estimated to be $86.58. In addition, the cost of interest, the minimum equity return, and pre-tax incentive return need to be added. These costs are calculated using the capital cost in Table 2. These data show the total in-plant cost to be $106.78 per ton of ammonium sulfate. This in-plant cost of ammonium sulfate is used in the next section to calculate the plant sale price for compacted material. A general sales and administrative cost ($4.00 per ton of ammonium sulfate) added to the in-plant cost, yields an estimated sale price of $110.78 of no compaction is needed to produce crystals of the required size.

Price Comparison with Commercial Products- As recorded in "Green Markets," a respected publication of the fertilizer industry, the March price for granular ammonium sulfate in Illinois for the past 3 years were $137 to $154/ton, $134 to 141/ton, and $123 to $135 $/ton for 1995, 1994, and 1993 respectively. These data give an average market price of granular ammonium sulfate of $138/ton.

The average market price of granular ammonium sulfate ($138/ton) exceeds the estimated cost of ammonium sulfate from the proposed process ($110.78/ ton), by a margin of 25 percent. However, there is a margin of error of ±30 percent in the cost estimates. The product could have a very competitive price if the crystals produced fall in the required size range (1.2 to 3.3 millimeters) for granular products.

Costs Including Compaction- If desired size crystals can not be produced, compaction of the smaller crystals will be necessary. A cost estimate (Tables 4 to 6) was made including the additional cost of compaction. In this estimate, the raw material costs include ammonium sulfate at the in-plant transfer price ($106.78/ton) and a binder cost at $0.6/ton. The total raw material cost, therefore, is $107.38 per ton. The additional operating cost for compaction was estimated to be $8.40 per ton. After capital costs, taxes and insurance were added, the total estimated production cost was $126.49/ ton. This results in an estimated in-plant price of $143.09 per ton. When general sales and administrative cost are added, the sale price would be $147.09 per ton. This is about $10 per ton higher than the average March commercial price for the last 3 years, but, close to the average March price for this year ($146).

CONCLUSIONS AND RECOMMENDATIONS

Considering that the costs are for a conceptual plant design and as such subject to the usual margin of error, the results of this study indicate that the proposed process could be economically feasible if crystals of 1.2 to 3.3 millimeters can be produced without compaction. Because the average market price of granular ammonium sulfate ($138/ton) exceeds with the estimated cost of ammonium sulfate without compaction from the proposed process ($110.78/ ton), a profit margin of 25 percent could be possible. If smaller crystals are produced and compaction is necessary, cost estimates show a negative margin between the market price and the sale price. This study indicates the need both to refine the crystallization process and, perhaps, to find other potential markets for

the by-product calcium carbonate.

ACKNOWLEDGMENT & DISCLAIMER

This report was prepared by the authors through a research project supported, in part, by grants made possible by the U.S. Department of Energy (DOE) cooperative Agreement Number DE-FC22-PC92521 and the Illinois Coal Development Board (ICDB) and the Illinois Clean Coal Institute (ICCI). Neither the authors nor any of the subcontractors nor the U.S. DOE, ISGS, ICDB, ICCI nor any person acting on behalf of any of them assumes any liability with respect to the use of, or for damages resulting from the use of, any information disclosed in this report. The authors are grateful to Drs. J. H. Goodwin and S.B. Bhagwat, staff members of the ISGS, for their reviewing of this manuscript.

REFERENCES

Bennett, R.C., Product Size Distribution in Commercial Crystallizer, Chemical Eng. Prog. Vol. 58, No. 9, 1962.

Chou, M.I. M., J.A. Briunius, Y.C. Li, J.M Lytle, and M. Rostam-Abadi, Manufacture of ammonium sulfate fertilizer from FGD-gypsum, preprint of the American Chemical Society Fuel Chem. Div., Chicago, August 20-24, 1995.

Compaction, IFDC Technical Bulletin EFD6-T-25, June, 1983.

Green Markets, March 1993, March 1994, and March 1995.

Hillenbrenner, J., City Water Light and Power, Springfield, IL via telephone during March 1995.

Higson, G.I., The Manufacture of Ammonium Sulphate from Anhydrite, Chemistry and Industry, 750-754, September 8, 1951.

Journal of Chemical Engineering 1993 and 1994. Economic Factors Relating to Cost of Plant Facilities.

Kachelman, D.L., Fluid Fertilizer Reference Manual, TVA Report Y 210 November, 1989.

Kenton, J.R., Fertilizer Components: Ammonium Sulfate, Encyclopedia of Chemical Processing and Design, vol 21, 274-283, Marcel Dekker, Inc., New York, 1985.

Kirk-Othmer, Encyclopedia of Chemical Technology, fourth edition, vol. 2, 706, John Wiley & Sons, New York, 1992.

Meline, R.S., H.L. Faucett, C.H. Davis, and A.R. Shirley Jr., Pilot-Plant Development of the Sulfate Recycle Nitric Phosphate Process, Ind. Eng. Process Des. Develop., vol. 10, 257-264, 1971.

Perry, R.H., and D.W. Green editors, Perry's Chemical Engineers Handbook, 6th Edition, McGraw Hill, 1984.

Sauchelli, V., Fertilizer Nitrogen, American Chemical Society's Series of Chemical Monographs, Reinhold Publishing Co, 1964.

Table 1. Plant Equipment and Costs

Unit	Dollars
Absorption Tower Tower, Air filter, Pumps, and handling equipment and Installation	$ 625,000
Gypsum Converter Equipment, Foundations, auxiliary equipment, and Installation	$1,500,000
Concentrator Auxiliaries and Incidentals Equipment and Installation	$ 330,000
Crystallizer crystallizer, centrifuge, and Installation	$2,330,000
Solids Handling Dryer, Cooler, Screens Elevator, Conveyors, Dust controlling system, and Installation	$2,100,000
Total	$6,885,000

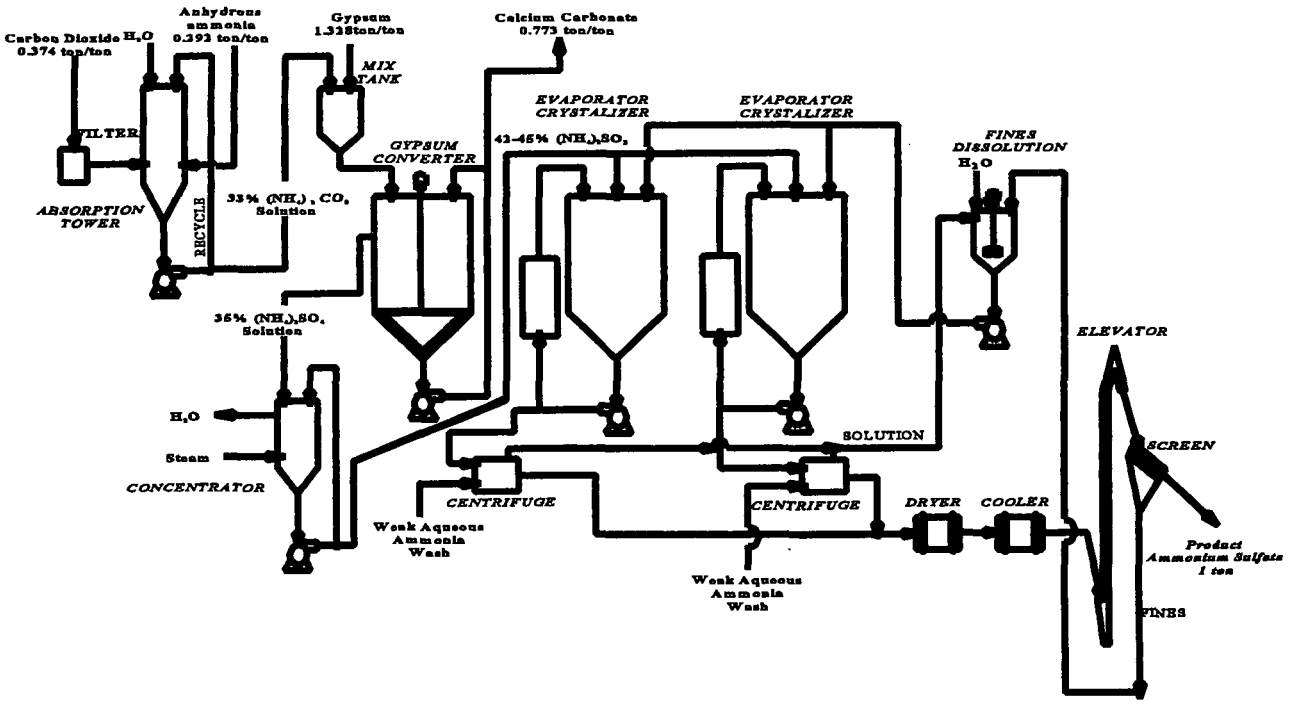

Figure 1: Flow Diagram of the process to convert gypsum to ammonium sulfate.

Table 2. Plant Capital Investment for Ammonium Sulfate (non-granular) Production at a capacity of 422 tons per day or 150,000 tons per year.

ITEM NO.		COST (x 10^6 $)
A. Fixed Capital - Depreciable		21.985
■	Installed Equipment	6.885
■	Design Engineering, etc.	3.400
■	Site Preparation	1.000
■	Auxiliary Facilities	3.525
■	Dry Storage	2.000
■	Incidental and Overheads	5.175
B. Fixed Capital - Nondepreciable		0.94
■	Spare Parts, 2% A	0.44
■	Land	0.50
C. Working Capital - Nondepreciable		1.293
■	30 - day raw materials cost	0.739
■	15 - day Inventory Value	0.554
D. Total Fixed Capital (A+B)		22.923
E. Total Capital (A+B+C)		24.218
F. Average Capital (0.53 A+B+C)		13.885

Table 3. Cost estimate - Production of ammonium sulfate crystalline fertilizer from FGD-gypsum at a capacity of 422 tons per day or 150,000 tons per year (355 days)

Raw Materials	Units	Units/ton	$/Unit	Cost, $/ton
Ammonia	TON	0.292	200	58.40
Gypsum	TON	1.328	0	0
Carbon Dioxide	TON	0.374	0	0
Total raw material cost			**A**	58.40
Operating				
Direct labor (calculated 0.408 man-hrs/ton X $17.00/hr)				6.94
Maintenance (calculated 0.15mh/ton x $20/hr)				3.00
Utilities (estimated)				12.61
Supplies (20% maintenance)				0.60
Plant overhead ($/ton) calculated				2.99
Operating costs,			B	26.14
Cr. for rec. limestone (0.773 tons/ton $(NH_4)_2SO_4$ X $15/ton)			C	11.60
Net operating cost			**B - C**	14.54
Capital				
Depreciation 6.7% A (from Table 2)/TY*				9.82
Ins. & taxes 2.5% (A+B, from Table 2)/TY				3.82
Total capital cost			**D**	13.64
Others				
Interest 10% F (from Table 2) X 0.5/TY				4.62
Minimum equity return 0.075x F(from Table 2) X 0.5/TY				3.47
Pre-tax incentive return 0.075x E(from Table 2)/TY				12.11
Total other costs			E	20.20
In-Plant Transfer				
General Sales & administrative cost			**F**	4.00
Ex-gate price, $/ton		**A + (B - C) + D + E + F**		**$110.78**

*TY is tons of ammonium sulfate produced in one year.

Table 4. Compaction Plant Equipment and Costs

Unit	Dollars
Compaction Plant Equipment, Installation, Additional building, offsites	$ 16,000
Total	$ 16,000

Table 5. Additional Capital investment for Compaction of Ammonium Sulfate

ITEM	COST (x 10^6 $)
A. Fix Capital - Depreciable	17.47
■ Installed Equipment	16.00
■ Start-up Allowance	0.48
■ Construction Capital	0.99
B. Fixed Capital-Nondepreciable	0.00
C. Working Capital-Nondepreciable	2.11
30 - day raw materials cost	1.37
15 - day Inventory Value	0.74
D. Total Fixed Capital (A+B)	17.47
E. Total Capital (A+B+C)	19.58
F. Average Capital (0.53A+B+C)	11.36

Table 6. Cost estimate - Production of ammonium sulfate crystalline fertilizer from FGD-gypsum at a capacity of 422 tons per day or 150,000 tons per year (355 days), with compaction.

Raw Materials	Units	Units/ton	$/Unit	Cost, $/ton
Ammonium Sulfate	TON	1	106.78	106.78
Binder	TON	0.01	0.60	0.60
Total raw material cost			A	107.38
Operating				
Direct labor (calculated 0.408 man-hrs/ton X $17.00/hr)				2.70
Maintenance (calculated 0.15mh/ton x $20/hr)				1.00
Electricity (45kwh/ton X $ 0.10 /kwh) (estimated)				3.00
Supplies (20% maintenance)				0.20
Plant overhead ($/ton) calculated				1.50
Total operating costs,			**B**	8.40
Capital				
Depreciation 6.7% A (from Table 2)/TY*				7.80
Ins. & taxes 2.5% (A+B, from Table 2)/TY				2.91
Total capital cost			**C**	10.71
Others				
Interest 10% F (from Table 2) X 0.5/TY				3.97
Minimum equity return 0.075x F(from Table 5) X 0.5/TY				2.84
Pre-tax incentive return 0.075x E(from Table 5)/TY				9.79
Total other costs			**D**	16.60
In-Plant Transfer				
General Sales & administrative cost			**E**	4.00
Ex-gate price, $/ton			**A + B + C + D + E**	$147.09

*TY is tons of ammonium sulfate produced in one year.

COAL COMBUSTION FLY ASH--
OVERVIEW OF APPLICATIONS AND OPPORTUNITIES IN THE USA

Sam Tyson, P.E. and Tom Blackstock, P.E.
Executive Director and Director of Technical Services
American Coal Ash Association, 2760 Eisenhower Ave, Suite 304,
Alexandria, VA 22314

Keywords: fly ash, CCBs, ash utilization

ABSTRACT

The American Coal Ash Association, Inc. (ACAA) is an organization representing the coal combustion byproducts industry. Since 1968, the goal of ACAA has been to gain recognition and acceptance of coal fly ash as an engineering material on par with competing virgin, processed and manufactured materials by advancing uses that are technically sound, commercially competitive and environmentally safe.

An annual survey of coal-burning electric utilities is conducted by ACAA to determine the quantities of coal fly ash produced and used in the USA. In 1993 approximately 43.4 million metric tonnes(47.8 million short tons) of coal fly ash were produced. Approximately twenty-two percent or 9.5 million metric tonnes (10.5 million short tons) was used while the remaining portion was deposited in disposal areas. The major markets for coal fly ash include cement and concrete products, structural fills, road base stabilization, flowable fills, mineral filler in asphalt, grit for snow and ice control, grouting, coal mining applications, and waste solidification and stabilization.

INTRODUCTION

An annual survey of electric utilities is conducted by ACAA to determine the quantities of CCBs produced and used in the United States (Ref. 1; ACAA 1994). In 1993 approximately 80.3 million metric tons (88.5 million short tons) of CCBs were produced in the U.S. in the form of fly ash, bottom ash, boiler slag and flue gas desulfurization (FGD) material. Approximately twenty-two percent of the combined production of these byproducts was used, while the remaining portion was deposited in disposal areas. Production and use quantities for these byproducts are summarized in Table 1.

Table 1. Production and Use of Coal Ash.
[1993 Data; Million metric tons (million short tons)]

	Fly Ash	Bottom Ash	Boiler Slag	FGD Mat'l
Production	43.4 (47.8)	12.8 (14.2)	5.6 (6.2)	18.4 (20.3)
Use	9.5 (10.5)	3.8 (4.2)	3.1 (3.4)	1.0 (1.1)
% Use	22%	30%	55%	6%

It is clear from survey data gathered by ACAA over the years that the annual use of 18.2 million metric tons (20.3 million short tons) of CCBs represents a major continuing effort by a number of parties, including the electric utility producers of CCBs and their marketers. It is equally clear, however, that

significant quantities of CCBs are not used each year. Therefore it is essential for ACAA to promote the use of coal combustion byproducts in numerous applications that are technically sound, commercially effective and environmentally safe.

CCBs are engineering materials and are similar in use to competing virgin, processed and manufactured materials. CCBs are affected by local and regional factors, which include production rates, processing and handling costs, transportation costs, availability of competing materials, seasonal adjustments, and the experience of materials specifiers, design engineers, purchasing agents, contractors, and other construction professionals.

COAL FLY ASH APPLICATIONS

It is instructive to consider the total amounts of coal fly ash that are used in the leading markets based on ACAA's 1993 survey results, presented in Table 2.

Table 2. *Summary of Fly Ash Uses.*
[1993 Data; Million metric tons (million short tons)]

Fly Ash Uses	Million Tons	
	Used	Percent
Cement and concrete products	6.17(6.8)	65.0
Road base/subbase	0.91(1.0)	9.5
Structural fills, embankments	0.83(.91)	8.7
Flowable fill	0.34(.38)	3.6
Filler in asphalt mixes	0.10(.11)	1.0
Grouting	0.02(.02)	0.2
Waste stabilization	0.40(.44)	4.2
Other	0.76(.84)	17.8
Total Used	9.53(10.5)	100.0

CEMENT AND CONCRETE PRODUCTS

In 1993 approximately 6.17 million metric tons(6.8 million short tons) of coal fly ash was used in the *U.S.* in cement and concrete products (Ref. 1; ACAA 1994). The amount of coal fly ash in typical structural concrete applications ranges from 15 to 35 percent by weight, with amounts up to 70 percent for massive walls and girders, concrete road bases, and dams.

Various concrete mixtures are produced with coal fly ash including 2500 to 6000 psi normal weight and lightweight concretes, high strength (>6000 psi) concrete, early strength concrete for form removal requirements, low-slump paving concrete, controlled low strength material (*CLSM*), and architectural concrete.

With the principal exception of high strength concrete, all of these coal fly ash concrete mixtures are routinely air-entrained for added workability and for resistance to freezing and thawing. A state-of-the-art report on the use of coal fly ash in concrete has been prepared by the American Concrete Institute (ACI) (Ref. 2; ACI, 1987). Fly ash for use in concrete is covered in an ASTM specification (Ref. 3; ASTM, 1994).

Flowable Mixtures (CLSM)

ACI Committee 229 deals with certain flowable grout-like materials under a general designation, "Controlled Low Strength Materials" (CLSM). Such materials have compressive strengths of 1200 psi or less, as currently defined by ACI, and may also represent a wide range of fly ash contents. Applications of CLSM currently being reviewed by ACI 229 include but are not limited to: backfills, structural fills, insulating fills, road and slab base, trench bedding and so on.

While flowable mixtures can be produced without fly ash, it is very easy demonstrate that economical mixtures with the most desirable characteristics, including flowability, cohesiveness, minimal bleeding, and controlled density, can be produced only with fly ash in combination with relatively small amounts of portland cement. The percentage of fly ash used in grout mixtures may be in a wide range from 20 to 95 percent by weight.

CLSM mixtures can be proportioned to provide a desired flowability and unit weight, and to have a compressive strength which is equal to or greater than that of well-compacted soil. CLSM can also be designed for a maximum strength where future excavation may be necessary.

The use of CLSM flowable mixtures is open to numerous innovative engineering solutions for everyday problems that would otherwise be viewed as traditional soils backfilling and foundations problems.

ROAD BASE AND SUBBASE

The ACAA pavement manual (Ref. 4; ACAA, 1991) offers pavement design engineers, materials engineers, and construction managers guidance in the design and construction of low- to high-strength "pozzolanic stabilized mixture" ("PSM") base and subbase layers having coal fly ash in combination with activators, aggregates and water.

To capture the long-term service and cost-saving features of PSM design, the document details a mixture proportioning system, a thickness design procedure, and established mixing and construction techniques. The user can apply the contents of this manual with professional advice to produce satisfactory pavement structures of acceptable uniformity in accordance with current specifications and QC/QA requirements of individual state departments of transportation.

The ACAA pavement manual is supported by guidelines and guide specifications in four chapters that comprise a publication (Ref. 5; AASHTO, 1990) developed by a Joint Committee of the American Association of State Highway and Transportation Officials (AASHTO), the Associated General Contractors (AGC) and the American Road and Transportation Builders Association (ARTBA).

STRUCTURAL FILLS

Fly ash may be used as a borrow material in the construction of fills. When the fly ash is compacted in lifts, a structural fill is constructed which is capable of supporting buildings or other structures. An embankment is constructed when the fly ash is placed to support roads or to impound water. The size of structural fills/embankments that have previously been constructed with fly ash ranges from small fills, consisting of a few thousand cubic yards of material covering less than one acre, to fills covering several acres.

When used in structural fills and embankments, fly ash offers several advantages over soil and rock. These advantages include low unit weight and high shear strength. The compacted maximum dry density of fly ash is typically within the range of 70 to 105 pcf. Compared to fills of silty sand that have a compacted maximum dry density of about 115 pcf, placing fly ash over weak, compressible foundation soils results in lower total settlement. Hauling costs will also be reduced because there is less tonnage for a given volume of fill. Another significant characteristic of fly ash used as a fill material is its strength. Compacted fly ash is as strong or stronger than many compacted soils. Class C ash will self-harden, resulting in a fill that is stronger than most compacted soil.

REGULATORY AND LEGISLATIVE ISSUES

The U.S. Environmental Protection Agency (EPA) issued a final regulatory determination on the four large volume CCB streams from coal-burning electric utilities in August 1993 (Ref. 6; EPA, 1993). The EPA determined that "large volume wastes from coal-fired electric utilities pose minimal risks to human health and the environment. Therefore, it is unnecessary to manage these wastes as hazardous." This determination continues to provide for the management of CCBs under Subtitle D of the Resource Conservation and Recovery Act (RCRA).

The U.S. Department of Energy (DOE) issued a report on the barriers to the increased use of CCBs in July 1994 (Ref. 7; DOE, 1994). The report is expected to have a significant effect on the use and management of CCBs. This report was developed as the result of the Energy Policy Act of 1992 [Public Law No. 102-486, October 24, 1992] in which DOE was charged with the task of conducting a detailed and comprehensive study on the "institutional, legal and regulatory barriers to increased utilization of CCBs by potential governmental and commercial users".

The recommendations in the DOE report address a network of related barriers which can be overcome only through cooperative efforts among federal and state government and industry. ACAA has addressed many of these issues in its business plan and will expand these activities in the future.

SUMMARY

Throughout ACAA's history, its goal has been to gain recognition and acceptance of CCBs as engineering materials on par with competing virgin, processed and manufactured materials by advancing CCB uses that are technically sound, commercially competitive and environmentally safe. It is clear from survey data gathered by ACAA over the years that the annual use of some 18.2 million metric tons (20 million tons) of CCBs represents a

major continuing effort by a number of parties, including CCB producers, marketers and other organizations. It is equally clear, however, that significant quantities of CCBs are not used each year. Therefore it is essential for ACAA to promote the use of coal combustion byproducts in numerous applications.

REFERENCES

1. 1993 Coal Combustion Byproduct Production and Consumption, American Coal Ash Association, Inc., Washington, D.C., 1994, 1 page.

2. Use of Fly Ash in Concrete, American Concrete Institute, Committee 226 Report, ACI Materials Journal, Detroit, September-October 1987, pages 381-409.

3. Standard Specification for Fly Ash and Raw or Calcined Natural Pozzolan for Use As a Mineral Admixture in Portland Cement Concrete, ASTM C 618, American Society for Testing and Materials, Philadelphia,PA, 1994, 3 pages.

4. Flexible Pavement Manual, American Coal Ash Association, Inc., Washington, D.C., 1991, 64 pages plus Appendices.

5. Guidelines and Guide Specifications for Using Pozzolanic Stabilized Mixture (Base Course or Subbase) and Fly Ash for In-Place Subgrade Soil Modification, AASHTO/AGC/ARTBA Joint Committee, Task Force 28 Report, 1990, 40 pages plus Appendices.

6. Environmental Fact Sheet, Large-volume Wastes from Coal-fired Electric Utilities Exempt as Hazardous Waste, EPA530-F-93-014, United States Environmental Protection Agency, Washington, D.C., August 1993, 2 pages.

7. Barriers to the Increased Utilization of Coal Combustion/Desulfurization Byproducts by Governmental and Commercial Sectors, DOE Office of Fossil Energy, Morgantown Energy Technology Center, July 1994, 36 pages.

HIGH STRENGTH LIGHT WEIGHT FLY ASH COMPOSITES

Gerald P. Wirtz, John M. Bukowski, H. Dale DeFord and Asif Ahmed
Department of Materials Science and Engineering
University of Illinois at Urbana-Champaign
Urbana, IL 61801

Keywords: Fly Ash, Extrusion, Monolithic Honeycombs

ABSTRACT

Fly ash is a valuable by-product of coal-fired power generation. After beneficiation to recover valuable minor constituents, a fine powder of spherically shaped, largely amorphous, calcium aluminosilicate particles is left, which is well suited for processing into useful shapes without further milling. With the addition of Portland cement or lime, the formed body may be autoclaved at near 200°C to form a pozzolanic bond between fly ash particles. Light weight is achieved by extruding honeycomb structures with parallel open channels. Maximum strength to weight ratio would be achieved for pore-free honeycomb walls. The strength to density ratio of the honeycomb structures is independent of weight, since both weight and strength decrease linearly with fractional channel volume.

INTRODUCTION

The long range objective of this effort is to utilize fly ash from coal burning power plants to manufacture lightweight construction materials. To this end, selected processing methods from advanced ceramics and advanced cement based materials were adapted, chief among them the extrusion of fine monolithic honeycomb structures. This technology was developed by the automotive industry for the manufacture of cordierite catalyst carriers. While high surface area and high thermal shock resistance are the principal attributes of interest in automotive exhaust catalyst carriers, high strength, low weight, thermal insulation and acoustic isolation are of primary interest in construction materials. Building components envisioned range from brick size blocks to 4x8 foot panels, as well as a variety of posts, beams and other configurations. The size of components which could be produced in this study was severely limited by the extrusion equipment.

Since the density of silicates is largely dominated by the silica network, which is the lightest component, achieving densities less than about 2.3 gm/cc in a silica rich composition such as fly ash or Portland cement can only be achieved by incorporating open space in the structure. The most obvious way of accomplishing this is to increase the porosity of the final body. The difficulty is that the strength of a ceramic body decreases exponentially with porosity according to the Ryshkewitch equation[1,2]:

$$\sigma = \sigma_o e^{-\beta P} \tag{1}$$

where σ_O is the theoretical, pore-free strength of the material, P is the fractional porosity and β is an empirical constant for the material. Rewriting equation (1) for a honeycomb structure, the theoretical strength will be multiplied by the area fraction of the solid walls in cross section and the porosity in the equation will be replaced by the porosity within the solid walls:

$$\sigma = A_w \sigma_o e^{-\beta P_w} \tag{2}$$

Defining the macroscopic bulk density of the honeycomb structure, ρ_b, as the weight of the honeycomb divided by its total volume, the area fraction of the walls perpendicular to the extrusion direction can be expressed as the ratio of this bulk density to the density of the walls, ρ_w. The pore fraction in the walls will be one minus the solid fraction in the walls. The solid fraction in the walls will be equal to the ratio of the wall density to the theoretical density of the fly ash. The Ryshkewitch equation may thus be expressed for a honeycomb structure as:

$$\sigma = \frac{\rho_b}{\rho_w} \sigma_o e^{-\beta\left(1-\frac{\rho_w}{\rho_o}\right)} \tag{3}$$

Rewriting equation (3) slightly, the macroscopic strength to density ratio may be related to the maximum, pore free, strength to density ratio and the fractional porosity of the honeycomb walls.

$$\frac{\sigma}{\rho_b} = \frac{\sigma_o}{\rho_o} \frac{e^{-\beta P_w}}{(1 - P_w)} \tag{4}$$

Equation (4) says that for zero porosity in the honeycomb wall, the strength to density ratio of the honeycomb will correspond to the pore free strength to density ratio. For a given wall porosity, the density of the honeycomb will be determined by the relative dimensions of the channels and walls in the honeycomb, which are fixed by die design. The strength will scale in exactly the same fashion.

Achieving any given macroscopic density requires fabricating honeycombs with specific numbers of channels and wall thicknesses. Assuming square channels of side d with wall thickness t, the

relationship between honeycomb dimensional parameters and macroscopic bulk density may be written:

$$\frac{t}{d}\left(1+\frac{1}{n}\right)=\sqrt{\frac{1}{1-\frac{\rho_b}{\rho_w}}}-1 \qquad (5)$$

where n is the total number of channels in the sample being tested. In the limit of large n, the bulk density may be expressed as a function of the wall density and the ratio of the wall thickness to the channel width.

$$\rho_b=\rho_w\left[1-\frac{1}{\left(1+\frac{t}{d}\right)^2}\right] \qquad (6)$$

The fundamental approach to achieving high strength lightweight honeycomb structures is to develop the extrusion process to produce honeycombs with dense, thin walls, and to develop the curing process to further enhance the wall density in the final structure. Extrusion parameters, such as pressure and extrusion rate, affect the green density of the extruded body, which will be reflected in the final solidified product. Similarly, plasticizers, water and lubricants may be transient components of the green body. In leaving the body during firing or drying they leave behind void spaces in the structure which can affect the ultimate density. The relative fractions of these components added to promote extrudibility affects the ultimate wall density of the honeycomb structure, and thus the ultimate strength. Porosity in the green extruded body may be reduced during autoclaving by filling the pores with reaction products. In fired bodies, the porosity is reduced by normal vitreous sintering, with concomitant changes in sample dimensions. In autoclaved bodies, residual plasticizer and binder will affect both density and the hydration reaction.

SAMPLE PREPARATION

The minimum achievable wall thickness in the extruded honeycomb will be limited by the maximum particle size of the fly ash in the mix. The raw fly ash was therefore separated by sieving into fractions of particle size greater than 90 μm and less than 90 μm. The latter comprised greater than 98 weight % of the ash and was used exclusively in the extrusion of honeycombs.

Extrusion batches need to have sufficient plasticity to allow flawless knitting of the honeycomb walls during extrusion, with sufficient stiffness to support thin walls (0.05-0.13 cm). This required optimization of the water and binder additions, adequate shredding of the batch before extrusion to enable thorough de-airing, and optimization of the speed of extrusion. Methyl cellulose (MC), with additions of polyethylene oxide (PEO) to improve water retention during extrusion, was the initial binder studied, in the range of 0.5-5 weight % of solids[3]. Binders and plasticizers used in hydrothermally processed honeycombs had to be chosen to avoid adversely affecting the hydration reactions which are responsible for strength development. Methyl cellulose exhibits limited solubility in hot water, and appeared to impede the development of strength during autoclaving. In subsequent batches, the methyl cellulose was replaced by a mixture of hydroxyethyl cellulose (HEC) and polyethylene glycol (PEG), with small amounts of PEO again added. These exhibit higher solubility in hot water, and higher strengths were attained on autoclaving.

All specimens were extruded on a 40 ton, vacuum de-airing, piston extruder (Loomis Products Co.), with dies fabricated in house. A 2.54 cm square honeycomb with rounded corners and a nominal wall thickness of 0.16 cm, has evolved as the standard test piece, but different configurations have been fabricated. Fly ash samples containing 10-100 weight % Type 1 Portland cement (OPC, ordinary Portland cement) were hydrated at 60°C for 1-7 days after extruding, then autoclaved at temperatures from 150-210°C for 1-24 hours.

RESULTS AND DISCUSSION

Variables whose effects on strength were systematically measured included composition, reaction temperature and reaction time. Within very broad limits, the effects of each of these variables on strength mirrored their effects on sample porosity. Figure 1 shows the measured crushing strength as a function of fractional porosity of sintered samples, determined from density measurements on the samples. The data are plotted on a semilogarithmic plot in accordance with equation (1). Samples in Figure 1 were prepared by a variety of methods, and with a variety of compositions. Samples sintered at moderate temperatures (800-1000°C) contained up to 5% borax or boric acid as a sintering aid. Pure fly ash samples were sintered at temperatures above 1100°C. High porosity cast samples were foamed and contained 5-10% calcium lignosulfonate as a foam stabilizer[4]. Extruded cylinders contained from 1-5% methyl cellulose. The autoclaved honeycombs shown in the figure for comparison contained 40% OPC. The solid line in Figure 1 represents the linear regression fit of the data to equation (1). The empirical constants in equation (1) corresponding to this fit are: $\sigma_o = 615$ MPa, and $\beta = 6.6$.

The data on extruded honeycombs in Figure 1 are plotted as if the open channels in the honeycomb were ordinary porosity, and can be seen to exhibit as much as an order of magnitude greater strength for a given weight than the cast cylinders. This serves to illustrate the advantage of the honeycomb configuration for achieving high strength, light weight materials, but the

appropriate equation to compare these data qualitatively would be equation (4). Alternatively, the crushing force can be divided by the cross-sectional area of the wall to give the wall strength, which can be plotted against the wall porosity to compare directly with Figure 1. Figure 2 shows such a plot of wall strength vs. wall porosity, where the wall porosity was determined by mercury intrusion porosimetry. Included in the plot is the solid line representing equation (1) with the values of the empirical constants determined from Figure 1. Two different compositions are represented in Figure 2, 30% and 40% OPC, both autoclaved at 180°C, the former for 12 hours, the latter for 13 hours. The average strength of the latter is higher, as might be anticipated in light of the higher OPC content and longer curing time. The difference, however, can be attributed entirely to the difference in porosity of the two compositions. They both fall within the anticipated range for agreement with equation (1), with empirical constants determined from fly ash samples fired at high temperatures and containing no Portland cement. Mechanistically, this indicates that the strength of samples in both figures was determined by the strength of the fly ash framework. The mechanism of bonding between fly ash particles did not affect the strength achieved. The fact that in all autoclaved samples tested thus far the wall porosity has exceeded 20% is of major relevance to the direction of future work.

Figure 3 shows electron micrographs of fractured surfaces of autoclaved honeycomb samples containing 40 and 10 weight % Portland cement. In the former, the fracture is transgranular, passing through the fly ash grains. The transgranular nature of the fracture in Figure 3A is particularly notable when the fracture passes through hollow fly ash particles (cenospheres), as illustrated by the arrow (a) on the micrograph, but is also evident by the general planar character of the fracture surface, with little evidence that the body is made up of spherical fly ash particles. The fracture has the appearance of a typical ceramic fracture surface. In Figure 3B, by comparison, the fracture is clearly intergranular. The spherical fly ash particles are evident as the fracture proceeded between the particles, leaving many of the spherical surfaces unmarred. The 40 % OPC composition of Figure 3A exhibited about 8 times the crushing strength of the 10 % OPC sample of Figure 3B. In samples where the weakness of the bonding between particles permitted intergranular fracture, the strength was no longer represented by equation (1), at least not with the empirical constants determined from Figure 1.

Figure 4 shows an electron micrograph of the fracture surface of a sintered fly ash honeycomb, such as used to determine the empirical constants in equation (1) from Figure 1. Fracture is again clearly transgranular, and the only evidence of the spherical nature of the initial particles is the spherical pores observed where the fracture passed through the hollow cenospheres. The bonding mechanism in this case can be seen to be vitreous sintering, whereas the bonding in the samples of Figure 3 was the pozzolanic reaction of the lime in the Portland cement with the free silica at the surface of the fly ash particles to form tobermorite and other calcium silicate hydrates.

CONCLUSIONS

High strength light weight honeycomb composites can be formed by autoclaving a mixture of fly ash and Portland cement, as well as by typical ceramic firing of fly ash honeycomb structures at high temperatures. A comparison of strength and density of fly ash honeycomb samples with typical construction materials is presented in Table 1. Materials are listed in order of increasing strength to density ratio, which has been normalized to 1.0 for construction grade pine. Typical values for both autoclaved and sintered honeycombs from the present study are shown. Differences in the strength to density ratio of honeycomb samples is determined primarily by differences in the fractional porosity of the walls for honeycombs with very different compositional modifications, as well as processing variations. This is attributed to the fact that the fracture mechanism is the same and occurs through the fly ash grains. This indicates that the solid grains form the weak link in the system and that the strength is proportional to the cross sectional area fraction of the solid, which may be converted directly to density of the wall. When intergranular fracture was observed, as seen in Figure 3(B), the same strength-porosity relationship no longer held.

In no case was the wall density greater than 80% of theoretical for autoclaved honeycombs. With the experimentally determined value of $\beta = 6.6$, a wall porosity of 20% yields a strength to density ratio of only 33% of theoretical from equation (4). For the honeycomb samples in Table 1, the total porosity, as determined by mercury intrusion porosimetry, was about 25 and 18% respectively. These values would predict a maximum normalized strength to density ratio of about 5. There is clearly still much room for improvement. Future efforts will be concentrated on the attainment of greater wall densities, i.e., eliminating the porosity in the walls.

REFERENCES

1. E. Ryshkewitch, "Compression Strength of Porous Sintered Alumina and Zirconia– 9th Communication to Ceramography," J. Amer. Cer. Soc., 36, [2] 65-68 (1953)

2. W. Duckworth, "Discussion of Ryshkewitch Paper", J. Amer. Cer. Soc., 42, [8] 68 (1953)

3. H. D. DeFord and G. P. Wirtz, "Extrusion of Lightweight Construction Materials from Fly Ash", Ceram. Eng. Sci. Proc. 14[1-2] pp. 298-308 (1993)

4. J. R. Wylder, Processing and Characterization of a Foamed Fly Ash Construction Material, M.S. Thesis, University of Illinois at Urbana-Champaign (1989)

Table 1. Strength/density comparison with typical construction materials

Material	Bulk Density (gm/cc)	Compressive Strength (MPa)	(psi)	Normalized Strength/Density Ratio
Aerated Concrete	0.69	4.4	640	0.10
Concrete	2.2	35	5100	0.25
Clay Brick	2.3	45	6500	0.31
Steel	7.8	455	66000	0.91
Pine	0.48	30	4350	1.00
Autoclaved Honeycomb	1.13	95	14000	1.36
Fired Honeycomb	1.32	155	22500	1.89

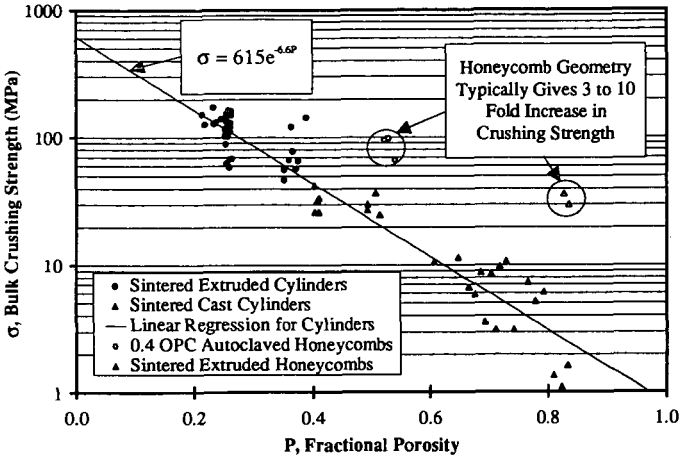

Figure 1. Crushing strength vs. fractional porosity for fired fly ash bodies.

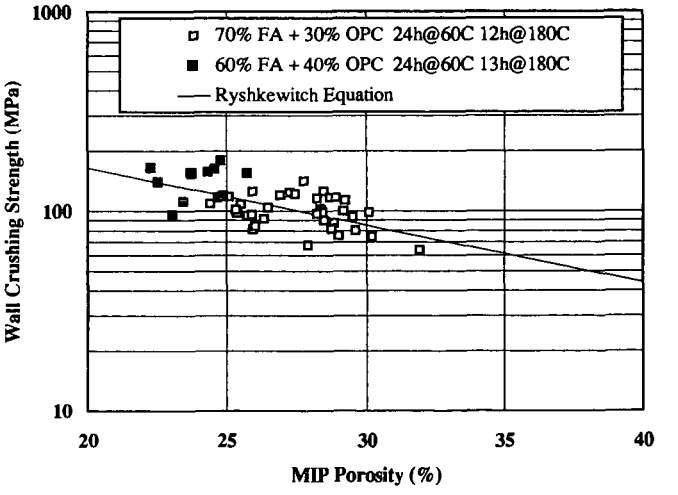

Figure 2. Crushing strength of the honeycomb wall vs. fractional porosity of the wall.

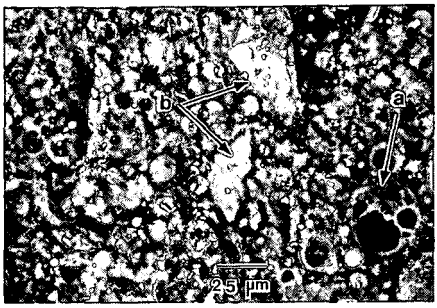

(A) SEM of 40 % OPC fly ash honeycomb illustrating transgranular fracture surface.
(a) Cross section of hollow fly ash particle (cenosphere)
(b) Unhydrated cement paste grains

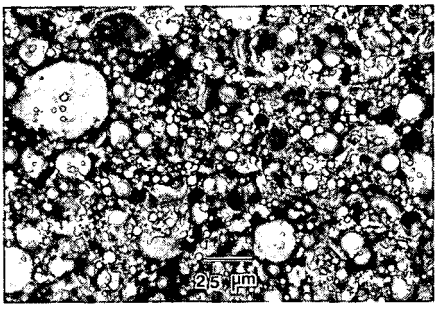

(B) SEM of 10 % OPC fly ash honeycomb illustrating intergranular fracture surface. Note spherical morphology retained by fly ash particles in fracture surface.

Figure 3. Scanning electron micrographs of fracture surfaces of fly ash honeycombs illustrating (A) transgranular fracture in 40% OPC composition, and (B) intergranular fracture and pullout in 10% OPC composition.

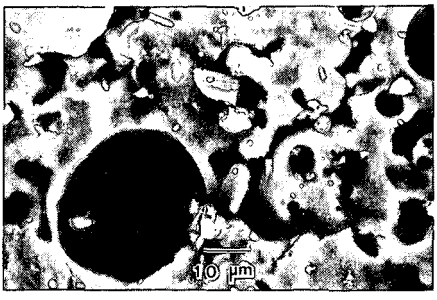

Figure 4. Scanning electron micrograph of fracture surface of pure fly ash honeycomb densified by firing at 1075 °C for 24 ho

UTILIZATION OF FLY ASH IN STRUCTURAL AND DECORATIVE CERAMIC PRODUCTS

R. E. Hughes, G. B. Dreher, M. R. Rostam-Abadi, D. M. Moore, and P. J. DeMaris
Illinois State Geological Survey
Champaign, IL 61820

Keywords: Utilization of fly ash, manufacture of bricks, decorative and structural ceramics

INTRODUCTION AND BACKGROUND

The main objective of this study is to promote the use of fly ash from electric power plants in Illinois in the manufacture of bricks. Fly ash that is produced during the burning of coal represents a continuing disposal problem and thus a disincentive to coal's use. Each year, approximately 5 X 10^6 metric tons of fly ash are produced from burning Illinois coals. Use of brick clays for ceramic products in the Illinois area amounted to about 0.5 X 10^6 metric tons in 1994. If significant amounts of fly ash were used in the manufacture of fired-clay products such as brick, the fly ash disposal problem would be reduced, a valuable construction product would be created, and mining of brick clays would be slowed. Furthermore, the clay minerals in the green bricks are dehydroxylated during the firing process. Fly ash already has been through dehydroxlyation, therefore this energy for dehydroxylation is "saved" during brick manufacture. Six tasks were defined to meet our objectives: 1) manufacture bricks that contain 20 wt% or more of fly ash under normal plant-scale conditions; 2) measure the firing characteristics of mixtures created by using extremes in chemical composition of Illinois fly ashes and brick clays and shales; 3) from those measurements, derive equations that predict the firing characteristics of any mixture of clay and fly ash; 4) optimize mixtures of brick clays with sources of fly ash near existing ceramic plants; 5) perform tests to determine the leachability of toxic constituents, if any, from the bricks; and 6) integrate the results of tasks 1 and 2 with preliminary engineering and market assessments to evaluate the feasibility of large-scale use of fly ash in fired-clay products.

Although general principles guiding the selection of raw materials for fired-clay products have been known for many years (Grim, 1962; Burst and Hughes, 1994), the complexity of the firing reactions suggested the need for improved methods (Hughes, 1993) of predicting the firing behavior of bricks and related products. This need is emphasized by our plant-scale experiments with Colonial Brick Company in Cayuga, Indiana. Because we lack adequate methods for prediction, we were obliged to resort to trial-and-error methods for our first plant-scale test. The improvement of methods for predicting the properties of fired fly ash, shale, and underclay mixtures is now possible, and an approach based on mineral content is expected to provide significant improvements in accuracy of prediction.

An improved method for the prediction of coal ash fusion temperature is an important outcome expected from this study. Laboratory methods for the estimation of coal ash fusion temperature are the same as those for testing ceramics. As for ceramic products, the methods used to predict coal ash fusion temperatures are notoriously inaccurate because they are based on chemical analyses. For the ceramic and the coal ash fusion tests, we suggest that equations based on mineralogical composition will yield improved accuracy and precision. A mineralogical basis for prediction also should elucidate the underlying mechanisms that cause problems and suggest solutions to those problems.

The manufacturing process at most brick plants is similar. Clays are blended in a crusher, pulverized, and water and dispersant are added in a pugmill to produce a plastic clay that can be extruded. The preferred raw materials for these fired-clay products occur as underclays and roof shales associated with coals. They contain variable amounts of three basic groups of minerals: 1) relatively low-melting-point illite, mixed-layered illite/smectite (I/S), and chlorite; 2) refractory kaolinite and mixed-layered kaolinite/expandables (K/E); and 3) somewhat refractory quartz. Common red-firing roof shales generally contain nearly ideal amounts of group 1 and 2, and adequate firing characteristics are obtained by blending clay-rich shale zones with sandier, quartz-rich zones. The mixture must contain enough clay minerals for adequate plasticity, and enough coarse grains to insure access of air so that the core of the brick is completely oxidized in the shortest possible time during firing.

Many of the shales immediately above coals (roof shales) in the Illinois Basin are nearly ideal raw materials. Their progressive change in grain size from smaller at the base to larger at the top, makes blending for plasticity and firing rate possible. Many underclays below Illinois coals are fireclays, which, unlike shales, contain more kaolinite and significant amounts of K/E. This K/E gives special properties to fired-clay products because it is composed at the atomic scale of a 2:1 clay mineral layer that melts at relatively low temperatures and a 1:1 layer that is refractory. Quartz also can have special properties during firing. Quartz acts as a framework grain in normal shale and fireclay bricks, but at high enough temperature, it can melt and act as a bonding agent. For these reasons, predictive equations must be made with different groupings of mineralogical factors.

Background information on clays for bricks and similar ceramic products is summarized in Hughes (1993). Slonaker (1977) showed that acceptable bricks were produced from feeds of 72% fly ash, 25% bottom ash, and 3% sodium silicate. A general discussion of the properties of fly ash that are important to its use in fired-clay products can be found in Kurgan, Balestrino, and Daley (1984). They reported that the high alkalinity of fly ash from Illinois could improve dispersion of the clay body during mixing and extrusion of bricks. Talmy *et al.* (1995) described two approaches for using 100% fly ash plus additives to make bricks.

The development and use of leaching tests for the measurement of environmental impacts of coal combustion residues was reviewed in Dreher, Roy, and Steele (1993). Improved methods for the mineralogical characterization of coal samples and coal combustion wastes have been described recently by Kruse *et al.* (1994) and Moore, Dreher, and Hughes (1995). Characterization methods for clay minerals are described in Hughes and Warren (1989) and Moore and Reynolds (1989).

If successful, the results obtained from this project should lead to an attractive solution, from an environmental and economic standpoint, for the recycling of fly ash to high-value marketable products. Success also could revitalize the ceramics industry in Illinois, an industry that has been in decline for several years. Finally, high-calcium fly ashes may be useful for capture of sulfur that volatilizes from brick clays during firing.

EXPERIMENTAL PROCEDURES

Brick manufacturing tests were made using fly ash from Illinois Power Company's Wood River Power Plant. Colonial Brick Company conducted a manufacturing run of about 5,000 bricks without fly ash and a similar number with about 20% fly ash added to the normal clay. A batch of bricks of each of the two compositions was fired side-by-side in the kiln and tested for standard market specifications, *i.e.*, samples of the bricks with and without fly ash were taken during firing to provide a measure of "clearing" or time required to completely oxidize the core of the bricks. Water absorption tests and of color determinations also were made by Colonial Brick on the fired products. These proved acceptable to them.

Mineralogical characterization was made by X-ray diffraction (XRD), X-ray fluorescence, instrumental neutron activation analysis, and a step-wise dissolution in 2N HCl with inductively coupled plasma (ICP) analysis of the supernates and XRD of the solids. The X-ray diffractometer was a Scintag® unit that used a Cu tube, a θ/θ goniometer, a 12-position sample changer, a liquid N_2-cooled germanium detector, and computer controls and peak deconvolution programs. The XRF spectrometer was a Rigaku® wavelength-dispersive model that has a chromium radiation source and a 6-position sample changer. The ICP spectrometer was a Jarrell-Ash Model 1155V vacuum spectrometer equipped with 35 element channels. Instrumental neutron activation analysis was accomplished by irradiating solid samples in a neutron flux at the University of Illinois Advanced TRIGA MARK II reactor. After suitable decay times, gamma-ray spectra for various elements in the irradiated sample were recorded by a multi-channel analyzer. For step-dissolution experiments, about 1 gm samples were ground in a McCrone micronizer®, ultrasonically dispersed in 50 mL of H_2O, and added to 550 mL of 2N HCl. Stirred, 40 mL aliquots were extracted from the suspension at selected intervals for up to a month, *e.g.*, 2 hr, 4 hr, 8 hr, etc. To increase solubility, one fireclay sample was heated to 500°C to dehydroxylate most of its kaolinite and K/E.

Leaching procedures developed by Dreher *et al.* (1988, 1989) are being used to determine the extent to which constituents of environmental concern might leach from bricks exposed to weathering. Batch extraction and wet-dry leaching experiments, in which the substrate is exposed to deionized water for a given time period, are being conducted on crushed and whole bricks. To simulate exposure in a building, five faces of the bricks are protected from leaching by application of an epoxy coating. Batch extraction experiments are being conducted at a solution-to-solid ratio of 4:1 for periods of 3, 10, 30, 90, and 180 days. Each solid was analyzed chemically and mineralogically prior to extraction and leaching experiments, and the solids from the 180-day extraction will be analyzed mineralogically.

Estimates of the composition of Illinois fly ashes were obtained from Moore, Dreher, and Hughes (1995) and by calculation from the composition of coals reported by Demir *et al.* (1994). These two sources of fly ash chemical composition were plotted in various ways to find the range of composition available as a replacement for clays in bricks (Figs. 1 and 2). Results from laboratory and plant tests will be analyzed by factorial analysis and regression analysis to obtain equations that measure the effect on fired properties of additions of each of the basic components from the raw materials.

RESULTS AND DISCUSSION

Plant-scale tests. The results of the production run were somewhat unexpected. During firing, we expected the fly ash to increase gas movement into and out of the bricks, but the reverse occurred. Essentially, the fly ash decreased the rate of oxidation. The bricks with fly ash also had noticeably more "scumming," which also was unexpected. This scumming causes a white to cream-colored dusting on the outside of the bricks and is mostly due to the migration of calcium sulfates to the surface during drying, firing, or both. We will attempt to confirm this assumption with chemical analyses. The problem can be corrected by adding barium carbonate, or possibly by moistening the fly ash and precipitating the salts, or it may be possible to simply select a fly ash with a smaller calcium sulfate content. A benefit resulting from the effect of fly ash on gas permeability was the lack of an expected increase in water absorption by the products. In general, the bricks from the manufacturing run were within local and regional market specifications. However, the scumming reduces their marketability.

On a matter of importance to the plant operator, the amount of dust associated with unloading fly ash at Colonial Brick was an unexpected problem that must be solved because of environmental regulations. It may be possible to wet the ash at the power plant or use pneumatic facilities at the brick plant.

Characterization of materials. The mineralogical and chemical analyses of clay and fly ash samples are given in Tables 1 and 2. The shales used are typical red-firing Pennsylvanian shales, which are common as the roof shale of most coals. At Colonial Brick Company's pit, about 30 ft of roof shale overlies a 6-12 in carbonaceous or coaly zone, which overlies about 6 ft of fireclay. The coaly zone may be equivalent to the Colchester (No. 2) Coal. Our second-year collaborator, Marseilles Brick Company, mines shale and fireclay from different pits. The shale is middle or upper Pennsylvanian and the fireclay occurs in the Cheltenham Formation, immediately below the underclay of the Colchester Coal.

For the approximately 25,000 samples of ceramic clays that have been collected since 1930 at the Illinois State Geological Survey, a database was constructed for this study. This database lists locations and material types. The location and selection of fly ash standards proved more difficult than the selection of clays. Data for each of the coals in Demir *et al.* (1994) were modified in an Excel© spreadsheet to estimate the chemical composition of fly ash from each of these coals (Figs. 1 and 2). The chemical composition of 8 fly ash samples that were part of the characterization study by Moore, Dreher, and Hughes (1995), and the chemical analyses of the fly ash and brick clays used in this investigation, were added to the spreadsheet and plotted (Figs. 1 and 2).

Most fly ashes contain more iron and calcium than brick clays (Figures 1 and 2). Because they were fused, the fly ashes may differ in the degree to which chemical constituents are segregated between phases and glass. However, to represent the range of available materials, we selected fly ash compositions that were relatively rich in: 1) $SiO_2 + Al_2O_3$, 2) Fe_2O_3, and 3) CaO. Differences in the contents of these constituents represent the important compositional variation for most Illinois fly ashes. In order to better understand the relationship between the chemical and mineralogical contents of coals, we plan to calculate regression equations of the chemical and mineralogical contents of the Illinois Basin Coal Sample Program (IBCSP) coals (Kruse *et al.*, 1994) and use those equations to estimate the mineralogical content of the 34 commercial coals of Demir *et al.* (1994).

Figure 2 shows that SiO_2:Al_2O_3 is nearly constant. This ratio ranges from 1.9 to 3.6 with a mean of about 2.5 in the data set of Demir *et al.* (1994), and a range of 2.3 to 3.9 with a mean of about 2.5 in the data of Moore, Dreher, and Hughes (1995). The differences in the contents of CaO, Fe_2O_3, K_2O, and Na_2O in fly ashes and brick clays account for most of the significant variation in these materials. For purposes of selecting standards for optimization studies, the fly ash used in production runs this year (Table 2) can be used to represent fly ashes that are rich in SiO_2 and Al_2O_3. Samples 2 and 8 from the set of fly ashes analyzed by Moore, Dreher, and Hughes (1995) can be used to represent CaO-rich and Fe_2O_3-rich types, respectively. We selected and analyzed two standard optimization clays from Marseilles Brick Company.

Step-dissolution analysis and optimization. We believe that the solution to the problem of predicting the firing behavior of mixtures of materials depends on the accurate measurement of the major and minor mineral phases that make up a material. For unfired materials, XRD analysis of the mineral content is the technique of choice. However, some of the clay minerals are difficult to determine accurately, and we have chosen step-dissolution methods with ICP and XRD analyses to improve the determinations (Cícel and Komadel, 1994; Moore, Dreher, and Hughes, 1995). Figures 3 and 4 show the results of step-dissolution analyses of shale samples used at Colonial Brick Company. Because chlorite has two octahedral sites that can be occupied by Al, Fe, or Mg, it is the most difficult non-mixed-layered clay mineral to determine by XRD. In addition, of the minerals of concern in the shale, it is the most soluble in HCl. Therefore, XRD analyses of the solid fraction of the samples showed a decrease in chlorite content as time of reaction in 2N HCl increased (Fig. 3). Similarly, results of elemental analyses of the supernates recorded the increase in chlorite-forming elements with increased reaction time (Fig. 4). These plots of elemental concentration versus time can be used to calculate a structural formula of the chlorite in the sample and will make the optimization equations more accurate. The formula for chlorite derived from Fig. 4 is $Al_{1.6}Fe_{2.9}Mg_{1.4}Mn_{0.1}Si_{3.0}Al_{1.0}O_{10}\bullet(OH)_8$.

After chlorite has been dissolved, step dissolution analysis of fireclays and shales becomes difficult because of the low solubility of the minerals remaining in the system. There are no easily dissolved minerals in fireclay and fly ash samples, therefore this becomes a major analytical problem. For fireclays, only 3 to 6% of the untreated sample was dissolved. A pre-treatment at 500°C increased the solubility of kaolinite and K/E, and gave meaningful estimates of the composition of those phases. To improve the method, it appears that we will have to grind the samples longer, leave them in acid longer, increase the strength of the acid, increase the temperature, or use some combination of these methods to dissolve all the amorphous material from fly ash samples.

Future studies. Recent studies of the firing behavior of bricks and related materials suggested that we may need to expand the number of tests used to measure fired-clay properties. This expansion will add tests for shrinkage, rate of burnout, hardness, strength, pyrometric cone equivalent (PCE), color, and water adsorption. Many of these determinations can be done on the samples used for PCE analysis and most of the tests would increase the analytical costs only moderately. The amounts of CaO, $CaSO_4$, and Fe_2O_3 (from pyrite and marcasite) in some fly ashes are too large to be used for manufacture many ceramic products. The excess calcium from these sources can be corrected for by adding water in the cooling part of the firing cycle. This method was used in the manufacture of bricks known as "Chicago Commons." The scumming problem from calcium sulfates in fly ash may be solved by adding 5-15% water to the fly ash and eliminating it by processing fly ashes into various fractions. Both the color and lower melting

point caused by high levels of Fe_2O_3 are best adjusted for by increasing the quartz and/or kaolinite content of the clay-shale. Problems with SO_2 emissions are common in brick production, and we plan to test high-Ca fly ash for its ability to capture sulfur from the clays during firing.

SUMMARY AND RECOMMENDATIONS

Additions of fly ash to bricks at the 20% level in plant-scale tests increased scumming and "burn-out" problems, but, contrary to our expectations, failed to increase water absorption. Although these problems are not expected to cause insurmountable difficulties, better characterization of the mineralogical composition of fly ashes is needed to find solutions to such problems.

Characterization of the clays used at Colonial and Marseilles Brick Companies showed that they are typical of the Pennsylvanian-age clays associated with coals of the Illinois Basin. A computer database of approximately 25,000 ceramic clays of Illinois was constructed, and the database of chemical composition of marketed Illinois coals reported in Demir *et al.* (1994) was processed to estimate the composition of fly ash that would be produced from burning each of those coals. The chemical composition of the eight fly ash samples from the study of Moore, Dreher, and Hughes (1995) also were added to a composite database. Characterization by XRD, XRF, INAA, and step-dissolution/ICP analyses of the fly ashes, shales, fireclays, green bricks, and fired bricks showed that the fly ashes contained more CaO and Fe_2O_3 than the brick clays. However, there is a wide range of chemical composition and an unknown variation in the mineralogical content of fly ashes. Low solubilities of minerals in fly ashes and fireclays made it difficult to use the step-dissolution method for the mineralogical characterization of those materials. Preheating fireclays to dehydroxylate kaolinite and mixed-layered kaolinite/expandables (K/E) in fireclays and more intense grinding of fly ashes seemed to give adequate step-dissolution results. Environmental leaching studies are being conducted to evaluate the leaching of potential pollutants.

To broaden the comprehensiveness of the fundamental studies, future studies will include determinations of water absorption, shrinkage, rate of burnout, hardness, color, and pyrometric cone equivalent (PCE) on mixtures of fireclay, fly ash, and shale. To reduce SO_2 emissions from brick clays, fly ashes rich in Ca will be tested to determine the amount of sulfur that can be captured during firing. Comparisons between the composition of fly ash calculated from the elemental compositions of coals and the actual fly ash samples and between predicted and actual coal ash fusion temperatures will be made to assess the accuracy of predictive methods from this study.

ACKNOWLEDGMENTS

The authors gratefully acknowledge the Illinois Department of Commerce and Community Affairs, Illinois Coal Development Board, Illinois Clean Coal Institute, and the U.S. Department of Energy. We also thank our project officer Dr. Daniel D. Banerjee, and Robert R. Frost and John D. Steele for chemical analyses.

REFERENCES

Burst, J.F. and R.E. Hughes. 1994. Clay-Based Ceramic Raw Materials; In D.D. Carr, (ed.), 6th Edition, Industrial Minerals and Rocks, Soc. Mining Eng., Denver, CO, 317-324.

Cícel, B., and P. Komadel. 1994. Structural Formulae of Layer Silicates: Quantitative Methods in Soil Mineralogy, Soil Science Society of America Miscellaneous Publication, p. 114-136.

Demir, I., R.D. Harvey, R.R. Ruch, H.H. Damberger, C. Chaven, J.D. Steele, and W.T. Frankie. 1994. Characterization of Available (Marketed) Coals from Illinois Mines: Ill State Geological Survey Open File Series No. 1994-2, 16 p.

Dreher, G. B., M. Rostam-Abadi, W. R. Roy, D. M. Rapp, S. C. Mravik, I. Demir, J. D. Steele, R. R. Ruch, and R. L. Berger. 1988. Factors Affecting Management of ISGS Aggregate Flotation Waste Solids. Final Technical Report to the Illinois Coal Development Board, Center for Research on Sulfur in Coal, Champaign, IL, 29 p.

Dreher, G. B., M. Rostam-Abadi, W. R. Roy, J. D. Steele, D. M. Rapp, W.-T. Chen, and R. L. Berger. 1989. Factors Affecting Management of Fine-Coal Cleaning Waste Solids. Final Technical Report to the Illinois Coal Development Board, Center for Research on Sulfur in Coal, Carterville, IL, 50 p.

Dreher, G. B., W. R. Roy, and J. D. Steele. 1993. Geochemistry of FBC Waste-Coal Slurry Solid Mixtures, Final Technical Report to the Illinois Coal Development Board, Center for Research on Sulfur in Coal, Carterville, IL, 26 p. and Appendix, 10 p.

Grim, R.E. 1962. Applied Clay Mineralogy. McGraw-Hill Book Company, Inc., New York, 422p.

Hughes, R. E., B. L. Bargh, and W. A. White. 1983. The Expansion and Weathering of Brick. Proceedings of the 18th Forum on the Geology of Industrial Minerals, Bloomington, Indiana, 183-197.

Hughes, R. E. and R. L. Warren. 1989. Evaluation of the Economic Usefulness of Earth Materials by X-Ray Diffraction. Proceedings of the 23rd Forum on the Geology of Industrial Minerals, R. E. Hughes and J. C. Bradbury, eds., North Aurora, Illinois, May 11-15, 1987,

Hughes, R.E., and P.J. DeMaris. 1992. DUCCR Program Final Report: Utilization of Coal Conversion Residues; Coal Combustion Residues Management Program, Southern Illinois University, Carbondale, IL, 49p.

Hughes, R.E. 1993. Clay Resources Associated with Lower Pennsylvanian Coals. In Preprints Symposium on Economic Resources of the Lower Pennsylvanian of the Illinois Basin, Indiana Geological Survey, Bloomington, IN, November 10-11, 1993, 29-37.

Kruse, C.W., R.E. Hughes, D.M. Moore, R.D. Harvey, and J. Xu, 1994, Illinois Basin Coal Sample Program, Final Technical Report to the Illinois Coal Development Board, Center for Research on Sulfur in Coal, Carterville, IL.

Kurgan, G.J., J.M. Balestrino, and J.R. Daley. 1984. Coal Combustion By-Products Utilization Manual, Volume 1: Evaluating the utilization option. Electric Power Research Institute, CS-3122, Volume 1, Research Project 1850-1, Palo Alto, CA, 3-1 to 3-34.

Moore, D. M., G. B. Dreher, and R. E. Hughes. 1995. New Procedure for X-Ray Diffraction Characterization of Flue Gas Desulfurization (FGD) and Fluidized Bed Combustion (FBC) By-Products. Final Technical Report to the Coal Combustion Residues Management Program, Carbondale, IL.

Moore, D. M. and R. C. Reynolds Jr. 1989. X-Ray Diffraction and the Identification and Analysis of Clay Minerals. Oxford University Press, New York, 337 p.

Slonaker, J. F.. 1977. The Role of Fly Ash Brick Manufacturing in Energy Conservation; Coal Research Bureau, College of Mineral and Energy Resources, W. Virginia University, Report No. 149, Morgantown, WV, 6p.

Talmy, I. G., C. A. Martin, A. G. Cade, and W. D. Sudduth. 1995. Utilization of Fly Ash in Building Materials; *In* Abstracts for the International Ash Utilization Symposium, Lexington, KY, October 23-25.

Table 1. Mineralogical composition (%) of Colonial Brick and Marseilles Brick clays

Sample	I/S	I	K/E	K	C	Q	Kf	Pf	Cc	Py	Other
sh3521A	10	25	0	8.9	11	39	0.1	5.9	0.0	0.0	
sh3521C	15	19	0	5.7	6.5	47	0.2	6.0	0.0	1.5	
fc3521B	45	10	0	7.8	0.0	34	0.0	1.3	0.0	2.1	
fc3521BR	45	10	0	7.8	0.0	33	0.0	1.3	0.0	3.1	
fc3538A	19	3.4	22	7.6	0.0	44	0.4	0.0	0.0	2.9	
sh3538B	17	18	0	3.1	7.4	48	0.4	5.8	0.0	0.0	
sh3528A	17	16	0	5.3	5.1	47	1.3	8.2	0.0	0.0	
sh3528AR	15	19	0	6.1	7.6	46	0.0	6.8	0.0	0.0	
fc3528B	27	6.9	14	7.6	2.1	37	0.0	1.7	0.8	2.1	
fc3528BR	33	6.4	13	7.0	1.6	34	0.4	1.4	0.8	2.0	
sh3548A	19	21	0.0	4.0	7.7	42	0.8	5.4	0.0	0.0	apatite?
sh3548AR	19	20	0.0	3.9	7.5	44	0.6	5.8	0.0	0.0	apatite?
fc3548B	18	2.5	32	9.0	0.0	33	0.0	0.0	0.4	4.5	
flsh3538E						11					glass, M, H
flsh3538F						12					glass, M, H
shbr3521F	16	19	0.0	5.7	5.8	48	0.2	5.6	0.0	0.0	apatite?
shbr3521G	17	27	0.0	6.5	8.3	36	0.0	4.9	0.0	0.0	apatite?
shbr3521J	15	20	0.0	4.9	7.7	46	0.4	5.3	0.0	0.0	apatite?
shbr3521K	15	19	0.0	4.0	6.4	50	0.7	5.6	0.0	0.0	apatite?
br3521D						25					glass, M, H
br3521E						21					glass, M, H
br3521H						27					glass, M, H
br3521I						28					glass, M, H

Key: Samples 3521, 3538 = Colonial Brick 3/94 and 4/95; samples 3528, 3548 = Marseilles Brick 10/94 and 6/95; I/S = mixed-layered illite/smectite; I = illite; K/E = mixed-layered kaolinite/expandables; K = kaolinite; C = chlorite; Q = quartz; Kf = K-feldspar; Pf = plagioclase feldspar; Cc = calcite; Py-Ma = pyrite-marcasite; M = mullite; H = hematite; R = repeat; sh = shale; fc = fireclay; flsh = fly ash; shbr = unfired brick; br = fired brick; (3521D, E, F, G = bricks with 20% fly ash; 3521H, I, J, K = bricks without fly ash).

Table 2. Chemical composition (%) of Colonial Brick Co. clays, Marseilles Brick Co. clays, and bricks from the manufacturing run at Colonial

Sample	SiO2	Al2O3	Fe2O3	CaO	MgO	K2O	Na2O	TiO2	LOI	P2O5	Sr	Ba	Zr
sh-3521A	61.33	17.7	6.52	0.57	1.9	3.09	1.08	0.98	6.44	0.16	0.14	0.53	0.23
shbr-3521C	60.81	17.66	6.47	0.6	1.91	3.07	1.07	0.97	6.82	0.16	0.15	0.54	0.23
sh-3538A	59.96	18.86	6.5	0.39	2.07	3.36	1.04	0.98	6.34	0.17	0.14	0.65	0.13
fc-3521B	57.47	21.37	4.71	1.67	1.47	2.68	0.35	1.1	7.98	0.16	0.25	0.44	0.25
fc-3538C	58.27	21.49	5.06	0.78	1.38	2.35	0.47	1.11	8.15	0.1	0.18	0.41	0.19
fc-3528A	59.22	26.18	1.99	0.31	0.5	0.96	0.04	1.27	8.93	0.06	0.16	0.09	0.29
sh-3528B	66.38	16.81	4.96	0.32	1.95	3.22	1.3	1.03	3.52	0.14	0.10	0.43	0.27
grbr1-3521F	61.09	18.18	6.12	0.88	1.78	2.83	1.04	1.01	6.27	0.17	0.20	0.62	0.17
grbr2-3521J	62.81	17.02	5.89	0.56	1.75	2.74	1.02	0.98	6.52	0.17	0.19	0.46	0.18
br1-3521D	64.71	19.71	6.68	0.86	1.95	3.08	1.08	1.07	0.13	0.18	0.21	0.69	0.18
br2-3521H	66.44	18.61	6.39	0.65	1.96	3.05	1.07	1.04	0.19	0.17	0.16	0.62	0.19
br2R-3521H	66.37	18.51	6.42	0.64	1.94	3.04	1.09	1.04	0.21	0.18	0.18	0.56	0.20
flsh1-3538E	54.5	25.5	6.39	2.55	1.29	2.22	1.13	1.34	3.42	0.19	0.75	1.27	0.24
flsh2-3538F	54.73	25.42	6.38	2.54	1.3	2.22	1.11	1.35	3.18	0.19	0.75	1.25	0.20

Key: Samples with clay numbers 3521 and 3538 are from Colonial Brick Co.; 3528 are from Marseilles Brick Co.; grbr1 = unfired brick with 20% fly ash; grbr2 = unfired brick without fly ash; br1 = fired brick with 20% fly ash; br2 and br2R = fired brick samples without fly ash; flsh1 and flsh2 are duplicate fly ash samples.

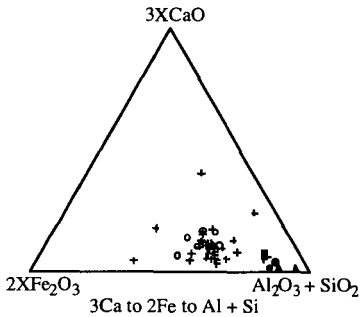

Figure 1. Triangular plot of $CaO:SiO_2+Al_2O_3:Fe_2O_3$. Symbols: + = data set of Demir et al. (1994); O = data set of Moore, Dreher, and Hughes (1995); ● = Colonial Brick Company's shale and fireclay; ▲ = Marseilles Brick Company's shale and fireclay; ■ = fly ash used for tests at Colonial Brick.

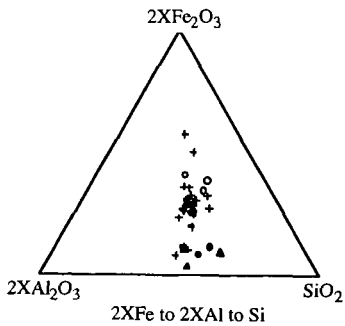

Figure 2. Triangular plot of $Fe_2O_3:Al_2O_3:SiO_2$. Symbols: + = data set of Demir et al. (1994); O = data set of Moore, Dreher, and Hughes (1995); ● = Colonial Brick Company's shale and fireclay; ▲ = Marseilles Brick Company's shale and fireclay; ■ = fly ash used for tests at Colonial Brick.

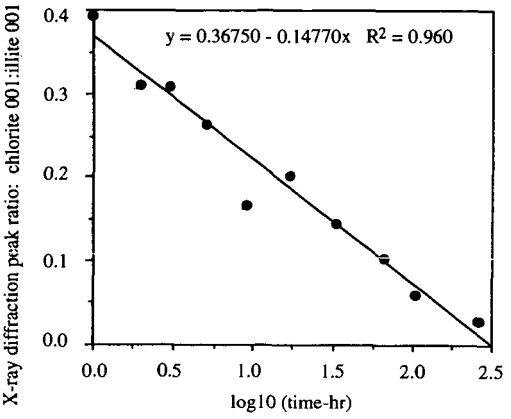

Figure 3. Plot of the XRD peak intensity ratio of the chlorite 001 to the illite 001 peaks from solid samples. This plot shows the dissolution of chlorite in 2N HCl with time. (See figure 4 for a plot of the dissolved species from chlorite.)

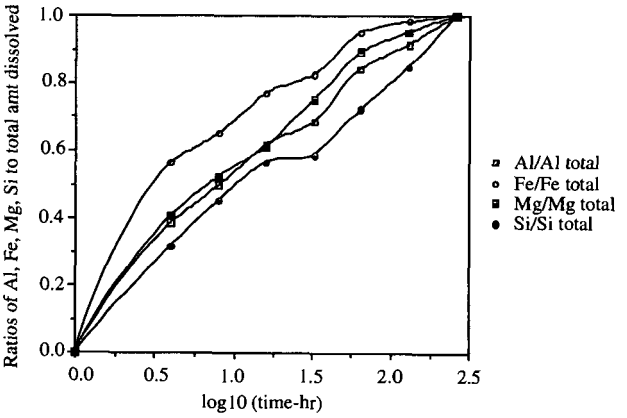

Figure 4. Plot of the ratio of Al, Fe, Mg, and Si ions in solution to the total amount of that constituent in solution at the end of the experiment. This plot shows variation in Al and Si versus Fe and Mg solution rate, which reflects the lower solubility of the tetrahedral sheet of the chlorite structure. The concentration when all chlorite has been dissolved gives a structural formula for the chlorite, *i.e.*, $Al_{1.6}Fe_{2.9}Mg_{1.4}Mn_{0.1}Si_{3.0}Al_{1.0}O_{10}{}^{*}(OH)_8$.

VALUABLE PRODUCTS FROM UTILITY FLY ASH

Joseph A. DeBarr[1], David M. Rapp[1], Massoud Rostam-Abadi[1] and Mark J. Rood[2]
[1]Illinois State Geological Survey, 615 E. Peabody Dr., Champaign, IL 61820
[2]University of Illinois, 3213 Newmark, 205 N. Mathews, Urbana, IL 61801

Key Words: fly ash utilization, activated carbon, magnetite

INTRODUCTION

Fly ash is a potentially important engineering raw material that has yet to be extensively utilized. Of the 48 million short tons of fly ash produced in 1993 from burning coal in power stations in the U.S., only 22% was utilized, with the major use occurring in cement and concrete products [1]. Utilization of fly ash represents a potential for utilities to both reduce costs and increase revenues. A major barrier to fly ash use is its variable nature, both chemical and physical, due to differences in source coals, boiler design and stack removal processes.

Because the variability of fly ash is manifested in the diversity of its chemical and mineral components, a novel way of exploiting the variability would be to physically separate these components and use them as raw materials for the manufacture of various value-added materials. Figure 1 shows components that may be separated from fly ash, and some of their potential uses. For example, the reactive aluminosilicate glass could be reacted to microengineer zeolites or other high surface area phases, or to prepare structural and insulation components. Unburned carbon can be converted to activated carbons or carbon black, or used as a supplementary fuel. Iron oxides (magnetite) can be used as a raw material for making ferrites (magnetic ceramics), in heavy media coal cleaning equipment to provide a high specific gravity suspension, and as cement additives. Cenospheres, hollow spheres composed mostly of silica, alumina and iron oxides, can be used as polymer fillers, in light-weight ceramics and as low dielectric constant substrates.

Recovery of useful components from fly ash can improve the economics of fly ash utilization and can offset costs associated with disposal. The Illinois State Geological Survey (ISGS) has a program to find new uses for fly ash. One objective of this work is to investigate the potential of recovering adsorbent carbon, magnetite and cenospheres from fly ash. Removing these components may improve the quality of the remaining fly ash so that it can be used in cement and concrete products. In this paper, results of preliminary efforts to recover adsorbent carbons and magnetite from fly ash are described.

EXPERIMENTAL

Fly ash was obtained from an Illinois utility burning high sulfur Illinois coal. The fly ash was sieved into plus 90-μm and minus 90-μm fractions. Only the plus 90-μm fraction was used in this work. Ash composition (major and minor oxides) was determined by X-ray fluorescence (XRF) spectrometry. Samples were dried overnight at 110°C, then ignited at 1000°C for one hour to determine loss-on-ignition (LOI). The ignited sample was fused at 1000°C for 15 minutes with 50% lithium tetraborate/50% lithium metaborate flux and formed into a 30-mm diameter disk. The specimen was analyzed with a Rigaku model 3371 wavelength dispersive X-ray fluorescence spectrometer with an end-window rhodium X-ray tube.

Magnetic components were recovered by dispersing 500 grams of fly ash in one liter of water and stirring by hand to wet the sample fully. A plunger type hand magnet was used to recover magnetic components that were transferred to another vessel. The procedure was repeated until very little magnetic component was collected by the magnet. The concentrate was dried and weighed to determine the amount of sample obtained.

The unburned carbon in fly ash was concentrated in a two-step process involving sieving through a 170-mesh screen and cleaning the -170 mesh particles by oil agglomeration/froth flotation. Activation of the carbon concentrate was done to develop further the surface area and porosity of the sample. About 10 g of carbon concentrate was placed in a ceramic boat (1.9 cm x 1.2 cm x 7.5 cm) and centered in a 5 cm ID x 90 cm mullite tube in a Lindberg split-tube furnace. The sample was heated at 20°C/min to 950°C in flowing N_2. The N_2 was replaced by 50% H_2O/50% N_2 for 1 h. The sample was then cooled under N_2 to room temperature.

The SO_2 adsorption capacities of samples were determined by thermogravimetric analysis (Cahn TG-131). In a typical run, a 30-50 mg sample was placed in a platinum pan and heated at 20°C/min in

flowing N_2 to 360°C to remove moisture and impurities. The sample was cooled to 120°C. Once the temperature stabilized, a mixture of gases containing 5% O_2, 7% H_2O and the balance N_2 was substituted for the N_2. Once there was no further weight gain due to adsorption of O_2 and H_2O, SO_2 was added in concentrations representative of a flue gas from combustion of high sulfur coal (2500 ppmv SO_2). The weight gain was recorded versus time by a computerized data acquisition system.

Surface areas were determined from the amount of N_2 adsorbed at 77 K using a dynamic sorption method in conjunction with a single point BET adsorption equation. Single point N_2 BET surface areas were determined from N_2 (77 K) adsorption data obtained at a relative pressure (P/P_o) of 0.30 with a Monosorb flow apparatus (Quantachrome Corporation).

RESULTS AND DISCUSSION

The results of analyses of the +90 μm and -90 μm fractions are shown in Table 1. The two major components of the fly ash, silica and alumina, were equally distributed between the two size fractions. Most other elements, except carbon (as evidenced by the LOI), are concentrated in the size fraction with smaller particle diameters. The majority of the carbon in this fly ash had particle diameters larger than 90 μm.

Magnetite

The magnetic concentrate represented about 1% of the feed fly ash. Microscopic evaluation of the concentrate revealed the material was black spherulites (about 90% of the sample) and that no magnetite crystals (octahedrons) were observable, suggesting the particles probably were composed of microcrystalline magnetite. X-ray diffraction spectrometry confirmed that the magnetic concentrate was predominantly magnetite. The spherulites were less magnetic than regular magnetite suggesting they also contained some nonmagnetic material. Semiquantitative analysis of the sample indicated that the concentrate was approximately 90% magnetite and most of the remainder was hematite. The spherulites were somewhat fragile, and could probably be easily ground. This could be a useful property if a simple grinding step could be done to liberate nonmagnetic material and provide a relatively pure microcrystalline magnetite product. Fly ash-derived magnetite has potential for application as a heavy medium in coal cleaning [2, 3]. It has been reported that the most effective magnetite for heavy medium cyclones is magnetite having a mean particle size of 12 μm [4]. A process called the Micromag process was recently patented and specifies that a majority of the magnetite particles be less than 5 μm in size.

Carbon

The unburned carbon in fly ash was concentrated from about 3 wt% to about 70 wt% in this study. Screening at 170 mesh resulted in a 11.6% carbon concentrate (assuming all the LOI is attributed to carbon, Table 1), and flotation increased the carbon content to 70 wt%. Screening has been reported effective for concentrating carbon in fly ash [2] as has air classification [2] and electrostatic separation [5, 6]. Others have used froth flotation to prepare a concentrate of up to 56 wt% carbon [7].

The surface area of the carbon concentrate was about 11 m^2/g. During activation, weight loss was 18%, and surface area of the carbon increased from 11 m^2/g to more than 160 m^2/g. It is known that surface area, corrected for ash content, increases monotonically during activation up to about 80% weight loss [8], suggesting that optimization of separation and activation steps may result in the production of even higher surface area carbons from fly ash.

A low-surface-area carbon has many potential applications. One such application would be in processes for removing air toxics from waste incinerator and utility flue gas [9, 10]. STEAG, a German-based multinational corporation, has licensed technology for carbon-based systems installed on commercial medical, hazardous and municipal waste incinerators in the European Community [9]. The carbon used in the STEAG process, Herdofenkoks, is an activated char produced from lignite, with pore surface area of 300 m^2/g [11]. The SO_2 adsorption capacity of a carbon is reported to be a reliable guide to acceptability in the STEAG process [12]. The kinetics of SO_2 adsorption for a carbon prepared by the ISGS from Illinois coal [13] are compared in Figure 2 with that for Herdofenkoks. The ISGS activated carbon had a N_2 BET surface area of only 110 m^2/g, but had an SO_2 adsorption capacity of 7% by weight after 4 h, almost twice that of the Herdofenkoks. Early pilot scale test results showed that the ISGS activated carbon was effective in the STEAG process. The activated carbon prepared in this study from fly ash adsorbs much more SO_2 than either the ISGS or Herdofenkoks carbons (Figure 2), suggesting that it has potential for application in the STEAG process.

CONCLUSIONS

A quality adsorbent carbon and a quality magnetite concentrate were recovered from an Illinois utility fly ash. There remains significant room for improvement in the quantity and quality of both these products recovered from fly ash. The quantity of recoverable cenospheres has not yet been evaluated. Co-recovery of cenospheres, currently a commercial product, could make the economics of processing fly ash even more attractive. Adsorbent carbons sell for up to $2,500 per ton, magnetite for approximately $60-$70 per ton and cenospheres for as much as several hundred dollars per ton. Removing these valuable products from fly ash may improve the characteristics of the remaining ash for application in cement and concrete products. Future efforts will focus on recovery of products from fly ashes with a wide range of characteristics.

ACKNOWLEDGMENTS

This work is to continue with support, in part, by grants made possible by the Illinois Department of Commerce and Community Affairs through the Illinois Coal Development Board and the Illinois Clean Coal Institute.

REFERENCES

1. American Coal Ash Association, 1993, "Coal Combustion Byproduct (CCB) - Production and Use," pamphlet, American Coal Ash Association, Alexandria, VA.
2. Boux, J. F., 1969, "Canadians Pioneer New Fly Ash Processing System," *Minerals Processing*, **10:3**.
3. Roy, N. K., Murtha, M. J. and Burnet, G., 1979, "Use of Magnetic Fraction of Fly Ash as a Heavy Medium Material in Coal Washing," Proceedings of the 5th International Ash Utilization Symposium.
4. Stoessner, R.D., Chedgy, D.G., and Zawadzki, E.A., 1988, "Heavy Medium Cyclone Cleaning 28x100 Mesh Raw Coal," from *Industrial Practice of Fine Coal Processing*, 1988 SME, Edited by R.R. Klimpel and P.T. Luckie, 57-64.
5. Makansi, J., 1994, *Power*, **Aug**, 37-41.
6. Inculet, I.I., Bergougnou, M. A. and Brown, J.D., 1977, "Electrostatic Separation of Particles Below 40 Micron in a Dilute Phase Continuous Loop," *Institute of Electrical and Electronic Engineers Transactions*, **1A-13:4**.
7. Groppo, J.G., Robl, T.L. and McCormick, C.J., 1995, "A Selective Beneficiation Process for High LOI Fly Ash," Proceedings of the 1995 International Ash Utilization Symposium, Lexington, KY, October 23-25.
8. Lizzio, A.A and Radovic, L.R., "On the Usefulness of Total Surface Area for Predicting Carbon Gasification Reactivity Profiles", 19th Biennial Conference on Carbon, University Park, PA, 1989.
9. Brueggendick, H. and Pohl, F.G., 1993, "Operating Experience with STEAG's Activated Carbon Process-a/c/t™ in European Waste Incineration Plants," brochure from STEAG AG.
10. Tsuji, K. and Shiraishi, I., 1991, "Mitsui-BF Dry Desulfurization and Denitrification Process Using Activated Coke," in Proceedings of the EPRI SO_2 Control Symposium, Washington, D.C., p. 307.
11. Thielen, W. and Seipenbusch, J., 1992, "Flue Gas Cleaning with Activated Coke in Waste Incineration," *La Rivista dei Combustibili*, **46 (4)**, p. 129.
12. Rummenhol, V., 1994, Presentation to Illinois Coal Development Board, Illinois Clean Coal Institute and Illinois State Geological Survey, Champaign, IL, March 2.
13. Lizzio, A.A., DeBarr, J.A. and Kruse, C.W., 1995, "Development of Low Surface Area Char for Cleanup of Incinerator Flue Gas," Proceedings of the 22nd Biennial Conference on Carbon, San Diego, CA, p. 74.

Table 1. Composition of +90-μm and -90-μm fly ash (wt%).

Oxide	+90 μm	-90 μm
SiO_2	45.91	44.86
Al_2O_3	25.15	26.91
Fe_2O_3	4.38	7.10
CaO	6.31	9.46
MgO	1.61	2.26
K_2O	0.67	0.76
Na_2O	0.91	1.37
TiO_2	1.07	1.53
P_2O_5	1.12	2.12
MnO	0.01	0.01
SO_3	0.43	0.71
SrO	0.17	0.32
BaO	0.24	0.47
Loss on Ignition (carbon)	11.62	1.75

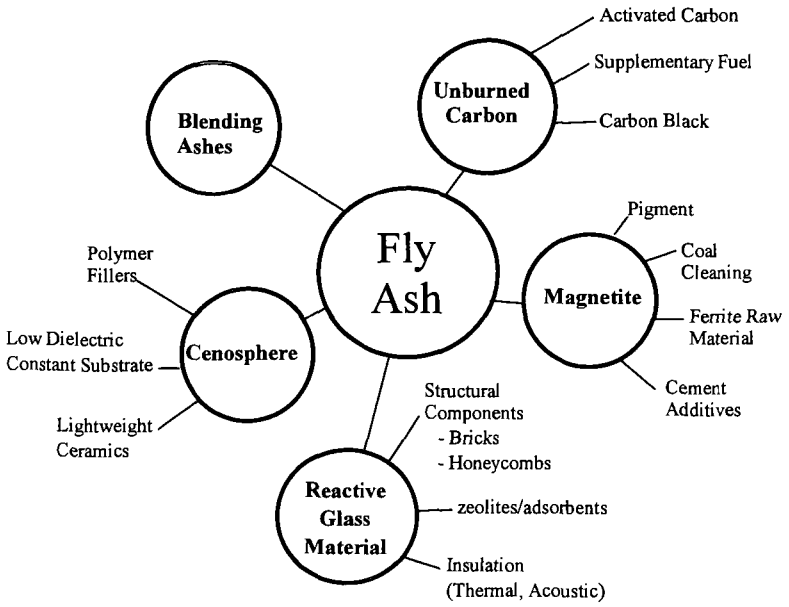

Figure 1. Components of fly ash.

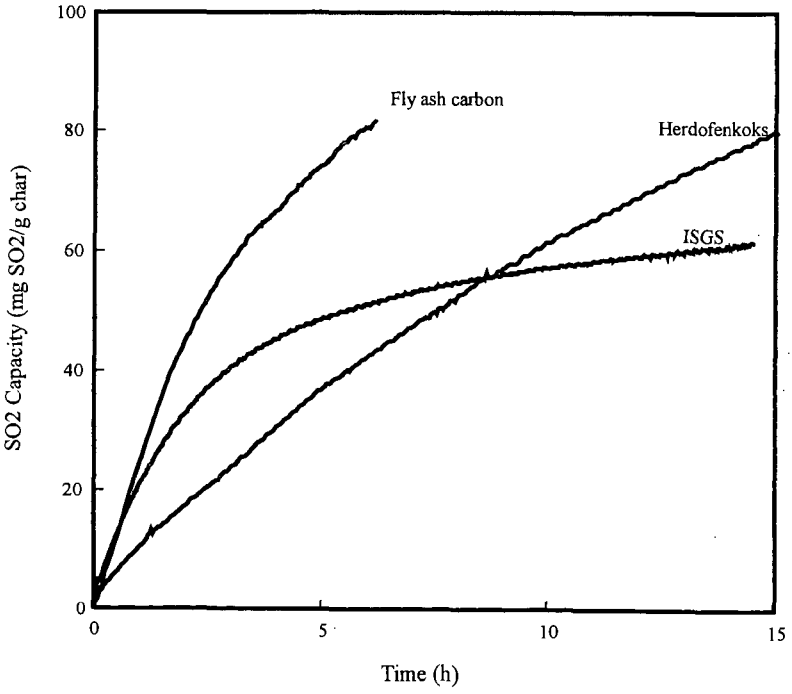

Figure 2. SO2 adsorption for activated carbons.

TRIBOELECTROSTATIC SEPARATION OF UNBURNED CARBON FROM FLY ASH

Heng Ban, Tian X. Li, John L. Schaefer and John M. Stencel
Center for Applied Energy Research, University of Kentucky
3572 Iron Works Pike, Lexington, KY 40511-8433, U.S.A.

Keywords: Fly ash; Triboelectrostatic; Beneficiation

ABSTRACT

Due to differences in the surface physical and chemical properties of the carbon and ash, particles of unburned carbon and fly ash can be electrically charged to opposite polarity, and can be separated by passing them through an external electric field. A laboratory scale triboelectrostatic separation system was used to study fly ash beneficiation. Fly ash samples, characterized by size analysis and carbon content, were subjected to triboelectrostatic separation. The separated fractions were collected and evaluated for carbon content, and subjected to SEM. The results indicate the potential for applying dry separation technology for removing unburned carbon from coal ash.

INTRODUCTION

Fly ash from pulverized coal power plants is a marketable commodity, provided acceptable levels of carbon are maintained.[1] With the advent of low NO_x burners, the carbon content in fly ash in many cases has increased to the point where it is no longer marketable and becomes a disposal liability. Dry triboelectrostatic separation technology is just beginning to be applied to recover purified ash from fly ash streams which contain high concentrations of carbon.[2] Due to differences in the surface physical and chemical properties of the carbon and ash, they can be electrically charged to opposite polarity by particle-to-particle or by particle-to-surface contact. By manipulating the polarity and magnitude of this charge, the carbon and ash can be separated by passing them through an external electric field, see Figure 1. The successful application of dry separation technology to ash purification would be significant because it would eliminate water handling and treatment problems associated with wet beneficiation methods.

Dry electrostatic separation technology has been utilized in the mineral processing industry and most recently has been considered for coal beneficiation.[3-7] The US DOE has funded several projects focusing on both the fundamentals and development of dry coal beneficiation technologies based on electrostatics.[8] As a consequence of these efforts, a greater understanding of factors relating to the particle charging and electrostatic separation has been achieved. While the cost of processing is a major factor in the economic feasibility of coal beneficiation, it is not as important in the case of fly ash beneficiation. Economic factors of equal or higher importance include the avoided cost of ash disposal and the market value of the processed ash. Depending on geographic location, it is possible that the application of efficient dry ash separation technologies could be very beneficial to coal utilization systems.

Very little has been published on the application of dry triboelectrostatic separation to fly ash beneficiation. There is a need for optimizing dry fly ash separation technologies because of the vast amount of coal ash produced in the US and the growing interest in applying superior technologies with respect to their economical and environmental performance. In this paper, results from the triboelectrostatic separation of two coal fly ashes are presented. These experiments were conducted at a laboratory scale. The design of the triboelectrostatic separation system and the data obtained on the ashes in this study will be used in future work to optimize ash separation using feed rates typical to industrial and utility systems.

EXPERIMENTAL

A laboratory scale triboelectrostatic separation system, shown in Figure 2, was used in the fly ash benificiation study. The fly ash was metered by using a vibratory feeder, contained in a sealed environment tank, into a pneumatic transport tube where it was entrained in a N_2 carrier gas. The gas-particle mixture was then passed through a tribocharging unit where the fly ash was charged by particle-particle or particle-wall frictional contact. The exit of the charger was connected to a separation chamber which contained parallel copper plates across which was established a high intensity electric field. A filter was placed at the bottom of the separation chamber to catch any entrained fly ash particles. The exit of the separation chamber was connected to an induced draft fan.

About 10 grams of ash sample were weighed and used for each separation test. The average carrier gas flow velocity was about 15 m/s. The electric field strength was maintained at 200 kV/m.

The fly ash samples were acquired from either ESP hoppers or storage silos at two pulverized coal boilers. Prior to separation tests, the samples were evaluated for particle size and carbon content.

After the triboelectrostatic separation, samples were collected from predetermined locations throughout the separation chamber, and their weight and carbon content determined. Representative sample fractions were also prepared and examined using scanning electron microscopy (SEM) and energy dispersive spectrometry (EDS).

RESULTS AND DISCUSSIONS

During separator operation, fractions of carbon and ash were deposited on the electrodes. For both electrodes, the depositions appeared to be long narrow ribbons of material, starting from near the exit of the transporting tube and extending to the end of the copper plates. Analysis of sequential axial sections of the depositions showed the carbon content to be highest at the top of the negative electrode and lowest at the top of the positive electrode. The carbon content on the positive electrode increased with distance while that on the negative electrode decreased with distance. In other words, the ash was the purest at the top of the positive plate and the carbon the purest at the top of the negative plate. Since the carbon and ash content on the electrodes could be represented by a continuous distribution, it was possible to make an arbitrary split of the separated products that satisfied desired purity requirements. However, as in any physical separation processes, higher purity products are achieved at the expense of lower yield.

A procedure was established for separated sample collection and analysis. For each test, there were a total of ten sample fractions collected; eight from four axial regions of the two electrodes, one from the center filter, and one removed from the vertical plexiglass windows. These fractions along with the feed were weighed and analyzed for their carbon content. An eleventh data point, which represents the material which was not captured anywhere in the separator, was determined by performing a mass and carbon balance. The separation results were plotted in a manner similar to a washability or release analysis curve, using the analogy of each fraction being either a float or sink product. These data include an assessment of mass balances. A second stage separation could be performed by putting the fraction collected on the center filter back to the feeder, and process the data with those from the first stage separation.

Carbon and ash recovery, and particle size and carbon distributions, for the fly ash sample A are shown in Figure 3-5. This sample was obtained from a utility boiler burning bituminous coal having an intermediate sulfur content. Over 65% of the ash was recovered with a carbon content of less than 3%, while about 50% of the carbon in the ash was recovered with a carbon content greater than 35%. The particle size distribution data show that there is a significant amount of the ash with sizes greater than 150 μm and with sizes below 25 mm. This wide distribution of particle size presents a significant challenge to dry separation systems due to an order of magnitude range in aerodynamic drag and gravitational forces. For this particular ash, the carbon concentrations for each size fraction are in a descending order, as shown in Figure 3, from the highest in the largest size fraction to the lowest in the smallest size fraction.

Separation results for fly ash sample B are presented in Figure 6-7. This sample was obtained from a utility burning intermediate-to-high sulfur coal. The ash recovery data is plotted for a one stage and a two stage processing scheme. The application of the second stage increased the ash recovery by about 15% and, hence, may be important to the overall processing scheme. These data show that nearly 55% of the ash was recovered with a carbon content of less than 3% while over 60% of the carbon could be recovered with a carbon purity greater than 40%. These results suggest the utility of dry ash separation. Important chemical and physical properties of the fly ashes which affect or control efficient dry ash separation are currently under investigation.

CONCLUSIONS

This study has shown that dry triboelectrostatic separation of fly ash has the potential to be an effective method of separating unburned carbon from fly ash. Laboratory tests on a simple parallel flow separator showed that 60-80% of ash could be recovered at carbon contents below 5%, and 50% of carbon could be recovered at carbon concentrations over 50%. Additional studies should be initiated to evaluate the effects of ash properties on separation with the goal of optimizing the beneficiation process.

REFERENCES

1. Manz, O.E., 1993, Worldwide Production of Coal Ash and Utilization in Concrete and Other Products: *Proceedings, 10th International Ash Use Symposium, Volume 2: Ash Use R&D and Clean Coal By-Products*, EPRI, Orlando, FL, p. 64/1-64/12.

2. Whitlock, D.R., 1993, Electrostatic Separation of Unburned Carbon from Fly Ash: *Proceedings, 10th International Ash Use Symposium, Volume 2: Ash Use R&D and Clean Coal By-Products*, EPRI, Orlando, FL, p.70/1-70/12.

3. Schaefer, J.L., J.M. Stencel and H. Ban, 1992, Non-Intrusive Measurement of Particle Charge

Relating to Electrostatic Dry Coal Cleaning: *Proceedings, 9th Annual International Pittsburgh Coal Conference*, University of Pittsburgh, Pittsburgh, PA, p. 259-264.
4. Ban, H., J. Yang, J.L. Schaefer, K. Saito and J.M. Stencel, 1993, Measurement of Charge and Charge Distribution on Coal and Mineral Mater During Electrostatic Dry Coal Cleaning: *Proceedings, 7th International Conference on Coal Science*, Banff, Alberta, Canada, Vol. 1, p. 615-618.
5. Ban, H., J.L. Schaefer and J.M. Stencel, 1993, Velocity and Size Effect on Particle Triboelectrification: *Proceedings, 10th Annual International Pittsburgh Coal Conference*, University of Pittsburgh, Pittsburgh, PA, p.138-143.
6. Schaefer, J.L., H. Ban and J.M. Stencel, 1994, Triboelectrostatic Dry Coal Cleaning: *Proceedings, 11th Annual International Pittsburgh Coal Conference*, University of Pittsburgh, Pittsburgh, PA, Vol. 1, p. 624-629.
7. Ban, H., J.L. Schaefer, K. Saito and J.M. Stencel, 1994, Particle Tribocharging Characteristics Relating to Electrostatic Dry Coal Cleaning, *Fuel*, **Vol. 73**, p.1108-1115.
8. Finseth, D., T. Newby and R. Elstrodt, 1993, Dry Electrostatic Separation of Fine Coal: *Proceedings, 5th International Conference on Processing and Utilization of High-Sulfur Coals*, University of Kentucky, Lexington, KY, p. 91-98.

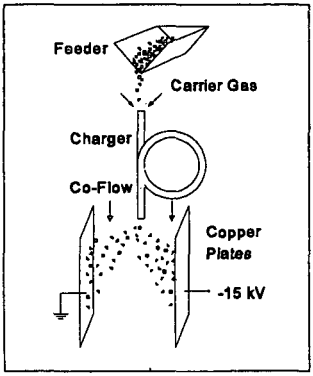

Figure 1: Electrostatic separation principle

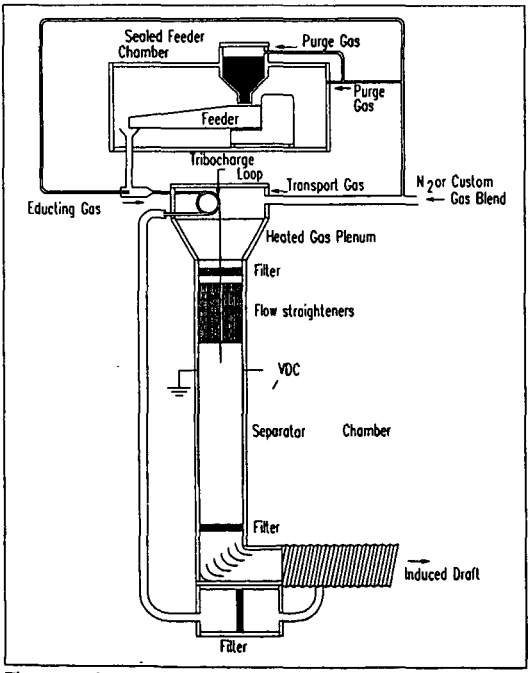

Figure 2: The schematic of the test system.

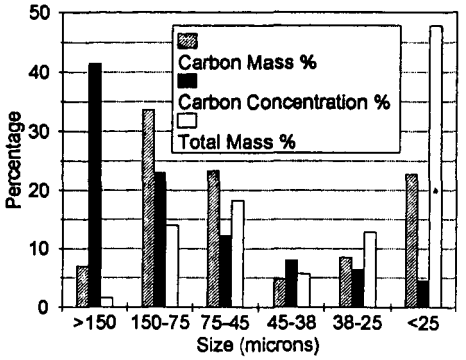

Figure 3: Percentage fly ash weight, carbon concentration, and carbon mass distributions in each size fractions for fly ash sample A.

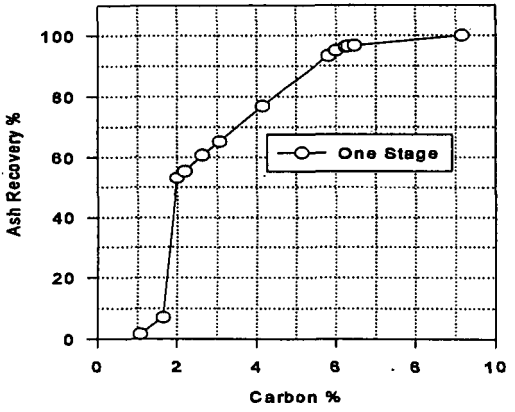

Figure 4: Ash recovery curve for sample A.

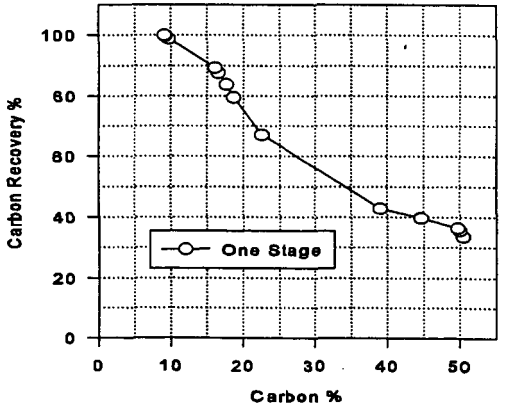

Figure 5: Carbon recovery curve for sample A.

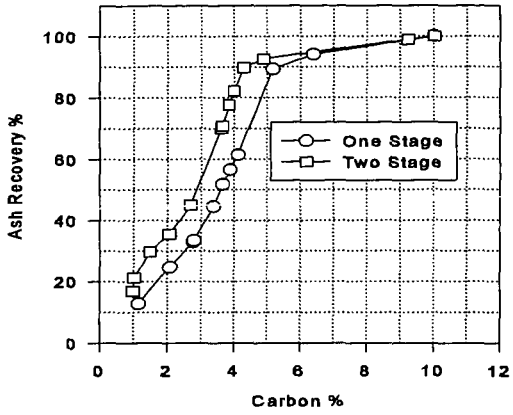

Figure 6: Ash recovery curve for sample B.

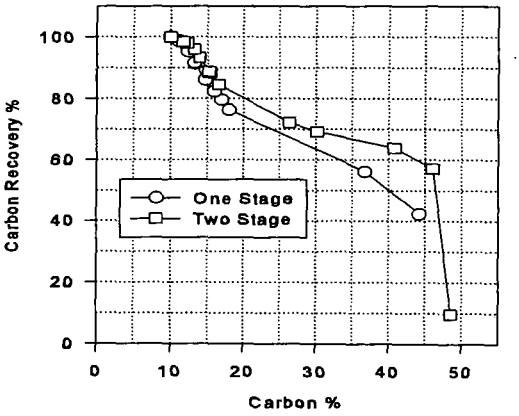

Figure 7: Carbon recovery curve for sample B.

REGENERATION AND REUSE OF A LIME-BASED SORBENT FOR SULFUR OXIDES

S. B. Jagtap and T. D. Wheelock
Chemical Engineering Department
and Engineering Research Institute
Iowa State University
Ames, Iowa 50011

Keywords: Lime-based sorbent, sulfur oxides, regeneration

INTRODUCTION

The purpose of this work was to study the feasibility of regenerating and reusing lime employed as a sorbent for sulfur oxides in an industrial, circulating fluidized bed boiler that is fired with petroleum coke. At present ground limestone is supplied continuously to the boiler, and the resulting sulfated bed ash and fly ash are discarded. By regenerating the sorbent, much less limestone would be required and waste disposal would be minimized.

Since the sorbent is converted to calcium sulfate in the boiler, regeneration requires converting calcium sulfate back to calcium oxide. Previous studies showed that such conversion can be achieved by employing reductive decomposition with carbon monoxide as indicated below (1,2):

$$CaSO_4 + CO = CaO + CO_2 + SO_2 \qquad (1)$$

By such means it is also possible to produce by-product sulfur dioxide in sufficient concentration for conversion into sulfuric acid or possibly elemental sulfur.

To study the feasibility of regenerating and reusing the lime sorbent, samples of sulfated bed ash and fly ash from an industrial boiler were subjected to a number of regeneration and sulfation cycles, and changes in the apparent reactivity and sorptive capacity of the materials were observed. The experiments were conducted by employing thermogravimetric analysis (TGA) which made it possible to monitor sulfation and regeneration by observing the change in sorbent weight.

EXPERIMENTAL METHODS AND MATERIALS

The limestone supplied to the boiler is largely calcium carbonate with the principal impurity being silica. Chemical analysis of samples of fluidized bed ash and fly ash from the boiler showed the principal components of the ash to be $CaSO_4$ (58.2%, 33.6%), CaO (30.4%, 29.3%), $CaCO_3$ (1.8%, 21.5%), and SiO_2 (2.1%, 7.2%). For each component, the first number is for bed ash and the second number is for fly ash. Both materials were also found to contain small amounts of iron, vanadium, and nickel oxides arising from the combustion of petroleum coke. Approximately 98% of the bed ash particles were larger than 230 mesh size, whereas 82% of the fly ash particles were smaller than this size. The composition of the bed ash indicates that 37% of the CaO was converted to $CaSO_4$ in the boiler, while the composition of the fly ash suggests a lower level of conversion.

For some regeneration and sulfation experiments larger particles of fluidized bed ash or limestone were used as received, whereas for other experiments the materials were pelletized first, and fly ash was always pelletized first. The pellets were formed in a double-acting stainless steel die by application of high pressure with a hand-operated hydraulic press. The pellets were 6.35 mm in diameter and 1-2 mm thick. For some experiments the pellets were used directly, whereas for others the pellets were crushed, and the material screened.

The experiments were conducted with conventional TGA apparatus consisting of a vertical tubular reactor in which a balance pan for holding the reacting solids was suspended from a Cahn model 2000 electrobalance. Both the 10 mm diameter pan and 25 mm diameter reactor were made of quartz. The reactor was surrounded by a temperature-controlled electric furnace. During operation the reactor was supplied with a mixture of gases produced by combining various pure component gases which were metered separately by calibrated rotameters.

When starting with sulfated particles of fluidized bed ash or fly ash, the particles were first heated in a stream of nitrogen to 1100°C. The particles were then regenerated by treatment with a reducing gas mixture consisting of 2% CO, 5% SO_2, 20% CO_2, and 73% N_2. When the reaction appeared complete, the gas mixture was replaced by nitrogen and the temperature was lowered to 900°C. At this point the particles were sulfated by treatment with a gas mixture consisting of either 1% or 3% SO_2, 5% O_2, and sufficient N_2 to make up the balance. When the reaction appeared complete, the cycle was repeated.

The conversion during each sulfation step was based on the following relation:

$$\text{Sulfation (\%)} = \frac{\text{moles } SO_3 \text{ adsorbed}}{\text{moles Ca present}} \times 100 \qquad (2)$$

For each regeneration step the conversion was estimated by employing the relation shown below.

$$\text{Conversion (\%)} = \frac{\text{Wt. loss during regeneration}}{\text{Wt. gain during sulfation}} \times 100 \qquad (3)$$

RESULTS AND DISCUSSION

A number of runs were made with the TGA apparatus to determine the regeneration and sulfation characteristics of the parent limestone, fluidized bed ash, and fly ash. Typical results obtained with bed ash are shown in Table 1. For this experiment the bed ash was pelletized, crushed, and screened to provide -25/+40 mesh particles. The particles were first regenerated and then subjected to the seven cycles of sulfation and regeneration listed. The first sulfation step required 98 min. and resulted in the conversion of 44.6% of the CaO to $CaSO_4$. The subsequent regeneration step only took 25 min. and appeared to result in the complete conversion of $CaSO_4$ to CaO. As the cycles were repeated, both the cycle time and the extent of sulfation decreased gradually from cycle to cycle. The decrease in sulfation indicated that an increasing portion of each particle became inaccessible or unreactive. This result could have been caused by sintering and closure of some of the particle micropores. Nevertheless, even during the eighth cycle of sulfation (recalling that the first cycle took place in the boiler), the capacity of the sorbent was still 26% of the maximum theoretically possible if all of the calcium were converted to $CaSO_4$. Even more encouraging were the results of the regeneration step which always seemed to achieve nearly complete conversion of $CaSO_4$ to CaO.

Similar results were obtained with -25/+40 mesh unreacted limestone particles which were prepared in the same manner as the bed ash particles by pelletizing, crushing, and screening. Upon heating the limestone particles to 900°C in a stream of nitrogen, the $CaCO_3$ was converted to CaO. The particles were then subjected to a series of sulfation and regeneration cycles using the same conditions employed with bed ash. For the early cycles the level of sulfation was nearly the same as that observed with bed ash while for the later cycles it was slightly greater. The similarity in results achieved with the two materials suggests that the small amount of petroleum coke ash present in the bed ash had little effect on the sulfation and regeneration characteristics of the bed ash.

The results observed with -25/+40 mesh fly ash particles differed in several respects from those described above when the particles were prepared and treated like the bed ash particles. For the fly ash particles the time required for the sulfation step was about half that required for the other materials. The level of sulfation achieved in the first TGA cycle was 37.7% compared to 44.6% for bed ash, and in the fifth TGA cycle it was 19.7% compared to 31.4% for bed ash. Therefore, it is apparent that the sorptive capacity of the fly ash decreased more rapidly than that of the other materials. This result was probably due to the difference in grain size of the various materials. The initial particle size of the fly ash was considerably smaller than that of the bed ash. Consequently, when the two materials were heated to reaction temperature, there would have been a greater tendency for the fly ash particles to sinter causing a greater decrease in microporosity.

CONCLUSIONS

The results of this work indicate that it would be feasible to regenerate and recycle the sulfated bed ash produced by burning petroleum coke in a fluidized bed of limestone particles. Although the experimental results showed a decline in the sulfation capacity of bed ash particles as the number of sulfation and regeneration cycles increased, it was still possible to convert 30% or more of the CaO to $CaSO_4$ after five cycles. Regeneration was more rapid than sulfation, and it was nearly always complete. The results also indicate that it would be feasible to regenerate and recycle pelletized fly ash. However, the sulfation capacity of this material declined more with each cycle than the sulfation capacity of bed ash declined.

ACKNOWLEDGMENT

This work was supported by the Engineering Research Institute of Iowa State University.

REFERENCES

1. T. D. Wheelock and D. R. Boylan, Reductive Decomposition of Gypsum by Carbon Monoxide, *Ind. Eng. Chem.*, **52**, 215-218 (1960).

2. J. S. Oh and T. D. Wheelock, Reductive Decomposition of Calcium Sulfate with Carbon Monoxide: Reaction Mechanism, *Ind. Eng. Chem. Res.*, **29**, 544-550 (1990).

Table 1. Results of run made with granulated bed ash*

Cycle	Time, min.	Initial wt., mg	Final wt., mg	Δ wt., mg	Sulf., %	Regen / Sulf., %
1-S	98	39.2	58.5	19.3	44.6	
1-R	25	58.5	39.2	19.3		100
2-S	90	39.2	56.1	16.1	39.1	
2-R	24	56.1	39.3	16.8		104
3-S	89	39.3	54.2	14.9	34.5	
3-R	20	54.2	39.4	14.8		99
4-S	86	39.3	53.6	14.3	33.1	
4-R	22	53.6	39.4	14.2		99
5-S	86	39.4	53.0	13.6	31.4	
5-R	22	53.0	39.6	13.4		99
6-S	88	39.3	51.7	12.4	28.7	
6-R	20	51.7	39.4	12.3		99
7-S	80	39.3	50.7	11.4	26.4	
7-R	20	50.7	39.4	11.3		99

*Particle size: -25/+40 mesh
Weight before calcination: 54.6 mg
Sulfation conditions: 905-910°C, 1% SO_2, 5% O_2, 94% N_2
Regeneration conditions: 1105-1110°C, 2% CO, 5% SO_2, 20% CO_2, 73% N_2.

ABSORPTION STUDIES OF ACIDIC GASES USING DRY FGD WASTES.

Darrell N. Taulbee and Thomas L. Robl
University of Kentucky-Center for Applied Energy Research
3572 Iron Works Pike, Lexington, KY 40511

Keywords: Acid gases, absorption, CO_2, NO_2, H_2S, SO_2, Flue-gas desulfurization or FGD,

ABSTRACT

Utility boilers and tail-gas desulfurization units that utilize limestone-based sorbents to remove sulfur oxides generate ~20 million tons of flue-gas desulfurization (FGD) wastes each year in the U.S.[1] A substantial portion of the Ca in these wastes remains unsulfated (as CaO or $Ca(OH)_2$), particularly in units that produce *dry* wastes. When hydrated, these materials exhibit a strong affinity to absorb acid gases at ambient temperature in proportion to their available-calcium content and particle size. The work reported here is a continuation of previous investigations of CO_2 and H_2S absorption that includes more recent studies with NO, NO_2, and SO_2. The relative affinity for the gases examined thus far is $SO_2 > CO_2 > H_2S$. CH_4 and NO are not absorbed and NO_2 apparently decomposes at first to NO and HNO_3 before eventually being absorbed as calcium nitrate following depletion of hydration water. The role of available calcium and particle size on absorption capacity and mineralogic changes in the wastes during exposure are discussed.

INTRODUCTION.

In recent years, numerous flue-gas desulfurization (FGD) technologies that utilize limestone-based sorbents, such as fluidized-bed combustors (FBC), spray dryers, and wet scrubbers, have been or will be added to existing utility boilers in an effort to satisfy federally-mandated limits on SO_2 emissions. Such units are normally classified as either *wet* or *dry* depending on whether the absorbent is used in an aqueous slurry (wet) or as a dry or hydrated solid. In addition to differences in the proportions of sulfites and sulfates formed during sulfur capture, dry FGD by-products differ from their wet-scrubber counterparts in that a significant portion of the calcium in the dry waste remains unsulfated. The fraction of unreacted Ca, available as lime (CaO) or slaked lime ($Ca(OH)_2$) can be quite high (> 1/2) depending on scrubber design and operation.

When hydrated, dry FGD wastes strongly absorb acid gases at ambient temperature, e.g. CO_2. Further, absorption can be both rapid and near complete. Such a sorbent may have numerous commercial uses such as the removal of CO_2 from natural gas (the focus of a prior study[2]). Further, considering that about 95% of the ~20 million tons of flue-gas desulfurization (FGD) wastes generated annually in the US is discarded in landfills or holding ponds, commercial utilization of FGD wastes could stand to benefit from both a plentiful low-cost raw material as well as a significant savings in disposal.

In our ongoing study, gas absorption has been examined using waste samples generated in four commercial boilers, a Coolside demonstration-plant run[3], and four tests conducted in the Coolside pilot plant.[4] With the exception of a utility-derived fly ash that served as a control, all study samples are dry-FGD materials. In addition to the absorption studies with CO_2, CH_4 and H_2S previously reported, results from tests with NO, NO_2, and SO_2 are reported here.

EXPERIMENTAL.

Details for the most recent round of testing with NO, NO_2, and SO_2 plus a brief description of the reactor system, study samples, and run procedures are presented in the section to follow. The reader is referred to previous manuscripts for additional information on the latter.[2,5,6]

Absorption Reactors. A schematic of the reactor system shown with a pair of 4" x 3/8"-i.d. ss tube reactors as configured for hydrated solids is shown on the left of Figure 1. Essentially the same system was used to measure absorption by aqueous waste slurries except that a pair of 250 mL-capacity gas scrubbers were substituted for the tube reactors (Figure 1-right). It should be noted that due to the high solubility of SO_2 in and the tendency for NO_2 to decompose on contact with water, only tests with hydrated solids were conducted for these two gases.

Samples. A total of 11 waste samples have been used throughout this investigation.[2,5] Nine of the samples are fly ashes, designated with a -FA suffix. The remaining two, designated with a -BA suffix, are bed ashes. A Class F fly ash (L-FA) from a pulverized-coal-combustion (PCC) utility boiler served as a control and was the only non-FGD sample examined. The four fluidized-bed combustion wastes (FU-FA/BA and CC-FA/BA) were derived from circulating or entrained flow units operating on high-sulfur bituminous coal. Two types of dry, post-combustion flue-gas scrubber material were also examined, a spray-dryer ash from an industrial

boiler in the Midwest, and materials from the Coolside duct-injection technology. The Coolside materials include one sample generated in Ohio Edison's 1990 demonstration of the technology at its Edgewater power plant[3] (*CS*) as well as materials from the CONSOL's Coolside pilot plant in Library, PA (PP1-PP4).[4] The major differences in the waste samples with respect to absorption appears to be in the particle size (BA > FA) and the proportions of free lime which ranged from <3% in the L-FA control to ~20% or greater in the FU-FA, FU-BA, CC-BA, and PP4 samples. Because absorption of CO_2 has been reported for all 11 samples in a previous report, tests conducted in this round were limited for the most part to the FU-FA and PP4 which represent the two samples of fly ash with the highest free-lime content.

Run Procedures. All absorption tests were conducted at ambient temperatures. Hydrated samples were obtained by blending distilled water with dry waste under N_2. 0.5-2 g of the hydrated sample and 6 g of Ottawa sand were packed to the absorbent and bypass reactors, respectively. For the slurry tests, ~5 g of dry sample were added to 200 mL of distilled water in a 250-mL gas scrubber. The bypass scrubber contained distilled water only (200 ml).

Gas flow through the reactors was comprised solely of N_2 in the bypass line. Standard-gas blends containing various combinations of CO_2, H_2S, CH_4, and Ar were metered through the absorbent line.[2,5] Standard-gas blends containing 0.509 vol% NO, 3.82 vol% NO_2, or 3.81 vol% SO_2 were used in this round of testing. These blends were either quantitatively combined with high-purity Ar or with a blend of $Ar/CO_2/CH_4$ (30.3/49.6/20.1 vol%) prior to entering the reactor system. Argon was generally included in all blends as a tracer gas.

The exit streams from both the bypass and sample reactors were combined and continuously sampled with a capillary tube connected to the inlet of a VG-quadrupole mass spectrometer (QMS). The QMS was operated in a selected-ion-monitoring mode in which ion intensities for m/e 15-CH_3^+ (for methane), 18-H_2O^+, 20-Ar^{2+}, 28-N_2^+, 30-NO^+, 34-H_2S^+, 40-Ar^+, 44-CO_2^+, 46-NO_2^+, and/or 64-SO_2^+ were recorded at approximately 1-second intervals.

For both reactor configurations, data collection was initiated with the switching valve in the bypass position, i.e., the test-gas stream passing through the sand-packed bypass reactor. After a timed interval, the valve was rotated so that the test-gas stream was switched to the absorbent reactor as the N_2 stream was simultaneously switched to the bypass reactor. Following exposure, the valve was returned to the initial position to reestablish the QMS baseline. At the conclusion of a run, the QMS molecular-ion signal for each gas of interest was ratioed to the Ar-ion signal. The curves described by these ratios were then numerically integrated over the interval of exposure. By comparing these integrals to the test gas/Ar ratios obtained during passage through the bypass bed (before and after valve switch), the fraction of the test gas absorbed was determined. Since gas flows and sample weights are known, absorption could be converted to an absolute basis (standard cubic feet (SCF)/ton of waste. The same procedure was used for those runs in which more than one test gas was passed through the reactor in the same run.

RESULTS

It was shown in prior studies that the absorption of CO_2 required wetting of the dry FGD waste (hydration or slurry formation). For non-wetted samples, absorption proceeded at a prohibitively slow rate.[2,5] This is illustrated in Figure 2 where absorption of CO_2 is observed to increase in a linear manner up to about 25 wt% added water. Further water addition created a mud-like consistency accompanied by a dramatic decline in the apparent absorption capacity. This decline is presumably due to decreased permeability of the hydrated sample preventing gaseous CO_2 from freely entering the sample bed.

Absorption curves are shown in Figure 3 for a hydrated sample (top) and an aqueous slurry (bottom) prepared from PP4. This figure shows CH_4, CO_2, and H_2S response curves as these gases were concurrently passed through the reactor. These plots indicate that CH_4 was not absorbed, H_2S was moderately absorbed, and CO_2 was extensively absorbed. Closer inspection of the absorption curves reveals that the H_2S response rose to greater than baseline levels in both runs as H_2S was passed through the sorbent bed. This implies that some of the H_2S absorbed early in the exposure was displaced by CO_2 as the capacity of the PP4 sample was depleted. The absorption kinetics were more rapid for the hydrated sample than for the aqueous slurry though on an absolute basis, absorption was about twice as great for the latter (~3,800 SCF/t vs ~1,800 SCF/t). It was previously concluded that CO_2 incorporated into the hydrated sample to form calcite whereas absorption by the waste slurry resulted in capture as HCO_3^- ions which remain in solution. Thus, each CaO unit in the hydrated solids could capture one CO_2 molecule to form $CaCO_3$ or lead to the capture of two CO_2 molecules to form aqueous-phase HCO_3^- ions.

CO_2 absorption by waste slurries is plotted as a function of available-calcium content for the 11

study samples in Figure 4. The majority of the samples plot along a straight line with the exception of the two points on the lower right. These two outlyers represent the two samples of bed ash (FU and CC) whereas the other points in Figure 4 represent samples of fly ash. This plot emphasizes the dependency of CO_2 absorption on both available calcium and particle size. That is, the significantly larger particle size of the bed-ash samples as well as potential blockage of particle pores by chemisorbed SO_2 likely limits diffusion of CO_2 to the particle interior.

Tests with NO, NO_2, and SO_2. Absorption curves for NO, NO_2, and SO_2 are shown in Figure 5 as these gases were passed through either an aqueous slurry (NO) or a hydrated sample of PP4 (NO_2/SO_2). CO_2 was blended to the test-gas stream prior to routing to the absorption reactor for all three runs shown in Figure 5. The top plot shows essentially no absorption of NO. Likewise, no significant absorption of NO was measured when this gas was passed through the slurry without CO_2 (not shown) or when passed through a sample of hydrated PP4 (not shown).

The middle plot in Figure 5 shows simultaneous removal of NO_2 and CO_2. Both gases were extensively absorbed immediately after the valve switch to expose mode. However, ~5 min into the exposure, the response curve for CO_2 exceeded its baseline established during bypass mode (before and after exposure). This suggests that CO_2 initially absorbed was displaced as the run proceeded (absorption capacity of the slurry was depleted). Unlike CO_2 which is chemisorbed by portlandite ($Ca(OH)_2$) to form $CaCO_3$, it is not believed that NO_2 is absorbed as such. Rather, it appears to decompose on contact with hydration water to form HNO_3 and NO. This is supported by the NO and H_2O curves shown in the same plot. Immediately after switching to expose mode, the NO_2 signal is lower than that of NO. However, about 40-45 min into the run, the NO_2 response increases above that of NO concurrent with the depletion of H_2O. This is congruent with a decrease in NO_2 decomposition as the hydration water is consumed. HNO_3 ultimately reacts with portlandite to produce H_2O and calcium nitrate hydrate but not until much of the hydration water is depleted. Finally, integration of the CO_2-response curve revealed a net release of CO_2 of ~150 SCF/t. This production of CO_2 likely derives from calcite ($CaCO_3$) inherent to the FGD waste which is attacked by the newly-formed nitric acid (later discussion).

The bottom plot in Figure 5 shows SO_2/CO_2 absorption. Again, CO_2 was initially absorbed but later displaced by SO_2 as the run proceeded. Integration of the absorption curves (60 min interval) indicated an average absorption of ~3,800 SCF/t SO_2 and a net release of ~550 SCF/t CO_2. Again, the released CO_2 is believed to originate from pre-existing calcite in the PP4 sample as indicated by XRD. The calcite peaks were totally absent in the XRD spectra of wastes following exposure to SO_2. At the end of the 60' exposure, absorption of SO_2 and release of CO_2 is essentially complete. In contrast, during exposure to a blend of NO_2/CO_2 (Figure 5b), NO_2 decomposition and CO_2 displacement is not complete despite the fact that essentially the same volumes of NO_2 and SO_2 were flowed through the reactors during these runs. In a single run with SO_2 and NO_2 (w/o CO_2), SO_2 response began to return to baseline well before NO_2 which again exhibited an inverse relation to water availability. Thus, it would appear that SO_2 removal is controlled by the chemistry of the waste sample whereas NO_2 removal seems more dependent on water content.

Changes in mineralogy. X-ray diffraction (XRD) spectra of hydrated-PP4 waste samples are shown in Figure 6. The top plot (Figure 6a) is for a hydrated sample simultaneously exposed to CO_2 and H_2S, the middle spectrum (Figure 6b) is following exposure to NO_2/CO_2, and the bottom (Figure 6c) is following exposure to SO_2/CO_2. A spectrum of a hydrated sample of PP4 that had not been exposed to the test gases is shown in all three plots for comparison (darker lines). In the top plot, the major mineralogic change was depletion of portlandite ($Ca(OH)_2$) and formation of calcite ($CaCO_3$). There is no indication of CaS formation. When H_2S was passed through the sample without CO_2 (not shown), portlandite was again depleted only this time accompanied by the formation of an unidentified mineral with peaks near 9 and 20 (2-theta). The suspected stoichiometry of the unknown is $Ca(OH)_{2-x}(HS)_x$) though this structure is yet to be confirmed.

Again, depletion of portlandite from the parent to the exposed sample can be seen in Figure 6b in which NO_2 and CO_2 were passed through the hydrated sample. Several new peaks appear which are identified as a hydrated form of calcium nitrate. However, in runs aborted prior to water depletion, these peaks were not observed in the exposed sample. This is consistent with the decomposition of NO_2 to NO and HNO_3 since NO would be released and surface adsorbed HNO_3 would not exhibit an XRD pattern. Thus, the absorbed NO_x species must exist as either HNO_3 or in an amorphous structure. It is speculated that at some point during the exposure as water is depleted, the HNO_3 reacts with portlandite to form H_2O and $Ca(NO_3)_2{\cdot}2H_2O$.

Depletion of portlandite from the parent to the exposed sample is again evident in Figure 6c in

which a mixture of CO_2/SO_2 was used. The minor calcite peaks present in the parent are absent in the exposed sample. Several new peaks appear in the exposed sample which, for the most part, can be attributed to hannebachite ($CaSO_3 \cdot 0.5H_2O$). Thus, it appears that SO_2 is mostly incorporated by substitution for the hydroxyl ions in portlandite with some substitution for CO_2 in the inherent carbonates.

SUMMARY

Hydrated FGD wastes exhibit a strong affinity for CO_2, H_2S, and SO_2 ranging upwards of 4,000 SCF/t for SO_2 in tests with the PP4 and FU-fly ash. The relative order of affinity appears to be $SO_2 > CO_2 > H_2S$. NO_2 was found to decompose on contact with the hydrated samples to form NO and HNO_3 with eventual incorporation as hydrated calcium nitrate. Little or no absorption of CH_4 or NO was observed. In tests of CO_2 absorption, absorption capacity was found to be directly related to the available-calcium content and inversely to the particle size of the waste. Further, absorption did not proceed at a significant rate without the addition of water to the dry wastes. XRD analyses showed that exposure of hydrated FGD wastes to CO_2, H_2S, SO_2, and NO_2 resulted in the depletion of portlandite ($Ca(OH)_2$) and subsequent formation of calcite ($CaCO_3$), an unknown mineral, hannebachite ($CaSO_3 \cdot H_2O$), and initially either an amorphous nitrate/nitrite mineral or absorbed HNO_3 followed by formation of $Ca(NO3)_2 \cdot 2H_2O$, respectively.

ACKNOWLEDGEMENT

The authors wish to thank Dr. U. Graham, Dr. R. Rathbone, and M. Gust for assistance with the XRD analyses; G. Thomas, B. Schram, and M. Grider for sample analyses; and K. Baker of Jefferson Gas Transmission for useful discussions. This work was supported in part by the Morgantown Energy Techn. Ctr., USDOE, under Coop. Agreement DE-AC21-91MC28162 (such support does not constitute an endorsement by the USDoE of the views expressed in this manuscript).

REFERENCES.

1. *Coal Combustion Byproduct (CCB); Production & use: 1966-1993. Report for Coal Burning Utilities in the United States.* American Coal Ash Association, *1995*, Alexandria, VA, 68p.

2. Taulbee, D.N., Graham, U., Rathbone, R.F., and Robl, T.L.; *Prepr., ACS Div. of Fuel Chem.*, **1995**, *40, #4*, American Chemistry Society, Washington, DC, 858-862.

3. Kanary, D.A., R.M. Stanick, H.Yoon, et.al., **1990**, Coolside Process Demonstration at the Ohio Edison Company Edgewater Plant Unit 4-Boiler 13. *Proceedings, 1990 SO_2 Control Symposium* **3**, EPRI/U.S. EPA, Session 7A,, New Orleans, LA, 19p.

4. Withum, J.A., W.A. Rosenhoover and H. Yoon, **1988** *Proceedings, 5th Pittsburgh Coal Conf.* University of Pittsburgh, 84-96.

5. Taulbee, D.N.; Graham, U.; Rathbone, R.F.; Robl, T.L.; submitted for publication in *Fuel*, anticipated publication, late 1996.

6. Taulbee, D. N., *Prepr., ACS Div. of Fuel Chem.*, **1993**, *38, #1*, American Chemistry Society, Washington, DC, 324-329.

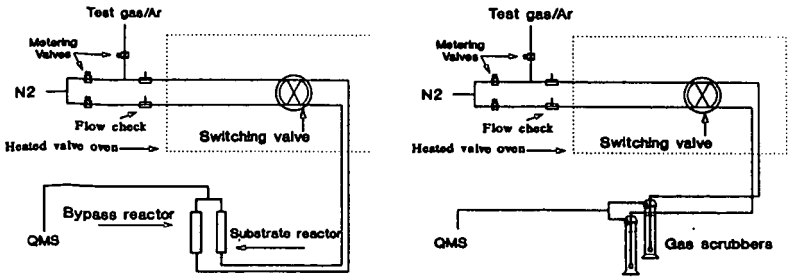

Figure 1. Schematic of the absorption reactors used to measure gas absorption by hydrated-FGD wastes (left) and waste slurries (right).

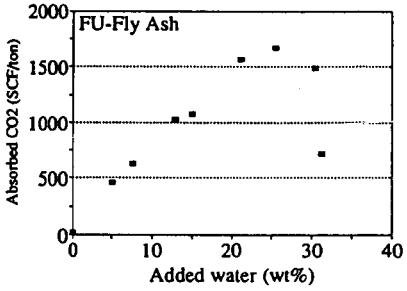

Figure 2. Absorption of CO_2 as a function of prehydration for samples of FU-FA.

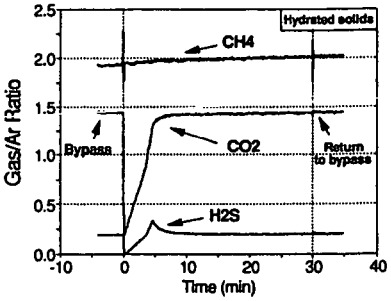

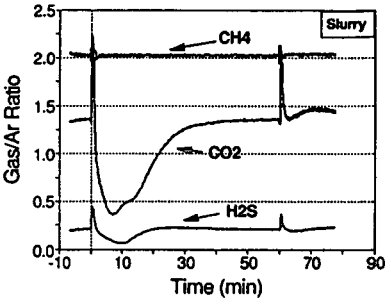

Figure 3. Absorption curves for CH_4, CO_2, and H_2S simultaneously passed through a hydrated sample (top) and aqueous slurry (bottom) of PP4.

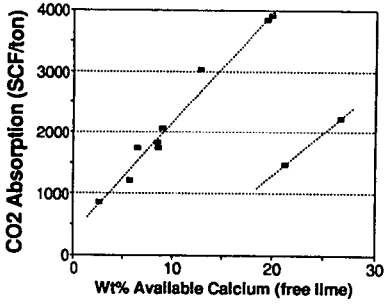

Figure 4. CO_2 absorption as a function of the available calcium. The two points on the bottom right represent samples of bed ash; all others are fly ash samples.

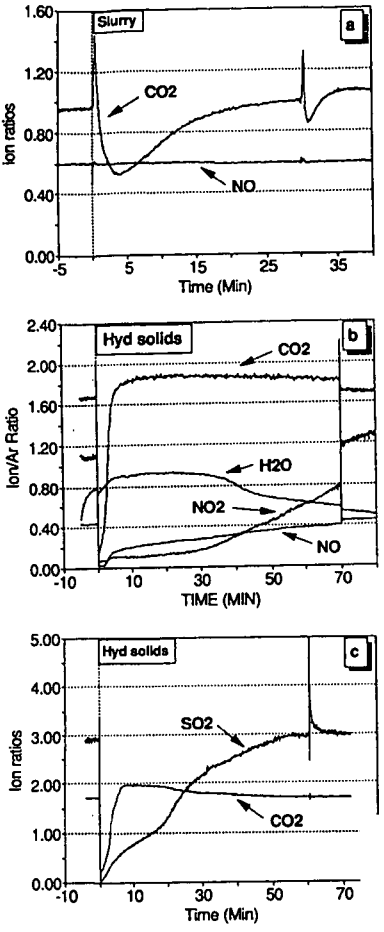

Figure 5. Test gas/Ar ion ratios for NO NO_2 (b), and SO_2 (c) during exposure hydrated PP4 (a) and PP4 slurry (b/c). C absorption shown in all three plots.

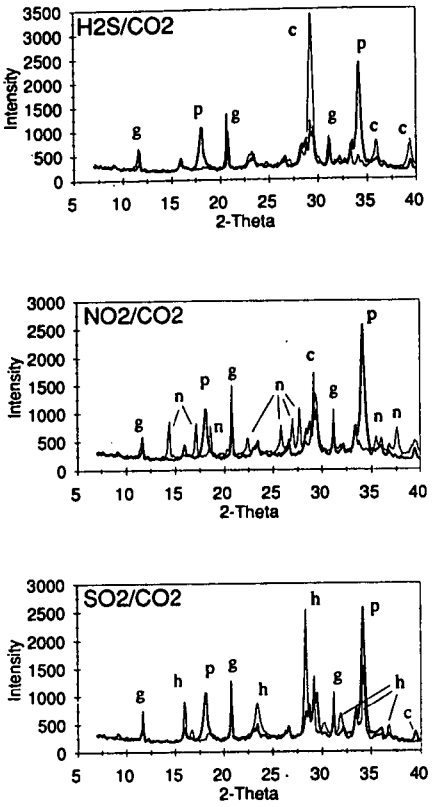

Figure 6. XRD spectra of PP4; hydrated only-darker lines; exposed sample-lighter shading. c-calcite ($CaCO_3$); n-calcium nitrate hydrate; g-gypsum ($CaSO_4{\cdot}H_2O$); h-hannebachite ($CaSO_3{\cdot}.5H_2O$); p-portlandite-($Ca(OH)_2$).

MICROANALYTICAL CHARACTERIZATION OF SLAGGING DEPOSITS IN A PILOT-SCALE COMBUSTOR

J. West and J.N. Harb
Department of Chemical Engineering and
Advanced Combustion Research Center
Brigham Young University
Provo, Utah 84602

Keywords: Slagging, coal ash deposits, SEMPC

INTRODUCTION

The purpose of this work was to characterize a set of deposit samples with respect to their compositions, phases present, and morphology. An understanding of how these properties change as a deposit grows is essential to developing a physical picture of deposit behavior, especially transitions in behavior from heterogeneous agglomerations of particles to highly sintered particles, or even a completely homogeneous molten phase that assimilates all impacting particles. Indeed, these deposit properties are of primary importance in determining the effect of deposition on heat transfer through the water wall, and on the removability of the deposit. These properties must be understood and quantified in order to predict deposition behavior.

ANALYSIS PROCEDURE

Analyses were performed on two water-wall samples from ABB-CE's Fireside Performance Test Facility (FPTF), a pilot-scale facility which operates at temperatures, heat fluxes and residence times representative of those found in full-scale units [1]. Both deposit samples were formed while firing the same U.S. Eastern Bituminous coal. The samples were cross-sectioned and prepared for analysis in a Scanning Electron Microscope (SEM). An ISIS microanalytical system equipped with X-ray and backscatter detectors was used to run a Scanning Electron Microscopy Point Counting (SEMPC) analysis [2] to determine elemental compositions at discrete points on the sample. Backscattered electron (BSE) images were also collected and evaluated, in which the brightness of a point is proportional to the atomic number of the species present at that point. Thus, in BSE images of these samples, regions with heavy elements such as iron are bright white, aluminosilicates are light grey, silicates are dark grey, and the epoxy mounting medium is black.

An important consideration in this work is the changes in deposit properties as the deposits grows, or increases in thickness. Thus, the samples analyzed were cross-sectioned, and analyses of these samples were conducted in 10-12 discrete regions of the deposit, from the initial layer to the outer region of the deposit. Since it is not possible in this forum to discuss each of the regions individually, we have chosen to discuss three regions representative of the changes taking place. Of particular interest in this study is the transition from 'inner layer' behavior to the strongly sintered outer layer, since this transition is often the one that leads to formation of tenacious or otherwise troublesome slagging deposits [3].

RESULTS AND DISCUSSION

Changes in morphology of the deposit samples provide an excellent framework from which to understand changes in other deposit properties and behavior. Figures 1, 2, and 3 are BSE images of three distinct regions of the deposit, referred to as the inner layer, intermediate region, and outer region, respectively. Both of the samples analyzed showed dramatic changes in morphology through the deposit in the direction of deposit growth. Figure 1 shows the morphology of the initial layer, which can be characterized by its small particle size and discrete and spherical particles. Immediately next to the initial layer, the particles become larger and less round and regular in shape and appearance. The intermediate region occurs as the particles show signs of sintering and/or agglomeration, as shown in Fig. 2. However, discrete Fe-rich and Si-rich particles are still evident throughout this region of the deposit. Next there occurs, in gradual increments, the increased sintering and assimilation of particles, culminating in a largely homogeneous phase at the outer region where crystallization can be observed (Fig. 3).

These changes in morphology are strongly connected to changes in the elemental and phase

compositions throughout the deposit. Figure 4 shows a triangular histogram of the compositions of Fe, Al and Si in the initial layer of the deposit, which has been normalized to elemental mole percents (not oxides). It can be seen that the bulk of the particles are kaolinite-type aluminosilicates with an Al/Si ratio of approximately one and a small amount of Fe. There are also significant amounts of Fe-rich and Si-rich particles present. Figure 5 is a ternary diagram which corresponds to the intermediate region of the deposit (Fig. 2). In this region, the deposit is heterogeneous. The number of Fe-rich and Si-rich particles has begun to decrease due to mixing with the aluminosilicate phases, resulting in the overall broadening of the range of compositions toward more Fe and Si-rich aluminosilicates. Note that the compositions are spread over a much wider region than in the initial layer. The heterogeneity is an indication of local assimilation of Fe-rich and Si-rich particles. At the outer region of the deposit, the compositions form into a more narrow band as the deposit becomes more homogeneous. A small increase in Al-rich aluminosilicates (Al/Si >1) is also observed, corresponding to the crystallization of mullite ($3(Al_2O_3)2(SiO_2)$) in the deposit.

In the samples studied, K was deposited selectively in the inner layer of the deposit. Table 1 shows the bulk elemental compositions from each of the regions analyzed, from inner to outer regions; the amount of K_2O present in the initial layer is significantly higher than that found in the deposit regions further from the wall. It should also be noted from Table 1 that, other than the initial layer, the bulk concentration remains largely constant throughout all regions of the deposit. Therefore, it is the phase distribution that changes in different regions of the deposit rather than the elemental composition.

Analysis of the distribution of K in the deposit phases shows that the amount of particles with more than 3 mole % of K decreased dramatically from the initial layer to the intermediate region of the deposit. This shift occurred as the potassium aluminosilicate particles were assimilated into other aluminosilicates. This assimilation tends to decrease the melting temperature of the resulting mixture, facilitating the assimilation of other particles and resulting in an increase in cluster size. Therefore, K-aluminosilicates played a significant role in the transition from the inner layer to the intermediate layer.

Although the elemental percent of Fe was relatively constant throughout the deposit (Table 1), the phases in which it was found changed significantly. The distribution of Fe-containing particles in the inner layer showed the presence of some Fe-aluminosilicates with relatively high amounts of iron (>10 mole %). These particles, presumably formed by coalescence of aluminosilicates and Fe-rich minerals in the coal, appeared to be assimilated early (just outside the inner layer). Iron assimilation appeared to be localized in the intermediate region of the deposit. In contrast, the iron content was much more homogeneous in the outer regions of the deposit.

CONCLUSIONS

For the coal and combustor system analyzed, the results indicate that both K and Fe have significant effects on deposition behavior in the early deposition stage. Both K and Fe act to accelerate the sintering and melting behavior of the aluminosilicates which make up the bulk of the deposit. In particular, Fe played an important role throughout the deposit, and its distribution was indicative of the extent of homogeneity of the deposit.

Through detailed microanalytical characterization of deposits from a combustor representative of a utility boiler, we have shown the presence of inherently different and distinct regions of the deposit. The transitions between these regions are the key to determining when undesirable deposit behavior is likely to occur, and are also important to determining the mechanisms which determine deposit behavior and properties in each region. Additional work is needed in this area to enhance the ability to quantify deposit behavior and properties at all stages of deposit growth and to develop mechanisms which can be applied in mathematical models to predict deposition behavior.

ACKNOWLEDGMENTS

This work was sponsored by the Advanced Combustion Engineering Research Center. Funds for this Center are received from the National Science Foundation, the State of Utah, 42 industrial participants, and the U.S. Department of Energy. We wish to thank ABB-CE for providing the samples from their FPTF.

REFERENCES

[1] Combustion Engineering, "Developing a Coal Quality Expert: Combustion and Fireside Performance Characterization Factors," Progress Report, July 1992.

[2] Jones, M.L., Kalmanovitch, D.P., Steadman, E.N., Zygarlicke, C.J., and Benson, S.A., "Application of SEM Techniques to the Characterization of Coal and Coal Ash Products" in H.L.C. Meuzelaar (Ed.), *Advances in Coal Spectroscopy*, Plenum Press, New York, 1991.

[3] Wain, T.F., Livingston, W.R., Sanyal, A., and Williamson, J., "Thermal and Mechanical Properties of Boiler Slags of Relevance to Sootblowing," in S.A. Benson (Ed.), *Inorganic Transformations and Ash Deposition During Combustion*, United Engineering Trustees, Inc., New York, 1992.

Table 1: Selected bulk elemental compositions at regions throughout the deposit (oxide mole %). Region numbers begin at the initial layer and increase through the outer region.

Region No.	Al_2O_3	SiO_2	K_2O	CaO	TiO_2	Fe_2O_3
1	34.66	50.77	3.27	1.49	1.56	6.21
2	33.37	55.9	2.13	1.24	1.6	4.65
3	33.23	53.36	1.91	2.09	1.66	6.97
4	32.85	56.36	1.59	1.64	1.48	5.57
5	31.51	56.52	1.65	1.68	1.44	6.64
6	31.77	56.92	1.68	1.36	1.45	6.28
7	32.69	56.18	1.57	1.38	1.73	5.91
8	30.96	58.35	1.44	1.31	1.5	5.85
9	31.08	56.94	1.66	1.37	1.39	7.03
10	27.96	52.56	1.33	1.4	1.24	7.85
11	30.71	57.42	1.66	1.35	1.31	7.08
12	30.75	57.67	1.74	1.5	1.47	6.43
13	31.84	56.47	1.69	1.52	1.45	6.63

Figure 1. BSE image of the initial layer of the deposit (600x).

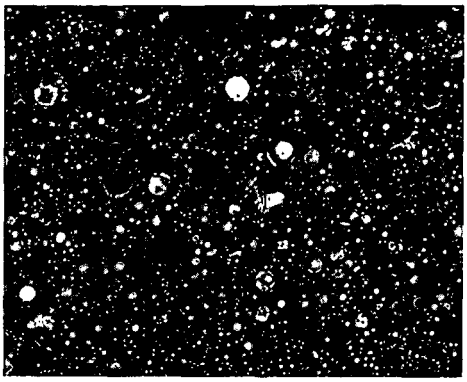

Figure 2. BSE image of the intermediate region of the deposit (300x).

Figure 3. BSE image of the outer region of the deposit (300x).

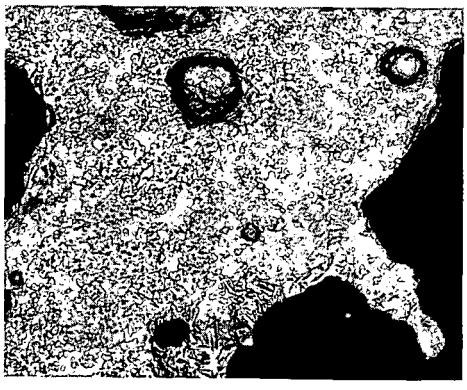

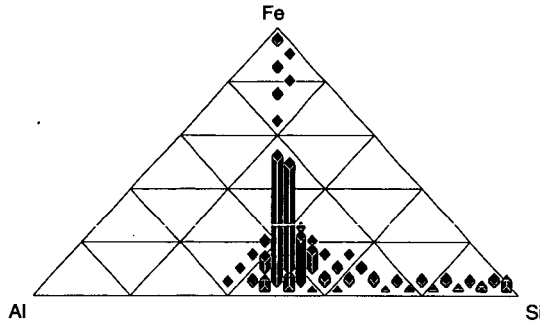

Figure 4. Frequency distribution of compositions found in the initial layer of the deposit (mole %).

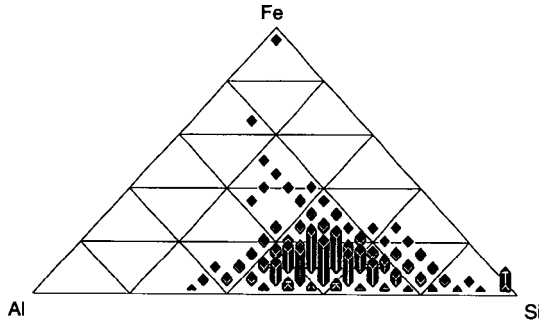

Figure 5. Frequency distribution of compositions found in the intermediate region of the deposit (mole %).

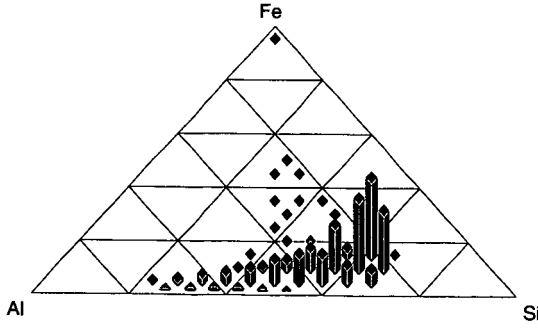

Figure 6. Frequency distribution of compositions found in the outer region of the deposit (mole %).

HYDROTHERMAL REACTION OF $CA(OH)_2$ WITH QUARTZ IN COAL

J. Wang and A. Tomita
Institute for Chemical Reaction Science,
Tohoku University, Sendai 980, Japan

G. H. Taylor
Research School of Earth Science,
Australian National University,
GPO Box 4, Canberra ACT2601, Australia

Keywords: Quartz; Coal; Demineralization

ABSTRACT

Quartz is generally most abundant as mineral matter in coal. In order to obtain fundamental information for chemical demineralization of coal with $Ca(OH)_2$, the hydrothermal reaction of $Ca(OH)_2$ with reagent quartz has been studied in detail. The results showed that the quartz was converted to various silicates, depending on autoclaving conditions. At a CaO/SiO_2 ratio of about 1, quartz was initially converted to $Ca_2SiO_4 \cdot H_2O$, then to tobermorite-like compounds, and finally to xonotlite. Higher temperature and longer reaction time are preferable to the complete conversion of quartz. The formed calcium silicates were susceptible to dissolution in acid.

INTRODUCTION

The presence of minerals in coal causes many serious disadvantages in coal utilization. A great deal of effort has been concentrated on removal of mineral matter from coal. Chemical cleaning has attracted much attention because of its high removal efficiency[1,2]. In general, however, high processing costs have been a major barrier to commercialization of these processes. We proposed a chemical leaching method by using a cheaper and less corrosive reagent, lime, for coal demineralization and found that 75% of the ash in Newstan coal could be removed from coal[3].

Among numerous mineral species present in coal, quartz, together with clays, carbonates and sulfides constitute the most common species[4]. Therefore, the understanding of the reaction between $Ca(OH)_2$ and quartz is of fundamental significance as far as coal demineralization by $Ca(OH)_2$ leaching is concerned. Although the reactions in the system of quartz/lime/water have been investigated in relation to cement and concrete production[5,6], the reactions were extremely complex and the products considerably varied with the hydrothermal conditions. The principal aim of this paper is to study the hydrothermal reaction between $Ca(OH)_2$ and reagent quartz from the standpoint of coal demineralization. On the basis of the results obtained by using pure quartz, the reaction between $Ca(OH)_2$ and quartz in coal is further examined.

EXPERIMENTAL

Pulverized lime used in this study contained 40 ± 15 % of $Ca(OH)_2$ (estimated by TG analysis) with other impurities of less than 2 %. α-Quartz (Kanto Chemical Co.) had a particle size distribution of -325 mesh: 30 %, 325-200 mesh: 68 % and 200-100 mesh: 2%.

Hydrothermal reactions were carried out at saturated steam pressures using an autoclave equipped with a stirrer. About 2.5 g of quartz powder with a pulverized lime was used for each run with 150 ml of distilled water. After being autoclaved, all specimens were dried at 105°C under a nitrogen atmosphere. The specimens were stored in tightly stoppered bottles. The coal demineralization method was in detail described elsewhere[3].

The assignment of products by X-ray diffraction (XRD) was carried out after drying at 105°C, whereas the semi-quantitative XRD analysis to determine the amount of unreacted quartz was made after heat treatment at 850°C. After this treatment, most of calcium silicates were nearly free of water and this procedure enables to evaluate the exact weight of sample on

an XRD sample holder. X-ray photoelectron spectroscopy (XPS) analysis was accomplished with Shimadzu ESCA 750 spectrometer. Scanning electron microscopes (SEM) used were Cambridge S360 with Tracor Northern EDAX equipment and Hitachi S2250N with Link System EDAX equipment.

RESULTS AND DISCUSSION

Hydrothermal reaction between $Ca(OH)_2$ and reagent quartz

Selected X-ray diffraction patterns for the samples obtained at 300°C are illustrated in Figure 1. Table 1 lists the reaction products obtained at various temperatures with a CaO/SiO_2 molar ratio of 0.93 ± 0.02. At 175°C, the major product was $Ca_2SiO_4 \cdot H_2O$ ($C_2S\bar{W}(A)$ according to Eitel's nomenclature[7]). Some other weak peaks were difficult to be identified, however they were probably due to compounds similar to tobermorite ($Ca_4Si_5O_{14} \cdot 5H_2O$)[5]. At 250°C and 300°C, the major product was also $Ca_2SiO_4 \cdot H_2O$ during a relatively short period of time, but tobermorite-like compounds were more distinct than at 175°C especially after 5 h. At 7 h, the XRD intensity for a new phase, xonotlite, became very strong and the peak for $Ca_2SiO_4 \cdot H_2O$ almost disappeared at both temperatures. When the temperature was raised up to 340°C, the tendency of the changes of products with time was virtually the same as observed for 300°C, although the reaction became more prompt. Only xonotlite was observed after 5 h.

The variations of quartz conversion with time during autoclaving at different temperatures are shown in Figure 2. When the autoclaving at 175°C was prolonged up to 12 h, about half of quartz was converted and $Ca(OH)_2$ disappeared completely (Table 1). A higher temperature is necessary to convert the rest of quartz. At higher temperatures, the quartz conversion took place in two stages. The first stage was a relatively rapid reaction in which the main reaction was the formation of $Ca_2SiO_4 \cdot H_2O$. Thus, it can be said that at a CaO/SiO_2 molar ratio of about 1, this stage roughly terminated when half of quartz was converted. In the second stage, the main reactions were the transformation of $Ca_2SiO_4 \cdot H_2O$ to tobermorite-like compounds and/or xonotlite. These reactions were relatively slow compared with the formation of $Ca_2SiO_4 \cdot H_2O$.

XPS analysis was used to determine the binding energy of Si_{2p} in reagent quartz and in two treated samples (No. 9 and No. 13 presented in Table 1). The XPS spectra showed that the chemical environment of Si greatly changed due to the formation of $Ca_2SiO_4 \cdot H_2O$ and xonotlite. This change may be related to greater solubility of the products in acidic solution.

Interaction between $Ca(OH)_2$ and quartz in coal

Newstan coal was taken as an example. The properties of this coal were presented previously[3]. The examination of this coal, by XRD analysis and SEM-EDAX analysis, showed that quartz and clay were dominated mineral phases in the original coal. When the coal was subjected to $Ca(OH)_2$ leaching followed by a dilute HCl washing, the XRD analysis showed that most of quartz could be removed. Figure 3 is the SEM-EDAX analysis of a treated sample obtained at 320°C and 1.5 h by use of 5% CaO before acid washing. The observed particle was strongly attacked by $Ca(OH)_2$, forming Ca-bearing phases. Elements in spot A were mainly Ca and Si, which might be a calcium silicate derived from the reaction between $Ca(OH)_2$ and quartz. The rich elements in Spot B were Ca, Si and some Al. This observation suggests another important reaction occurring between $Ca(OH)_2$ and clays in coal. The SEM analysis of the acid-washed sample indicated that the Ca-bearing silicate products were removed by the acid solution. After the acid-washing of the treated sample, the ash content was reduced from 9.2 % of the original coal to 2.6 %. As can be seen from Figure 2, the above autoclaving condition (320°C, 1.5 h) was not enough for a complete removal of quartz. Thus we tried to use a longer reaction time for demineralization of Newstan coal. The treatment at 300°C for 7 h produced a clean coal with much lower ash content, 1.0 %.

CONCLUSION

1. Upon the hydrothermal reaction with $Ca(OH)_2$, quartz formed various hydrated calcium silicates, depending on the autoclaving conditions. Increasing temperature from 175°C to 340°C significantly accelerated the reaction.

2. At a CaO/SiO_2 ratio of about 1, the reaction between $Ca(OH)_2$ and quartz initially resulted in $Ca_2SiO_4 \cdot H_2O$. As the reaction proceeded, $Ca_2SiO_4 \cdot H_2O$ progressively reacted with residual SiO_2 to form tobermorite-like compounds. Final product at higher temperature and longer time was xonotlite. Through these reactions, quartz could be completely converted to calcium silicates.

3. Quartz was a major mineral phase in Newstan coal. During the leaching of this coal, the quartz was reacted by $Ca(OH)_2$ forming Ca-bearing phases, which was removed by dilute HCl washing. The ash content could be reduced from 9.2 % to 1.0 %.

ACKNOWLEDGMENTS

The authors thank Dr. Y. Kobayashi of Tohoku University for many helpful discussions. New Energy and Industrial Technology Development Organization are also acknowledged for the financial support (International Joint Research Grant).

REFERENCES

1. Wang, Z. Y.; Ohtsuka, Y.; and Tomita, A. *Fuel Process. Technol.* **13**, 279-289 (1986).
2. Waugh, A. B.; Bowling, K. McG. *Fuel Process. Technol.* **9**, 217-233 (1984).
3. Wang, J; Kobayashi, Y; Tomita, A; Zhang, Z. G. *Proc. 8th International Conference on Coal Science*, Oviedo, Spain, 1995.
4. Jenkins, R. G. and Walker, P. L. Jr. in "Analytical Methods for Coal and Coal Products II"; Karr, Jr. C. Eds.; Academic Press, New York, 1979, 265-314.
5. Ahmed, A. H. M. and Taylor, H. F. W. *J. Appl. Chem.*, **19**, 245-246 (1969).
6. Kalousek, G. L. *J. Amer. Concrete Inst.*, **6**, 889-1011 (1955).
7. Eitel, W. "Silicate Science IV"; Academic Press: New York, 1966: p. 260.

Table 1. Products of hydrothermal reactions of $Ca(OH)_2$ with quartz at a CaO/SiO_2 molar ratio of 0.93.

No.	Conditions		Products*				
	Temp. (°C)	Time (h)	SiO_2	$Ca(OH)_2$	A	T	X
1	175	3	vs	m	s	w	-
3	175	7	vs	s	s	w	-
4	175	12	s	-	vs	w	-
5	250	1.5	vs	s	s	w	-
6	250	3	vs	w	s	m	-
7	250	5	s	-	vs	m	-
8	250	7	s	-	-	m	vs
9	300	1	vs	s	s	w	-
11	300	3	s	w	vs	w	-
12	300	5	m	-	s	m	s
13	300	7	-	-	-	-	vs
14	340	0.75	vs	w	s	s	-
17	340	5	-	-	-	-	vs

* A: α-Dicalcium silicate hydrate ($Ca_2SiO_4 \cdot H_2O$); T: Tobermorite-like compounds; X: Xonotlite ($Ca_6Si_6O_{18} \cdot H_2O$). vs: very strong; s: strong; m: medium; w: weak.

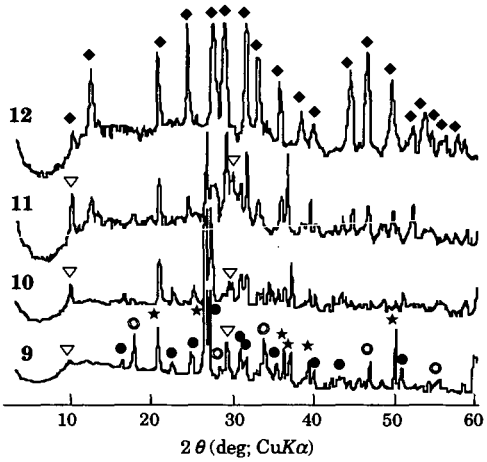

Figure 1 XRD patterns of the specimens obtained at 300°C. The sample numbers indicated correspond to those in Table 1. ●: $Ca_2SiO_4 \cdot H_2O$; ★: Quartz + $Ca_2SiO_4 \cdot H_2O$; ◎: $Ca(OH)_2$; ▽: Tobermorite-like compounds.

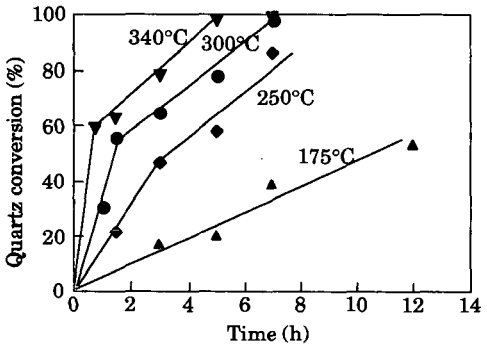

Figure 2 Quartz conversion during the hydrothermal reaction at a CaO/SiO_2 molar ratio of 0.93.

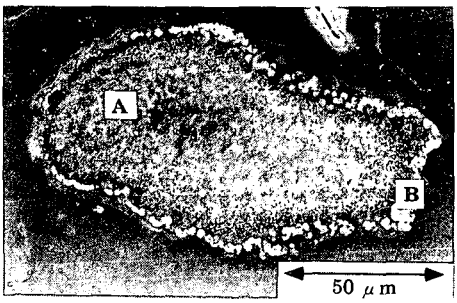

Figure 3 Scanning electron micrograph of mineral matter in coal after the reaction with $Ca(OH)_2$.

BEHAVIOR OF IRON BEARING MINERALS IN THE EARLY STAGES OF PULVERIZED COAL CONVERSION PROCESSES

Hari Babu Vuthaluru, Simon Eenkhoorn, Gerrit Hamburg and Peter Heere
Netherlands Energy Research Foundation ECN, Business Unit ECN Fossil Fuels
P.O. Box 1, 1755 ZG Petten, The Netherlands

Keywords: combustion, gasification, pyrite

ABSTRACT
Early stage transformations and deposition of iron bearing coal minerals, in particular pyrite (FeS_2) were studied. An atmospheric lab-scale facility was used to simulate the near burner environments in two different coal conversion processes: i) Low-NO_x pulverized fuel combustion and ii) Entrained-flow gasification. Particle sampling showed that for both environments, the pyrite was transformed quickly to pyrrhotite (FeS). In the deposition experiments this pyrrhotite impacts on the substrates.
In the deposition experiments, the chemical composition and the morphology of the slags formed under the two conditions showed clear differences. Special attention was payed to the role of sulphur. Based on these (preliminary) experiments, a mechanistic model is proposed for the transformations of pyrite in both pulverized coal conversion systems. Furthermore a description is given of a new experimental setup for future work at elevated pressures (up to 20 bar) to enable a closer simulation of pressurized entrained-flow coal gasification processes.

INTRODUCTION
In the Netherlands, oxygen-blown entrained-flow gasification has been selected as the most promising technology for large scale coal-based power generation. This is mainly due to its fuel flexibility, high efficiency and relatively low environmental impact. The world's first fully integrated Gasification Combined Cycle (IGCC) demonstration plant (250 MWe) based on (Shell) gasification technology is currently in operation in Buggenum.

To support and ensure a successful introduction of IGCC and other new coal-based power generation technologies, the coal-related research at ECN is extended to include these technologies. To this purpose, the staged flat flame burner concept has been adapted which was successfully applied earlier to simulate (low-NO_x) pulverized coal combustion conditions accurately on a laboratory scale (1,2). The atmospheric test facility was reconstructed from an open up-fired to a closed down-fired system, where the off-gases are flared. The facility was renamed as the Atmospheric Entrained-Flow Gasification and Combustion simulator (AEFGC-simulator). The coal/mineral particles are carried along in the combustion gas and thus the high initial temperatures and very rapid particle heat-up in both combustion and gasification can be simulated in this facility.

For entrained-flow gasification conditions, the mechanism of the formation of slags was explored by depositing the mineral particles onto alumina plates, simulating gasifier wall. The plates were held at a temperature of around 1450 °C, characteristic for that of the wall in an actual entrained-flow gasifier (3). Experience with slag production in the reducing environment of low-NOx burners (4,5) was used in the evaluation of the results.

EXPERIMENTAL
Laboratory-scale test facility
The test facility is an entrained-flow reactor with an integrated, premixed and multistage flat flame gas burner. A schematic view of the simulator is given in Figure 1. The burner consists of two sub-burners viz. an inner burner (10.9 mm) and an outer burner (60.7 mm). A tertiary gas stream (consisting of nitrogen) is applied to create suitable mixing profiles and to protect the tube from the hot secondary gas stream. Coal/char particles are fed through the inner burner and undergo rapid heating (> 10^5 °C/s) up to the high temperature level of the near-burner zone in the actual process. The particles are fed at a feed rate of approximately 1 g/h by means of a rotating brush feeder (4). The gas/particle flow is confined to a 76 mm ID (ceramic) reactor tube with a length of 550 mm. The tube is surrounded by a controllable heating section equipped with Kanthal Super 33 elements to create the required temperature history for the particles.

Coal choice
The experimental work has been performed with pyrite rich coal (Prince coal, Canada). Coal with a high content of iron minerals (pyrite) was chosen because iron is known to react with the reducing gasifier gas. Narrow size fractions (pyrite enriched) were used in the experiments. The specifications of this coal and preparation techniques have been described in detail elsewhere (4).

Sampling and analysis
Sampling of in-flame particles was carried out with a quench probe followed by a cyclone and a filter. Ash particles were sampled isokinetically from the hot gas at distances corresponding to residence times of 90, 120, 170 ms using a helium-fed quench probe under entrained-flow gasification conditions. However, for combustion conditions, ash particles were sampled at distances corresponding to residence times of 18, 22, 50 and 120 ms. Experimental conditions used in the present investigations are given in Tables 1 and 2. The samples were analyzed with SEM with simultaneous characterization of composition and morphology. In addition, a deposition probe was used for slagging tests. On this probe different substrate materials (high grade Al_2O_3 and SIC) were placed to simulate wall surface material. The plates were placed at distances corresponding to residence times of 50ms for combustion conditions and 90, 120, 170ms for gasification conditions. The plates were held in the particle stream for 15 minutes at a furnace wall temperature of 1500 °C. After completion of the test, cold helium gas was introduced along the plates via the tip of the probe holder. Perpendicular cross-sections through the deposit plates and attached deposits were examined with SEM for internal

structure. Single spots and complete layers were analyzed. Elemental mapping was also performed to obtain the profile for a given element in the layer. The measured gas temperatures for both low-NO_x combustion and entrained-flow gasification conditions are as shown in Figure 2.

RESULTS

Both the results obtained for low-NO_x combustion and entrained-flow gasification conditions are detailed in the following sections.

Ash formation experiments

Analysis of ash particles formed under entrained-flow gasification revealed the formation of cenospheres, clusters (50-60 μm) and some skeletal structures. Several small fragments were also found which consisted of Al, Si, Fe and K. Similar ash particles were formed under low-NO_x combustion conditions.

Figure 3 summarizes the measured sulphur to iron ratios both under simulated low NO_x conditions, as extracted from earlier work (5), and simulated entrained-flow gasification conditions. The measured ratio of S/Fe present as pyrite in the coal is shown in the figure for comparison purposes. From the figure it can be observed that for combustion conditions the pyrite transforms quickly to pyrrhotite (FeS) in 20 ms. At increasing residence times a further transformation to FeOS or FeO found to occur. For entrained-flow gasification, also a quick transformation to pyrrhotite occurs. However, here the pyrrhotite appears to be remain stable at longer residence times. Nevertheless, it should be noted that the gasification experiments were conducted with 1% H_2S in the gas, while no sulphur compound was added in the combustion experiments.

Deposition experiments

Low-NO_x combustion

Figure 4 shows the internal structure of the deposit. Elemental analysis closer to the plate showed enrichment in Al. This strongly suggests interaction of slag with substrate material (Alsint). The crystals at the top and bottom are spinels (iron-alumina). These deposits consisted of several dendrites enriched in iron were found (Figure 4). The iron enrichment in the top and first layer is presumably due to preferential crystallization of iron-alumina spinel at these regions. The slag matrix (second layer) was enriched in silicon. Analysis of the deposits showed no sulphur.

Entrained-flow gasification

Figure 5 shows the cross-sectional view of the deposit plate and the deposits collected at three locations within the reactor. All the deposits contained several bubbly regions. Slag flow was observed for the deposits collected at two locations (viz. 270 mm, 370 mm) within the reactor. However, for the deposits collected at a distance of 520mm, no slag flow was observed along the sides of the deposit plate. This is probably due to misalignment of the probe within the reactor. In addition, changing gas environments may have led to this sort of slag flow behavior. This requires further attention. The slag matrix in all deposits was rich in Fe, Si, Al and small proportions of O. Also some interaction of iron with SiC substrate material was seen. Especially the analysis of the white spots (see Figure 5a) at the interface revealed Fe and Si. No sulphur was found in the deposits.

MECHANISTIC MODEL FOR PYRITE TRANSFORMATIONS

Observed flame transitions of pyrite under low NO_x combustion and entrained-flow gasification conditions are shown in Figure 6. It appears from the experimental results that the first reaction process is not oxidation but decomposition of pyrite into pyrrhotite in both processes (see Figure 3). This may be explained by the evolution of sulphur gas which prevents the oxygen from reaching the particles (6). The rapid melting of the pyrrhotite was evidenced by the rounded shape of the collected particles. Overall, the present test results indicate that the final product for low NO_x combustion being Fe_2O_3 whereas for entrained-flow gasification Fe is the final product.

Although our preliminary experiments have shown that both combustion and gasification processes can be realized in the AEFGC-simulator, it would be more appropriate to conduct the gasification tests at elevated pressures. To enable these experiments at elevated pressures (up to 20 bar), new experimental facility based on the same concept has been built (the so-called Pressurized Entrained-Flow Gasification simulator). Commissioning work of this facility is currently in progress and it will be available for carrying out experiments at elevated pressures early 1996.

CONCLUSIONS

Preliminary experiments have shown that both the low-NO_x combustion and entrained-flow gasification experiments can be realized in the AEFGC-simulator. Irrespective of the gas conditions prevailing within the reactor, the deposits did not contain sulphur. Ash particles collected in the vicinity of the burner before deposition showed sulphur in the sample, suggesting the transformation of pyrite to pyrrhotite. Upon deposition the sulphur in pyrrhotite appeared to be released from the slag into the gas phase. End products in the slag for both low NO_x combustion and entrained-flow gasification processes were determined to be Fe_2O_3 and Fe respectively.

ACKNOWLEDGEMENTS

The authors acknowledge the financial support from the European Community under the Joule II Extension Program for the project "Slagging in Low-NO_x Combustion and Entrained-Flow Gasification". The authors are also thankful to Dr. H.M. ten Brink and Dr. J.H.A. Kiel for their valuable suggestions.

REFERENCES

[1] H.M. ten Brink, S. Eenkhoorn and G. Hamburg: *Slagging in entrained-flow gasification and low-NO_x firing conditions.* In: Proc. Engineering Foundation Conference on 'The Impact of Ash Deposition on Coal Fired Plants', June 20-25, 1993, Solihull, U.K. (ed. Williamson, J. and Wigley, F., UK, 1994), pp 113-122.

[2] H.M. ten Brink, S. Eenkhoorn and M. Weeda: *Flame transformations of coal-siderite.* In: Proc. Engineering Foundation Conference on 'The Impact of Ash Deposition on Coal Fired Plants', June 20-25, 1993, Solihull, U.K. (ed. Williamson, J. and Wigley, F., UK, 1994), pp 373-383.
[3] R. Wetzel: *PRENFLO-Pressurized Entrained-Flow Coal Gasification. Final Report Phase 2,* Report EUR 13091 EN, 1990.
[4] H.M. ten Brink, S. Eenkhoorn and G. Hamburg: *Flame-transformations of coal-pyrite,* ECN-report ECN-RX--95-037 [1995]. Also submitted to Fuel (July, 1995).
[5] H.M. ten Brink, S. Eenkhoorn and G. Hamburg: *A mechanistic study of the slag formation from iron-rich coals,* ECN-report ECN-RX--95-041 [1995]. Also submitted to Fuel Processing Technology (August, 1995).
[6] Srinivasachar, S. and A.A. Boni: *A kinetic model for pyrite transformations in a combustion environment,* Fuel 1989, 68, 29.

Table 1: Gas mixtures before combustion (gas flows in ln/min)

	Low-NO_x combustion		Entrained-flow gasification	
	Inner Burner	Outer burner	Inner Burner	Outer burner
CH_4	0.133	3.98	0.5	0.2
CO				15
CO_2			1.56	
O_2			1	1.67
H_2S			0.008	
Air	1.0	30.0		

Table 2: Experimental conditions

	Low-NO_x combustion	Entrained-flow gasification
Particle feed rate (in g/h)	1	1
Furnace temperature (°C)	1500	1450
Sampling residence times (ms) sample 1 sample 2 sample 3 sample 4	 18 22 50 120	 90 120 170 -
Deposit substrate	High grade Al_2O_3	High grade SiC
Deposit plate	15mm x 50mm, 2mm thick	15mm x 50mm, 2mm thick
Deposit formation time (min)	15	20

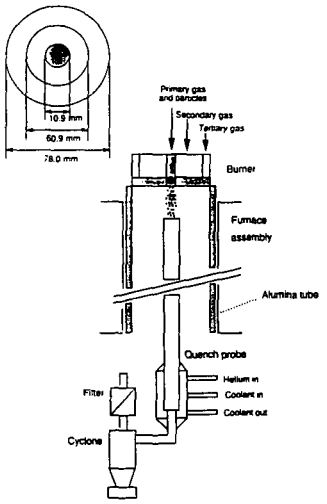

Figure 1: Atmospheric Entrained-Flow Gasification and Combustion simulator (AEFGC-simulator).

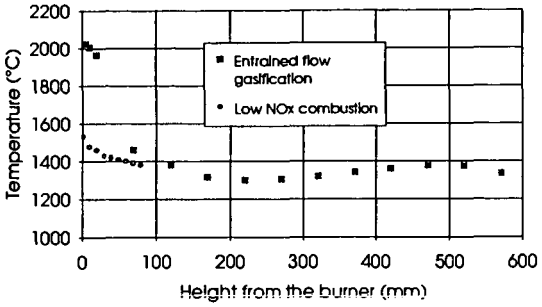

Figure 2: Measured gas temperature profiles within the reactor.

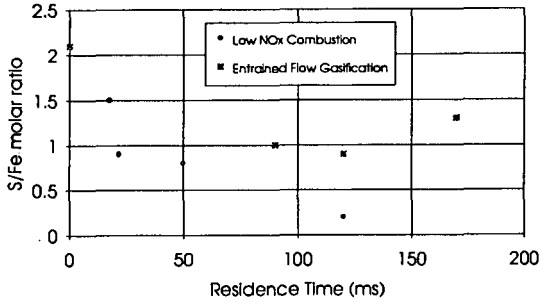

Figure 3: Sulfur to iron molar ratio against reaction time.

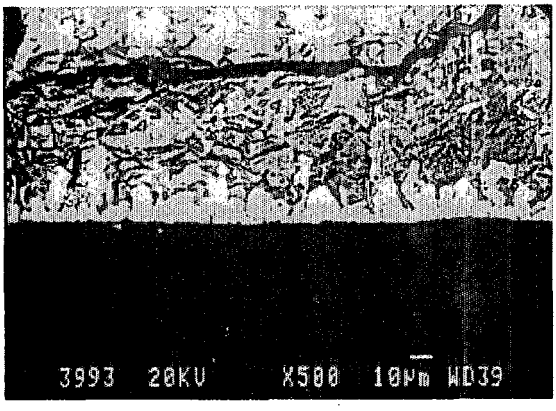

Figure 4: Cross-section perpendicular through the deposit plate (combustion experiments)

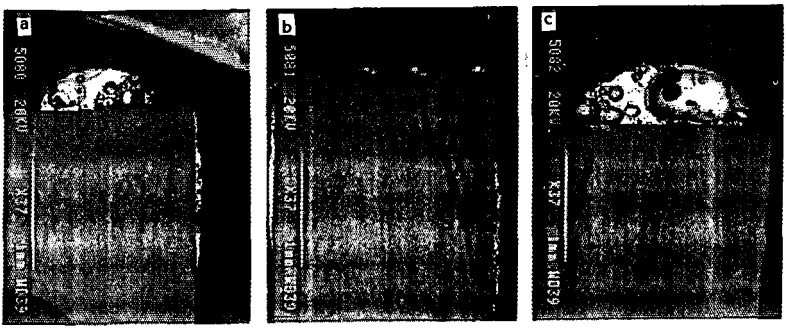

Figure 5: Cross-section perpendicular through the deposit plate (gasification experiments) at different probe locations. a) 270mm; b) 370mm; c) 520mm.

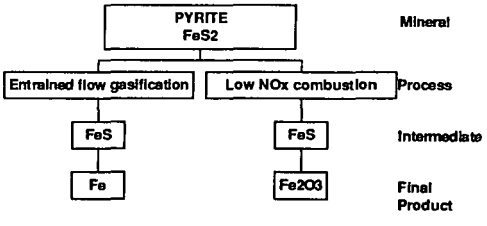

Figure 6: Mechanistic model for pyrite transformations

RELATIONSHIPS BETWEEN MAJOR INORGANIC ELEMENTS AND MINERALS IN COALS FROM THE ASHIBETSU DISTRICT, ISHIKARI COAL FIELD, JAPAN

Tatsuo Kimura
Energy Resources Department
National Institute for Resources and Environment
16-3 Onogawa, Tsukuba-shi, 305 Japan

Keywords: Minerals, Major inorganic elements, Correlation coefficient

INTRODUCTION

Information from both mineralogical and elemental analyses of coal is important for coal utilization technologies such as combustion, gasification, liquefaction, and coking, as well as for environmental considerations. The analyses have often been carried out separately. However, a combination of both analyses would bring more fruitful results than separate analyses concerning the nature of the mineral matter in coal. Two methods of coal sample collection for both analyses are available: collection of various kinds of coal samples on rank from different locations and collection of coal samples from different coal seams at the same location. The former method provides a wide range of information on coal mineral phases and elements and the latter provides precise specification of coal mineralogical and elemental characteristics. The goal of this study was to explore the relationships between major inorganic elements and mineral phases in coals by analyzing samples from different coal seams in the Ashibetsu district, Ishikari coal field, Japan. The geochemical implications of mineral abundances were previously reported (1-3).

ANALYTICAL PROCEDURES

Coal samples were hand picked along vertical transects from near roof to near floor at seven coal pit faces of six coal seams. Coal samples containing less than 40% ash were selected. Minerals were identified by X-ray diffraction analysis of the low-temperture ashes (LTA) obtained by ashing powdered coal samples in an oxygen plasma reactor. The major inorganic element (Si, Al, K, Ti, Na, Mg, Ca, Fe, Sr, P, F, and Cl) and total sulfur contents were determined by X-ray fluorescence analysis.

RESULTS AND DISCUSSION

Kaolinite and quartz are the most dominant silicate minerals in coals from the Ashibetsu district (Table 1), and were found from the very lowest ash to the highest ash coals. The silicate minerals, plagioclase, illite, illite/smectite (I/S) mixed-layer clay minerals, smectite and K-smectite were also found, but chlorite is very rare. Calcite and ankerite are the most dominant carbonate minerals. They occur as cleat and fracture fillings (3). Carbonates also occurred as siderite, dolomite (Fe-dolomite) and aragonite. Siderite and dolomite are syngenetic minerals which occur as aggregates of fine nodules (3). Pyrite was abundant in only one coal seam and marcasite was very rare. The low abundance of pyrite suggests that most of these coal seams were formed under fresh water environments. Gypsum, which was identified as bassanite or anhydrite in the LTA, and other five iron sulfate minerals occur in some coal samples as a result of weathering of pyrite. Apatite was present in more than 60% of the coal samples, and was sometimes accompanied by goyazite. Some coal samples contained boemite.

The high correlation coefficients between all pairings of ash, Si, Al, K, Ti, and Na (Table 2) indicates that these five elements are associated with silicate minerals. The correlation coefficient between Si and ash contents is the highest because Si is contained in quartz and all aluminosilicate minerals in the coal samples. Most of the Al is associated with aluminosilicate minerals, although a minor fraction is also associated with goyazite and boehmite.

The ash and K contents (Fig. 1) of the coal samples containing K-bearing clay minerals (illite, K-smectite, and/or I/S mixed-layer clay minerals) were closely correlated, indicating that K is contained as an interlayer cation in these clay minerals. The Al and Ti contents (Fig. 2) were closely correlated (correlation coefficient 0.83). Ti is thought to substitute for Al in clay minerals and the maximum amount of Ti substituted for Al was 12.5%. Several studies (4-7) have already pointed out that the correlation coefficients between any pair of ash, Si, Al, K, and Ti are high and that these elements are associated with silicate minerals in coal. However, the mineral species associated with these elements have not previously been determined.

Relatively high correlation coefficients for Na with ash, Si, Al, K, and Ti suggest that the Na content reflects the existence of Na-bearing minerals such as plagioclase, smectite, and I/S mixed-layer clay minerals. The weight ratio of Na to ash is higher for the coal samples containing two or three Na-bearing minerals than for those containing one Na-bearing mineral.

Fig. 3 shows ash versus Mg. The Mg and ash contents of the coal samples containing Mg-bearing clay minerals (illite, I/S mixed-layer clay minerals, smectite, K-smectite, and/or chlorite) were closely related.

The frequencies of mineral occurrences in the coal samples (see Table 1)

suggests that Mg is primarily associated with carbonate minerals and to a lesser extent associated with Mg-bearing clay minerals (Fig. 3). Most of the Ca exists in calcite and ankerite, although some occurs in apatite, dolomite and plagioclase. The great abundance of ankerite resulted in a comparatively high correlation coefficient (0.63) between Ca and Mg. Most of the coal samples contained less than 1.5% Ca and less than 0.2% Mg (Fig. 4).

The average Ca, Mg and Fe contents in the coal samples containing only calcite and ankerite as the Ca-, Mg-, and/or Fe-bearing minerals are 0.895% (29 samples), 0.097% (45 samples), and 0.290% (43 samples) respectively. Both the Ca and Mg contents of these coal samples are estimated to be approximately the same as those in recent plants (8). However, the Fe content is higher in these coal samples than those in recent plants and approximately the same as those in recent peats (8). This result implies that Ca, Mg and Fe in both calcite and ankerite could originate from the organic materials of plants and peats.

The coal samples have been classified based on their Mg and Fe contents into three groups (Fig. 5): (1) samples plotting along the Fe-axis (solid circles), (2) samples distributed diagonally from the origin (diamonds) and (3) samples containing moderately increasing Fe content with increasing Mg content (open circles). Fe in the first group is mostly associated with pyrite. Siderite and ankerite were the Fe-bearing carbonate minerals in the second group with the exception of one coal sample, which contained dolomite instead of ankerite. Ankerite was the only Fe-bearing carbonate mineral found in coal samples from the third group. The slope of the Fe to Mg weight ratio of samples from the third group almost matched that in ankerite. The difference between the slopes of the second and third groups is due to the presence of siderite in the third group, proving that the siderite in the coal samples is Mg-bearing siderite.

Fe occurs both in carbonate minerals (ankerite and siderite) and Fe in pyrite, marcasite and iron sulfate minerals. The high correlation of Fe with S is caused by several samples which contained higher amounts of pyrite and iron sulfate minerals.

A substantial number of the coal samples were rich in both P and Sr (Fig. 6). P occurs as apatite and goyazite but Sr occurs only as goyazite. As P and Sr show a high correlation coefficient (0.92), these two phosphate minerals are thought to be of similar origin. A similar correlation between P and Sr was reported for Eastern Tennessee coals (4).

No close correlation between F and P was observed. Since the P content as goyazite is evaluated by Sr content, the P content as apatite can be evaluated by subtracting the P content as goyazite from the total P content. The relationship between P content as apatite and F content (Fig. 7) has a straight line, indicating that fluorapatite is present. Apatite is thought to exist mostly as fluorapatite since most of the coal samples contain enough F to form fluorapatite. The remainder of the F is believed to be organically bound.

The Cl content in the coal samples was less than 0.04%. Fig. 8 shows Na versus Cl. Both inorganic and organic Cl appear to exist although the total Cl content is low. The correlation coefficients of Cl for Na, the other silicate related elements and ash are relatively high, suggesting that a certain amount of inorganic Cl is included in the coal samples. The correlation coefficient between Na and Cl increased with increasing Na-bearing clay mineral (smectite and/or I/S mixed-layer clay mineral) content, suggesting that inorganic Cl was incorporated into the coal seams by these clay minerals. Since the minimum Cl content was around 0.01% as the Na content approaches 0 (Fig. 8), at least up to about 0.01% of the Cl appears to be organically bound.

CONCLUSIONS

The major inorganic elements studied in the coal samples from the Ashibetsu district have been classified with respect to mineral sources. Si, Al, K, Ti and Na are associated with silicate minerals. K occurs as an interlayer cation in clay minerals. Mg is mostly associated with carbonate minerals and partly with clay minerals. Most of the Ca exists as calcite and ankerite, although part of the Ca exists as apatite. Fe was primarily found in carbonate minerals and pyrite. A minor fraction of the Al was associated with goyazite and boehmite. P occurs as fluorapatite and goyazite and Sr also occurs as goyazite. F exists not only as fluorapatite, but also appears to be organically bound. Cl also appears to exist in both inorganic and organic forms. Inorganic Cl is thought to be incorporated into the coal seams by clay minerals.

REFERENCES

1. T. Kimura and M. Kubonoya, Mining Geol., 41, 297-312(1991) (in Japanese).
2. T. Kimura and M. Kubonoya, Resource Geol., 44, 419-428(1994) (in Japanese).
3. T. Kimura and M. Kubonoya, Resource Geol., 45, 99-109(1995) (in Japanese)
4. L.A. Harris, H.E. Barrett and O.C. Kopp, Int. J. Coal Geol., 1, 175-193(1981).
5. A.E. Dorsey and O.C. Kopp, Int. J. Coal Geol., 5, 261-274(1985).
6. P.C. Lindahl and R.B. Finkelman, In Mineral Matter and Ash in Coal; K.S. Vorres, ed; ACS Sym. Ser. 301, Amer. Chem. Soc., Washington, DC, 61-69(1986).
7. G.O. Asuen, Int. J. Coal Geol., 9, 171-186(1987).
8. D.J. Casagrande and L.D. Erchull, Geochim. Cosmochim. Acta, 1391-1394(1977).

Table 1 Frequency of mineral occurrence in coal samples containing less than 40% ash.

Coal seam	-600 m L					-695 m L		Total
	Torakawa	Torashita -sanshaku	No.10	Upper No.8	No.8	Torashita -nishaku	No.8	
Thickness (cm)	165	156	105	366	71	115	452	
Number of samples	10	6	9	12	8	9	20	74
Silicates								
Quartz	10	5	8	10	8	8	14	63
Plagioclase	9	0	1	0	1	0	1	12
Kaolinite	10	6	9	12	8	9	19	73
Illite	1	0	0	4	2	1	1	9
Illite/smectite mixed -layer clay minerals	5	0	0	4	2	1	1	13
Smectite	5	0	1	0	0	0	0	6
K-smectite	6	0	2	0	0	0	0	8
Chlorite	0	0	0	0	0	1	0	1
Carbonates								
Calcite	9	6	9	3	8	8	19	62
Aragonite	0	0	0	0	3	0	0	3
Ankerite	6	3	9	6	7	3	19	53
Siderite	2	2	0	2	3	1	5	15
Dolomite	0	0	0	3	0	0	0	3
Sulfides								
Pyrite	0	6	2	1	0	4	5	18
Marcasite	0	1	0	0	0	0	0	1
Sulfates								
Gypsum	0	6	2	0	0	0	1	9
Melanterite	0	1	0	0	0	0	1	2
Szomolnokite	0	0	0	0	0	0	1	1
Conquinbite	0	0	0	0	0	0	1	1
Roemerite	0	0	0	0	0	0	1	1
Hydronium jarosite	0	0	0	0	0	0	1	1
Phosphates								
Apatite	8	1	5	8	5	6	13	46
Goyatzite	2	0	0	5	3	3	4	17
Boehmite	1	0	0	1	5	5	12	24

Table 2 Correlation coefficients for coal samples containing less than 40% ash.

	Si	Al	K	Ti	Na	Mg	Fe	Ca	Sr	P	Cl	F	S
Ash	0.96	0.72	0.75	0.64	0.61	0.31	0.08	0.25	0.15	0.25	0.49	0.01	0.08
Si		0.61	0.72	0.57	0.58	0.25	0.09	0.18	0.03	0.11	0.49	0.02	0.05
Al			0.77	0.83	0.58	0.05	0.09	0.11	0.43	0.50	0.38	0.15	0.04
K				0.68	0.16	0.12	0.05	0.08	0.20	0.45	0.07	0.13	
Ti					0.48	0.00	0.00	0.07	0.24	0.41	0.38	0.18	0.07
Na						0.16	0.13	0.03	0.12	0.22	0.66	0.26	0.13
Mg							0.26	0.63	0.15	0.13	0.11	-0.23	0.17
Fe								0.11	0.19	0.15	0.20	-0.17	0.81
Ca									0.09	0.17	0.12	-0.17	0.02
Sr										0.92	0.18	0.22	0.11
P											0.28	0.29	0.07
Cl												0.42	0.24
F													-0.17

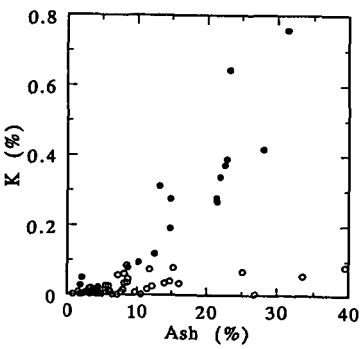

Fig. 1 Relationship between ash and K contents. Solid circle=coal samples containing K-bearing clay minerals.

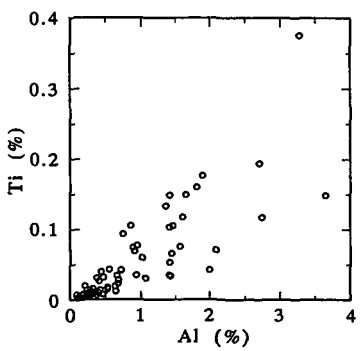

Fig. 2 Relationship between Al and Ti contents.

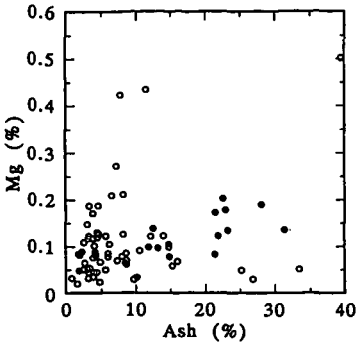

Fig. 3 Relationship between ash and Mg contents. Solid circle=coal samples containing Mg-bearing clay minerals.

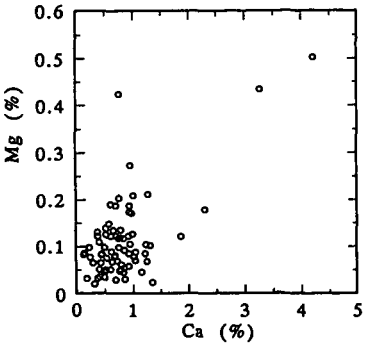

Fig. 4 Relationship between Ca and Mg contents.

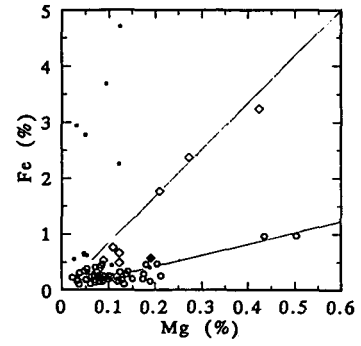

Fig. 5 Relationship between Mg and Fe contents. Solid circle, diamond, solid diamond, open circle=coal samples containing pyrite, both siderire and ankerite, both siderite and dolomite, and ankerite, respectively.

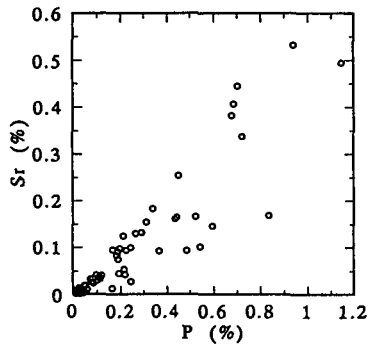

Fig. 6 Relationship between P and Sr contents.

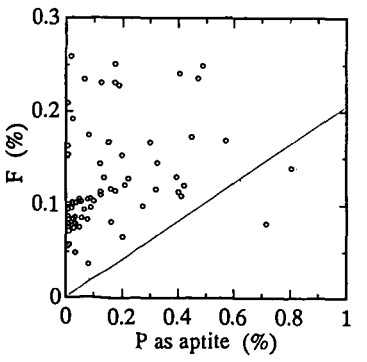

Fig. 7 Relationship between P content as apatite and F content. Solid line =F/P weight ratio of fluoroapatite.

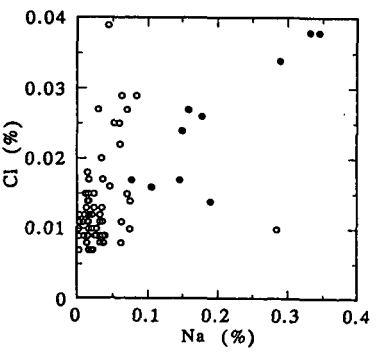

Fig. 8 Relationship between Na and Cl contents. Solid circle=coal samples relatively rich in Na-bearing clay minerals.

ASH CHEMISTRY AND SINTERING

Bengt-Johan Skrifvars, Rainer Backman, Mikko Hupa,
Åbo Akademi University, Combustion Chemistry Group
FIN-20520-Turku, Finland

Keywords: Ash chemistry, ash sintering, melt behavior calculations

INTRODUCTION

The thermal behavior of a fuel ash is one important factor to consider when fireside slagging and fouling problems in steam boilers are addressed. It is well known that different types of chemical reactions and melts in deposits play an important roie in the build-up of problematic fireside deposits.

Low viscous melts occur in steam boilers mainly when salt mixtures are present in the ash. Such are different mixtures of alkali and earth alkali sulfates, chlorides and carbonates. These mixtures do not melt at a certain temperature but form a melt in a temperature range which in some cases may be several hundreds of degrees. The amount of melt is crucial for the deposit build-up. For some boilers it has been found that roughly 10 - 20 weight-% melt in an ash mixture would be enough to cause extensive deposit formation, while 60 - 80 weight-% melt would already cause the ash to be so wet it would flow down a vertical tube and not cause any further deposit growth [1].

Another type of melt that causes deposits is the highly viscous silicate melt which occurs when silicon is present in the system. This type of melt causes mainly slagging problems in pulverised fuel fired boilers using coal or peat as fuel, but may occur also in fluidised bed boilers when quartz is used as the bed material. The silicate melts are problematic also because of their capability to form glassy phases which do not chrystallize when the temperature decreases back below their first melting points. Viscous flow sintering of glassy silicate particles may cause extensive fouling. The amount of the formed melt and its viscosity are two important factors to consider when looking at viscous flow sintering, besides those parameters expressed in the Frenckel equation [2].

Also chemical reactions may cause hard deposits [3]. Calcium is one element which has been found very active in this sense. If it arrives in the oxide form to a surface it has been found to cause extensive deposit build-up if it reacts with $SO_2(g)$ or $CO_2(g)$ at the surface.

When studying these phenomena one has to take the chemistry into consideration since these above mentioned mechanisms are all strongly dependent on which elements you have present in the deposit, as which component and in which surrounding gas phase they are placed.

In this paper we present some initial thermal behavior predictions made for 10 different ashes which have been studied in a broader project. In this project both laboratory scale testing, as well as theoretical tools were used for establishing the thermal behavior of the ashes. In this paper we wanted especially to focus on the prediction of molten phases in the ash and compare these with sintering tests performed on the same ashes.

EXPERIMENTAL

10 different ashes were chosen for the tests. These are presented in Table 1.

The ashes were characterized in three different ways. Firstly, they were analysed quantitatively, secondly, they were sintering tested with a compression strength test and thirdly, they were analysed with a combined differential thermal - thermogravimetric analyser (DT/TGA). Details of of these results are presented elsewhere [4].

The quantitative wet chemical analyses were re-calculated to components using stoichiometrical assumptions and thermodynamic considerations. The calculations assumed that all phosphour was present as calcium phosphate, carbonate as both potassium and calcium carbonate, rest calcium as oxide, all chlorine as potassium chloride, sulfur as both sodium and potassium sulfate, rest potassium as oxide and all silicon as quartz. Rest of analysed elements were assumed as their oxides and un-analysed elements (differences to 100% oxides) as unknown.

After this we calculated the melting behavior of the ashes using multi-component, multi-phase thermodynamic calculations and compared the results with the sintering test results we had achieved earlier in the study. In the melting behavior calculations we treated the ashes as if they would have consisted of four separate parts, one salt part consisting of the alkali sulfates, carbonates and chlorides (referred to as alkali salts in the further text), another silicate part consisting of the elements expressed as oxides, a third part consisting of calcium oxide and carbonate and a fourth part consisting of the phosphate and unknown elements.

Of these four parts, the silicates and salts were assumed to be those causing melt formation, while the calcium oxide/carbonate part would be active to react with flue gases and the inert part wouldn't affect deposit at all.

RESULTS

The results from the sintering tests are summarized in Figure 1. The results revealed significant differences in the sintering tendencies such as they were detected by the compression strength test. The temperatures at which the strength of the pellets started to increase varied from 625°C (ash #8) to above 1000°C (ash #7).

In Figure 2 the estimated amounts of different components present in the ash is shown. Focusing on the silicate and salt parts in the ash, one sees that the ashes #1 to 6 are fairly rich in silicates, while the ashes #7 to 10 are very rich in calcium oxide/carbonate with low amounts of silicates. The salt part varies significantly, from roughly 1% by weight for the ash #3 to 44% by weight for the ash #8.

Figure 3 summarises the results from the melting behavior calculations. The results are presented as the amount of melt, expressed as percentages by weight in the sample vs the temperature. The melting of the silicate part and salt part are treated and expressed separately in the figure. The calcium oxide/carbonate and the inert parts are added up to the total amount (100%).

Ash #1 reaches its first melting point, T_0, already at 525°C. At this temperature a very small amount of alkali salt forms a melt which is approximately 1/10 of a percent of the total ash. The amount of melt stays low throughout the calculated temperature range. At 770°C the silicate part in the ash reaches its T_0, forming immediately some 17% melt, causing the total amount of melt to increase to 19% melt in the ash. From here on the amount of melt increases very slowly with temperature to reach its maximum, 19% melt, at 1200°C. At this temperature the salt part contributes to the melt with only 3.5% by weight.

Ash #2 reaches its T_0 at 615°C. At this point the alkali salt part of the ash forms a small amount of melt. As the temperature increases to 750°C, the whole alkali salt part has become molten, the amount being 14% by weight. At 770°C the silicate part forms a 15% melt, the total amount being now 29% melt in the ash. From here on the silicate part continues to melt, ending up at 36% total melt in the ash at 1200°C.

Ash #3 forms a large amount of silicate melt at 770°C. At this point 35% of the ash is found in the molten phase. At 845°C the alkali salt part starts to contribute to the melt formation. At 895°C all the alkali salts have melted, the total amount of melt now being 55%. This amount increases still and reaches the maximum value of 65.6% melt in the ash at 1200°C.

Ash #4 forms an alkali salt melt at 625°C. At 770°C also the silicate part starts to melt, almost doubling the total amount of melt from 17% to 30%. The amount increases to about 33% at 810°C after which the increase slows down, however, still increasing the melt part to 40% which is reached at 1200°C.

Ash #5 forms also a first alkali salt melt at 625°C. The amount increases immediately to 15%. At 765°C the whole alkali salt part is molten, forming some 30% molten phase in the ash. At this same temperature the silicate part starts to melt, forming roughly 20% molten phase immediately. This increase the total amount of melt to 50% at this temperature. The amount increases still up to the maximum temperature 1200°C at which 57% of the ash has molten.

Ash #6 forms a very small amount of alkali salt melt already at 530°C. The amount stays very low (below 5%) throughout the calculated temperature range. At 780°C the silicate part starts to melt. The amount is up to some 1000°C low, but increases above 1000°C rapidly to reach its maximum of some 35% silicate melt at 1040°C. The total amount of melt is at this temperature 38% and does not exceed that number in the calculated temperature range.

The rest of the ashes, i.e. #7, 8, 9 and 10 form only alkali salt melts. Ash #7 has a T_0 of 575°C. The amount stays low to approximately 800°C and does not exceed the value of 20% in the whole calculation range. Ash #8 forms a first melt of roughly 20% at 615°C. The amount contunues to increase until the temperature reaches the value of 760°C. At this point 45% of the ash is molten. After this the amount does not increase anymore. Ash #9 behaves somewhat like ash #7, i.e. a T_0 of 535°C with a low amount of melt formed, up to a temperature of roughly 750°C, where the amount starts to increase up to the maximum value of 25% which is reached at 810°C. Ash #10 forms a first melt at 870°C. At this temperature the alkali salt part melts almost completely and forms a 25% melt of the total ash.

DISCUSSION

Comparing the sintering tendencies for the ashes #2, 5, 6, and 8 with the melting behavior calculations one finds fairly good correlations between the T_{20} temperature, i.e. the temperature where 20% of the ash is molten and the sintering temperatures, T_{sint}. For the ash #2 the T_{sint} is between 700° and 750°C, the T_{20} is 770°C. For the ash #5 the T_{sint} is between 650° and 675°C, and the T_{20} is 700°C. For the ash #6 the T_{sint} is between 950° and 1050°C, and the T_{20} is 1025°C and for the ash #8 the T_{sint} is between 625° and 650°C, the T_{20} being 625°C. In all these cases the melt probably caused the strength increase in the ash pellets tested. In the case with ashes #2 and 6 it seems probable that it was the silicate melt that caused the sintering, while it for the ashes #5 and 8 seemed to be the alkali salt melt causing the sintering.

For the ash #3 the compression strength test indicates sintering to start at roughly 800°C. The melting behavior calculations suggest, however, a significant melt formation already at 770°C, i.e. the melt behavior calculations overpredict the sintering. The viscosity of the formed melt may explain the temperature difference found when comparing the T_{20} to the T_{sint}. If we assume that the formed melt had a high viscosity, the time for the sintering caused by that glassy phase would have been longer than that for a low viscous glassy phase, indicating that the sintering measurements were not done long enough. In these tests 4 hours were used as the standardized sintering time. No viscosity measurements were, however, done at this stage.

For the ash #1 the melting behavior calculations suggest a molten phase below 20% from 770°C throughout the calculated temperature range. Some sintering was detected beyond 900°C. Since most of the formed melt for the ash #1 throughout the calculated temperature range was a silicate melt the viscosity of that may again explain the sintering. No viscosity calculations were however done.

For the ashes #7, 9, and 10 the melting behavior calculations predict melts up to roughly 20% of the total ash from 800°C for the ash #9, 850°C for the ash #7, and 880°C for the ash #10. For the ashes #9 and 10 a fairly good correlation can be seen between the T_{20} and the T_{sint} but for the ash #7 the sintering temperature and the melting behavior calculation does not correlate at all. In this cases no sintering was detected in the tested conditions. Obviously the component estimations presented in Fig. 2 fail in this case. The ash #7 contains fairly large amounts of analysed carbonate (expressed as CO_2 in Tab. 1). The melts predicted for this ash was all alkali salt melts, with potassium carbonate as the main component. If we assume that no potassium carbonate is present in the ash (all analysed CO_2 as calcium carbonate instead), the alkali salt part would decrease to 1/10 of its amount and hence, no large amount of melt could form.

For ash #4 the melt behavior calculations do not correlate well with the sintering measurements. The alkali salt part of the ash reaches its complete melting temperature T_{100} at 820°C, at which also most of the silicate melt to be formed is present. At this point roughly 35% of the ash should be molten. The sintering, detected by the compression strength test, does not, however, indicate any significant strength increase until 950°C. No clear explanation could be found for this behavior.

CONCLUSIONS

Silicate and salt melts may cause extensive deposit formation in steam boilers. The formation of these kind of melts can today be calculated with fairly acceptable accuracy, using multi-component, multi-phase thermodynamic equilibrium calculation. Good knowledge of which components are present in the ash and accurate thermodynamic data is, however, required.

Of ten ashes tested in laboratory conditions and predicted for their melting behavior, for six ashes the melt behavior calculations correlated well with the measured behavior. For the ashes #5, 8, 9, and 10 the alkali salts formed the major part of the melt while it for the ashes #2 and 6 seemed to be the silicate melt that caused the strength increase.

In two cases, for the ashes #1 and #3 the melt behavior calculations predicted a somewhat lower temperature for T_{20} than for T_{sint}. In these cases the calculations predicted a viscous silicate melt to be formed as the major phase. A possible cause for the higher T_{sint} may have been a high viscosity in the silicate melt, causing so slow sintering that the compression strength test didn't have time to detect it.

In the rest of the cases (two ashes) the melt prediction calculations seemed to fail to predict the sintering behavior detected by the compression strength test. A possible reason to this failure is errors in the assumed components used in the calculations.

REFERENCES
[1] Backman, R., Hupa, M., Uppstu, E.: Tappi J. 70 (6), 123 (1987).
[2] Frenkel, J. J.: Physics USSR 9 (5), 385 (1945).
[3] Skrifvars, B-J., Hupa, M., Hyöty, P.: J. Inst. Energy, 64 (461), 196 (1991).
[4] Skrifvars, B-J., Hupa, M.: Characterization of biomass ashes, presented at the Engineering Foundation Conference on "Applications of Advanced Technology to Ash-related Problems in Boilers", July 1995, Waterville Valley, New Hampshire, USA.

Table 1. The ash analyses of the studied fuels, expressed as weight-% of their corresponding oxides.

#	SiO_2	Al_2O_3	Fe_2O_3	P_2O_5	CaO	MgO	Na_2O	K_2O	SO_3	CO_2	Cl
1	65.7	1.7	1.4	5.0	2.7	1.8	0.3	4.6	1.4	0.0	0.2
2	56.3	0.5	0.6	1.9	6.3	1.4	0.2	12.6	2.9	1.3	2.1
3	48.8	6.4	1.9	3.0	3.9	5.5	0.8	18.9	3.5	3.1	0.0
4	44.1	5.1	2.3	2.1	6.7	3.6	0.3	16.0	5.2	1.9	1.8
5	34.2	0.4	0.5	2.1	9.1	2.0	0.1	24.7	2.3	6.1	3.2
6	34.0	4.7	4.4	3.0	17.3	11.4	0.4	17.1	1.2	0.5	0.5
7	7.3	1.5	1.3	4.8	44.8	5.8	0.8	11.3	1.5	5.2	0.0
8	3.3	0.3	0.3	7.6	27.7	3.1	0.7	28.4	1.9	22.3	4.4
9	0.6	0.3	0.3	6.0	35.1	10.4	2.3	13.6	2.0	27.6	0.3
10	0.6	0.1	0.7	10.7	28.8	4.4	0.2	22.5	5.9	23.5	0.2

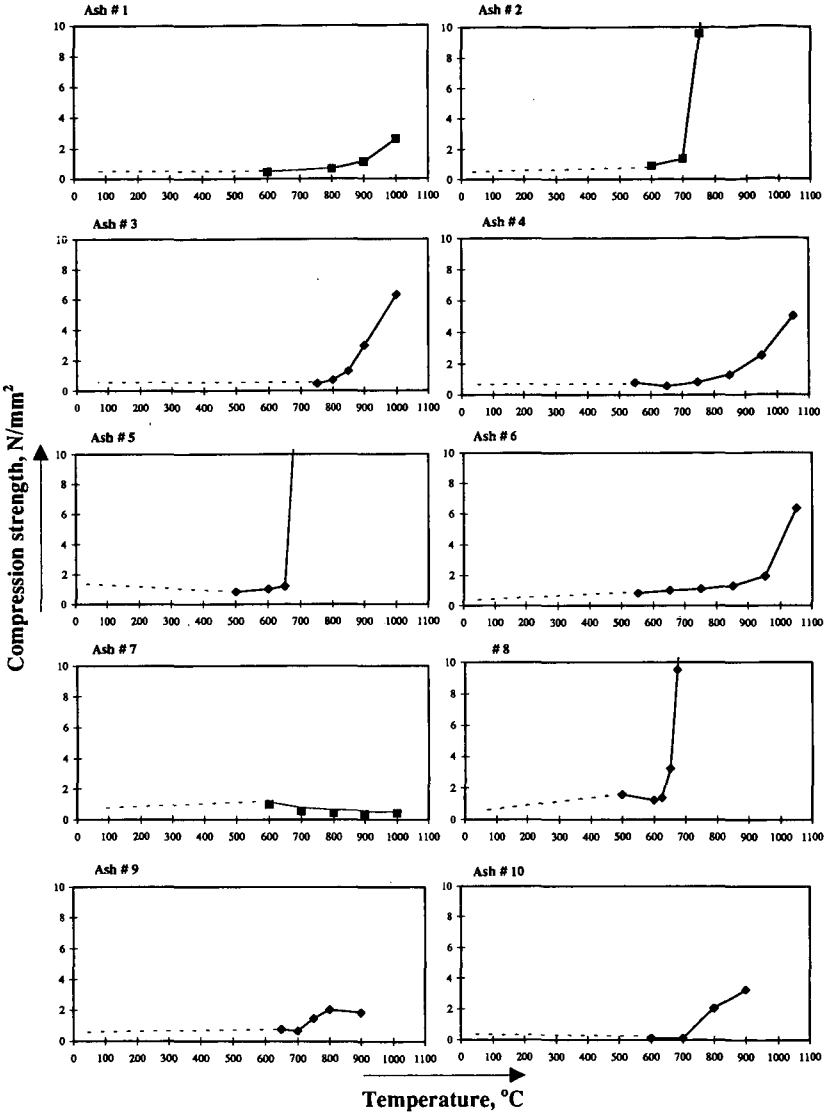

Figure 1. Sintering tendency for ten ashes, tested with the compression strength sintering test. 0-tests indicated in the left corner of each figure. Sintering time 4h, dry air atmosphere.

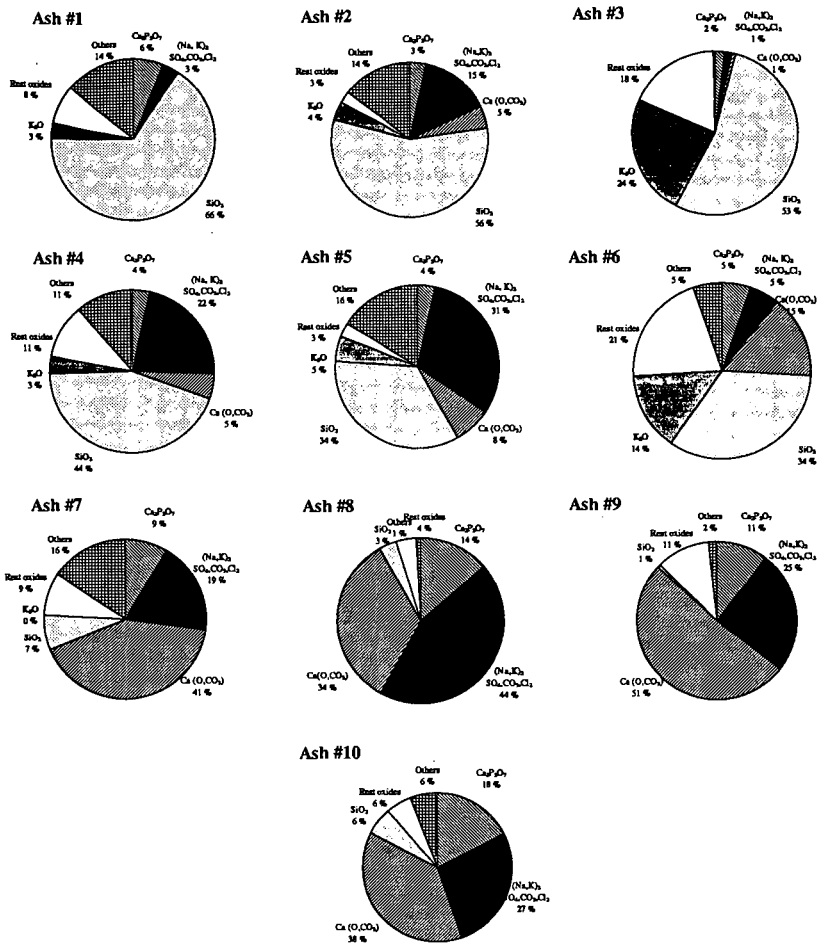

Figure 2. Stoichiometrically estimated amounts of different components (weight-%) present in the 10 ashes, presented in Table 1. The calculations assume that all phosphour is present as $Ca_2P_2O_7$, carbonate as both K_2CO_3 and $CaCO_3$, rest calcium as CaO, all chlorine as KCl, sulfur as both Na_2SO_4 and K_2SO_4, rest potassium as K_2O, all silicate as SiO_2, rest analysed elements as oxides and un-analysed elements as others.

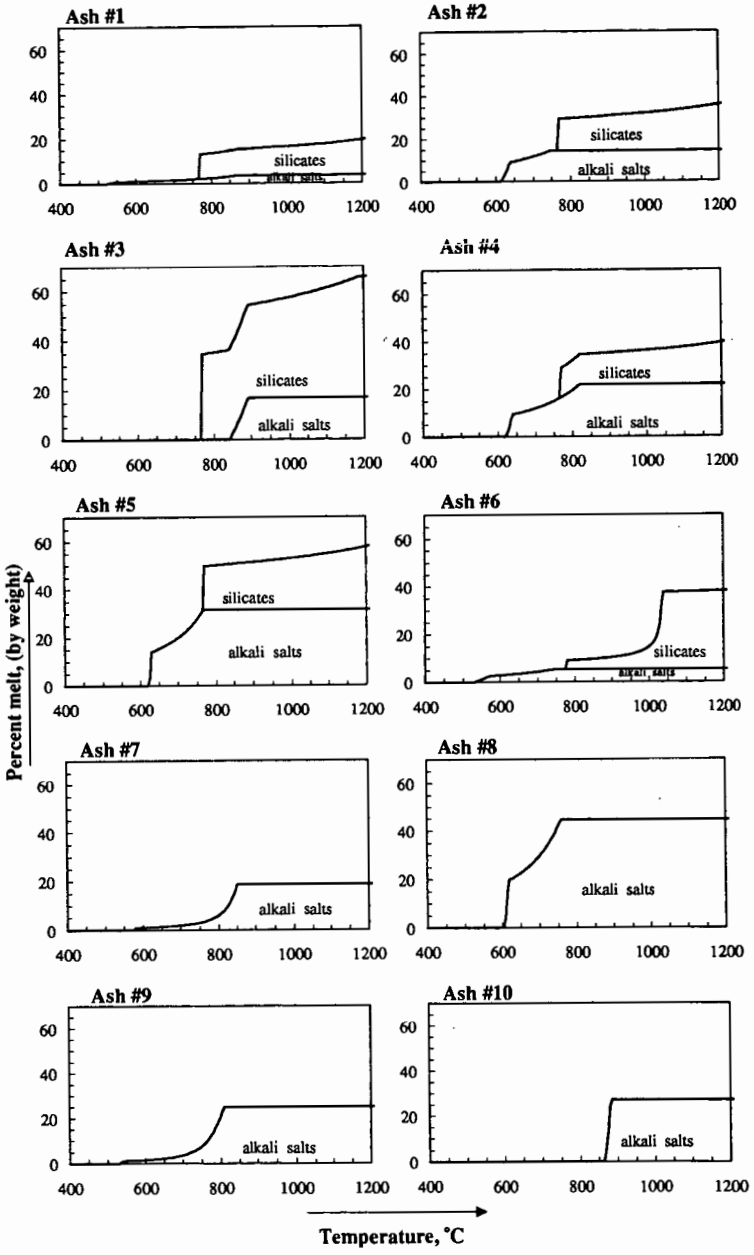

Figure 3. The melting behavior calculations, based on the components presented in Figure 2.

ASH FUSION TEMPERATURES AND THE TRANSFORMATIONS OF COAL ASH PARTICLES TO SLAG

S. Gupta, T.F.Wall, R.A.Creelman and R.Gupta
Department of Chemical Engineering
University of Newcastle, Callaghan, NSW 2308, Australia

Keywords: Ash fusion, viscosity and shrinkage.

ABSTRACT

A mechanistic study is detailed in which coal ash is heated with its shrinkage measured continuously up to a temperature of 1600°C. The temperatures corresponding to the rapid rate of shrinkage are shown to correspond to the formation of eutectics identified on phase diagrams. Samples were therefore heated to these temperatures, cooled rapidly and examined with an SEM to identify the associated chemical and physical changes. The progressive changes in the range of chemical analysis (from SEM), the extent of undissolved ash particles and porosity were then quantified and related to homogenisation, viscosity and ash fusion mechanisms.

INTRODUCTION

Ash deposition on furnace walls in pf (pulverised fired) furnaces is called slagging when it occurs in the high temperature areas of furnaces directly exposed to flame radiation and fouling in other regions such as tubes in the convection section of the boiler. The characterisation of coal ash for its tendency to slag and foul has been traditionally related to the bulk chemistry of the ash and ash fusion temperatures. There are well-documented shortcomings of these approaches relating to their uncertainties as predictive tools for plant performance, that is, poor repeatability and reproducibility of ash fusion measurements. Of particular concern is the estimation of the initial deformation temperature (IDT). IDT is the temperature at which the rounding of the tip of an ash cone is noted, which has been accepted as the temperature where the ash first softens and therefore becomes sticky. The nature of physical and chemical changes occurring during melting of coal ash has been investigated in the current study to provide an alternative procedure to the ash fusion test. The characteristic melting temperatures then are related to the transformations, and reactions of ash and these are interpreted in terms of their importance to fouling and slagging in furnaces.

EXPERIMENTAL

The current study is based on a range of samples selected from domestic power stations to those exported from Australia as steaming coals. Several export coals were selected on the basis of difficulty of the estimation of their IDT's. Laboratory ash was prepared for all the samples and ashes from some of the corresponding power stations were also obtained. Different laboratories reported a wide variation in IDT estimation, the difference being as great as 400°C in some cases.

Several techniques have been tried to investigate the fusibility of bituminous ashes in a related study as detailed elsewhere (Wall et al., 1995). The major events observed in these techniques are illustrated in Figure1. The top two plots in Figure1 are based on the HRL Test (Ellis, 1989). The electrical resistance and shrinkage of compacted ash pellets are recorded concurrently from room temperature to about 1350°C in this test. The third plot indicates the shrinkage of compacted ash pellets sandwiched between two tiles as developed at ACIRL (Coin, et al. 1995). The last plot is based on the TMA (thermomechanical analysis) technique developed by the CSIRO Division of Coal and Energy Technology. The current paper will be restricted to results obtained from the last technique.

TMA Technique (Thermomechanical Analysis)

Shrinkage measurements are frequently used in metallurgy and ceramic science to study the physical properties at high temperatures. Raask(1979), Ellis(1989), Lee(1991), Gibson(1991) and Sanyal(1993) have studied electrical resistance and shrinkage properties for sintering and fusion characteristics of ashes in the past. However, a systematic study comprising several types of measurements, laboratory ash and combustion ash with investigations of fusion mechanisms for temperatures up to 1600°C has been lacking. TMA technique involves measurements of the shrinkage of loose ash(~35mg.) in a specially designed sample holder which is located between a cylindrical graphite container with a flat bottom and a rod with a tapered end. As the assembly (ash) is heated from room temperature to 1600°C, the rod sinks into the ash and when eventually flows as slag into the annular gap between the rod and the container. The samples were heated in neutral environment as per AS (Australian Standards) requirements. The output of this experiment provides 3 to 4 'peaks' (maximum rate of shrinkage with temperature) of different intensity and at different temperatures which are related to melting characteristics of the sample as shown in Figure1. There is no significant shrinkage in most of the samples below 900°C. The temperatures associated with particular shrinkage levels were noted as T(x%).

Studies to Identify Transformations

Compacted ash pellets were heated under standard AS reducing conditions and rapidly quenched in air to freeze the samples. The chemical composition of liquid phases and slags were determined from sectioned samples of these pellets using a scanning electron microscope (SEM) and electron dispersive spectrum (EDS). Micrographs of the samples were also obtained to compare the porosity and extent of undissolved particles. Bulk density of some of the samples has also been measured at different temperatures.

RESULTS

Mechanism of Ash Fusion

The current observations are based on twenty nine samples. Most of the samples can be grouped into four categories, and represented by particular samples as follows: i) ash with a high SiO_2/Al_2O_3 ratio, low Fe_2O_3 and poor reproducibility for the IDT e.g. EN3; ii)ash with a SiO_2/Al_2O_3 ratio within the norm of Australian coals, low Fe_2O_3, and very poor reproducibility for the IDT e.g. EN6; iii) ash with high Fe_2O_3(11%) e.g. EQ1with good reproducibility and iv) and ash with high CaO(16%), e.g. ET2 with good

reproducibility for the IDT. TMA measurements provided 'peaks' identifying rapid fusion events during heating. These 'peaks' have been related to formation of eutectics identified on appropriate phase diagrams (Wall, et al., 1995). Shrinkage results demonstrated occurrence of the peaks in three distinct groups. Lower temperature peaks up to 1100°C were related to eutectics in SiO_2 - Al_2O_3 - K_2O system and 1200°C peaks to SiO_2 - Al_2O_3 - FeO system. Peaks in the range 1220°C to 1440°C have been correlated to FeO and CaO reactions with various proportions of SiO_2 and Al_2O_3.

Homogeneity and Porosity of Samples:

The melt composition will change continuously with temperature till ash is transformed completely to a homogeneous liquid. The chemical composition of slag should then be of the bulk ash. The melt composition was determined for at least 10 points per sample at one temperature using SEM and EDS mode. Major variation in the melt composition is due to different extent of dissolution of silica particles. SiO_2(wt.%) concentration in the melt has been selected to illustrate the homogenisation of liquid phase. SiO_2 in melt reaches to bulk ash composition rapidly in high iron sample EQ1 as shown in Figure2, where the EN3 and EN6 melt approach to the bulk ash composition at a higher temperature.

Ternary diagrams have also been used for describing the change in melt composition. The chemical composition from point analysis was normalised to three component system i.e. SiO_2 -Al_2O_3 - CaO for ET2 and SiO_2 -Al_2O_3 - FeO for other samples. The normalised analyses of EN6, EQ1 and ET2 are presented on ternary diagrams of SiO_2 - Al_2O_3 - FeO and SiO_2 - Al_2O_3 - CaO as shown in Figure3. EQ1 and ET2 melt composition range narrows to that of bulk ash at lower temperatures as compared to EN6(Figure3). CaO appears to be most important constituent for rapid homogenisation at various stages.

At low temperatures diffusion rates are slow therefore melt formation proceeds slowly. As the ash is heated open pore network transforms to micropores and a minimum porosity. Melting and reaction occurs to form the first liquid phase that has a composition close to iron cordierite. This liquid may start flowing to fill the open network and hence contribute to initial densification. The reaction of this melt phase with specific solids (SiO_2 rich) until progressive depletion of the solids occurs and finally slumping of the pellets as the proportion of the liquid increases significantly. Air entrapped in the sample causes pore formation. It was observed that pore formation increases with iron content. Most of the porosity is either closed or in the form of spherical pores. Majority of the samples indicate that T(50%) (temperature corresponding to 50% shrinkage) is associated with closed and spherical pore structure. Gibson(1991) also observed similar trends. Bulk porosity keeps on decreasing till formation of closed pores takes place. Closed porosity is found to be increasing rapidly after T(50%) in most of the cases. The bulk density estimated from pellet dimensions also indicated that high alkali samples acquire minimum porosity at lower temperatures compared to high silica samples. It was also observed that temperatures corresponding to minimum porosity lie between 1200° to 1300°C. Physical changes before 50% shrinkage may depend on the permeability of liquid through the open porosity. After 50% shrinkage, the rate of shrinkage may depend on the rate of dissolution of residual silica in the melt (i.e. amount and particle size of quartz in the initial sample). Image analysis of electronmicrographs of various samples indicated less than 25% undissolved particles at T(50%).

AFT and Alternative Shrinkage Temperatures

The traditional AFT test involves observation of four temperatures (IDT, ST, HT and FT) depending on the physical state of the ash cone. Huffman(1981) observed that at IDT most of the melting is completed and it was also estimated that glass phase was more than 75%. Figure5 shows the linear shrinkage associated with IDT and some 'peak' temperatures. The first peak, i.e. first important fusion event in majority of the samples was observed around ~10% shrinkage of ash. The second peak occurred at <30% shrinkage of most of the samples, except for high iron and high CaO, which are associated with ~50% shrinkage at the second important event. It can be seen that IDT is associated with approximately ~50% shrinkage for EQ1 and ET2 samples of good reproducibility and around 60% for poor reproducibility samples e.g. EN3 and EN6 (Figure 4). The IDT clearly does not represent first shrinkage event.

The temperatures corresponding to these fusion events may be used for ash deposition characterisation. Figure 5 illustrates a ranking criteria for ash deposition based on temperature vs shrinkage plot for many samples. The samples requiring higher temperatures for a given shrinkage level are expected to be associated with least deposition, while those at the bottom are expected to be most troublesome. Hence ET2 (high CaO) would provide worst deposition, whereas PQ2(least alkali) should provide least deposition. However, the location of a particular sample within this ranking will depend on the temperature in different regions of the plant. In practical terms, this implies that ranking will depend on the temperature in different parts of the plant.

Correlation of shrinkage with ash viscosity, and sticky particles

The current understanding of the of the ash deposition is based on the stickiness of the particles. If the particles are sticky they will adhere to a surface on impact. Many studies have related stickiness to the viscosity of the particles which, in turn, has been calculated from the chemical composition. The viscosity calculated from the known composition of the ash samples therefore provides a basis for estimating theoretical temperatures for particles to be sticky, which can be related to the extent of shrinkage measured at these temperatures. Boni et al. (1990) suggested that ash particles with viscosity $>10^7$ Pas are not sticky and will not collect on the heat transfer surface. The sintering and slagging has also been related to viscosity of ash particles by Raask (1985). Figure 6 indicates the range of viscosity of the liquid slag generated from the ash samples which is calculated from the Urbain correlation (Urbain et al., 1981) based on the ash chemistry. This figure also provides the shrinkage range of importance to ash deposition. All ash samples fall within the viscosity range of 10^5 to 10^7 Pas at 25% shrinkage (Figure 7). Therefor it may be suggested that this shrinkage level is appropriate as criterion for ash stickiness. Examination of electronmicrographs from quenched samples also indicate the significant proportion of liquid phase

corresponding to these temperatures. It can be seen from this figure that ash particle impinging onto walls will be sticky at a similar temperature at which liquid formation has been observed in the pellets.

CONCLUSIONS

1. IDT clearly does not represent the first fusion event.
2. T(25%) is found to be associated with significant particle deformation.
3. T(50%) is related to formation of closed or spherical pores, which corresponds to >75% melt phase.
4. The temperatures corresponding to particular shrinkage events may be used as alternate ash fusion temperatures.

ACKNOWLEDGMENTS

We are most grateful to Mr. Dick Sanders of Quality Coal Consulting Pty. Ltd. for managing the project, selecting samples and providing insights into the AFT procedures. The study was supported by the Australian Coal Association Research Program with Mr. Grant Quinn of BHP Australia Coal as project monitor. The assistance of Dr. John Saxby at CSIRO is greatly appreciated.

REFERENCES

Boni et al. (1990), Transformations of Inorganic Coal Constituents in Combustion System, DOE Report No. AC22 - 86PC 90751, March (1990).

Coin, C., Reifenstein, A.P. and Kahraman H. (1995), Improved Ash Fusion Test, Engineering Foundation Conference on Application of Advanced Technologies to Ash - related Problems in Boilers, USA.

Ellis, G.C. (1989), The Thermomechanical, Electrical Conductance and Chemical Characteristics of Coal Ash Deposits, NERDDP Project No. 1181 Final Report Volume III, SECV R & D Dept, Australia.

Gibson, J.R. and Livingston, W.R. (1991), The Sintering and Fusion of Bituminous Coal Ashes, Engineering Foundation Conference on Inorganic Transformations and Ash Deposition During Combustion, Palm Coast, Florida.

Huffman, P.G., Huggins F.E. and Dunmyre G.R. (1981), Investigation of the High Temperature Behaviour of Coal Ash in Reducing and Oxidising Atmospheres, Fuel, 60, 585-597.

Lee, G.K. et al. (1991), Assessment of Ash Sintering Potential by Conductance and Dilatometry, Pittsburgh Coal Conference.

Raask, E. (1979), Sintering Characteristics of Coal Ashes by Simultaneous Dilatometry - Electrical Conductance Measurements, J. Thermal Analysis 16, 91.

Raask, E. (1985), Mineral Impurities in Coal Combustion. Hemisphere Publishing Corporation USA.

Sanyal, A. and Mehta, A.K. (1994), Development of an Electrical Resistance Based Ash Fusion Test. The Impact of Ash Deposition in Coal Fired Furnaces, p445-460, Taylor and Francis, Washington.

Urbain G. et al. (1981), Trans. J. Br. Ceram. Soc., Vol. 80, p139-141.

Wall, T.F. et al. (1995), Coal Ash Fusion Temperatures - New characterisation Techniques, and Associations with Phase Equilibria, Engineering Foundation Conference on Application of Advanced Technology to Ash - Related Problems in Boilers, New Hampshire, USA.

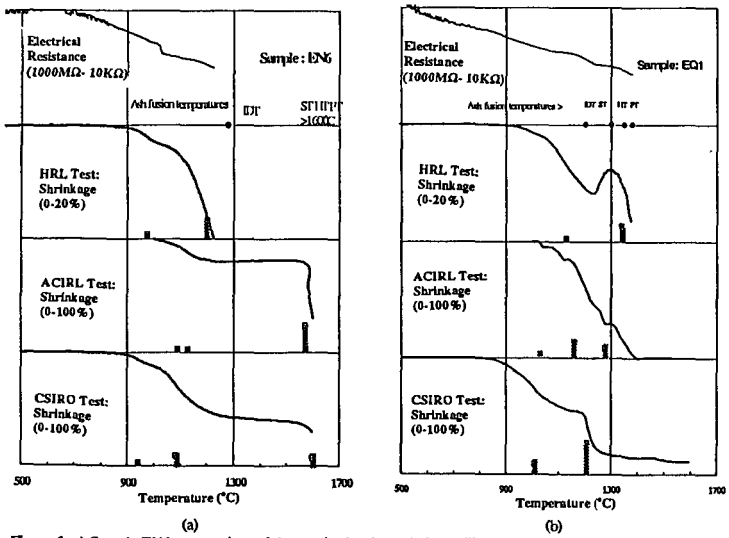

Figure 1. a) Sample EN6, comparison of the results for the techniques. Top plot - electrical resistance data from HRL test, bottom of three plots - shrinkage experiments reported as progressive ash sample linear dimension on heating. The bars indicate 'peak' temperatures of rapid change in ash sample heating, b) Sample EQ1.

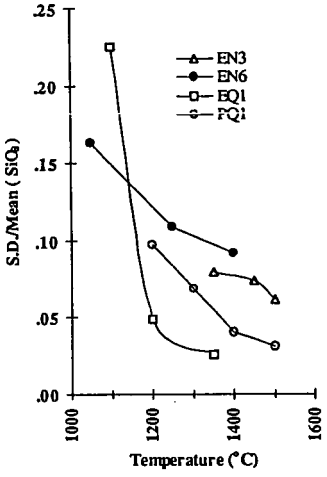

Figure 2. Variation in SiO_2 composition in melt phase, for different samples expressed as the standard deviation normalised to the mean.

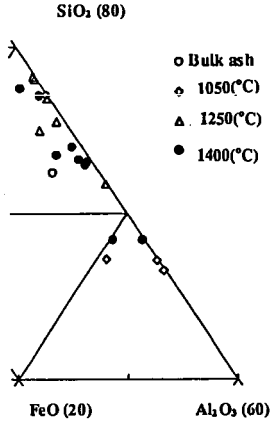

Figure. 3(a)

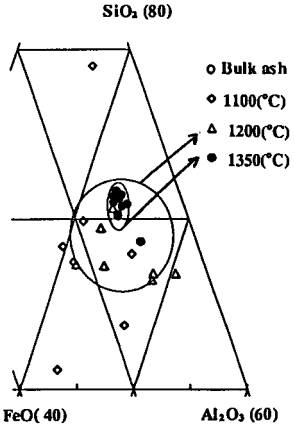

Figure 3(b)

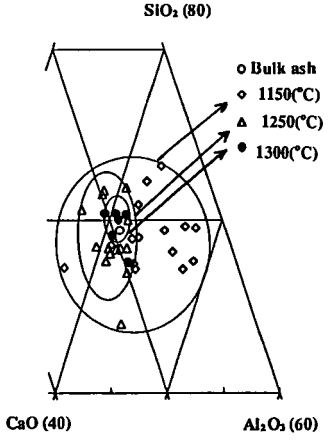

Figure 3(c)

Figure 3. Ternary plot for melt compositions for a) EN6, b)EQ1 and ET2.

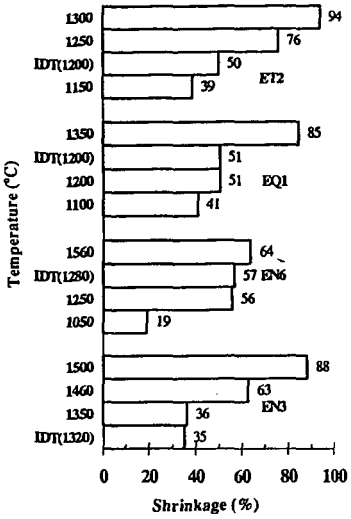

Figure 4. Shrinkage(%) at peak temperatures and IDT for samples EN3,EN6,EQ1 and ET2.

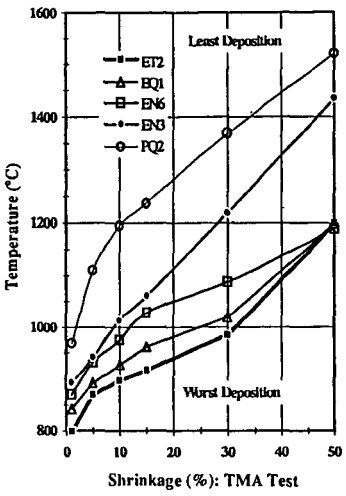

Figure 5. Relative sample ranking plot for ash deposition based on shrinkage(%) temperatures.

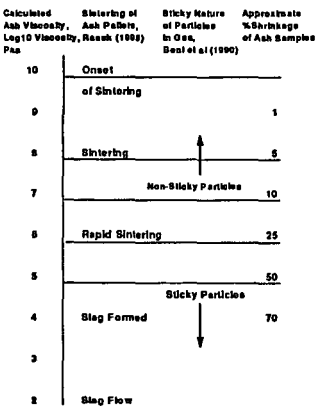

Figure 6. Association between physical state of ash, sintering and sticky nature of particles in the furnace.

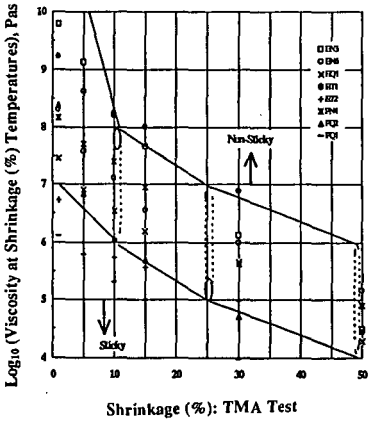

Figure 7. Correlation of calculated viscosity (Urbain' Model) and different levels of shrinkage with regions for sticky and nonsticky particles.

PHASE RELATIONSHIPS IN COAL ASH CORROSION PRODUCTS

DAVID KALMANOVITCH
DB RILEY, INC.
WORCESTER, MA

ABSTRACT

The corrosion of heat transfer surfaces in coal-fired utility boilers is a major concern to the efficient operation of these units. Despite the importance of the corrosion there has been limited research on the relationship between the ash components on the tube surface and the interactions and reactions between the various components and the steel surface. Mechanisms such as molten phase corrosion, sulfidation, and high temperature oxidation have been identified as leading to extensive wastage of tube metal. However, while the corrosion process can be identified using techniques such as metallography and x-ray diffraction there is limited insight into the role of the coal mineralogy and ash deposits on the surface in the corrosion process.

This paper describes research into the formation of molten or semimolten phases within ash deposits which are associated with corrosion of superheater and reheater fireside surfaces. For example, the phases potassium pyrosulfate ($K_2S_2O_7$) and potassium aluminum sulfate ($K_2Al_2SO_7$) have been determined by x-ray diffraction to be present in deposits where fireside corrosion has occurred. However, both these phases are not directly derived from coal minerals or the common matrix observed in ash deposits. The examination of the reactions and interactions within deposits which result in the formation of these and other phases associated with corrosion will be discussed in the paper.

INTRODUCTION

The high temperature corrosion of pressure parts in utility boilers is a major aspect of the design and operation of the system. The ideal design of heat transfer surfaces would be a material which would be resistant to creep damage and exhibit no corrosion. In reality the economics of boiler design requires the use of steels which are not only susceptible to creep damage (at temperatures above 650° C and pressures above 14 MPa) but also susceptible to corrosion. The corrosion is important as the reduction in wall thickness caused by the wastage results in reduced capacity to contain steam pressures, increased hoop stresses within the tube, and in reduced creep life. Therefore, it is very important that the corrosion process occurring on the fireside surface of heat transfer surfaces be understood and thereby reduced by either fuel choice or change in design/operating conditions.

The high temperature corrosion of heat transfer surfaces is usually observed in coal fired systems and confined to superheater and reheater components. In many cases the corrosion is localized to the tubing with the highest metal temperatures within the component such as the outlet portion. The metal temperatures in this location are either known or measured and are functions of unit design and operation. However, a knowledge of the metal temperatures is only a part of the issue with respect to the corrosion process. A major aspect is the reactions and interactions of the phases within the ash deposit and the relationship between these phases and corrosion processes.

The most aggressive form of fireside corrosion occurs with a molten phase. The mechanism is referred to as molten ash corrosion or liquid ash corrosion. Wastage rates of up to 0.5 mm per year for tubes 10-20 mm thick are not uncommon and can result in rapid reduction of component planned life expectancy. Despite the importance of the corrosion process there has been limited research to date with respect to the relationship between the coal ash properties (coal mineralogy), the ash deposit formed on the fireside

surface and the presence of molten ash corrosive phases. In recent years, however, significant efforts have been placed on the understanding of ash deposition processes. From this research methods to characterize and predict ash behavior on heat transfer surfaces have been developed. In addition to understanding the growth of deposits, itself important to the design and operation of utility boiler systems, these techniques and models have now been applied to understanding the relationships between the deposit and the tube metal surface.

When considering the corrosion process it is important to understand the nature of the tube metal surface. The type of metal used can be a ferritic alloy such as SA213-T22 (iron based alloy with a nominal 2.25 wt% chromium and 1.0 wt.% molybdenum) or an austenitic alloy such as SA213-304 (type 304 stainless steel). In both cases, resistance to high temperature oxidation and corrosion is due to the presence of an intact adherent external protective scale. In the case of the ferritic alloy this scale is predominantly magnetite (Fe_3O_4). For austenitic alloys, the protective scale is chromium oxide. Phases within the deposit which affect the integrity of this scale will result in wastage of the tubing. It is the molten phases formed during the liquid phase corrosion mechanism which are most aggressive towards the protective scale. Under these conditions the high mobility of corrosive ions and the removal of corrosion products including the protective scale results in increased wastage.

Therefore, it is important to understand the phase relationships within deposits and how these phases contribute to the corrosion process. This requires a description of ash deposits and the techniques used to characterize the interactions and reaction with respect to the corrosion interface.

CHARACTERIZATION OF ASH DEPOSITS

Ash deposits are formed from the coal minerals present in the fuel. The common minerals observed in coal are listed in Table 1 along with the nominal chemistry. As the minerals are geological in nature some minerals are poorly defined chemically. The minerals are not distributed uniformly throughout the coal and may be associated with the coal maceral (inherent) or excluded from the coal matrix (extraneous). Furthermore, there is a great variation in size of the mineral grains between different coal sources. The variation of the mineralogy results in a variation in the nature of the ash produced. However, while the ash may be different the bulk chemical composition may show less variation. This difference makes it very difficult to relate the chemical composition of the ash to the behavior of the ash in a combustion system. The mineralogical transformations of the minerals during combustion are complex and do not lend themselves to simplistic correlations. The coal mineralogy is established using a technique called computer controlled scanning electron microscopy (CCSEM). This technique determines the size and chemistry of the various minerals observed in coals. Specifically, CCSEM analysis establishes the size distribution of mineral species in the sample.

Knowing the mineralogy of the coal is the first step in understanding the deposits and their relation to corrosion. It is important to establish the mineralogy of the ash produced in the combustion system. This is performed by again using CCSEM analysis on ash which has passed through the system (fly ash). The comparison of the mineralogy of the coal and the mineralogy of the fly ash allows determination of the complex phase transformations of the minerals. Furthermore, by establishing the mineralogy of the ash it is possible to identify precursors to deposition and potential corrosive molten phase formation within the deposit.

The second stage is to examine and understand the phase relationships within the deposits present on a corroded tube. This analysis is in addition to the forensic analysis of failed or corroded superheater and reheater tubes. Normally, the tube sample is subjected to visual and metallurgical analysis. In cases where fireside corrosion is suspected, the ash deposit is sometimes subjected to x-ray diffraction and chemical analysis. It is from the powder x-ray diffraction analysis of the ash on the tube that the basis of the phase relationship within the deposits and the corrosion was postulated. Table 2 lists some of

the phases associated with high temperature corrosion and the melting point of these phases.

All the phases listed in Table 2 have melting points around the metal skin temperature of the tube. There are a number of issues to discuss with respect to the phases listed. First, the detection of these phases is performed by x-ray diffraction analysis. This analysis only detects crystalline phases and therefore, does not identify "molten" or amorphous phases. The second issue is the application of melting point data for complex salt mixtures. Mixtures of salts such as those found in these deposits will have eutectic and liquidus temperatures below that of the melting point of the pure end members. Therefore some knowledge of the mixture is necessary in order to assess the impact of the phase on melting. This data is obtained by performing an analysis called scanning electron microscopy point count (SEMPC) at and around the corrosion interface. SEMPC was developed to determine the phase assemblage of coal ash deposits. The technique involves the analysis of over 200 random points using scanning electron microprobe analysis methodologies. The chemical analysis of each point is then processed through a normative computer program which establishes if the point can be classified as a given phase. For example, a point is classified as quartz when the chemical analysis contains essentially pure silicon and oxygen (oxygen is determined by difference). More complex phases such as mullite ($3Al_2O_3.2SiO_2$) are classified based on the presence of essentially silicon,, aluminum, and oxygen with the silicon and aluminum at the correct molar ratio (within a reasonable tolerance). The analysis involves the identification of crystalline and amorphous phases. The results are used to determine the type of bonding in an ash deposit and the role of the various phases in deposit growth and development of strength. This involves the application of models of ash transformations and viscosity. Furthermore, the ability to identify and quantify the various amorphous or molten phases allows determination of key characteristics which are related to the chemical composition. These characteristics include the eutectic temperature of a selected region or phase and the potential for reaction with another phase. The eutectic temperature is obtained from phase equilibria.

The potential for reaction is obtained by looking at the base to acid ratio of the individual points classified as amorphous in the SEMPC analysis. Highly basic phases will tend to be more reactive towards acidic phases than other basic phases. Thus it can be seen that SEMPC analysis can have great value in establishing the characteristics of corrosion interfaces. The technique can identify the various phases which are present including the amorphous phases. The eutectic and melting characteristics can be obtained from suitable phase equilibria data and models. Mass transfer of corrosion products and corrodents can be determined using a model of viscosity. Corrosion potential is determined by examining the propensity for interaction between the different amorphous phases (acidic or basic) with the basic or amphoteric oxides of the protective scale. Another advantage of the application of the SEMPC technique to the study of ash corrosion is the ability to determine the relationship between key components within the deposit. For example, while it is difficult to identify the presence of a potassium pyrosulfate phase by x-ray diffraction it is possible to identify phases rich in potassium and sulfur with molar ratios corresponding closely to that of pyrosulfate (i.e. K/S = 1.0 while potassium sulfate has a molar ratio of K/S = 2). Furthermore, the presence of iron with this and similar "corrosive" phases indicates the role of this phase in the corrosion process. Another area where the SEMPC analysis can be used is to establish the change in chemistry and phase within the deposit. As noted above, a phase commonly associated with high temperature corrosion is that of potassium aluminosulfate. This phase is of particular interest as there is no direct precursor to this phase from the coal mineralogy. In most coals all the aluminum is observed with clay species such as kaolinite and illite. Furthermore, the potassium is also mainly associated with the illite clay in coals. A simplistic reaction pathway for this phase would be:

Kaolinite ($Al_4Si_4O_{10}(OH)_8$)+ Illite ($K_{1-1.5}Al_4Si_{7-6.5}Al_{1-1.5}O_{20}(OH)_4$)+$SO_3$ = $KAl_2(SO4)$ (s) + melt

The melt phase would be a mixture of potassium aluminosilicates, the composition of which would be dependent on the original mineral chemistry and the amount of

potassium aluminosulfate formed. Clearly, significant disassociation of the aluminosilicates is necessary to facilitate the reaction of the aluminum and potassium from the reactants. This is not observed in most coal ash deposits where the Si/Al molar ratio (a defining parameter for most clay species) tends to remain constant. The SEMPC technique not only allows one to detect and quantify the amount of potassium aluminosilicate, amongst other phases, but can give valuable insight into the nature of the melt phase. In relation to corrosion the following question is postulated: is the potassium aluminosulfate the corroding phase or is the amorphous phase associated with the potassium aluminosulfate which causes the corrosion.

An example of SEMPC data is given below. The deposit was from a superheater tube where corrosion had been noted based on ultrasonic thickness measurements. The deposit was scraped off and submitted for SEMPC analysis. The phase assemblage is listed in Table 3. The phases include iron oxide, mullite, calcium silicate, calcium sulfate, ferric sulfate, pyrrhotite (FeS), pyrite, aluminosilicate (resembling kaolinite clay) and unclassified phases. The unclassifieds represent the amorphous phases. As part of the SEMPC analysis the points are averaged to obtain a "bulk" chemical composition. This chemical composition corresponds to the average chemistry of the region selected for the analysis and represents the region where the corrosion occurs. The ability to separate the different phases, and thus the corresponding chemistry, allows a determination of the average composition of the amorphous phases. Both these chemical compositions are listed in Table 4. The data shows that the bulk composition of the deposit was enriched in iron oxide, sodium oxide, and sulfur trioxide compared to the original coal ash (12% Fe_2O_3, 1 % Na_2O, 3% SO_3). The amorphous phase was further enriched in SO_3, Na_2O, and K_2O and depleted in CaO and Fe_2O_3. This data shows that the corrosion was due to the presence of a corrosive alkali sulfate phase. However, further analysis can be performed on the SEMPC results. For example, Figure 1 shows a ternary molar plot of Fe, S, and Na for all the points rich in iron, sulfur, and sodium. The graph shows that sulfur is only associated with the points with 5-10 mole % sodium. However, no definitive phase can be ascertained confirming the amorphous nature of the corroding phases. Similar graphs can be produced to establish the relationships between selected components in order to develop a more accurate assessment of the effect of ash chemistry and mineralogy. Furthermore, from this data methods to predict the corrosive potential of a given coal ash with gas and metal temperatures can be developed.

CONCLUSION

The phase relationships in coal ash deposits and their effects on high temperature corrosion have been introduced. The complex nature of deposition and corrosion can be studied by the application of advanced analytical techniques such as computer controlled scanning electron microscopy (CCSEM) and scanning electron microscopy point count (SEMPC). The valuable data from these techniques combined with design and operating conditions can be used to develop methods to control coal ash corrosion.

Table 1

Common Minerals Observed in Coal

Mineral name	Nominal Chemistry
Quartz	SiO_2
Pyrite	FeS_2
Kaolinite	$Al_4Si_4O_{10}(OH)_8$
Illite	$K_{1-1.5}Al_4Si_{7-6.5}Al_{1-1.5}O_{20}(OH)_4$
Calcite	$CaCO_3$

Table 2

Melting Point of selected phases observed in ash deposits

Compound	Melting Point/°C
$K_3Fe(SO_4)_3$	618
$K_3Al(SO_4)_3$	654
$Na_3Fe(SO_4)_3$	624
$Na_3Al(SO_4)_3$	646
$KFe(SO_4)_2$	694
$NaFe(SO_4)_2$	690

Table 3

Phase Assemblage of Deposit as Determined by SEMPC

PHASE	VOLUME %
MULLITE ($3Al_2O_3.2SiO_2$)	0.5
CALCIUM SILICATE ($CaSiO_3$)	0.5
IRON OXIDE	18.6
ANHYDRITE ($CaSO_4$	1.0
FERRIC SULFATE ($Fe_2(SO_4)_3$)	4.0
PYRRHOTITE (FeS)	2.0
PYRITE (FeS_2)	1.0
ALUMINOSILICATE (KAOLINITE)	1.0
UNCLASSIFIEDS	71.4

Table 4

Chemical Composition of Ash Deposit

OXIDE	BULK	AMORPHOUS
SILICA	18.1	21.5
ALUMINA	10.3	12.0
IRON OXIDE	36.2	24.7
TITANIUM DIOXIDE	0.5	0.5
PHOSPHOROUS PENTOXIDE	0.3	0.4
CALCIUM OXIDE	1.2	0.6
MAGNESIUM OXIDE	1.0	1.1
SODIUM OXIDE	3.4	4.1
POTASSIUM OXIDE	1.9	2.5
SULFUR TRIOXIDE	26.8	32.1

Figure 1

Ternary plot of sodium, sulfur and iron.

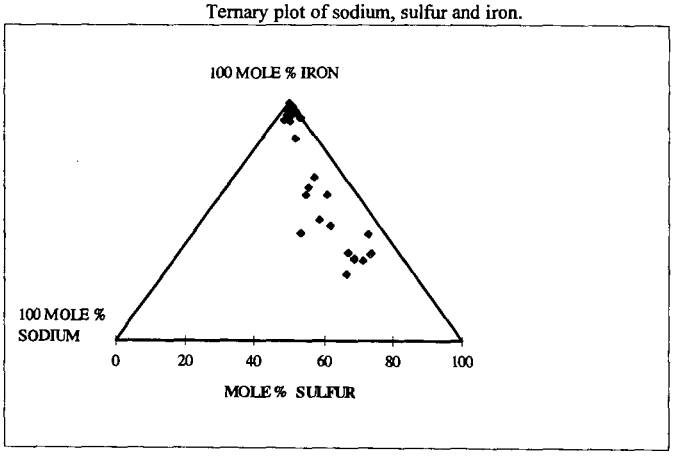

INFLUENCE OF ASH DEPOSIT CHEMISTRY AND STRUCTURE ON PHYSICAL AND TRANSPORT PROPERTIES

Larry L. Baxter
Combustion Research Facility
Sandia National Laboratories
Livermore, CA 94550

Keywords: Combustion, Ash, Heat Transfer in Porous Media

Abstract

Boiler ash deposits generated during combustion of coal, biomass, black liquor, and energetic materials affect both the net plant efficiency and operating strategy of essentially all boilers. Such deposits decrease convective and radiative heat exchange with boiler heat transfer surfaces. In many cases, even a small amount of ash on a surface decreases local heat transfer rates by factors of three or more. Apart from their impact on heat transfer, ash deposits in boilers represent potential operational problems and boiler maintenance issues, including plugging, tube wastage (erosion and corrosion), and structural damage.

This report relates the chemistry and microstructural properties of ash deposits to their physical and transport properties. Deposit emissivity, thermal conductivity, tenacity, and strength relate quantitatively to deposit microstructure and chemistry. This paper presents data and algorithms illustrating the accuracy and limitations of such relationships.

Introduction

Ash deposit properties in boilers depend on both deposit structure and composition. Thermal conductivity and emissivity, the two properties with the greatest impact on heat transfer, demonstrate strong and complex dependencies on both deposit structure and composition. The effects of deposit structure relate largely to the phases present in the deposit and the extent of sintering or contact between individual particles. This paper focuses on the effects of emissivity and porosity variations on heat transfer through boiler deposits.

Heat and mass transfer through porous media depend on macroscopic and microscopic structural properties of the media. Upper and sometimes lower bounds for transfer coefficients can be established based on easily measured structural properties, but precise expressions for transfer rates depend on a high level of structural detail, commonly beyond what could reasonably be expected to be available in practical applications. Our approach is to identify the limits and increase the level of sophistication of our models up to the point that we make the best use of available information.

Results

A useful idealization for illustrating the major effects of deposit structure on thermal conductivity is a solid of known porosity and thermal conductivity and with no conduction in the gas phase. Quanta of vibrational energy (heat) move randomly through this solid. A temperature gradient in the solid is represented by spatial differences in the population of phonons. We seek an expression relating the efficiency at which phonons can move through the porous material to its physical structure. In this simple model, heat transfer proceeds through the solid phase at its customary rate but stops when it encounters the void phase.

Spatial autocorrelation functions relate the probability of two locations being the same phase (solid or void) as a function of distance between them. Generally, autocorrelation functions are bounded by ± 1 and are identically unity at displacements of 0. Characteristically for real materials, they also decay to a limiting values in a smooth but not necessarily monotonic fashion. For isotropic material, the limiting value is the volume fraction of the phase present at a displacement of 0. If the presence of void vs. solid phase is represented as a random event, there are fairly general conditions under which the autocorrelation becomes an exponential decay, with the spatial constant of the exponent a measure of average grain size.

In addition to the amount of solid vs. void volume in the material, the connectedness of the solid phase plays a large role in determining the heat transfer rate. There are higher order correlation functions and connected correlation functions that statistically give clues to the connectedness of a phase. The concept of tortuosity is the approach we have taken, where the tortuosity is defined as the shortest average path length through the solid phase between two points divided by the straight-line distance between the same points. As the solid phase becomes less connected, the tortuosity increases. Using these three most readily available characteristics of the solid phase, the solid volume fraction, the mean particle size, and the tortuosity, we have developed a model for the dependence of the average thermal conductivity on structural properties. We are currently pursuing means of extending the model to nonisotropic conditions more sophisticated descriptions of deposit structure. In its current state, the heat transfer model depends on material porosity and tortuosity

of both the condensed and gaseous phases, in addition to the thermal conductivity of the two phases.

Aside from the anisotropies of the material, this approach largely ignores the efficiency of the connections between particles. Particles that connect at a single point or over a very small area typically conduct heat far worse than those that are connected over large fractions of their projected areas. In some analyses, the connection points dominate the heat transfer process. This connectedness is captured somewhat, but not entirely, in the concept of the tortuosity. We will examine this aspect of our model in the future. In its current state, it may somewhat over-predict the heat transfer rate in porous media.

The over-prediction is partially compensated by the effect of our initial assumptions. In the original model, the void space was assumed to be non-conducting and radiative heat transfer through the material is ignored. In reality, both intra-media radiative heat transfer and conduction through the gas phase occur. At present, we allow these two simplifications in the model and recognize that they are somewhat balanced by the incomplete descriptions of connectedness of particles in the condensed phase.

In its current state, the heat transfer model reveals some useful insights. These will be illustrated by models of heat transfer through artificially conceived by realistic deposits under boiler-like conditions. The deposits are assumed to exist on cylindrical surfaces and the analysis at this point is limited to one dimension, i.e., the radial dimension.

One dimensional, transient heat transfer through a cylindrical surface is described by

$$\rho \hat{C}_p \frac{\partial T}{\partial t} = k\left[\frac{1}{r}\frac{\partial}{\partial r}\left(r\frac{\partial T}{\partial r}\right)+\frac{1}{r^2}\frac{\partial^2 T}{\partial r^2}\right] \tag{1}$$

Where traditional symbols are used for density, heat capacity, temperature, time, and radial direction and the effective thermal conductivity is represented by k. If the transient term is ignored, the partial differential equation becomes an ordinary, second-order differential equation of the form

$$0 = k\frac{1}{r}\frac{d}{dr}\left(r\frac{dT}{dr}\right) \tag{2}$$

which can be solved directly. Two constants, a and b, are involved in the solution as constants of integration in the first and second steps of the solution as follows

$$a = r\frac{dT}{dr} \tag{3}$$

and

$$T = a\ln(r)+b \tag{4}$$

By equating the surface heat flux at the fireside of the deposit with the heat flux conducted through that deposit at that location,

$$-k\left.\frac{dT}{dr}\right|_{r=r_2} = q \tag{5}$$

the first constant can be evaluated as

$$a = \frac{-qr_1}{k} \tag{6}$$

The second constant is evaluated by equating the temperature at the inner surface of the deposit to the boiler tube surface temperature

$$T(r_i)=T_i=\frac{-qr_i}{k}\ln(r_i)+b \tag{7}$$

which yields

$$b=T_i+\frac{qr_i}{k}\ln(r_i) \tag{8}$$

rendering a final solution of the form

$$T(r)=T_i-\frac{qr_i}{k}\ln\left(\frac{r}{r_i}\right) \tag{9}$$

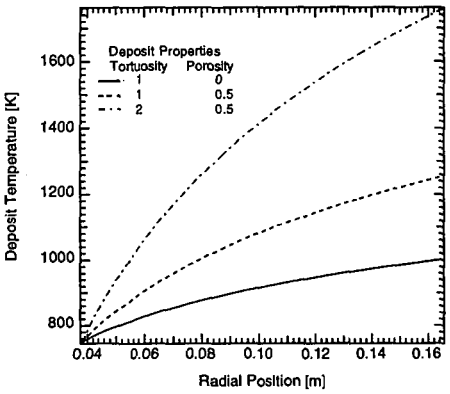

Figure 1 Parametric variation of deposit temperature as a function of position for various values of the solid volume fraction and tortuosity. See text for details of incident heat flux, etc.

This form reduces to a linear dependence of deposit temperature on distance in the limit of small deposit thickness relative to the radius of curvature. An example temperature profile is illustrated in Fig. 1 for the case of a five-inch deposit resting on a three-inch, outside-diameter steam tube with a 750 K surface temperature exposed to a heat flux of 10 kW/m^2 and with a thermal conductivity of 2.22 W/(m K). Both the porosity and tortuosity are considered to be unity in the base case, with both parameters being varied by a factor of two to illustrate the effects of deposit properties on the temperature profile. The temperature range depends linearly on the tortuosity and inversely on the porosity such that a change in either quantity changes the difference between deposit surface temperature and tube surface temperature by the same factor. The extent of curvature in the prediction is determined by geometry, not deposit physical properties. Deposits with solid volume fractions lower than (more porous than) 0.5 and tortuosities higher than 2 are common in many systems.

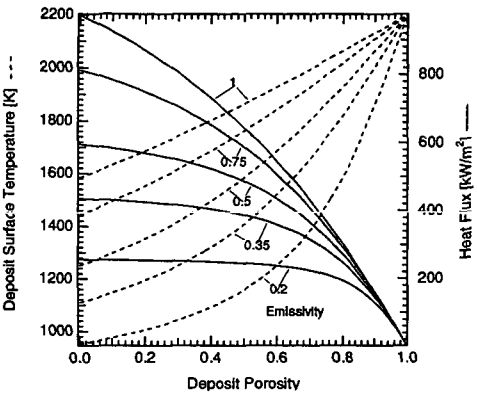

Figure 2 Deposit surface temperature and heat flux as a function of porosity and emissivity assuming no intra-deposit radiative heat transfer and a non-conducting gas phase. Tortuosity is assumed to be unity.

The previous predictions assumed that the incident heat flux, whether from radiation or convection, does not change as deposit surface temperature changes. In practice, incident heat flux is strongly coupled to deposit surface temperature. As an illustration, the heat transfer model predictions for the furnace section of a typical boiler are illustrated below. Only radiative heat transfer is considered, with an assumed black body radiative temperature of 2200 K, deposit thickness of 2 mm, deposit solid phase thermal conductivity of 2.22 W/(m K), and a waterwall composed of 750 K walls made of four inch OD tubes. Predictions of deposit surface temperature and heat flux are illustrated for a range of porosity and deposit emissivity values. Intra-deposit radiative heat transfer and intra-deposit conductive heat transfer through the gas phase are neglected and deposit tortuosity is assumed to be unity. None of these assumptions is generally accurate. They are made here to allow illustration of the impact of porosity and emissivity on heat transfer.

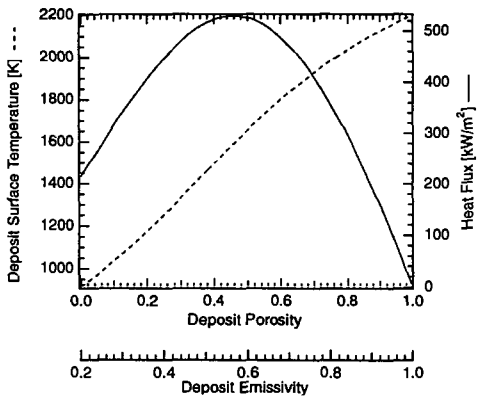

Figure 3 Deposit surface temperature and heat flux under the same assumptions as in Figure 2 but assuming a linear relationship between emissivity and porosity.

The parametric graph indicated in Fig. 2 belies the potential complexity of the relationships between deposit physical properties and heat transfer rates. While the trends in Fig. 2 indicate relatively smoothly varying and monotonic relationships between emissivity or porosity and heat flux, in practice the relationship may not be monotonic. In many cases of practical interest porosity and emissivity are correlated. Heat fluxes under such conditions may not vary monotonically with physical properties. Figure 3 illustrates the trends with an assumed linear relationship between porosity and emissivity, as read by the dual abscissae. As the relationships become more complex, and as factors such as intra-deposit radiative heat transfer and tortuosity are included, the relationships can become increasingly complex.

Structural properties of ash vary temporally, effecting changes in both porosity and tortuosity. A common example is sintering or melting of deposits, accompanied by increases in particle-to-particle contacting area and decreases in tortuosity and porosity. A simple example is illustrated in Fig. 4. In an idealized case of uniform spheres, a change in linear dimension of less than 15 % is accompanied by a change in contacting efficiency of theoretically zero in the initial case to 50 % in the slightly sintered case. This gives rise to proportional changes in tortuosity and the porosity changes from 0.48 to 0.17. Such changes lend themselves to mathematical treatments in predicting heat transfer through ash deposits. Similar treatments describe the effect of condensation or sulfation on deposit microstructure. These have been used in the past to explain the development of deposit properties ranging from tenacity to strength.

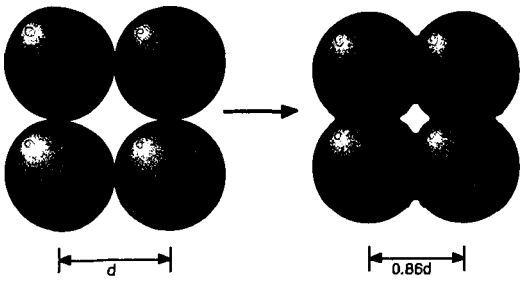

Figure 4 Conceptual illustration of the changes in contacting efficiency and tortuosity with sintering/melting.

As a practical example, Figure 5 is a scanning electron micrograph of a deposit produced during combustion of rice straw in Sandia's Multifuel Combustor. The deposit was generated on the wall of the MFC combustor and accumulated over a 3 hour test period. The wall temperature was 900 °C, the gas temperature was 1000 °C, and the gas composition is estimated to contain 6 % oxygen. Most of the deposit has a glassy appearance, with occasional nodules under the otherwise smooth surface.

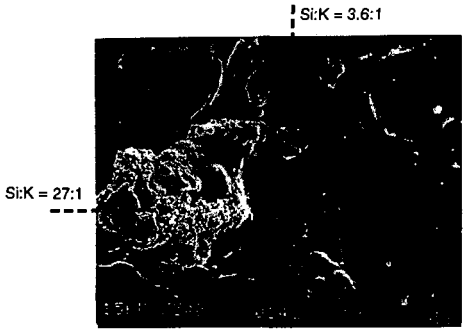

Figure 5 Scanning electron micrograph of a portion of a rice straw deposit collected from a ceramic surface in the MFC. The porous, silica based material was exposed by fracturing the deposit though one of the nodules evident in many locations on the smooth, glassy surface.

The deposit composition is determined as a function of location on the surface using electron dispersive spectroscopy in a scanning electron microscope. Both phases are composed principally of silicon. By comparison with the nodules, the glassy phase contains more nonsilaceous material. More than half of the nonsilaceous fraction is potassium.

For example, the melting point of silica decreases from about 1700 °C to less than 750 °C as potassium is introduced to form potassium silicates. Incorporation of additional materials, in particular other alkalis and alkaline earth materials, usually lowers the melting point further still. The silicon to potassium ratio observed in the glassy portions of the deposit illustrated in Figure 5 is about 3.4 on a mass basis, or about 81 % SiO_2 to 19 % K_2O. An equilibrium mixture of such material becomes completely molten at approximately 1300 °C. This is slightly above the temperature of deposit, but the addition of calcium and other heteroatoms to this mixture reduces the melting point significantly. The nodular material, on the other hand, has a much higher melting point. These changes in phase have obvious effects on the microstructure of the deposit and hence on its physical and transport properties.

Conclusions

Ash deposit microstructure influences the mechanical and transport properties by impacting the degree of connectedness between particles and the tortuosity of heat transport through the deposit. Mathematical models are used to predict the impact of microstructural features on bulk deposit properties and on resulting boiler performance. Deposit surface temperatures can change many hundreds of degrees, depending on deposit thermal and structural properties. Heat fluxes are also dominantly influenced by similar structural properties. Two properties that encapsulate much of the deposit microstructure effect are the porosity and tortuosity. Rational models of the dependence of thermal conductivity on these parameters are presented with predicted results. Experimental examples of how tortuosity and porosity develop in deposits, depending on deposit phase, are also presented.

ALGEBRAIC INTERPRETATION OF COMPOSITION PHASE CLASSIFICATION CRITERIA FOR CCSEM.

Peter N. Slater, M. Bret Abbott, and John N. Harb
Department of Chemical Engineering and Advanced Combustion Engineering Research Center
Brigham Young University
Provo, UT 84602

Keywords: CCSEM, Fly Ash, Classification

INTRODUCTION

Data from computer controlled scanning electron microscopy (CCSEM) are typically interpreted by grouping particles into bins based on their elemental compositions. Some of the bins correspond to well-defined mineralogical species or phases with known properties. Other bins are defined for convenience so that similar particles can be grouped together. Experience has shown that it is difficult to predict *a priori* what phases will be determined in an analysis; this is particularly true in the case of fly ash samples which are largely amorphous at combustion temperatures. Often a large number fraction of the analyzed particles do not fit any of the predefined phases and are classified as unknown. In such cases, it is difficult to interpret the analysis results since nothing is known about a large fraction of the sample. It is desirable then to have a means of extracting some sort of composition information from the unclassifiable particles. This paper addresses the problem of defining new bins to describe particles which do not fit into the predefined classifications using an algebraic formulation of the criteria.

METHOD

CCSEM reports particle compositions as n-dimensional vectors, where n is the number of elements analyzed. Typically, n is equal to twelve and the elements are Na, Mg, Al, Si, P, S, Cl, K, Ca, Ti, Fe, and Ba. To determine whether or not a given composition belongs to a phase, numerical tests or criteria are applied. These tests are linear inequalities, e.g., $Si + Al \leq 80$, or ratios, e.g. $Si/Al \leq 2$, which can be expressed as linear inequalities. Therefore, the test for membership in a phase can be written as a system of linear inequalities. Using matrix notation, the test can be written $Ax \leq b$, where the rows in the matrix A and the vector b correspond with the individual criteria.

Consider for example, a simple system with two elements, X and Y, and two phases, A and B with constraints as follows:

Phase A	Phase B
$x \leq 40$	$x \geq 80$
$y \leq 40$	$y \leq 40$
	$x + y \leq 100$

It is implicitly assumed that compositions are limited by zero below and by one hundred percent above. The algebraic forms for these two phases would be:

Phase A	Phase B
$\begin{bmatrix} 1 & 0 \\ 0 & 1 \end{bmatrix}\begin{bmatrix} x \\ y \end{bmatrix} \leq \begin{bmatrix} 40 \\ 40 \end{bmatrix}$	$\begin{bmatrix} -1 & 0 \\ 0 & 1 \\ 1 & 1 \end{bmatrix}\begin{bmatrix} x \\ y \end{bmatrix} \leq \begin{bmatrix} -80 \\ 20 \\ 100 \end{bmatrix}$

Note that the sign of the first constraint for phase B has been changed so that it could be written in the less than or equal to form. The phases can also be represented as regions in the x-y plane, as illustrated in Figure 1. Any composition (x,y) falling with the square region at the lower left would be classified as phase A. Likewise, phase B would comprise any composition falling within the triangular region at upper right. Any other composition, such as the points indicated in the figure, would be unclassified.

The unclassifiable points in Fig. 1 appear in two distinct clusters. One is nearer to phase A and the other is nearer to phase B. The observation that unknown particles tend to appear in clusters when plotted in this fashion and that a cluster would of necessity lie closest to one phase is the basis for the algebraic classification scheme: find the distance to each of the defined phases and then group the composition with the phase having the shortest distance.

Finding the distance from a point to a given phase is an optimization problem called a quadratic program. The quadratic objective function is the square of the Euclidean distance from the composition to a composition that meets the phase's criteria. By minimizing this objective function subject to the criteria, the composition within the phase closest to the given composition is determined. Examination of the resulting groupings of unknown compositions from a complete CCSEM analysis reveals trends and clusters of points which can be used to define new phases. This classification scheme is shown in Fig. 2.

The algorithm has been implemented using a sparse matrix data structure to minimize the memory and computational requirements. Several thousand known compositions can be classified

in minutes on a 75MHz Pentium computer. Using a numerical Sequential Quadratic Programming (SQP) algorithm to solve the quadratic programs on an HP 9000/755 workstation, several thousand unknown compositions can be classified in about an hour. The number of optimizations required is m·p, where m is the number of unknown particles and p is the number of known phases. Given this dependence, it has proven wise to start with a relatively small number of particles, several hundred rather than several thousand, and define new phases based on the initial results before proceeding to the complete data set. This dramatically reduces the number of optimizations.

RESULTS AND DISCUSSION

The method has been applied to the analysis of ash derived from Pittsburgh #8, an eastern subbituminous coal, and ash from Black Thunder, a western subbituminous coal from the Anderson seam of the Powder River Basin. ASTM ash analyses of the elemental oxides from both coals are presented in Table 1. Note the low-rank Black Thunder contains a great deal of organically bound calcium and relatively few discrete mineral grains. Its ash, therefore, is expected to be significantly influenced by the organically bound constituents. The inorganic content of Pittsburgh #8, however, is primarily discrete minerals. The major mineral species found in the Pittsburgh coal are pyrite, quartz, aluminosilicates, potassium aluminosilicates, pyrite, and calcite [1]. The ash of Pittsburgh #8 is controlled by the transformations (coalescence and fragmentation) of the discrete minerals during combustion.

Ash data from both coals were classified using a typical set of phases. This set consisted of 47 well-defined phases [3] and several more loosely-defined aluminosilicate phases. The results of the classification are presented in Table 2. The heavy line separates the loose phases from the phases that were more well-defined. Minor phases have been omitted from the table for brevity. The phase set used is clearly inadequate for characterizing these ashes; 58% of the Black Thunder and 24% of the Pittsburgh #8 particles were unclassifiable. In fact, only 14% of the Black Thunder and 7.54% of the Pittsburgh #8 was classified with the well-characterized bins, and the majority of that was quartz.

In the Pittsburgh #8 ash, 39% of the particles contained five mole percent or more iron. Of these, 19% or nearly half of the iron-bearing particles were unclassifiable. Given the importance of iron in ash deposition behavior, it is essential to know more about its occurrence in the ash than is provided by the this typical phase set.

The algebraic classification scheme was applied to the Black Thunder ash using the 47 well-defined phases. Results are tabulated in Table 3. The quantities are reported in percentage of original particles (classifiable plus unclassifiable). Minor phases (less than 1% of total) have been omitted. Only values for Mg, Al, Si, Fe, and Ca are reported since these five elements were found to be sufficient to characterize the bins. Of course, other elements do play a role in the properties of individual particles and the category as a whole. Their omission in the table does not imply that they should be ignored when the CCSEM analysis is interpreted. The table includes the mean value and standard deviation for each of the elements included.

Using the 47 phases, 85% of the Black Thunder ash particles were unclassifiable. The algebraic classification scheme was able to classify 82% of the particles into eight major phases. The contents of the various bins are distinct from one another, as evidenced by the differences in the means of the major elements which characterize each bin. The "near quartz" category has the highest mean silicon content, 76%. Several bins share the same major elements, but in clearly distinguishable compositions. It is sometimes desirable to further subclassify these bins; preliminary work has shown that classifications based on the ranking of the four most abundant elements in a particle is a good basis for distinguishing composition within a nearest-phase category.

To focus on the distribution of iron in the 24% of the particles that were found unclassifiable, the algorithm was applied to the Pittsburgh #8 ash using the phase set which included the loosely-defined bins. The results for the major iron-containing bins are presented in Table 4. Bins were chosen for inclusion based on the fraction of the total iron-bearing particles they contained; bins with less than one percent have been omitted. It is clear that most of the unclassifiable particles contain iron and that they can be grouped into nine major categories. The means in these categories are distinct, indicating that the algorithm has indeed differentiated the particles.

In most cases, particles did not fit into their nearest phases because they contained too much of a minor constituent. Cutoffs are typically five mole percent. In the "near Fe-Al-Silicate" phase, 44% of the particles contained too much calcium, 32% contained too much potassium, and 18% contained too much sodium. Many particles violated more than one constraint; i.e. they contained too much of two or more elements. Examination of the reasons why particles do not fit the known phases yields insight into both the ash composition and the mechanisms by which it formed.

CONCLUSIONS

Particle composition classification schemes must be designed to provide meaningful information about specific ash samples due to the variability in the parent fuels and combustion conditions. Using a generic set of phases, large fractions of the particles are often unclassifiable.

The algebraic interpretation of the phase criteria provides a straightforward means of classifying these particles with no assumptions about the dominant elements or the form that the new classifications should take. The classifications thus made provide a number of distinct categories that can be used to characterize the ash.

ACKNOWLEDGMENTS

The authors wish to thank David P. Kalmanovitch for his invaluable assistance in formulating the criteria used to identify crystalline phases. Rachel Newsom and Eyas Hmouz undertook the tedious work of translating the phase criteria for use with the algebraic classification program. This work was funded by the U.S. Department of Energy under the University Coal Research Program, Grant No. DE-FG22-93PC93226. Additional funding was provided by the Advanced Combustion Engineering Research Center (ACERC) at Brigham Young University. Funds for ACERC are received from the National Science Foundation, the State of Utah, 42 industrial participants, and the U.S. Department of Energy.

REFERENCES

1. Harb, J.N. (1994) Investigation of Mineral Transformations and Ash Deposition During Staged Combustion, Quarterly Progress Report #3, U.S. Department of Energy Contract DE-FG22-93PC93226.
2. Richards, G. H. (1994) Investigation of Mechanisms for the Formation of Fly Ash and Ash Deposits for Two Powder River Basin Coals, Ph.D. Dissertation, Brigham Young University, Provo, UT, 84602.
3. Kalmanovitch, D.P. (1991) Personal Communication

Table 1. Ash Oxide Analyses (SO_3-free) of Black Thunder and Pittsburgh #8 Coals

Weight % of Ash	Black Thunder [2]	Pittsburgh #8 [1]
SiO_2	36.7	47.86
Al_2O_3	19.7	21.79
Fe_2O_3	6.1	18.01
TiO_2	1.5	1.06
CaO	25.5	6.69
MgO	5.7	1.16
Na_2O	1.7	0.75
K_2O	0.4	1.73
P_2O_5	1.1	0.37

Table 2. Phase Distribution of Ash Particles

Phase	Black Thunder (% of particles)	Pittsburgh #8 (% of particles)
Quartz	12.38	5.31
Iron Oxide/Carbonate	0.0	2.23
Plagioclase Solution	1.76	0.0
Kaolinite	12.54	35.77
Ca-Al-Silicate	6.2	3.61
Na-Al-Silicate	5.35	1.8
K-Al-Silicate	1.44	8.67
Fe-Al-Silicate	0.21	14.55
Fe-Silicate	0.37	2.37
Unclassified	57.57	24.53

Table 3. Nearest Phase Classifications of Black Thunder Ash

Phase	Nearest Phase	%		Mg	Al	Si	Ca	Fe
1	Quartz	3.4	ave	2.0	8.2	76.1	5.6	1.6
			std	7.5	4.3	19.2	7.8	2.8
2	Ca-Aluminate	3.6	ave	11.7	29.8	4.6	45.1	6.5
			std	4.2	2.8	2.9	2.8	2.5
3	Tri Ca-Aluminate	35.4	ave	14.1	21.5	4.7	48.8	7.7
			std	5.5	7.8	3.4	6.8	3.9
4	Gehlenite	4.3	ave	8.9	26.5	12.4	38.4	8.7
			std	4.2	7.6	5.5	5.9	7.5
5	Gehlenite-Na melilite	2.7	ave	5.9	28.2	25.4	28.9	5.4
			std	3.0	4.9	7.8	6.4	5.7
6	Akermanite-Na melilite	5.8	ave	10.7	14.3	30.7	33.7	5.9
			std	7.2	6.9	15.5	7.9	5.8
7	Anorthite	1.3	ave	3.6	37.2	32.1	18.4	3.6
			std	2.4	4.4	5.5	3.9	3.2
8	Plagioclase Solution	25.2	ave	0.6	38.2	50.3	3.3	1.4
			std	1.4	9.7	8.5	4.5	3.4

Table 4. Nearest Phase Classification of Iron Particles in Pittsburgh #8 Ash

Phase	Nearest Phase	%		Na	Mg	Al	Si	S	K	Ca	Fe
1	Gehlenite-Na melilite	0.65	ave	0.8	1.8	23.9	27.4	4.0	0.4	24.8	13.4
			std	1.4	2.1	4.0	7.8	6.8	1.2	6.1	6.6
2	Akermanite-Na melilite	1.35	ave	1.5	5.4	15.0	26.4	3.3	0.1	25.3	17.8
			std	2.0	5.6	4.7	10.2	5.1	0.5	6.6	10.4
3	Anorthite	0.58	ave	0.5	2.1	32.5	34.7	1.8	0.7	15.0	10.3
			std	0.8	2.2	2.6	2.9	3.1	0.9	2.6	3.5
4	Plagioclase	1.2	ave	3.4	2.4	29.0	36.9	4.1	2.1	8.9	10.6
			std	2.7	2.3	4.8	5.5	6.3	1.7	3.5	4.5
5	Kaolinite	2.71	ave	0.7	0.9	21.3	68.1	3.0	1.6	1.2	2.1
			std	1.2	1.7	15.3	18.1	2.9	1.5	1.9	1.8
6	Ca-Al-Silicate	3.66	ave	1.2	4.3	28.4	35.0	1.8	1.1	19.0	5.8
			std	1.5	7.6	9.0	11.2	2.8	1.4	12.9	2.7
7	K-Al-Silicate	2.01	ave	3.9	1.4	31.1	39.8	3.4	7.7	1.3	4.4
			std	4.6	2.4	12.4	14.9	4.7	9.7	2.1	2.9
8	Fe-Al-Silicate	8.99	ave	2.7	2.9	30.0	37.4	1.4	3.2	4.2	15.5
			std	2.1	4.4	7.1	9.0	2.8	2.1	3.4	11.7
9	Iron Silicate	1.76	ave	1.9	1.7	10.9	23.5	4.9	0.6	5.0	49.6
			std	4.5	4.2	7.0	22.6	8.5	1.1	7.9	20.3

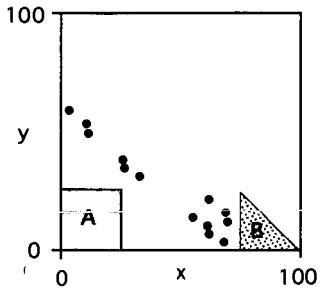

Figure 1. Phases A and B

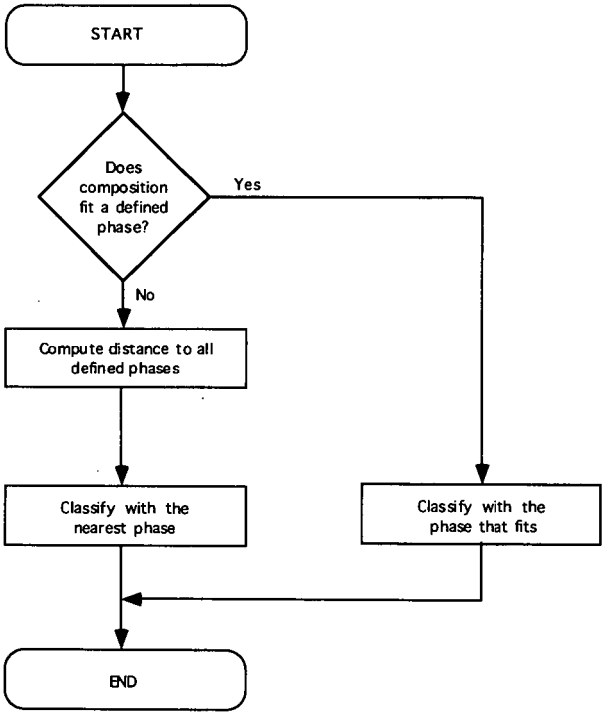

Figure 2. The Algebraic Classification Algorithm

SLAGGING BEHAVIOUR OF PEAT ASH

Heikkinen, R., Laitinen, R. S., Patrikainen, T., Tiainen, M., Virtanen, M.
Department of Chemistry, University of Oulu, Linnanmaa,
SF-90570 Oulu, Finland

Keywords: peat ash, slagging, SEM

INTRODUCTION

The use of peat for energy production in Finland dates back to early 1970's. For the present, the peat combustion is responsible for over 5 % of the energy production in Finland. Many of the major Finnish power plants still use pulverised fuel, but the utilisation of fluidised bed boilers is rapidly increasing. Boilers of this type are best suited for fuel with a low energy value because the increased efficiency is beneficial for the community heat distribution.

The Toppila power plant of Oulu Energy Company in the city of Oulu, Finland has two units. The older one, Toppila I, is a 250 MW boiler using pulverised peat as fuel. The new Toppila II boiler is a 310 MW circulating fluidised bed boiler. The power plant uses 15 000 m^3 of peat per day with full load.

The the slagging behaviour of peat ash varies depending on the bog peat is ogirinating. The plant shutdown because of extensive slagging may cause significant economical losses in the entire chain of energy production. Therefore the slagging behaviour of peat ash needs to be predicted already from peat prior to its combustion.

In coal ash chemistry the slag formation is connected to the presence of iron, sulphur, alkaline and earth alkaline metals in ash. These meatls act as fluxing agents in aluminium silicate systems.[1-3] Several predictive indices have been developed for coal in order to estimate the slagging tendency of coal ash.[4] These indices are based on the bulk analysis carried out in laboratory conditions using standard ashing methods.[5] These indices have been criticized, because the ash is not formed in the actual turbulent conditions with fast heating rate and real gas phase composition.[6] New methods have been developed to understand the sintering and slagging events. These methods use coal analyses, power plant parameters, ash analyses together with CCSEM, analyses from probe samples, fly ash samples, bottom ash samples, aerosols etc.[4,7-10]

RESULTS AND DISCUSSION

In this study we report the slagging behaviour of five peat samples (**A-E**) of different origin.With the exception of **B** the samples were collected from Toppila I and originate from Northern Finland. Samples of standard ash were analysed by using ICP- and DCP-AES , X-ray diffraction (XRD), and scanning electron microscopy with energy dispersive X-ray microanalysis (SEM-EDS). Table 1 presents the both the CHNS-analysis of the original peat sample and the elemental bulk compositions of standard ash from each sample.

The ash of peat **A** that is known to have a strong tendency to slag contains remarkable quantities of iron and relatively small amounts of aluminium and silicon oxides. The content of alkaline metals is quite low. The ash of peat **B** also known to be problematic contains a remarkably high amount of calcium. The sulphur content is also higher than in the harmless peat types **C**, **D**, and **E**.

X-ray diffraction powder diagrams were recorded with a Siemens D5000 diffractometer. Ash samples were carefully ground and mixed with ethyl alcohol to make a slurry which was spread on a glass plate for the diffraction experiment. Quartz, albite and anorthite are the most common minerals in peat ash. The tendency of peat ash to slag seems to correlate with high amounts of haematite and maghemite (peat **A**) or anhydrite (peat **B**).

Scanning electron microscopy (Jeol JSM-6400 and Link eXL system with the image analysis software) provides simultaneous information on the chemical composition and mineral content of fuel ash particles.

The mineral content of original peat is very low and the particles seem to be scattered throughout the organic material. Therefore we could not observe any minerals in peat. It was only after standard ashing [5] that inorganic material was visible in the SEM image.

The SEM images were produced by applying constant accelerating voltage of 15 kV and the current of $1.70 \cdot 10^{-6}$A. The magnification was 430X. When possible, the minimum of one thousand particles were analysed.

The composition of peat ash based on CCSEM can be visualized by using appropriate distribution diagrams (see Figure 1). The classification yields useful information when the corners in these "ternary" digrams are defined in terms of the total content of selected oxides. The composition at each corner is chosen in order to gain information about the potential glass formation in the slag particles. It can easily be seen from the diagrams in Figure 1 that the phase distribution in the ash particles of the harmless peat **E** is different from that in the severely slagging peat **A**. It is obvious that the content of iron-rich particles is greatly enhanced in the problematic peat ash. While the bulk analyses shown in Figure 2 do not provide information about the composition of discrete particles, they do reflect the differences in the particle distribution between the slagging and harmless fuel in a qualitative fashion (c.f. Figure 1).

The slagging indices were calculated from the bulk analysis of peat ash. As these indices have been developed for coal and depend on the sulfur content found in coal,[4] they are not suitable for the prediction of slagging behaviour of peat ash due to the very low sulphur content in each peat sample. This is exemplified in Figure 3 that shows the slagging index, R_s, of the standard ash for each peat sample **A-E**. In each case the slagging index implies relatively unproblematic behaviour upon combustion. It is known, however, that the peat **A** and **B** show a severe tendency to slag, whereas the peat **C**, **D**, and **E** are known to be relatively harmless. As seen from Figure 3, the slagging index does not carry information even on the relative slagging tendency. This is due not only to the low sulphur content but also due to the differences in the contents of silicon, phosphorous, sodium, potassium, calcium, and iron.

Two extensive tests in an actual power plant boiler have also been carried out. Samples were collected from the fireside by use of the slagging probes. Analyses were made from samples taken from fuel, slagging probes, and fly ash. The evaluation of the results is currently in progress, but it already seems apparent that the standard ash does not behave similarily to the actual boiler ash in all respects.

CONCLUSIONS

It is one of the corner stones in coal and glass chemistry [1,11] that alkaline metals, alkaline earth metals, iron, sulphur and phosphorous are able to lower the melting point and increase the viscosities of fuel ash particles. This phenomenom may lead to a severe slagging problem in the boiler superheater and wall area. It is important to design predictive tools for the ash slagging in order to prevent the major economical losses caused by a possible plant shutdown.

The mineral material in peat differs to a certain extent from that in coal. For example, both coal and peat contain iron in significant amounts. Coal, however, contains sulfur in larger amounts than peat, because iron is found as pyrite in coal, whereas in peat it occurs as siderite or as haematite. Therefore, we are currently developing a new classification technique to establish the mineral distribution of peat and peat ash particles. The method is based on CCSEM. The conventional classification utilizing CCSEM is based on the identification of mineral phases from the elemental composition of the particles. This approach might not be useful in the case of ash particles, since extensive glass formation takes place upon combustion. Therefore, the particle distribution is best judged on the basis of oxide distribution as illustrated in Figure 1. The choice of suitable corned compositions enables meaningful deductions to be made about the actual phases in the ash particles. The mineral composition of bulk ash can be studied with XRD powder diffraction. The tendency of ash vitrification, however, can also be observed from the shape of the diffraction diagrams.

REFERENCES

(1) Raask,E., *Mineral Impurities in Coal Combustion*,Hemisphere, New York,1985, 485 pp.

(2) Boni,A.A.; Helble, J.J.; Srinivasachar, S., EPRI, Effects of Coal Quality on Power Plants-Second International Conference, Saint Louis, Missouri, Sep 19-21,1990, p. 1.15-1.38.

(3) Huffman, G.P.; Huggins, F.E.; Shah, N.; Shah, A., *Progr. Energy Comb. Science* **1990**, *16*, 243-251.

(4) Winegardner, E. C., *Coal Fouling and Slagging Parameters*, ASME Publ.,1974.

(5) *Annual Book of ASTM Standards, Vol. 05.05 Gaseous Fuels; Coal and Coke*, American Society for Testing and Materials, 1989, D 3174-89, p. 302.

(6) Skorupska, N.M.; Couch,G., Engeneering Foundation Conference, June 20-25, 1993, Solihull, England, p. 137-150.

(7) Skrifvars, B.-J., *Report*, **1989**, *89-13*, Åbo Akademi,.

(8) Beér, J.M.; Sarofim, A.F.; Barta, L.E., Engineering Foundation Conference, March 10-15,1991, Palm Coast, Florida, p. 71-94.

(9) Hutchings, I.S.; West, S.S.; Williamson, J., Engineering Foundation Conference, July 16-22, 1995, Waterville Valley, New Hampshire, Session V.

(10) Lind, T.-L.; Kauppinen, E.I.; Valmari, T.; Klippel, N.; Mauritzson, C., Engineering Foundation Conference, July 16-22, 1995, Waterville Valley, New Hampshire, Session VII.

(11) Rawson, H. *Inorganic Glass-Forming Systems*, Academic Press, London, 1967, pp. 317.

Table 1. Ultimate and ash analyses of peat (**A**,**C-E** peat from domestic sources; **B** peat from abroad). **A** and **B** exhibit severe slagging. **C-E** are harmless.

Ultimate analysis	A %	B %	C %	D %	E %
C	49,1	50,3	52,9	51,0	52,0
H	6,08	5,84	6,34	6,66	6,39
N	2,77	1,44	2,50	2,79	1,27
S	0,22	0,31	0,27	0,21	0,13
O	32,9	35,6	33,8	33,5	36,6
ash	8,96	6,51	4,18	5,81	3,58
Standard ash composition of peat					
Na	0,02	1,10	0,43	0,43	1,48
Mg	0,78	2,92	2,32	1,15	1,68
Al	3,20	4,64	4,41	4,23	6,79
Si	6,17	17,31	8,87	17,40	19,64
P	4,62	1,34	2,28	2,35	1,97
K	0,06	0,96	0,83	2,47	2,75
Ca	7,99	21,53	17,14	8,00	9,17
Ti	0,06	0,31	0,15	0,14	0,50
Fe	61,37	7,68	38,97	27,79	18,56
B	0,19	0,04	0,23	0,15	0,21

* calculated value

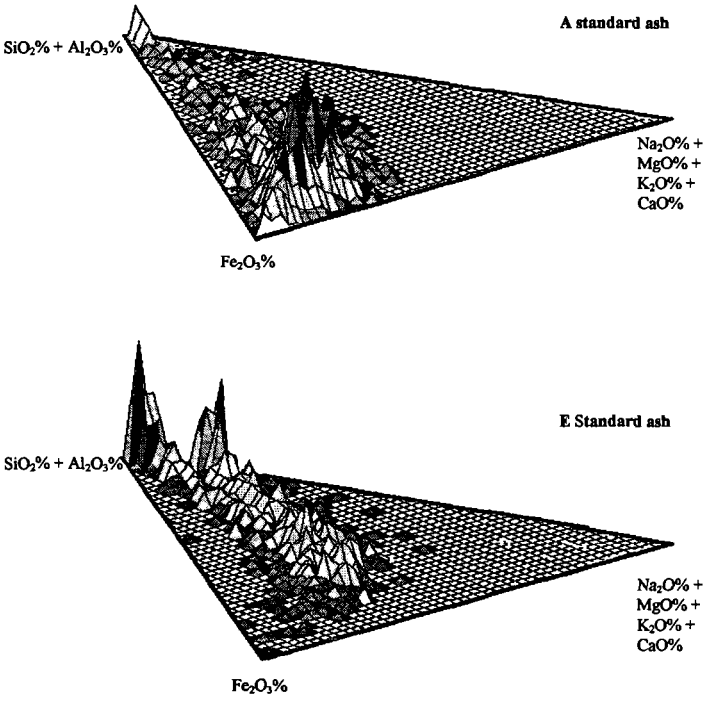

Figure 1. The compositional distribution of ash particles in slagging (**A**) and harmless (**E**) peat. The height of the column relates to the fraction of particles with the indicated composition. The ash particles of peat **A** are concentrated in the iron-rich region in the diagram implying the presence of low melting iron-silicates.

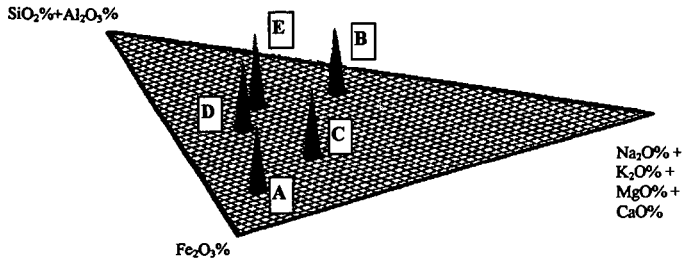

Figure 2. The bulk composition of standard ash from peat **A-E**.

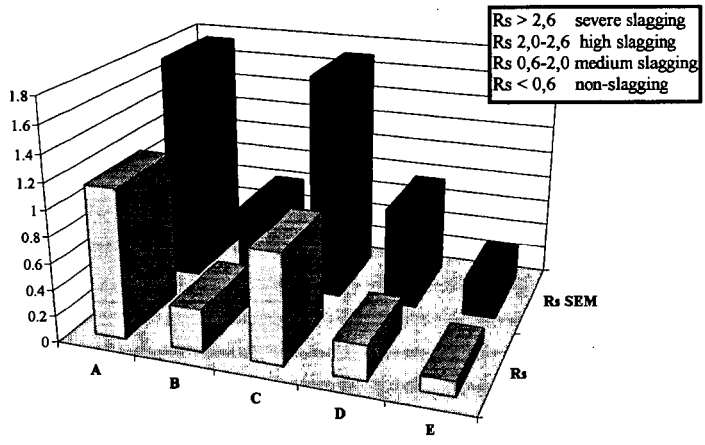

Figure 3. The slagging index [4] was calculated both from the bulk ash composition (R_s) and from the particle compositions as determined with SEM-EDS (R_s SEM). Both indices show the same trends. As indicated in the figure, these values are typical for non-slagging or medium slagging ash. However, due to the very low sulfur content in peat, R_s index is not directly applicable to peat. In fact **A** and **B** have turned out to exhibit severe slagging behaviour.

IMPACT OF CHAR AND ASH FINES ON POROUS CERAMIC FILTER LIFE

M. A. Alvin
Westinghouse Electric Corporation
Science & Technology Center
Pittsburgh, PA 15235

Keywords: Char, ash, filtration.

ABSTRACT

Although frequently inert, char and ash fines can potentially have a deleterious impact on the life of porous ceramic filters that are currently being utilized in advanced coal-fired applications. This paper reviews several of the char and ash related issues that have been encountered in various Westinghouse Advanced Particulate Filtration systems which limited filter life.

INTRODUCTION

During the past 10-15 years, Westinghouse has been involved in the development of Advanced Particulate Filtration (APF) systems for removal of char and ash fines that are released during coal and biomass gasification or combustion. Initially individual porous ceramic filter elements were installed in slipstreams at the Kellogg Rust-Westinghouse (KRW) fluid-bed gasification test facility in Madison, Pennsylvania, and at the New York University combustion test facility in Westbury, New York. Recently these efforts have been expanded to the use of multiple cluster arrays containing 384 or 748 filter elements within a common pressure vessel at the American Electric Power (AEP) pressurized fluidized-bed combustion (PFBC) demonstration plant in Brilliant, Ohio, and at the Sierra Pacific integrated gasification and combined cycle (IGCC) test facility in Reno, Nevada.

Numerous phase changes and generally a loss of material strength were encountered during use of the monolithic first generation filters under PFBC conditions at AEP, as well as during operation in Ahlstrom/Foster Wheeler's pressurized circulating fluidized-bed combustion (PCFBC) test facility in Karhula, Finland.[1,2] When catastrophic failure of the first generation monolithic filter elements occurred, it generally resulted from thermal fatigue or shock of the oxide-based alumina/mullite matrices, or from creep crack growth of the nonoxide-based clay bonded silicon carbide filter materials. Advanced second generation, fracture toughened, fiber reinforced filter elements are currently being developed and installed in W-APF systems in an attempt to mitigate catastrophic failure of the porous ceramic matrix during process operation. The stability and/or changes within the second generation filters materials are being evaluated in on-going test programs at the Westinghouse Science and Technology Center in Pittsburgh, Pennsylvania.[3]

Although the composition and morphology of the first and second generation filter materials change during exposure to advanced coal-fired and biomass process environments, the porous ceramic filter elements generally remain intact, surviving exposure to the process temperature and gas chemistry. Unfortunately failure and performance limitations (i.e., reduced gas flow permeability; decreased particle removal efficiency; etc.) have been encountered due to ash related issues as (1) bridging; (2) filter bowing; (3) inner wall blinding; (4) inner bore plugging; (5) wedging of fines between the ceramic filter flange and metal holder mount; (6) auto-ignition; and (7) membrane debonding in alkali-laden systems. The following section provides an overview of Westinghouse's field experience where filter life and performance have been limited by the deposition and adherence of char and ash fines.

FIELD EXPERIENCE

American Electric Power — Pressurized Fluidized-Bed Combustion

During the early test campaigns at AEP, the Westinghouse APF system was challenged with inlet dust loadings of 600 ppmw, consisting primarily of fine ash particles with a mass mean particle size of 1-3 μm. As a result of the small particle size and the tendency for the particles to sinter, dust built-up between filter elements, and along the dust sheds and plenum support pipes, forming compact bridges. Ash bridging lead to bowing and distortion of the clay bonded silicon carbide candles at process operating temperatures of 620-790°C, as well as random catastrophic failure of filters during plant startup and shutdown. Post-test inspection of the filter arrays indicated the close proximity and/or contact of the bottom closed end caps of adjacent bowed candles, and the fresh fractured surfaces at the base of the filter flanges.

When failure occurred during the early test campaigns at AEP, fines were released into the clean gas plenum and exhaust gases. During pulse cleaning, fines were reentrained and back pulsed into the inner wall of the remaining intact filter elements. Due to the relatively extensive open porosity of the 15 mm clay bonded silicon carbide filter support wall, fines filled the porous wall to depths of ~1-3 mm from the inner surface, reducing gas flow permeability through the elements.

Alternately during the later test campaigns at AEP, when the primary cyclone was inactivated, the filter array was challenged with dust loadings of 18,000 ppmw, consisting primarily of ash particles with a mass mean size of 27 μm. Ash bridging was not encountered after 1110 hours of operation at temperatures of 760-845°C. A tenaciously bonded ash cake formation, however, resulted along the metal filter holder mounts along the top arrays. Enhanced sulfur sorption occurred along the fines that encapsulated the top filter holder mounts, leading to the formation of magnesium sulfate hydrate ($MgSO_4 \cdot 6H_2O$) and anhydrite ($CaSO_4$).[4] The high thermal expansion of the ash fines which wedged in between the filters and metal holder mounts potentially caused failure of several of the low load beating elements to occur during multiple plant startup and shutdown cycles.

Once random failure of the filters was encountered, ash was released into the effluent stream, which was then back pulsed into the inner bore of the remaining intact filter elements. Due to the high particulate loading during conduct of the final test campaign at AEP, compact plugs of ash accumulated within the inner bore of select filter elements. Again due to the high thermal expansion of the ash in comparison to the ceramic filter matrices, crack formations resulted generally near the end caps of the clay bonded silicon carbide, alumina/mullite, and fiber reinforced chemically vapor infiltrated (CVI) silicon carbide candles after numerous plant startup and shutdown cycles. Although failure of these elements did not occur during process operation, removal and elimination of the elements from continued testing was warranted.

Comment

Irrespective of the high load bearing capabilities of the first generation monolithic filters, or the low load bearing capabilities of the advanced second generation filament wound or fiber reinforced filter matrices, successful extended operating life and performance of porous ceramic filters in high temperature coal-fired process applications will require mitigation of ash bridging events. Process control will also require that sorption of gas phase sulfur species be accompanied by subsequent removal of the fines without deposition and retention of tenaciously bonded dust cake layers along metal support structures. The tenaciously bonded sulfur-enriched ash conceivably limited the life of the low load bearing advanced filter elements, and lead to a labor intensive effort for removal of the remaining intact monolithic alumina/mullite and clay bonded silicon carbide candles, and second generation CVI-SiC composite filter elements.

Ash filling, blinding of the inner wall, or plugging of the inner bore leads to reduced gas flow permeability through the porous ceramic filter matrices and possibly decreases the dust cake removal capabilities during pulse cleaning. In addition, development of crack formations and a substantially increased weight of the elements results, and the capability to regenerate or clean the filter elements off-line becomes virtually limited. Obviously successful extended operating life and performance of the hot gas filtration system will require that ash bridging and wedging along the exterior of the filter elements, and ash filling, blinding, and/or plugging along the inner wall and bore of the filter elements be eliminated.

Ahlstrom — Pressurized Circulating Fluidized-Bed Combustion

During operation of the W-APF at the Ahlstrom PCFBC test facility in Karhula, Finland, 128 alumina/mullite candle filters were initially installed and operated at temperatures of ~900°C.[2] Failure of several of the elements was considered to have occurred during the first test campaign as a result of ignition of carbon monoxide-rich process gas in the presence of oxygen when the main air compressor malfunctioned. Generally the ~900°C PCFBC operating temperatures were considered to lower the thermal fatigue characteristics of the alumina/mullite matrix, through the formation of microcracks along the inner bore of the candle, which ultimately reduced the strength of the conditioned filter elements.

After removal of the alumina/mullite candles and installation of the clay bonded silicon carbide filters testing continued at temperatures of ~830°C. Creep crack growth of the clay bonded silicon carbide filters resulted, ultimately leading to elongation of the filter body and random

catastrophic failure. As a result, efforts fostered the development of advanced high temperature, creep resistance binder-containing, clay bonded silicon carbide candle filters.

Foster Wheeler — Carbonizer and Combustor Test Facilities

In 1992, Westinghouse installed and operated an APF system at the Foster Wheeler carbonizer test facility in Livingston, New Jersey. Twenty-two alumina/mullite candles formed the filter array. Initially one element failed, and char fines were back pulsed into the inner bore of the remaining filter elements. During startup in an oxidizing environment, combustion of the fines resulted, and catastrophic failure of several of the alumina/mullite filter elements occurred. Although alternate first or second generation filter elements had not been subjected to similar operating conditions, limited survival of these materials to withstand auto-ignition is expected.

In 1993 an alternate array of candles was installed in the W-APF system and operated under second generation PFBC conditions at the Foster Wheeler. During a ~210 hour test segment, the cyclone plugged and the filter vessel was filled with ash fines, causing failure of several of the filter elements. Post-test inspection of the array indicated that a tenaciously bonded sodium-potassium sulfate eutectic melt formed along the outer surface of the filter elements, which then served as the collection site for the adherence of $CaSO_4$, CaO and $CaCO_3$ fines.[5] The formation of the eutectic melt readily caused debonding of the membrane along the outer surface of the clay bonded silicon carbide filters. The alumina/mullite candles were virtually unaffected. Additional reactions of the binder phase in the clay bonded silicon carbide filter elements with gas phase alkali released in the Foster Wheeler second generation PFBC effluent stream were also observed.

The deleterious impact of auto-ignition of char fines, as well as the formation of the mixed alkali eutectic phase and bed carry-over require more stringent process control in order to achieve successful long-term operation of the ceramic filter elements in the advanced particulate removal systems.

Texaco — Entrained-Bed Gasification

Westinghouse utilized cross flow filters during the early test campaigns at the Texaco entrained-bed gasification test facility in Montebello, California. Failure was encountered when the stacked plate alumina/mullite cross flow filters delaminated, and when char fines became wedged between the cross flow flange and metal filter holder mounts. Wedging and failure along the flange had also been observed during long-term durability testing of the cross flow filters under simulated high temperature, high pressure, PFBC conditions at the Westinghouse test facility in Pittsburgh, Pennsylvania.

During the later test campaigns, clay bonded silicon carbide and alumina/mullite candle filters were retrofitted into the Westinghouse filter vessel at Texaco. After ~400 hours of operation, the candles were removed, and were observed to be coated with a tenaciously bonded dust cake layer. Removal of the FeO(OH), $FeAl_2O_4$-enriched cake from the outer surface of the filter elements was extremely difficult, which ultimately lead to the removal of the membrane of the clay bonded silicon carbide candle filters.[5]

Biomass Gasification

In 1994 and 1995 Westinghouse operated a twelve filter element array at the IGT biomass fluidized-bed gasification test facility in Chicago, Illinois. Post-test inspection of the clay bonded silicon carbide filter elements after ~21 and ~30 hours indicated that either an ~5.3 mm brown or ~1-2 mm black dust cake layer remained along the outer surface of the filter elements. The Fe_3O_4, Fe_2O_3, C, K, and SiO_2-enriched dust cake layer which was easily removed from the filters generally retained the contour of the candle body.[4] Debonding and/or removal of the outer membrane of the clay bonded silicon carbide candles was not observed after short-term operation in the 675-916°C biomass gasification environment.

FILTER ELEMENT LIFE AND REGENERABILITY

Porous ceramic filter elements can be utilized for extended service operation as demonstrated by Westinghouse during conduct of the five test campaigns at AEP where several surveillance clay bonded silicon carbide candles successfully survived 5855 hours of operation. At AEP Westinghouse also demonstrated the regenerability of the clay bonded silicon carbide candles by initially brushing the ash cake layer from the outer surface of the filter elements, followed by water washing and drying. Nearly complete gas flow permeability was recovered for the filter

elements in this manner. If ash blinding occurred along the inner wall or fines formed a compact inner bore plug, complete regenerability of the elements was not possible.

FILTER ELEMENT CONSTRUCTION

During field operation, the texture or roughness of the outer surface, as well as changes in the wall thickness of the filter elements dramatically impact the adherence and/or removal of the dust cake layer. As the texture or roughness of the surface increases, residual ash cake thickness tends to increase, leading to a reduced gas permeability through the filter wall. An optimal construction of the filter element is a uniform wall thickness along the length of the body and closed end cap areas. In this manner uniform removal of the dust cake layer can be accomplished during pulse cleaning.

FUTURE EFFORTS

Westinghouse will continue to explore the impact of char and ash fines on the stability of the porous ceramic filters during future testing at the Sierra Pacific Pinon Pine gasification test facility in Reno, Nevada, and at the Southern Company Services integrated gasification and combined cycle (IGCC) test facility in Wilsonville, Alabama, and at the Pacific International Center for High Temperature Research (PICHTR) biomass gasification demonstration plant in Hawaii. Testing is currently on-going at the Foster Wheeler/Ahlstrom test facility in Karhula, Finland, where advanced first and second generation monolithic and fiber reinforced filter elements are being subjected to 900°C PCFBC test conditions. As a result of these efforts, the ultimate viability, performance and robustness of the first and second generation porous ceramic filter elements will be challenged under a relatively wide gamut of process operating conditions — all of which are required to define successful long-term operation of the advanced high temperature particulate filtration systems.

REFERENCES

1. M. A. Alvin, "Advanced Ceramic Materials for Use in High Temperature Particulate Removal Systems," 1995 AIChE Annual Meeting, Miami, FL, November 17, 1995.

2. M. A. Alvin, R. E. Tressler, T. E. Lippert, E. S. Diaz, and E. E. Smeltzer, "Durability of Ceramic Filters," Coal-Fired Power Systems 94 — Advances in IGCC and PFBC Review Meeting, Morgantown, WV, June 21-23, 1994.

3. M. A. Alvin, T. E. Lippert, E. S. Diaz, and E. E. Smeltzer, "Filter Component Assessment," Advanced Coal-Fired Power Systems '95 Review Meeting, Morgantown, WV, June 27-29, 1995.

4. M. A. Alvin, "Advanced Coal-Fired and Biomass Ash and Char Formations," 12th International Pittsburgh Coal Conference, Pittsburgh, PA, September 11-15, 1995.

5. M. A. Alvin, "Characterization of Ash and Char Formations in Advanced High Temperature Particulate Filtration Systems," Fuel Processing Technology, Vol. 44, Nos. 1-3, September 1995, pp. 237-283.

THE ROLE OF PHYSICAL FACTORS IN MASS TRANSPORT AND PHASE TRANSFORMATION IN INTERGRANULAR MELTS DURING COAL ASH SINTERING AND DEPOSIT DEFORMATION

Jan W. Nowok, John P. Hurley, and Steven A. Benson
Energy & Environmental Research Center
University of North Dakota
PO Box 9018
Grand Forks, ND 58202-9018

Keywords: Coal ash deposits, ductile properties, mass transport phenomena

ABSTRACT

The role of physical properties of melts such as viscosity, diffusion, and surface–interfacial tensions in sintering and deformation mechanisms of ash deposits above the glass transformation temperature is discussed. The differential thermal analysis (DTA) technique was applied to measure glass transformation and crystallization temperatures. Sintering of selected coal ashes was performed as a function of temperature in air. The mechanical properties of sintered ashes were measured below and above T_g. It was found that a correlation exists between sintering propensities of amorphous ashes and plastic deformation of deposits above T_g, which both depend on the mass transport phenomena in the intergranular liquid phase.

INTRODUCTION

In combustion and gasification technologies a great need exists to define the lowest temperature at which the fouling propensity of fly ash on heat-exchange surfaces is maximally reduced. Numerous experimental studies have been reported in the literature that emphasize the role of interparticle melts in the sintering behavior of fly ashes. Using a quasichemical approximation, researchers were able at first to give a qualitative description of the liquid-phase composition that causes rapid deposit growth. Specific interactions between ash particles with dissimilar chemical compositions usually cause the formation of an interparticle silicate melt with a nonuniform structural composition, the unstable physical properties of which affect intergranular mass transport. The structural heterogeneity of silicate melts depends on two major contributions to the free energy of mixing: configurational entropy of mixing, which favors mutual miscibility, and dispersion forces, which energetically favor phase separation. A formulation of the chemical composition and structural homogeneity of melts to account for intergranular transport in the liquid phase is applied here. The preparation procedure for homogeneous aluminosilicates derived from coal ashes was described in an earlier article.[1] Mass transport through an intergranular liquid phase near and above the temperature of glass transformation, T_g, in sintering and superplasticlike deformation of ash deposits is described here.

HYSTERESIS IN MELT–CRYSTAL TRANSFORMATION AND GLASS TRANSFORMATION TEMPERATURE

Figure 1 illustrates the variation of Beulah slag viscosity with temperature, on cooling. The rapid increase of viscosity below the temperature of critical viscosity (T_c) is caused by slag crystallization.[2] Figure 2 shows the differential thermal analysis (DTA) results for Beulah glass and two more selected glasses derived from coal ashes on heating. The exotherms are caused by the formation of crystalline phases. Generally, hysteresis in the slag–crystal transformation manifests itself as a difference in crystallization temperatures on cooling of a melt and on heating of a glass. This effect does not suggest that melt transformation occurs at two different free energies. On cooling, the free energy of a supercooled melt is similar to that of nucleation and crystalline-phase growth on the liquidus. On heating, however, the additional energy for nucleation and further crystal growth of the same crystalline phase(s) comes from strain energy created during fast cooling and interfacial energy in the case of polycrystalline amorphous material. The strain energy results from the formation of an unrelaxed matrix during structural relaxation of the melt. The formation of a crystalline phase 1) in the bulk of the slag will increase its viscosity and simultaneously change its flow characteristics and 2) in an intergranular melt will increase deposit strength.[1]

The temperatures of glass transformation, T_g, on heating, are indicated in Figure 2. The ideal T_g corresponds to structural relaxation, at which the melt remains in equilibrium, and crystallization does not occur. This takes place only when the quench rate is high enough.[3] It has been demonstrated empirically that shear viscosity is of the order of 10^{13} poise at T_g, and various thermodynamic quantities such as compressibility, specific heat, and thermal expansion are discontinuous.[4] In this context, the glass transition is simply a reflection of the appearance of the elastic component. A remarkable aspect of glass transition is that it suggests changes in deposit behavior from brittle below T_g to ductile above T_g. This means that a glassy slag and/or intergranular amorphous phase will start to flow.

Figure 3 illustrates the variation in the crystallization temperature and temperature of glass transition with the base:acid ratio. Generally, both temperatures, T_c and T_g, increase with lowering base:acid ratio.

The T_g can be evaluated using an empirical equation [1] if the liquidus temperature of an aluminosilicate system is known:[5]

$$T_g/T_c \approx 2/3 \qquad [1]$$

Calculated temperatures of glass transformation for amorphous ash slags, included in Figure 3, correspond to those determined by DTA.

DENSIFICATION AND SUPERPLASTICLIKE DEFORMATION

Figure 4 illustrates changes in the apparent density of sintered amorphous coal ashes with temperature. The minimum on the curves corresponds to the maximum volume of deposits resulting from the volume of material and closed pores.[6] Usually, the densification process is defined as a pore filling by a liquid-phase flow and pore shrinkage, depending on the physical properties of the melt. The sintering process in Beulah and Montana ashes begins at about 700° and 750°C and occurs at temperatures lower than the glass transition temperatures, $T_g \approx 800°$ and $\approx 830°C$, respectively. This process seems to be caused by strain and interfacial energies stored in surface layers of unrelaxed ash particles, which enhance the diffusion coefficient of ions. Stress has long been known to affect the diffusion process in glass components. A quenched glass usually has a higher ionic transport rate than its crystalline form.

Figure 5 shows the compressive stress–strain relationship in sintered Illinois ash slag determined below and above the temperature of glass transformation, $T_g \approx 940°C$. Interestingly, the ash deposit is brittle below T_g and exhibits ductile properties above 900°C as a consequence of the disappearance of the elastic property of the intergranular amorphous phase. It is apparent that mean compressive stress decreases as the ash base:acid ratio increases (Figure 6). This suggests that the yield strength of the deposit depends on the thickness of the intergranular liquid phase and decreases with the increases in the base:acid ratio. Generally, the uniform yield (flow) stress as recorded on Figures 5 and 6 is attributable to superplasticlike deformation of materials, which is observed during stretching of a body as a large elongation without cracking. In glass ceramics, superplasticlike behavior may arise either by the viscous flow mechanism of intergranular layers or diffusion, which may be similar either to viscous[7] or to diffusional[8] creeps. Most silicate glasses containing modifying oxides are close to ideal elastic solids below the glass transition temperature.[9] There is, however, a small delay of elastic effect, likely resulting from the motion of alkali ions.

DISCUSSION

Intergranular mass transport in coal ashes sintered above the temperature of glass transformation (T_g) can be compared to that in capillarylike media that is based on viscous–diffusional mass transport.[10] In this model of liquid-phase sintering, the motion of the melt is caused by activated motion of the meniscus, which may occur either by viscous flow or by volume diffusion. The movement of the meniscus originates from the interface of atomic/ionic motion, creating a dynamic surface tension in the liquid phase. Intergranular mass transport through the liquid phase requires a sufficient quantity of melt, above some critical thickness, which may be provided by the dissolution of silicate from ash particles into the melt. In heterogenous systems, this can create gradients of chemical potential, possibly introducing nonequilibrium conditions.

Superplasticlike deformation in ash deposits may occur above the temperature of glass transformation (T_g). Two major independent factors allow superplasticlike deformation in a polycrystalline material with a liquid phase to occur. The first factor is a repetitive cycle of plasticity and dissolution of particle-to-particle connections; the second is compressive stress, which will segregate a small fraction of liquid to triple junctions.[11] Thus, the model of superplasticlike deformation of ash deposits above T_g seems to be similar to that of the transport of matter through the liquid phase in the liquid-phase sintering mechanism. The migration of intergranular melt is a response to the imposed gradients of hydrostatic pressure across the specimen caused either by surface tension, in the case of sintering, or by compressive stress, in case of superplastic deformation.

LITERATURE CITED

1. Nowok, J.W.; Benson, S.A.; Steadman E.N.; Brekke, D.W. *Fuel* **1993**, *72*, 1055.
2. Nowok, J.W. *Energy & Fuels* **1994**, *8*, 1324.
3. Leutheusser, E. *Phys. Rev.* **1984**, *29A*, 2765.
4. Fumiko Yonezawa. *Solid State Physics* **1991**, *45*, 179.
5. Baret, G.; Madar, R.; Bernard, C. *J. Electrochem. Soc.* **1991**, *138*, 2836.
6. Nowok, J.W.; Benson, S.A.; Jones, M.L.; Kalmanovitch, D.P. *Fuel* **1990**, *69*, 1020.
7. Dryden, J.R; Kucerovscy, D.S.; Wilkinson, D.S.; Watt, D.F. *Acta Metall.* **1989**, *37*, 2007.
8. Chen I-W.; Liand, An Xue. *J. Am. Ceram. Soc.* **1990**, *73*, 2585.
9. Bansal, N.P.; Doremus, R.H. *Handbook of Glass Properties*; Academic Press: Orlando, 1986; p 306.
10. Nowok, J.W. *J. Mater. Res.* **1995**, *10*, 401.
11. Maehara, Y.; Langdon. T.G. *J. Mater. Sci.* **1990**, *25*, 2275.

TABLE 1. Composition of Coal Ashes (weight percent expressed as equivalent oxide)

ID	Description	B:A	SiO_2	Al_2O_3	Fe_2O_3	TiO_2	CaO	MgO	Na_2O	K_2O	P_2O_5
A	Beulah	0.64	27.5	15.0	16.3	1.6	24.8	5.9	8.1	0.1	0.6
B	NIPSCO	0.64	31.1	15.1	13.0	1.3	29.4	6.9	1.2	2.1	0.3
C	SUFCo	0.37	51.3	11.0	9.6	0.4	22.1	2.0	2.7	0.0	0.8
D	Montana Subbituminous	0.28	47.2	24.0	5.4	1.1	15.5	4.7	0.7	0.7	0.7
E	Pittsburgh 1	0.17	47.8	18.1	18.0	0.8	9.4	3.0	1.5	1.1	0.1
F	Pittsburgh 2	0.15	48.7	18.7	18.7	0.9	8.3	1.6	1.1	1.8	0.2
G	Illinois	0.12	48.6	23.1	14.3	1.2	5.6	1.6	0.5	3.1	0.3
H	Gascoyne	0.73	35.2	11.5	8.8	1.5	27.6	7.5	6.7	0.1	1.0

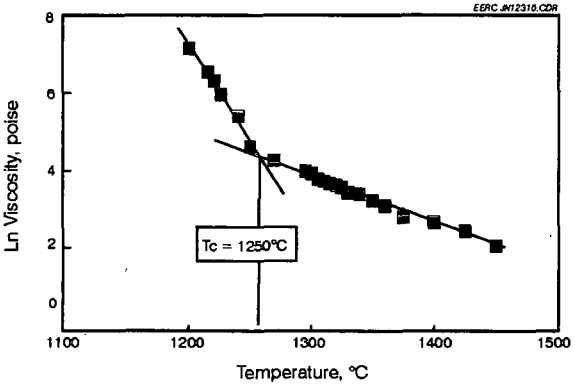

Figure 1. Logarithm viscosity-temperature relationship for Beulah ash slag, as determined on cooling.

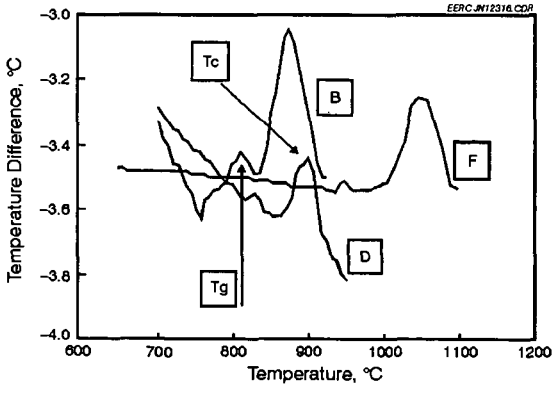

Figure 2. DTA curve of NIPSCO (B), Montana subbituminous (D) and Pittsburgh 2 (F) ash glasses, as determined on heating. DTA measurements were performed using a DuPont 2100 instrument in air at a heating rate of 8°C/min.

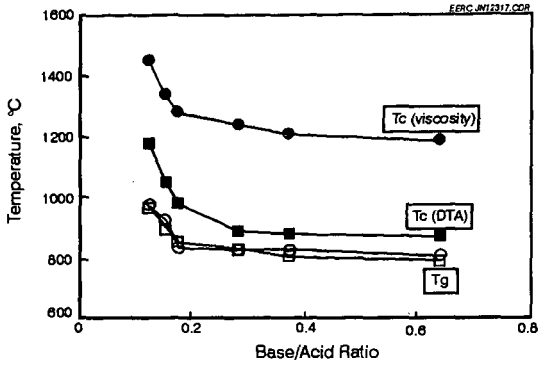

Figure 3. The relationship between the temperature of glass crystallization, glass transformation, and base:acid ratio in ash slags. The calculated values of T_g are represented by □. The chemical compositions of the coal ashes are listed in Table 1.

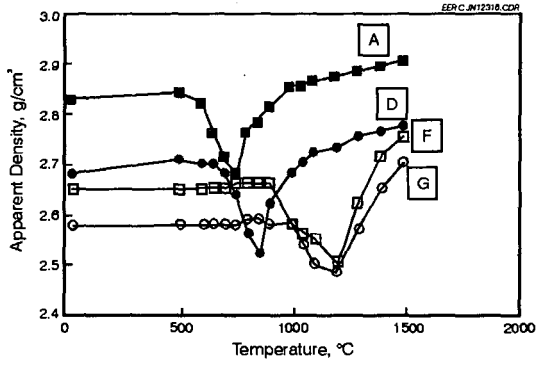

Figure 4. Dependence of apparent density upon sintering temperature for selected ash slags. The chemical compositions of the coal ashes are listed in Table 1.

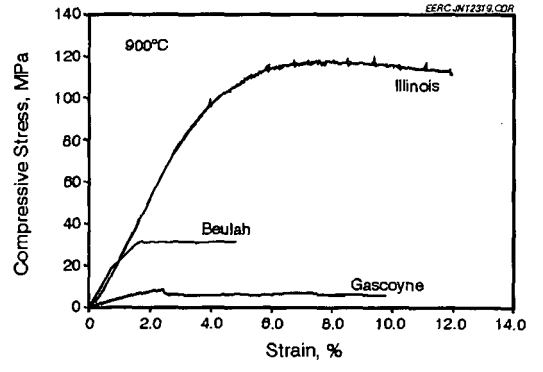

Figure 5. Compressive stress vs. strain in Illinois coal sintered at 1100°C for 20 hr in air. The deformation rate was $2 \cdot 10^{-5}$ m · min^{-1}.

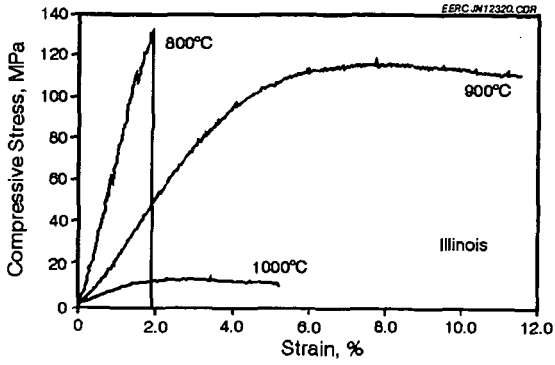

Figure 6. Compressive stress vs. strain in Illinois, Beulah, and Gascoyne ashes sintered at 1100°C for 20 hr in air. The deformation rate was $2 \cdot 10^{-5}$ m · min^{-1}.

GASIFICATION SLAG RHEOLOGY IN TITANIUM-RICH, IRON AND CALCIUM-ALUMINOSILICATE GLASSES

D. D. Brooker, M. S. Oh*, J. C. Groen.
Texaco, Inc., P.O. Box 509, Beacon, NY 12508,
*Hongik Univeristy, Dept. of Chemical Engineering, Seoul, Korea

Keywords: gasification, slag viscosity, titanium-rich aluminosilicate glass

INTRODUCTION

The Texaco Gasification Process (TGP) employs a high temperature, high pressure slagging gasifier to produce synthesis gas for power, hydrogen, and chemicals. During gasification most of the ash collects on the refractory wall to form a molten glass or slag. The viscosity of the slag plays a key role in determining operating conditions. Insufficient operating temperatures can cause erratic slag flow from the unit, while excessive operating temperatures can result in rapid refractory wear.

Waste streams that are high in titanium (e.g. plastics and tires where TiO_2 is used as a pigment) are being tested for gasification by Texaco. Texaco has developed a process to liquify both used plastics and tires with heated oil to produce a pumpable feed referred to as plastic-oil or tire-oil. Other major elements found with the titanium in these feeds include calcium, aluminum, iron, silicon, and zinc. The zinc sublimes during gasification, leaving behind a titanium-rich calcium-aluminosilicate glass with various amounts of iron.

The rheology of iron and calcium-aluminosilicate glasses within a gasifier has been studied through experimentation under reducing conditions, and by comparing this data to empirical models. Our initial study[1] indicated that: i) most calcium-rich gasification slags should exhibit the classical behavior of a newtonian glass (a continuous slow increase in viscosity as the temperature decreases), and ii) iron-rich slags can exhibit either newtonian or non-newtonian behavior (very low viscosity at high temperatures with a rapid increase in viscosity at some critical temperature (T_{cv})). At temperatures below T_{cv}, the slag is thought to change from a homogeneous fluid to a mixture of a fluid and rapidly crystallizing phase(s). Slag rheology under oxidizing conditions has been modeled rather successfully with empirical models based on slag composition. These models include Watt-Fereday,[2] Urbain[3], Si Ratio[4], or modifications of those models[5]. However, these models are limited to 0-5% TiO_2, and do not predict T_{cv}.

A study by Monteiro, et al[6], using titanium-rich, calcium-aluminosilicate glass was conducted in which up to 15% TiO_2 was used as a nucleation catalyst. The end result was a reduction in the melting point of the glass by the titanium dioxide. To extend the data base to higher titanium levels, in both calcium and iron-rich, aluminosilicate slags under reducing conditions, viscosity testing was conducted using 0-30% TiO_2 added to both synthetic glasses and gasification slags obtained from commercial units. The experimental viscosity curves were then compared to the empirical curves to determine how well the empirical curves could predict high titanium slag rheology under reducing conditions.

EXPERIMENTAL

Set Up: A Haake Rotovisco RV-100 system with a coaxial cylinder sensor system was employed for viscosity measurements. The sensor system, stationary crucible, and rotating bob with tapered bottom, all composed of high density alumina, are placed in a high temperature furnace. The heating elements (Kanthal Super ST) of the furnace are completely isolated from the viscometer assembly by a mullite tube which runs from the top to the bottom of the furnace. This protects the brittle heating elements from breaking during loading and unloading of the sensor system. The furnace temperature control and the data acquisition of shear rate vs. shear stress were obtained through PARAGON software on an IBM PC. To simulate a reducing condition, a 60/40 mix of CO/CO_2 was passed over the sample at a flow rate of 300 cc/min. The gas mixture entered from the bottom of the furnace and exited through the top. The viscometer was calibrated with a National Bureau of Standard (NBS) borosilicate glass (Standard Reference Material 717).

Procedures: A cylindrical crucible is placed in the furnace. The crucible is locked into the bottom plates of the furnace to prevent the crucible from rotating. The bottom plates are composed of low density alumina to minimize conductive heat loss from the sample. The CO/CO_2 sweep gas is turned on, and the furnace is heated to 1480° C. When the furnace reaches 1480 °C, a few grams of pelletized ash are fed from the top. This feeding process is slow enough to allow the pellets to completely melt and degas before the next feeding to prevent the slag from boiling over the sides of the crucible. Once the desired level of the melt is obtained, the bob is lowered from the top, guided by an alignment pin and a stopping plate. This method allows for the viscometer to be assembled in the same way every time, assuring

that the bob is placed in the middle of the slag sample, both horizontally and vertically. Once the viscometer assembly is complete, the temperature is decreased at the rate of 56° C/hr. The viscosity measurements are made every 10 minutes. After the experiment, the slag is cut as shown in Figure 1 and polished for Optical Microscopy (OM) and Scanning Electron Microscopy (SEM) phase analysis. The elemental composition of the slag before and after the viscosity experiments were determined by Inductively Coupled Plasma Emission Spectroscopy (ICP-ES) and phase analysis was conducted by X-Ray Diffraction (XRD).

During the viscosity measurements, the rotation rate of the bob is ramped from 0 to 65 rev/min for 3 mins and back to 0 for the next 3 mins. The shear rate is varied from 0 to 18.2 s^{-1}. The resulting shear rate-shear stress curve is that of a newtonian fluid at high temperatures and characteristic of a non-newtonian fluid at low temperatures. For the viscosity-temperature plot, the viscosity at the highest shear rate was used. Temperature calibration of the equipment was conducted as reported in Oh, et al[1].

Materials: Six synthetic glasses and two coal slags were used in the test program. The synthetic glasses consisted of +99.0 percent pure oxide components as listed in Table 1a. Composition 1 was formulated to match the chemical composition of the ash for a potential plastic feedstock. For Compositions 2 and 3, approximately 10% and 27.5% TiO_2 were added, respectively, to the base case. Barium and magnesium oxides were eliminated from Compositions 4 and 5, and the amounts of calcium and silica were changed while the TiO_2 was held constant. Composition 6 was similar to Composition 3, but without barium oxide being added to the mix.

The coal slags used in the test program were; i) SUFCo (Hiawatha seam, high volatile C bituminous rank) from a commercial plant, and ii) Pittsburgh #8, a bituminous coal, gasified in a pilot unit. The samples were washed and screened to remove most of the carbon. Titanium dioxide was then added at 20% of the slag weight. The chemical composition of the SUFCo slag used in this study contained more calcia, and less silica than previous SUFCo slags that have been used for the calibration runs. For reference purposes, both SUFCo slag viscosities are plotted together.

RESULTS

Final Slag Composition: Both the alumina crucible and bob partially dissolved into the slag and raised the concentration of alumina. Table 1b gives the final composition of the slag, and these values were the ones used in the empirical models. Approximately three percent alumina was added to the SUFCo slag and one percent to the Pitts. #8, which is consistent with previous runs. The calcium and titanium-rich slags dissolved much more alumina, apparently because of the lower slag viscosities at high temperatures. The final chemistry of Composition 2 was not analyzed for this study, because the crucible was destroyed twice before a reasonable viscosity curve could be generated (a phase analysis study is being conducted on the slags from these failed runs in which the chemical analysis will be reported).

Slag Viscosity: Figure 2a contains the viscosity curves of four synthetic slags, SUFCo slags, and SUFCo slag with titanium as a function of temperature. The only slag that exhibited a classic newtonian behavior was the SUFCo slag. Each of the synthetic slags exhibited non-newtonian behavior to varying degrees in which the slags had very low viscosities until a critical viscosity temperature was reached in which the viscosities increased moderately, and then quickly, which led to the spindle snapping. Based on the curves generated during this study; i) at low calcium and high titanium concentrations, the slag starts out fluid, but reaches a critical viscosity at a high temperature (1370° C), ii) at high calcium and moderate titanium levels, the slag is very fluid at low temperatures (1150° C), and iii) at high calcium and high titanium levels, the slag is fluid even at high temperatures, and then reaches a critical viscosity at intermediate temperatures (1270° C).

Figures 2b and 2c contain the viscosity curves of SUFCo and Pitts. #8 slags. Both slags exhibit glassy (newtonian) slag behavior. The result of adding titanium to the SUFCo slag is consistent with the corresponding synthetic slag in that the titanium lowered the viscosity. A critical viscosity may have begun at 1150° C, but the run automatically terminated. For the high iron, Pitts. #8 slag, the addition of titanium appears to have no effect on the viscosity. As a point of reference, the Pitts.#8 slag used in this study is newtonian in behavior compared to the Pitts. #8 generated in our original study which had a dramatic viscosity rise at the critical temperature.

Crystalline Phase Formation: The furnace was turned off at 1190° C and the slags were rapidly cooled by the CO/CO_2 gas mix. After cooling, the crystalline phases and glasses in the slags were examined by SEM. The phases identified were TiO_2 (rutile) and $CaAl_2Si_2O_8$ (anorthite). Both phases were physically aligned with one another. All samples were sent to a university for further analysis and will be reported on at a later date.

DISCUSSION

None of the slags exhibited sharp increase in viscosity at their normal critical viscosity temperature as seen in some previous tests. Therefore, the chemical compositions of the final slags were used in the various models to determine how well the models correlated with the experimental data. Based on the limitations of the models as shown in Table 2, the Watt-Fereday model most closely matches the test conditions.

The actual viscosity of each slag was plotted against the four models. Based on these plots, the Urbain model most closely matches the slag viscosity for the calcium-rich slags, and all of the titanium-rich slags. The only slag samples that the Urbain model did not predict well were the high iron, Pitts. #8 and the intermediate calcium, titanium-rich slag (none of the models were in agreement with this composition).

Even though the Urbain model most closely matches the data, at high titanium concentrations the model predicts higher viscosities than the test run data. The most likely cause for the discrepancy would be the formation of a calcium-titanium-silicate glass phase that has; i) a lower melting point than the calcium-aluminosilicate glass, and ii) a flatter liquidus within its phase boundaries than anorthite. The large crystalline phases that formed during cooldown appear to have little effect on the viscosity as indicated by their orientation to the flow direction within the slag as it spun around the bob.

The Watt-Fereday and Si Ratio model gave the best fit for the high iron slag. Again, based on the compositional limit in Table 2, the Watt-Fereday model contains the most elements within the boundary conditions. In previous runs with Pitts. #8, hercynitic spinels came out of solution rapidly creating a critical viscosity. The difference between the Pitts. #8 used during this testand that used in the prior work was; i) the presence of more iron, and ii) the iron was more likely to be in the +2 valence state (the slag was reduced in the gasifier, while the Pitts. #8 ash used in the first study may not have fully reduced during testing).

The lack of change in viscosity of the Pitts. #8 slag when titanium was added was unexpected. The glass phase should be of fayalite composition which has a low melting point. In previous tests, hercynitic spinels crystallized out of solution, and one would suspect that with the added TiO_2, $FeTiO_3$ (ilmenite) which was present would crystallize out of solution near 1300° C and affect the viscosity more noticeably. The combined presence of $FeAl_2O_4$ and $FeTiO_3$ should abruptly raise the slag viscosity which was not seen. Several additional runs, along with phase prediction will be done in the future.

CONCLUSIONS

The slag viscosity data for calcium and titanium-rich feeds are consistent with previous studies in that; i) titanium will lower the melting point of a calcium aluminosilicate glass for TiO_2 up to 27.5%, and ii) the higher the calcium concentration, the more fluid the glass will be with or without titanium, for CaO contents up to 30%. The most consistent model for the calcium-titanium aluminosilicate system under reducing conditions is the Urbain Model. For higher iron slags, the Watt-Fereday Model appears to be a better system for predicting viscosity. However, a high iron slag will have a greater likelihood of nucleating a high melting spinel or ilmenite phase, causing a critical viscosity to develop as iron is rapidly withdrawn from the glass phase.

REFERENCES

1. Oh, M. S., Brooker, D. D., DePaz, E.F., Brady, J. J., and Decker, T. R. 1995; Effect of crystalline phase formation on coal slag viscosity. Fuel Processing Technology, 44, 191-199.
2. Watt, J. D., and Fereday, F., 1969. Flow properties of slag formed from the ashes of British Coal; I. Viscosity of homogeneous liquid slags in relation to slag composition. J. Inst. Fuel, 42, 99-103.
3. Urbain, G., Cambier, F., Deletter, M., and Anseau, M. R., 1981. Viscosity of silicate melts. Trans. J. Brit. Ceram. Soc., 80:139.
4. Corey, R. C., 1964. Measurements and significance of the flow properties of coal-ash slag. US Bureau Mines Bull. No. 618.
5. Schobert, H. H., Streeter, R. C., and Diehl, E. K., 1985. Flow properties of low-rank coal ash slags. Implication for slagging gasifiers. Fuel, 64:1611.
6. Monteiro, R. C. C., Silva, F. I. F, and Lima, M. R. A., 1992. Effect of the addition of TiO_2 and ZrO_2 on the crystallization of calcium aluminosilicate glasses. XVI International Congress on Glass. Vol. 5.

TABLE 1A - CHEMICAL ANALYSES (ICAP) - STARTING MATERIAL

	SUFCo	Pitt. 8	Run1	Run2	Run3	Run4	Run5	Run6
SiO2	62.7	44.2	42.1	37	30.5	50	40	30
Al2O3	11.9	23.7	14.9	13.5	11	15	15	11
CaO	11.5	3.5	26.5	23.8	19.3	10	20	19.3
TiO2	1.1	1.1	0	10.8	27.4	20	20	27.3
Fe2O3	6.2	22.3	9.4	8.4	6.6	5	5	6.6
MgO	2.3	1	3.8	3.2	2.6	0	0	2.6
Na2O	2.6	1.7	0	0	0	0	0	0
BaO	0	0	3.25	2.9	2.4	0	0	0

TABLE 1B - CHEMICAL ANALYSES (ICAP) - END MATERIAL

	SUFCo + TiO2	Pitt. 8 + TiO2	Run1	Run3	Run4	Run5	Run6	Run6b
SiO2	53.4	33.3	40.5	27.1	46.7	40.4	29.7	30.1
Al2O3	15	24.6	21.2	21.4	18.5	15.6	17.1	15.5
CaO	9.6	2.7	20.4	14.6	8.1	18.6	15.6	16.1
TiO2	13	20	0	24.9	20.6	20.6	26.7	27.5
Fe2O3	5.4	18.6	9.3	8.1	5.9	5.4	6.6	6.6
MgO	1.9	0.6	3.4	2.4	0.2	0.2	2.6	1.9
Na2O	2.3	1.4	0	0	0	0	0	0
BaO	0	0	2.3	1.6	0	0	0	0

TABLE 2 LIMITATIONS OF MODELS

Oxides	Wt %	Normalized Wt %	Riboud	Urbain	W-F	SiRatio
SiO2	40.4	40.6	34-56	43-73	30-60	30-59
Al2O3	15.6	15.6	0-12	8-14	15-35	15-30
FeO	5.3	5.4	8-46	2-28	3-30	5-31
MgO	0.2	0.2	8-46	0-7	1-10	1-15
CaO	16.6	16.6	8-46	1-9	2-30	0-30
Na2O	0	0.0	0-22	0-4	0	0
K2O	0	0.0	0-22	0-5	0	0
TiO2	20.6	21.0	0	0	0	0
P2O5	0	0.0	0	0	0	0
MnO	0	0.0	0	0-0.3	0	0
ZrO2	0	0.0	0	0	0	0
B2O3	0	0.0	0	0	0	0
CaF2	0	0.0	0-15	0	0	0

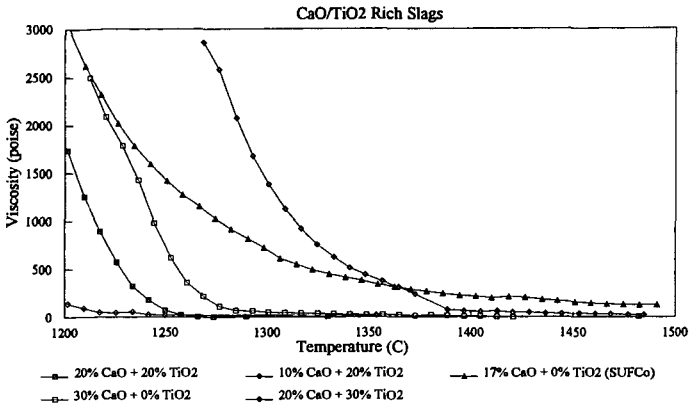

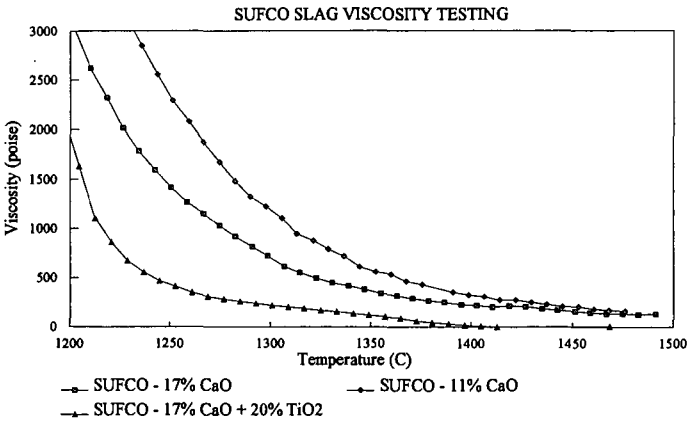

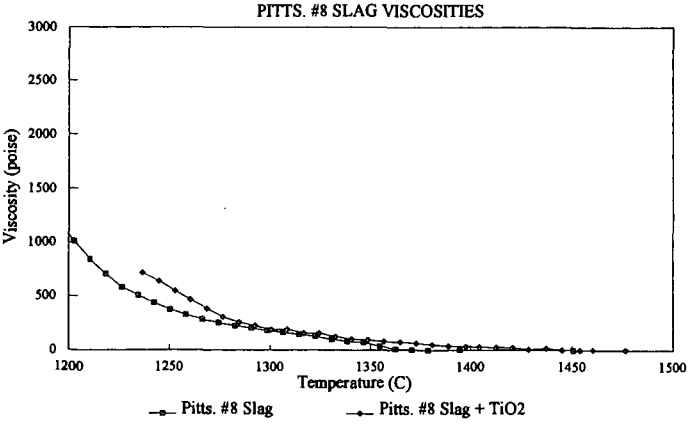

Figures 2a-c. Slag viscosity measurements of various slags.

DISSOLUTION OF LIME INTO SYNTHETIC COAL ASH SLAGS.

Liza Elliott[1], Shen Mao Wang[1], Terry Wall[1], Fred Novak[2], John Lucas[1], Harry Hurst[2], John Patterson[2], Jim Happ[3].
[1]Department of Chemical Engineering
Newcastle University, Australia. (Callaghan 2308)
[2]CSIRO Division of Coal & Energy Technology
North Ryde, Australia, 2113.
[3]CRA Advanced Technical Development
1 Research Ave, Bundoora, Australia, 3083.

Keywords: CaO, lime, dissolution, slags, coal ash.

ABSTRACT

One of the alternate processes presently being investigated to produce electrical power from coal is Integrated Gasification Combined Cycle (IGCC). The ash that remains when the coal is gasified in this process, is removed by granulating the molten ash at 1400 - 1500°C. To reduce the melting temperature of the coal ash to this level, a flux, usually limestone, is added with the coal to the gasifier. The rate of dissolution of the flux is uncertain.

This paper reports the investigation of the rate of lime dissolution into synthetic coal ashes, consisting of SiO_2, Al_2O_3 and CaO. Results previously reported have shown that the free dissolution of fine particles (50-200μm) is mass transfer controlled. To investigate forced dissolution, a high temperature viscometer was used to rotate a cylinder of lime in the molten slag for a given period. At temperatures between 1450°C and 1650°C, reaction products of $3CaO.SiO_2/3CaO.Al_2O_3$, $2CaO.SiO_2/3CaO.Al_2O_3/12CaO.7Al_2O_3$ form around the lime pellet. The concentration gradient involved in the mass transfer was defined, and initial studies of the diffusion coefficients were completed.

INTRODUCTION

Entrained flow gasifiers partially combust coal at elevated temperatures and pressures to create a product gas consisting of carbon monoxide and hydrogen, which is combusted in a gas turbine to produce electrical power. The ash that remains after this combustion, must melt to allow the resulting slag (molten ash) to run down the walls of the gasifier and is tapped from the base of the gasifier. The minimum temperature experienced by the ash within the gasifier is usually between 1400 and 1500°C. The ash must therefore be molten at these temperatures for the ash to be efficiently removed from the gasifier.

Coals with high ash fusion temperatures require the addition of a flux with the coal to lower the melting point of the ash. The alternative, increasing the operating temperature lowers the process efficiency, which is undesirable. Usually this flux is $CaCO_3$, which, when exposed to the atmosphere within the gasifier breaks down into CaO and CO_2. The flux reduces the viscosity of the resulting slag (depending on the ash being considered).

This paper considers the dissolution process of lime into synthetic coal ash slags, that consist of: silica, alumina and lime for forced dissolution and silica, alumina, lime and ironoxide for free dissolution. Our preliminary results have shown that for no convection, dissolution from small lime particles in a synthetic ash is mass transfer controlled and a dicalcium silicate layer formed around the lime particles.[1]

Matsushima[2] et al. investigated the forced dissolution rate of lime in SiO_2-Al_2O_3-CaO and SiO_2-FeO-CaO slags and found a $2CaO.SiO_2$ layer around the solid lime, though he suggested that the layer did not sit next to the lime but was separated by a slag layer. Matsushima determined a boundary layer size by an equation using dimensionless numbers, (determined for the dissolution of steel) and by determining the mass transfer constant $k=\frac{D}{\sigma}$ by a mass transport equation and assuming $D=5.5*10^{-6}$ cm^2/s. Samaddar et al.[3] investigated the dissolution of alumina, mullite, anorthite and silica in CaO-SiO_2-Al_2O_3 melts with a similar technique as used here. Cooper et al.[4] also used this technique to study sapphire dissolution and Taira et al.[5] studied dissolution of alumina in similar slags, while Gudenau et al.[6] and Olsson et al.[7] studied the dissolution of carbon into hot metal baths.

METHOD

Free Dissolution.

Small particles of lime, with average diameters of 275, 500 and 750 μm were mixed into synthetic coal ash mixtures: $60SiO_2$-$30Al_2O_3$-$6Fe_2O_3$-4CaO(wt%). The mixtures of ash and lime were

placed in a platinum crucible and heated in a vertical tube furnace to 1400, 1500 or 1600°C for a defined time in an argon atmosphere. At the end of the experiment, the melt was removed from the furnace and quenched.[1] The regions around the lime particles were studied quantitatively under the Scanning Electron Microscope using EDAX to establish concentration profiles, and the amount of unreacted lime determined by an oxalic titration method.[3]

Forced Dissolution.
Cylindrical pellets of lime were produced by pressing powdered lime in a die and then sintering the pellets in a muffle furnace for two hours at 1550°C. Samples of slag were premelted from reagent grade oxides, producing a homogeneous melt prior to dissolution experiments. Each slag sample was produced in a molybdenum crucible liner, ensuring no dissolution of carbon from the outer graphite crucible occurred. The slag compositions selected are based on coal ash silica to alumina ratios (2 to 3.35). The range of lime content in slag (15 to 25 wt%), was chosen to ensure the melt would be completely fluid at temperatures used in this set of experiments.

At the beginning of each dissolution experiment, a pellet was suspended on a molybdenum rod above a melt in a vertical tube furnace, refer Figure 1, allowing the pellet to heat to approximately the same temperature as the melt. The furnace atmosphere was kept at a mildly reducing composition by the graphite crucible, which reacted with any oxygen entrained into the furnace with the nitrogen purge gas. Each melt was maintained at temperature for at least thirty minutes to allow the melt to equilibrate. The pellet was then lowered into the melt and rotated at the desired speed for a given period of time. To remove the pellet at the end of a test, a molybdenum cradle containing the crucible the pellet still in position in the melt, was lifted out of the furnace into a cooling tube. Nitrogen was directed onto the crucible to cool it as quickly as possible, as shown in Figure 2. This required three to five minutes.

The frozen melt in the crucible was sectioned through the vertical axis of the pellet and polished before the concentration profile around the lime pellet was determined using a Scanning Electron Microscope. The change in size of the pellet was also measured.

The thickness of the boundary layer was determined by fitting an exponential equation to the lime concentration profile. The boundary layer size is assumed to be the distance from the lime source to the point where the lime concentration does not change (within 1%). The diffusion coefficient for lime dissolving into $SiO_2/Al_2O_3/CaO$ slags was determined from equation 1:

$$-j = \frac{dx}{dt} = \frac{D\left(C_i - C_\infty\right)}{\sigma\left(1 - V_i C_i\right)} \qquad \text{eqn } 1^{(3)}$$

Where j is the flux of lime, x the amount of lime (in cm) removed from the lime pellet, t the time of dissolution, D the lime diffusion coefficient, σ the boundary layer size, C_i the saturation lime concentration at experimental temperature, C_∞ the bulk slag lime concentration and V_i a volume fraction, or $\frac{\rho_s}{\rho_l}$ (the ratio of the density of the solid and liquid phases).

RESULTS

Free Dissolution
A $3CaO.Al_2O_3 + 2CaO.SiO_2$ layer (reaction zone) was found to form around the lime particles, with no separation of the layer from the lime by slag, after which the lime concentration falls to the bulk slag concentration. Figure 3 shows the lime concentration outside the crystalline phases does not fall evenly as it is affected by dissolution of lime from adjacent particles. Using the model of a shrinking particle in a fluid with changing concentration, the rate of mass transfer through the melt was found to be the rate limiting step in the dissolution process, as shown in Figure 4.[1]

Forced Dissolution
A typical concentration profile in the slag around the pellet is shown in Figure 5. The figure shows a reaction zone followed by an area that exhibits a concentration profile typical of diffusion control. The reaction zone is a combination of $2CaO.SiO_2$ and $3CaO.SiO_2$. The corresponding alumina phase: $3CaO.Al_2O_3$, on the CaO-Al2O3-SiO_2 phase diagram, is only seen at the end of the reaction zone, though it is believed to occur throughout the reaction zone in fine defined ribbons around the alumino-silicate crystals. This behaviour of the two types of crystals forming an unhomogeneous layer around the lime is shown in maps of the reaction zone from the Scanning Electron Microscope, Figure 6. The brighter the points appears on the image, the higher the concentration

of that species. The aluminium concentration in this region is higher than can be completely accounted for in the compound $3CaO.Al_2O_3$ Some $12CaO.7Al_2O_3$ is also being created in this region, though no discrete particles can be determined as it is finely divided amongst the other tricalcium-aluminate crystals.

Other samples showed very little evidence of $3CaO.SiO_2$ in the reaction zone, consisting mainly of $2CaO.SiO_2$, as shown in Figure 7. This figure also shows the existence of $3CaO.Al_2O_3$, again with some $12CaO.7Al_2O_3$, to account for the alumina content found, at the interface of the lime pellet and the reaction zone. To produce these compounds the alumina concentration rises well above the bulk slag alumina concentration. This indicates that these phases are crystalline.

The diffusion coefficients calculated from the concentration profile of lime from the end of the "reaction zone" to the bulk slag concentration are given in Table 1. The diffusion coefficient calculated from the forced diffusion experiments are variable. Work is continuing on this area. These initial experiments appear to indicate that temperature may have a greater effect on the size of the reaction zone than the speed of rotation. The size of the boundary layer appears to be affected by both the change in temperature and the speed of rotation. The size of the boundary layer should theoretically decrease with increasing rotational speed, while increasing temperature will decrease the viscosity, affecting the boundary layer size. The results shown are inconclusive and further work is required.

CONCLUSIONS

- The rate limiting step of dissolution of lime into molten ash is the mass transport of the lime into the slag, for both forced and free dissolution.
- A crystalline layer of $2CaO.SiO_2$ or $3CaO.SiO_2$ interspersed with $3CaO.Al_2O_3$ form around a lime particle dissolving into molten ash.
- The driving force for the mass transport step appears to be the difference between the CaO concentration at the reaction zone and the bulk slag.

ACKNOWLEDGMENTS

The authors acknowledge the financial support of CRA Advanced Technical Development. The CSIRO authors acknowledge the financial support of the NSW State Energy Research and Development Fund, the Australian Coal Association Research Program and the Energy Research and Development Corporation (Australia).

REFERENCES

1. Wang S. M. et al. Experimental Studies and Computer Simulation of Dissolution of Lime Particles into Coal Ash Slags. Australian Symposium on Combustion and the Fourth Flame Days, University of Adeliade, South Australia, November 9-10,1995.
2. Matsushima. M., et al. A Fundamental Study on the Dissolution Rate of Solid Lime into Liquid Slag. Transactions ISIJ, Vol 17, 1977, p442 - 449.
3. Samaddar B. N. et al. Dissolution in Ceramic Systems:11, Dissolution of Alumina, Mullite, Anorthite and Silica in a Calcium-Aluminum-Silicate Slag. Journal of the American Ceramic Society, Vol. 47, 1964, p249 - 254.
4. Cooper A. R. et al. Dissolution in Ceramic Systems: 1,Molecular Diffusion, Natural Convection, and Forced Convection Studies of Sapphire Dissolution in Calcium Aluminium Silicate.Journal of the Americam V|ceramic Society, Vol 47 (1) 1964, p 37 - 43.
5. Taira, S. et al. Kinetic Behaviour of Dissolution of Sintered Alumina into CaO-SiO2-Al2O3 Slags, ISIJ International Vol 33, (1) 1993 p116 - 123.
6. Gudenau et al. Dissolution of Carbon Brocks in Hot Metal Baths (Auflosung sverhalten von Kohlenstoffsteinen im Roheisenbad. Stahl Eisen Vol. 111 (2), 1991 p89 - 94.
7. Olsson, R.G. et al. Rate of Dissolution of Carbon in Molten Fe0C alloys.
Transactions of the Metallurgical Society of AIME, Vol236, 1966 p426 - 429.
8. Russell, R.O. Journal of Metals, 19 (8), 1967. P104.

FIGURES

Table 1:Diffusion Coefficient Estimates from equation 1.

SiO_2/Al_2O_3	CaO %	Rotational Speed rpm	Temperature °C	Reaction layer thickness mm	Boundary layer thickness mm	Diffusion coefficient. $cm^2/s*10^{+5}$
3.35	25	83.25	1550	0.0544	7.2484	6.9
3.35	25	83.5	1450	0.056	5.39	11.4
3.35	25	37.15	1450	1.328	5.8	6.89
3.35	25	20	1450	0.0587	2.35	2.04
3.35	25	110	1450	0.0267	0.518	0.326
2.25	15	83.5	1550	0.039	0.933	0.784
2.25	20	74	1450	0.384	9.539	6.5
2.25	20	74	1650	0.190	4.7664	8.5

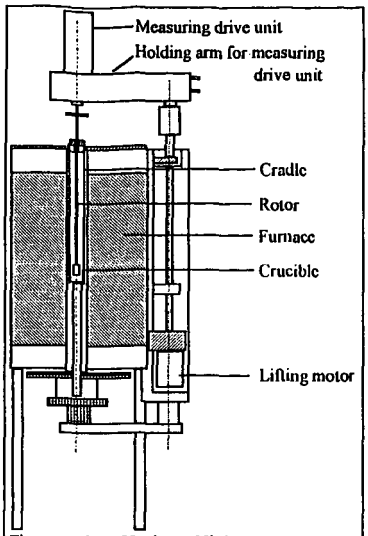

Figure 1: Haake High Temperature Viscometer used for forced dissolution experiments

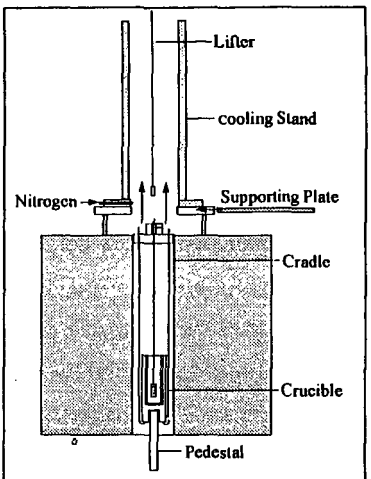

Figure 2: Cradle used to lift crucible to cooling tube.

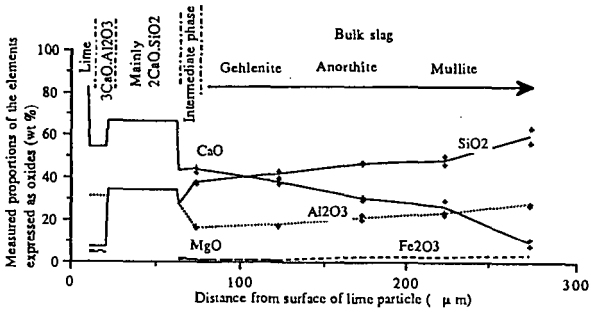

Figure 3: Free Dissolution Concentration Profile around a 750μm lime particle in slag at 1500°C

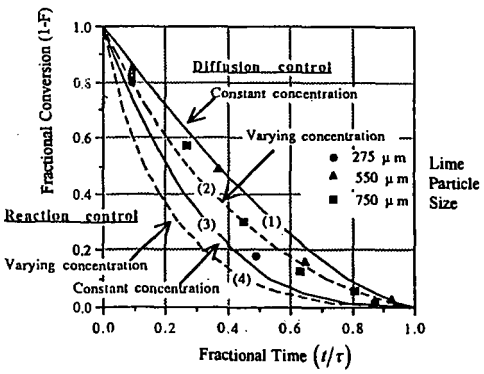

Figure 4: Free Dissolution Experiments: Comparison of Experimental Results with Theoretical Curves for Dissolution Rates Controlled by Diffusion and Reaction Kinetics.

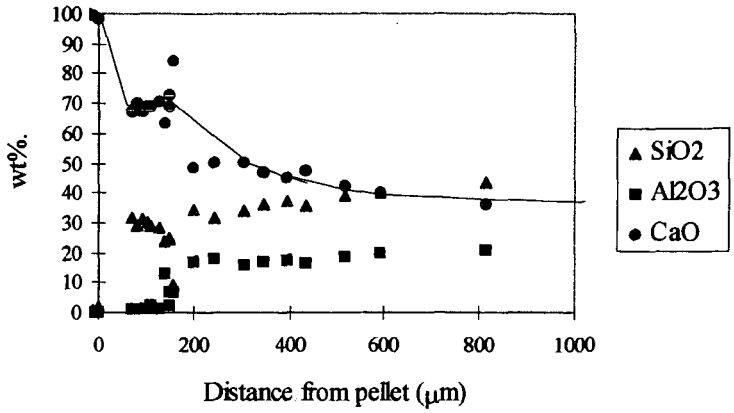

Figure 5: Forced Dissolution Concentration Profile around lime Pellet, SiO_2/Al_2O_3=2.25, at 1450°C

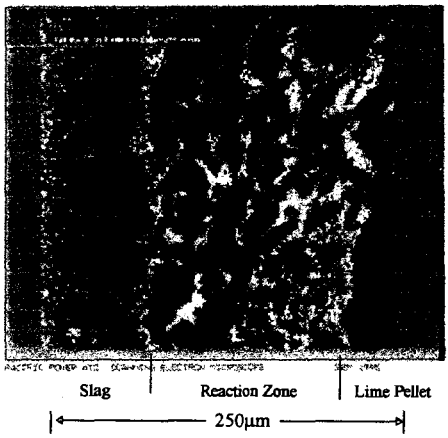

Figure 6: Aluminium Intensity Map

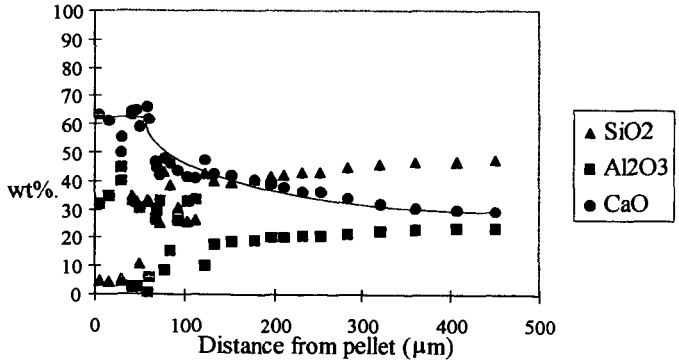

Figure 7: Forced Dissolution Concentration Profile around lime Pellet, SiO_2/Al_2O_3=2.25, at 1650°C

THE EFFECTS OF ATMOSPHERE AND ADDITIVES ON COAL SLAG VISCOSITY

John P. Hurley
Tina M. Watne
Jan W. Nowok
Energy & Environmental Research Center
PO Box 9018
Grand Forks, ND 58202-9018

Keywords: Slag, viscosity, and coal slag

ABSTRACT

The viscosities of a Powder River Basin slag were measured in air, air + 10% water vapor, and a reducing atmosphere. The temperature of critical viscosity (T_c), below which the viscosity increases dramatically, was approximately 1250°C in air and air + water vapor, but dropped to 1180°C when measured in the reducing atmosphere. Since the corrosivity of the slag is much higher when its viscosity is low, the slag will be highly corrosive at the substantially lower temperature in reducing gas. The addition of alumina increased viscosity and T_c making the slag less corrosive, while magnesia additions dropped viscosity but increased T_c. These changes imply that magnesia additions will make the slag slightly more corrosive in its liquid range, but that the slag will harden and become less corrosive at a higher temperature than without the magnesia addition. The changes in T_c were more substantial when measured in the presence of water vapor in the case of alumina additions, but less substantial in the case of magnesia additions.

INTRODUCTION

As coal reacts in an energy system, the inorganic material in the coal reacts to form silica-rich ash. If the temperature of the ash is high enough, it will completely fuse, forming a molten slag. This slag is very erosive and corrosive to energy system materials with which it comes in contact. The viscosity of the coal ash slag determines its flow rate which affects its erosivity, and the diffusivity of ions within the slag which affects its corrosivity. Several phenomenological models based on linear regression analysis of slag composition-versus-viscosity data have been developed to predict the viscosity of coal ash slags in combustor systems.[1-4] However, these models only work well in predicting slag viscosity at the conditions under which the composition-versus-viscosity data were developed, and it is not well understood how far the predictions can be extended to other system conditions such as variations in local atmosphere. In addition, the models do not predict the temperature at which crystallization starts in the slag, known as the temperature of critical viscosity T_c, below which the viscosity sharply rises. This means that the minimum temperature to which the models can be applied or to which slag can be expected to flow is not well known.

In this article, we report the impact of three gas compositions, each of which may be expected in various regions of a coal-fired boiler, on the viscosity and critical temperature on a high-calcium coal slag produced from a Powder River Basin coal. We also demonstrate how these properties can be manipulated with the use of coal additives in order to reduce their corrosiveness to energy system materials.

EXPERIMENTAL

The viscosity of the slags were measured under three atmospheres: air, air + 10% water vapor, and $H_2/CO/CO_2$ (31/45/24). In addition, reagent-grade magnesium oxide (45 wt%) or aluminum oxide (20 wt%) was added to the slags under both air and air + 10% water vapor conditions. Viscosities were measured with a Haake RV-2 Rotovisco system with a DMK 50/500 dual measuring head, which is a rotating bob viscometer. In this system, the torque on the viscometer bob is converted to an electrical signal to a computer, which controls the rotation at 64 rpm. For oxidizing atmosphere tests, the bob was fabricated from platinum–rhodium (90/10) alloy. For reducing atmosphere tests, the bob was fabricated from molybdenum. In both cases, the bob was 22 mm long with a 30° taper at both ends. The top of the bob terminated in a 16-mm-long, 6-mm-diameter shaft accommodating a 420-mm-long by 3-mm-diameter stem. The bob was immersed until the slag just covered its top. The coal slags were prepared by melting ash powders at 1500°C in air in a platinum crucible and quenched on a brass plate at room temperature. The glasses were crushed, put into alumina crucibles, and heated to 1500°C. The viscosity of the slags were measured over the range of 10 to as high as 4000 poise unless crystallization was seen to occur along the walls of the alumina container, at which point the measurements were terminated. Measurements were started at a temperature of at least 100°C above the temperature of critical viscosity, and the temperature was decreased in 20°C intervals. The bob was rotated in the slag for approximately 40 minutes after each temperature was reached before a reading was taken. The viscometer was calibrated with National Bureau of Standards silicate glasses 710 and 717. The accuracy of the tests is approximately ±5%. Compositions of the original ash is listed in Table 1.

TABLE 1

Compositions of Coal Ashes, wt% oxide basis

	Oxide Coal
SiO_2	38.8
Al_2O_3	20.8
Fe_2O_3	6.1
TiO_2	1.5
P_2O_5	1.1
CaO	23.2
MgO	6.5
Na_2O	1.4
K_2O	0.3
SO_3	ND[1]

[1] Not detected.

RESULTS AND DISCUSSION

Figure 1 shows the viscosity-versus-temperature curves for the Powder River Basin coal slag in air, air + 10% moisture, and reducing conditions. The curves are very similar for both the air and air + moisture tests, with T_c approximately 1250°C and the viscosity of each slag around 20 poise at 1400°C. However, under the reducing conditions, T_c dropped considerably to 1180°C, and the viscosity of the slag at 1400°C was only around 5 poise. These changes cannot be explained merely by the reduction of iron in the slag from a network former (3+ ion) to a network modifier (2+ ion) since there is so little in the slag.

Figure 2 shows the effects of the additions of alumina and magnesia to the slag when measured in air. As expected, the addition of a network former like alumina increased the viscosity of the slag at 1400°C from 20 to 40 poise. In addition, the temperature of critical viscosity was increased dramatically from 1250°C for the original ash to 1330°C with the alumina addition. X-ray diffraction showed the formation of plagioclase ($[Ca,Na][Al,Si]_4O_8$) and spinel ($MgAl_2O_4$) crystals in the melt below T_c. In contrast, the addition of magnesium, a network modifier, to the melt decreased its viscosity as expected, but increased T_c even more, to around 1350°C. Crystals forming in that melt included spinel and monticellite ($CaMgSiO_4$). The changes in viscosity indicate that alumina additions would decrease the corrosivity of a Powder River Basin slag, while magnesia additions may slightly increase corrosivity. However, because T_c is increased in each case, either addition would dramatically lower slag corrosivity at material temperatures 80° to 100°C higher than the T_c of the slag alone.

Figure 3 shows the effects of the additions of alumina and magnesia to the slag when measured in air + 10 moisture. As was true for the measurements in air, adding alumina raised the viscosity and T_c of the slag but much more substantially, with the viscosity increased by 60 poise at 1400°C while T_c rose by 140°C. This increase in viscosity would reduce the corrosivity of the slag to energy system materials, dramatically reducing the corrosivity of the slag at temperatures below 1400°C. The additions of magnesia also created similar changes as when measured in air. The viscosity of the slag at 1400°C dropped by approximately 10 poise, but T_c rose by only 50°C to 1310°C.

CONCLUSIONS

The viscosity and T_c of a Powder River Basin slag is not substantially different when measured in air or in air + 10% water vapor, but both are substantially reduced when measured in an $H_2/CO/CO_2$ atmosphere. The reduction is more than would be expected from the conversion of iron from a 3+ ion to a 2+ ion. Adding alumina, a network former, increased viscosity and T_c when measured in air, but more substantially when measured in air + 10% water vapor. The addition of magnesia, a network modifier, to the slag dropped the viscosity and raised T_c, but the change in T_c was less substantial in air + water vapor than when measured in air alone. Either addition will have small effects on corrosivity of the slags above T_c, but will dramatically reduce corrosivity below the new T_c of the modified slags. Also, since combustor gas contains more water vapor than air alone, we suggest that in order to gauge the effect of additives on slag viscosity accurately, viscosity measurements should be made in an atmosphere containing water vapor.

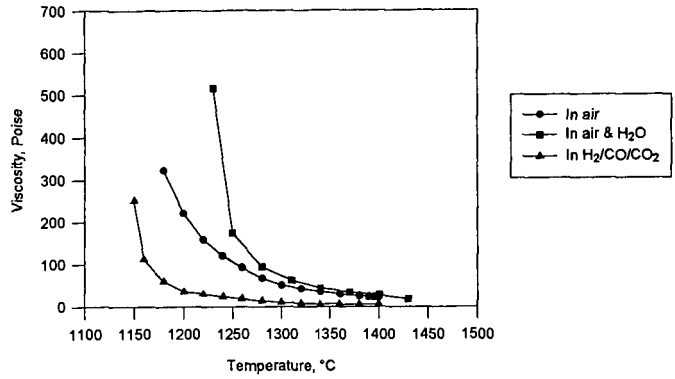

Figure 1. Viscosity-versus-temperature curves for the Powder River Basin coal slag in air, air + 10% moisture, and reducing conditions.

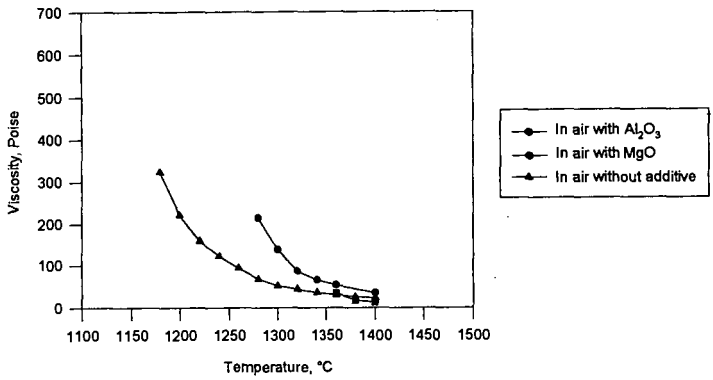

Figure 2. Viscosity-versus-temperature curves measured in air for the Powder River Basin coal slag, slag plus alumina, and slag plus magnesia.

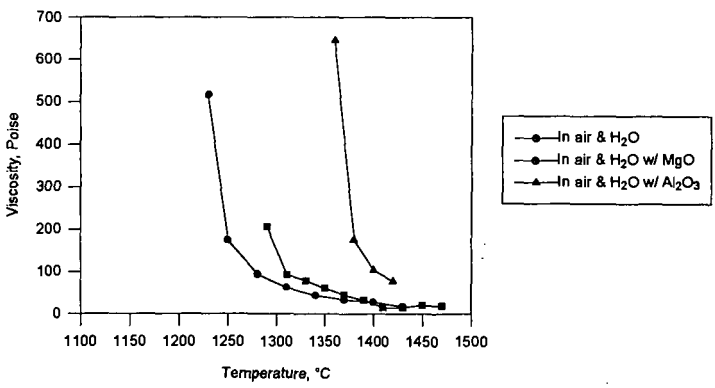

Figure 3. Viscosity-versus-temperature curves measured in air + 10% moisture for the Powder River Basin coal slag, slag plus alumina, and slag plus magnesia.

REFERENCES

1. Urbain, G.; Cambier, F.; Deletter, M.; Anseau, M.R. *Trans. J. Br. Ceram. Soc.* **1981**, *80*, 139.

2. Kalmanovitch, D.P.; Frank, M. *In* Proceedings of the Conference on Mineral Matter and Ash Deposition from Coal; Engineering Foundation, Santa Barbara, 1988, p 89.

3. Jung, B.; Schobert, H.H. *Energy and Fuels* **1992**, *6*, 387–398.

4. Nowok, J.W.; Hurley, J.P.; Steadman, E.N. *In* Proceedings of the Conference on the Impact of Ash Deposition on Coal-Fired Plants; Engineering Foundation, Solihull, England, 1993.

COAL SOLUBILIZATION BY NON-CATALYTIC TRANSFER HYDROGENATION WITH FORMATE

Soon Chuan Lim and Edwin N. Givens
University of Kentucky, Center for Applied Energy Research
3572 Iron Works Pike, Lexington, KY 40511-8433

Keywords: Liquefaction, hydrothermal treatment, carbon monoxide, formate, water

Abstract

Non-Catalytic transfer hydrogenation using formate as the hydrogenating agent significantly reduces the severity necessary for solubilizing coal. Moisture and mineral matter free solubilization of coal up to 94% in pyridine was observed for a Wyodak coal that was treated at 340 °C for 1 hr with CO and aqueous NaOH. Loss of oxygen from coal as CO_2 agrees with a forced balance based upon elemental and mass recoveries. A hydrogen consumption of 0.6 wt %, calculated from this balance, agrees with hydrogen consumptions independently determined based upon CO conversion. The hydrogen to carbon ratio in the total water-insoluble product increased to 0.88 versus a corresponding value of 0.80 in the starting coal. The pyridine soluble and insoluble fractions had H/C values of 0.97 and 0.59, respectively. Reaction in the absence of added salt produced a water-insoluble product that was 50% soluble in pyridine and had a H/C value of 0.79.

Introduction

CO-promoted hydrothermal treatment of low-rank coals has been found by several groups to be quite effective for converting these coals to soluble products.[1] A group at Exxon reported that hydrothermal treatment of a Wyoming subbituminous coal in the presence of CO at 345 °C for 6 hours produced a material that was largely soluble in THF and was more soluble than material produced by hydrothermal treatment in the absence of CO.[2] Treating the coal under the same conditions in decalin failed to increase the solubility relative to that of the raw coal. Hydrothermal treatment substantially depolymerized the coal making it more reactive for producing distillate product in a hydrogen donor solvent.[2,3] The hydrothermal product was enriched in hydrogen and had reduced oxygen content. The CO-aqueous system presumably promotes decarboxylation of oxygen-containing constituents and cleavage of ether and ester groups attached to aromatic ring systems. Under these reaction conditions, a Martin Lake, Texas lignite heated in $^{13}CO/D_2O$ was shown to produce formate ion with most of the deuterium in the reacted D_2O being transferred into the coal.[4] The recovered CO_2 contained 60% $^{12}CO_2$ from the coal, presumably formed via decarboxylation, and 40% $^{13}CO_2$ from ^{13}CO via the water-gas-shift reaction. Adding alkali metal salts to the CO/H_2O mixture presumably increases the concentration of formate ion further enhancing the solubility of the product.[5] In the work reported here, the reactivity of a Wyodak coal under hydrothermal conditions in the presence of CO and sodium hydroxide is discussed.

Experimental

Wyodak coal from the Black Thunder mine in Wright, Wyoming, was ground to -200 mesh, riffled and stored in tightly sealed containers. Ultimate analysis: carbon, 73.9%; hydrogen, 5.2%; nitrogen, 1.3%; sulfur, 0.6%; oxygen, 19.0% (by difference). Ash content (dry basis) was 6.12 wt%. All results are expressed as weight percent moisture and ash-free coal (maf).

In the experiments conducted in a 300 ml stirred autoclave, 50 g of as-received coal containing approximately 20% moisture were mixed with 4.2 g NaOH in 75 ml. of distilled and de-ionized water. The reactor was sealed, leak tested and pressurized with CO to 1000 psig. In experiments in the absence of base, only 40 ml of water was added. Heat-up time from ambient to reaction time at 340 °C was approximately 3.5 hr. The reaction was allowed to proceed at this temperature for an additional hour. The reactor was cooled to ambient temperature within 1.5 hr. A gas sample was collected and analyzed by gas chromatography and the solid products were removed from the reactor, washed with distilled and de-ionized water and dried at 40 °C under vacuum. Soluble humic acids were recovered from the aqueous phase by precipitating the colloidal material with HCl (pH 1-2) followed by centrifugation and drying. The acidified aqueous layer was further extracted with ether. Product distribution and recovery of water-insoluble product, humic acids and ether solubles, on a maf basis, are shown in Table 1. A 5 g sample of the water-insoluble product was extracted with THF in a Soxhlet thimble for 18 hours. The Soxhlet extraction technique was exceptionally slow since colored material continued to exude from the thimble after a week of continuous extraction. A smaller sample (0.5 g) of product was placed in 200 mL of pyridine or THF and extracted using a sonication/vacuum filtration

technique at ambient temperature. Samples ultrasonicated in either solvent for 10 min filtered rapidly within minutes under vacuum at ambient temperature. Material was collected after solvents were removed, dried overnight at 80 °C at 16 kPa and weighed to determine solubility in the solvent. A reliable pyridine solubility value could not be obtained for the water-insoluble product from treating coal in the absence of NaOH. Material that was ultrasonicated in pyridine clogged the filter paper within minutes. The same material also clogged the Soxhlet thimble filters which resulted in less material dissolving in pyridine than in THF (see Table 2). This underscores the different properties of the material generated when salt was present during the reaction.

Discussion

The water-gas-shift reaction in the presence of NaOH is quite sensitive to temperatures between 250 and 340 °C with CO conversion increasing from <10% up to approximately 90%, respectively. At 300 °C in the presence of ~0.3 M NaOH, the conditions under which many of the earlier runs were made, the shift reaction goes to the extent of about 20-25%. In the absence of NaOH, the CO conversion at 340 °C is only ~40%. At 300 °C, very little H_2 is actually recovered, most of it being incorporated into the water-insoluble product. At 340 °C, about half of the H_2 that is formed is recovered. In every case, the amount of hydrocarbon gases formed in the reaction was quite small.

The amount of humic acids and ether-extracted material (fulvic acids) in the aqueous phase was small, being 1.3% in the presence of NaOH. The highest yields of these products (~7%) were observed at 300 °C, either at low CO pressures or in the absence of CO. Solubility of the water-insoluble material indicates the degree to which reaction occurred. Previously, solubilities in THF and pyridine were determined using a Soxhlet apparatus. The materials generated at 340 °C could not be evaluated in this manner since the extraction thimbles readily blinded. It was found that solubilities of the NaOH treated materials in these two solvents could be determined at ambient temperature using a sonication technique in which the extracted THF and pyridine solutions filtered quite readily without blinding the filter paper. Higher pyridine and THF solubilities were obtained using the ultrasonication technique compared to Soxhlet extraction. For the reactions run with NaOH, pyridine and THF solubilities reached 94 and 78 wt % (maf product basis), respectively. The ultrasonication technique could not be used on the product produced in the absence of added NaOH since it readily blinded the filter paper when filtered.

Chemical compositions of water-insoluble product and the solvent-separated fractions from the NaOH treated coal are shown in Table 3. For the 82.3 wt % of water-insoluble product plus humic acids, the 8% ash content was too high relative to the 5.5% concentration in the starting coal. In the absence of NaOH the ash content was closer to the expected value. In both cases, there was a decrease in the oxygen content from 17.9% in the starting coal to 4.7% in the water-insoluble product for the NaOH-treated coal and 5.2% for the NaOH-free case. Approximately 75% of the oxygen was removed in both cases. The hydrogen-carbon ratio for the NaOH-treated coal increased to 0.88 versus a value of 0.80 for the starting coal. By contrast, the H/C ratio of the product generated in the absence of base is essentially the same as that of the starting coal, indicating a loss of hydrogen in the reaction. The hydrogen concentration in the pyridine soluble fraction (0.97 H/C) is higher than in the starting coal (0.80 H/C), whereas the concentration in the insoluble fraction is much less (0.59 H/C). Oxygen concentration is much higher in the insoluble fraction. Note that the oxygen values for the solvent separated fractions are higher than observed in the water-insoluble product. This suggests a possible reactivity upon exposure to air since no special precautions were followed in handling these samples. The concentrations of nitrogen and sulfur in the solvent separated products are similar to the total water-insoluble product suggesting enrichment of nitrogen in the pyridine insoluble product.

Mass and elemental balances were calculated for the 300 mL autoclave experiments. The balance for the experiment run in the presence of NaOH, as shown in Table 4, was calculated by correcting the ash concentration in the water-insoluble product, which includes the humic acids and ether-soluble product, to a level consistent with the ash in the starting coal and adjusting the remaining elements to account for this correction. Since the gas analysis showed that hydrocarbon gases were quite small (see Table 1) the other products are water, CO and CO_2. Because very large concentrations of CO are present as a reactant and much of the CO_2 is formed as a result of the water-gas-shift reaction, the amount of these carbon oxides that are formed from carbon in the coal cannot be measured directly. The ratio of the additional oxygen and carbon needed to force the balance of these two elements in the product is greater than the 2 to 1 ratio in CO_2. Therefore, in the product, of the 78% of the oxygen in the starting coal that was absent from the water-insoluble product, most was present as CO_2 (60% of the original oxygen) with the remaining 18% of the original oxygen being present as

water. Formation of CO_2 is consistent with the results of Horvath and Siskin.[4] The hydrogen necessary to form the water was 0.42 wt % of ash-free coal, while the total hydrogen consumed in the reaction was ~0.6 wt % of the coal. Using these assumptions, all of the starting material is accounted for in the products.

The elemental balance for the experiment made in the absence of NaOH (see Table 5) showed that more carbon and less hydrogen was recovered in the water-insoluble product than for the NaOH treated coal. In fact, the amount of hydrogen was less than in the starting coal. Forcing a carbon balance indicated that less oxygen could be removed as CO_2 and the amount of water necessary to balance the oxygen was much higher. Of the 75% of oxygen removed from the coal, 23% was removed as CO_2 and 52% as water. The net H_2 consumption of 1.0 wt % hydrogen, which would have been formed via the water-gas-shift reaction, accounted for 85% of the hydrogen incorporated into the water. The remaining hydrogen came from the coal accounting for the decrease in hydrogen in the water-insoluble product.

The heating value of the treated coals were calculated using the equation developed by Boie and used by Ringen and co-workers.[6]

$$H_g(\text{cal/g}) = 8400C + 27765H + 1500N - 2500S - 26500$$

where H_g is the gross heating value and C, H, N, S and O are the normalized weight fractions of these elements in the sample. Multiplication by the factor 1.8 converts the results to units of Btu/lb.

	with NaOH	without NaOH	Coal
Heating Value, Btu/lb maf	16,400	16,000	12,900

The heating values for both CO-treated coals were significantly higher than the starting coal.

Summary

Reacting Wyodak coal with CO and H_2O at 340 °C, both in the presence and absence of base, produced materials having reduced oxygen contents. Oxygen removals in excess of 75% were obtained regardless of whether base was present. Addition of base gave a material which was highly soluble in both pyridine (95%) and THF (78%), whereas the solubility of the material produced in the absence of base was less. Water-insoluble materials produced in both cases had significantly higher heating values than the starting coal. Forced elemental balances based upon the absence of any significant hydrocarbons in the gaseous product provides insight into the probable reaction pathways for removal of oxygen. In the presence of base, a large part of the oxygen leaves as CO_2 while in the absence of base the water pathway is far more dominant. In both cases, the significant removal of oxygen can have a large economic impact on processing costs for low rank coals.

References

1. Lim, S. C.; Rathbone, R. F.; Rubel, A. M.; Givens, E. N.; Derbyshire. F. J. Energy and Fuels, 1994, 8, 294
2. Stuntz, G. F.; Culross, C. C.; Reynolds, S. D. United States Patent No. 5,026,475, June 25; 1991.
3. Vaughn, S. N.; Siskin, M.; Katritzky, A.; Brons, G.; Reynolds, N.; Culross, C. C.; Neskora, D. R. United States Patent No. 5,151,173; Sept. 29, 1992.
4. Horvath, I. T.; Siskin, M. Energy Fuels 1991, 5, 933-934.
5. Ng, F. T. T.; Tsakiri, S. K. Fuel 1993, 72, 211.
6. S. Ringen, J. Lanum and F.P. Miknis Fuel, 1979, 58, 69

Table 1. Product distribution from aqueous CO treatment of Wyodak coal

	with NaOH[a]	without NaOH[b]
Gaseous Product		
Hydrogen, mol %	32	8
CO, mol %	7	52
CO_2, mol %	61	34
Hydrocarbon gases, mol %	<0.5	<0.5
Water-Insoluble Prod, wt% maf	81	85
Humic acids + ether solubles, wt% maf	1.3	n.d.

a. Wyodak coal, 1000 psig CO cold, 4.2 g NaOH, 75 mL H_2O, 340 °C, 300 mL reactor.
b. Wyodak coal, 1000 psig CO cold, 40 mL H_2O, 340 °C, 300 mL reactor.

Table 2. Solubility of water-insoluble product from CO-treated coal (maf basis)

Treatment	Ultrasonic/Filtration		Soxhlet Extraction	
	THF	Pyridine (RT)	THF	Pyridine
with NaOH	78	94	55	88
without NaOH	N.A.	N.A.	54	50

Table 3. Elemental analysis of CO-treated coals

	Starting coal	CO-treated coal			
		with NaOH			without NaOH
Element		Water-Insoluble	Pyridine Soluble	Pyridine Insoluble	Water-Insoluble
Carbon	70.3	79.5	85.2	40.5	81.0
Hydrogen	4.7	5.8	6.9	2.0	5.3
Nitrogen	1.0	1.7	1.5	1.5	1.7
Sulfur	0.5	0.4	0.3	0.3	0.4
Oxygen	17.9	4.7	6.1	16.9	5.2
Ash, SO_3-free	5.5	8.0	-	38.9	6.3
H/C atomic ratio	0.80	0.88	0.97	0.59	0.79

Table 4. Elemental balance for NaOH-treated coal

	Coal	Water Insoluble Product[a]	CO_2	H_2O	Total
Carbon	70.32	66.3	4.0		70.3
Hydrogen	4.68	4.83		0.42	5.25
Nitrogen	1.04	1.42			1.42
Oxygen	17.92	3.92	10.67	3.33	17.92
Sulfur	0.5	0.33			0.33
Ash	5.54	5.54			5.54
Total	100.00	82.3	14.67	3.75	100.72

a. Ash concentration corrected to starting coal.

Table 5. Elemental Balance for 300 mL Reactor Run without NaOH

	Coal	Water-Insol Product	CO_2	H_2O	Total
Carbon	70.32	68.76	1.56		70.32
Hydrogen	4.68	4.50		1.17	5.67
Nitrogen	1.04	1.44			1.44
Oxygen	17.92	4.41	4.16	9.35	17.92
Sulfur	0.5	0.34			0.34
Ash	5.54	5.54			5.54
Total	100.00	85.00	5.72	10.52	101.23

STEAM PRETREATMENT FOR COAL LIQUEFACTION

O. Ivanenko, R.A. Graff, V. Balogh-Nair, C. Brathwaite
Departments of Chemical Engineering and Chemistry
The City College of New York, New York, NY, 10031

Keywords: Coal, Liquefaction, Pretreatment

INTRODUCTION

Development of commercially viable and environmentally sound processes for coal liquefaction remains a formidable challenge. Although advances in coal liquefaction technology in recent years have led to the production of liquids of improved quality, this improvement has been achieved mainly by increased consumption of expensive catalyst. Catalyst and capital equipment costs are major factors in the high price of the coal-derived liquids.

One way to improve the economics of direct liquefaction is to modify the coal feed before solubilization. A variety of physical and chemical methods of coal treatment prior to low severity liquefaction have been found to significantly improve yield and quality of the product, making it superior to those obtained at high severity conditions. Many studies have shown that treatments such as alkylation, acylation, partial oxidation and alkali hydrolysis weaken and rupture the cross-linked bonds and result in a partially depolymerized coal. Although all of these methods of enhancing coal reactivity somewhat improve liquefaction yield, none has yet been employed as a process step in liquefaction. Chemical treatment methods remain in the laboratory mainly because they employ expensive and sometimes hazardous reagents.

The work described here is based on the use of steam as a pretreatment agent in noncatalytic coal-donor solvent liquefaction. Advantages of this approach are that steam is among the cheapest of reagents and does not incorporate undesired chemical residues into the coal structure.

Studies have already demonstrated the effectiveness of exposing Illinois No.6 coal to subcritical steam in the temperature range 320-360°C at 50 atm as a pretreatment for room temperature pyridine extraction and for flash pyrolysis (Graff and Brandes, 1987). It was observed that the pyridine extraction yield from steam treated coal gradually increases and reaches a maximum at a pretreatment temperature of 340-350°C. At temperatures above 370°C the effect is extinguished. Yield of liquids in coal pyrolysis was more than doubled and the total volatiles yield was increased by about 20%. When steam treated coal was exposed to ambient air, both pyrolysis and extraction yields were reduced to the level of raw coal. Analysis of pyrolysis liquids from pretreated Illinois No.6 coal showed a decrease in molecular weight with a simultaneous increase in oxygen content compared to raw coal (Graff *et al.*, 1988). Based on the results of analyses performed on raw and steam pretreated coal (Brandes *et al.*, 1989) it was concluded that during steam pretreatment new hydroxyl groups are introduced. As a result, the covalent cross-links in coal are greatly reduced yielding a partially depolymerized coal, potentially, an improved feedstock for liquefaction processes.

With this success of steam pretreatment in pyrolysis, it was logical to test its application to direct liquefaction. Previous attempts by others to obtain an improvement in liquefaction yield by this method had, however, failed. As noted above, pyrolysis studies showed that heating coal above 360°C could destroy the effect of pretreatment. It was, therefore, reasoned that the heating of pretreated coal to liquefaction temperatures must be done rapidly to minimize deleterious retrogressive reactions. A tubing bomb or stirred autoclave (employed in the conventional way) would not be adequate to carry out liquefaction under rapid heating conditions. One way to achieve high heating rates is to use a method in which a slurry of pretreated coal is injected into a hot liquefaction reaction vessel (Whitehurst *et al.* 1976). A system of this type, with some modifications, was designed, assembled, tested and used for the liquefaction tests. Furthermore, as it is known that the benefits of pretreatment are observed only if exposure of steam treated coal to air is rigorously avoided, it is necessary to conduct all operations with pretreated coal under an inert atmosphere. To satisfy this requirement, a nitrogen filled glove bag is used for sample workup and the oxygen concentration of the bag monitored by mass-spectrometer. To verify successful pretreatment, the pyridine extraction yield is determined for each steam treated coal sample.

In this work liquefaction tests of raw and steam pretreated Illinois No. 6 coal were made to determine the pretreatment effect on yield of liquids and on quality of product. These tests were conducted using the slurry injection autoclave described above pressurized with hydrogen and using tetralin as the donor solvent. The effect of exposure of treated coal to air and the role

of coal slurry heating rate were examined at three different conditions of liquefaction severity.

EXPERIMENTAL METHODS

Coal Sample. Pretreatment and liquefaction experiments were conducted with Illinois No.6 coal from the Pennsylvania State University Sample Bank (DECS-2) ground under nitrogen to pass 200 mesh using a gas impact pulverizer (Trost). Ground coal was riffled, placed in a glass jars, flushed with inert gas, sealed, and stored under refrigeration.

Steam Pretreatment. Steam pretreatment was conducted in a continuous flow of steam using the procedure described by Graff and Brandes (1987) and Graff *et al.* (1988, pp 3-5). The coal was reacted with 50 atm steam at 340°C for 15 minutes (optimum pretreatment conditions for Illinois No.6 coal).

Liquefaction. Liquefaction experiments were conducted with raw coal, steam treated coal and steam treated coal exposed to air under conditions of both rapid and slow heating, using tetralin as a hydrogen donor solvent. The liquefaction apparatus (Figure 1) consists of a 300 ml stirred autoclave (Autoclave Engineers EZE-Seal, model #P-419) and coal slurry injection system (loading reservoir and 1000 psia rupture disc assembly which separates the reservoir from the autoclave). Nitrogen and hydrogen are supplied from high pressure cylinders.

Rapid heating liquefaction is conducted as follows:

Sixty grams of deoxygenated tetralin are placed into the reaction vessel and the autoclave is sealed. After the system is leak tested with nitrogen at 2000 psia with the bypass line valve open, the reactor is flushed with hydrogen at atmospheric pressure and then heated using an electric furnace and keeping the bypass line valve closed. While the reactor is heated, slurry is prepared in a nitrogen filled glove bag from the pretreated coal and the solvent. The slurry is made of 1/3 part of coal and 2/3 parts of solvent using about 20 grams of coal. When the autoclave has been preheated to operating temperature, two syringes are filled, one with about 40 ml of slurry and one with 20 ml of solvent. The syringes are attached to the loading line, the loading valve is opened, and the slurry reservoir is sequentially filled with 10 ml of solvent, coal slurry (full contents of the syringe), and, finally, 10 ml of solvent. The loading valve is then sealed and hydrogen at the desired pressure is applied. This causes the rupture disc to burst, injecting slurry into the reactor and pressurizing the system. The valve above the reservoir is then closed. The reaction temperature is maintained with ± 5°C accuracy. The run duration is measured from coal injection. Then the heater is turned off, removed from the autoclave and the run is terminated.

In slow heating liquefaction tests the same procedure is employed except that slurry is injected when the autoclave is at room temperature. The reaction mixture is then heated to operating temperature. The reaction time count starts when the desired operating temperature is reached.

After the liquefaction run is completed and the reactor cooled down, coal conversion is determined using Soxhlet extraction as described by Joseph (1991). The liquid product is classified as hexane solubles (oils + gases), toluene solubles (asphaltenes), and THF solubles (preasphaltenes). In later runs, after cool down, vent gas from the autoclave is analyzed continuously sampling the gas vented from the autoclave directly into a mass spectrometer (Extranuclear Laboratories, Inc.; Model C50). The total gas yield, including volatiles loss during pretreatment (8 wt% at the conditions used), is determined and then subtracted from the value of hexane solubles (oil + gas) to obtain the yield of oils alone.

RESULTS AND DISCUSSION

Liquefaction runs were conducted with Illinois No. 6 coal at three sets of conditions:

High severity: 400°C, 1500 psia, 30 minutes,
Low severity a: 350°C, 1500 psia, 30 minutes, and
Low severity b: 385°C, 1500 psia, 15 minutes.

The results are shown in Tables 1, 2, and 3, classified according to the liquefaction conditions employed. All yields are based on the moisture and ash free (maf) raw coal charge.

High Severity Liquefaction. First, raw coal was examined under slow (run C2) and rapid (runs 2 and 8) heating liquefaction conditions. Then, a series of tests with steam treated coal were conducted: runs 6 and 12 were carried out under rapid heating conditions. The importance of preventing the exposure of pretreated coal to oxygen (run 11) and the importance of rapid heating (run 10) for the liquefaction were also demonstrated. Results are shown in Table 1.

The total yield of liquid product from raw coal obtained at rapid heating conditions appears to be slightly lower than at slow heating due to the longer overall reaction time in a slow heating run. The yield of oils, however, is increased and preasphaltene yield is decreased. No improvement in the yields was observed when steam pretreated coal was subjected to the liquefaction under slow heating. Compared to raw coal, a lower total yield as well as a lower yield of each fraction were obtained. In rapid heating liquefaction, however, the yield of hexane solubles are substantially increased while asphaltenes are reduced. When steam treated coal is deliberately exposed to ambient air for one hour before slurrying with deoxygenated tetralin, the pretreatment effect deteriorated. The oil yield decreased even below the value for raw coal with rapid heating. Total yield also decreased. Asphaltene yield is higher and preasphaltenes yield is lower when an exposure to air is prevented.

Low Severity Liquefaction a. Raw and steam pretreated coal were tested under rapid heating conditions at reduced severity (low severity liquefaction a). In addition to liquid product characterization, the amount of gas formed in the process was also determined. Liquefaction yields are shown in Table 2.

The results obtained under these reduced severity conditions show no improvement in the liquefaction yields between raw and steam pretreated coal. (That the pretreatments were successful was confirmed by the increased pyridine extraction yields.) Steam pretreatment did, however, increase gas yield at the expense of oils.

A possible explanation for the lack of improvement in yields after steam pretreatment may be found in the temperature history in the autoclave. The coal slurry (made of raw or steam treated coal) was injected into the autoclave preheated to 350°C. In all cases the injection caused the temperature to drop below 300°C. This was followed by a recovery to 350°C in about 1.5 minutes. Consequently, the sample had passed through a region below 360°C where retrogressive reactions occur, resulting in low yield of the liquid product and in a higher yield of gas. Perhaps, the chosen reaction temperature itself, 350°C, is where retrogressive reactions occur.

Low Severity Liquefaction b. To keep the reaction temperature higher after slurry injection and during the reaction, the low severity liquefaction temperature was increased to 385°C (which is above the upper limit of pretreatment), the reaction time reduced to 15 minutes, and the pressure was left unchanged at 1500 psia. The procedure was also slightly modified: the autoclave was initially preheated to 400°C. After the temperature drop caused by the slurry injection, the temperature was raised to 385°C. The results are shown in Table 3. In all rapid heating liquefaction experiments the reaction temperature never dropped below 320°C.

Low severity liquefaction b tests show a strong improvement in the quality of product resulting from steam pretreatment under rapid heating conditions (runs no. 31 and 34 compared to runs no. 32 and 33). The yields of hexane solubles were increased with a slight reduction in the total gas make. Remarkably, the oil yields are doubled while preasphaltenes are reduced. This improvement in the liquid quality occurred together with an increase in the total yield of liquids.

Exposure of steam treated coal to air (runs no. 35 and 36) resulted in a drop in the yield of hexane solubles and oils almost to the level of raw coal. The total yield of liquids also decreased. In slow heating liquefaction (runs no. 37 and 38), the total yield of liquids has dropped compared to rapid heating, but is still higher than raw coal under rapid heating. Of the three liquid fractions, only hexane solubles are distinctly affected by heating rate. Under slow heating conditions the highest total gas make was observed, the total yield of hexane solubles and oils alone have intermediate value between raw and steam treated coal under rapid heating. The higher total yield under slow heating liquefaction may result from a longer reaction time (it takes up to 30 minutes to preheat autoclave to 385°C), since the liquefaction process starts before the reactor temperature reaches 385°C, even under low pressure.

Summarizing these results, the behavior of Illinois No.6 coal in low severity b liquefaction follows the same trends as high severity. The best results, highest total yield and yield of hexane solubles, are obtained from steam pretreated coal under rapid heating conditions. Moreover, the improvement in the hexane solubles is achieved as a result of an increase in the yield of oils and a decrease in gas yield (at least at low severity). The liquefaction yields (total yield and hexane solubles) obtained from steam treated coal under slow heating conditions have intermediate values between raw and steam treated coal under rapid heating. When steam treated coal is deliberately exposed to air, the total yield drops to the level of raw coal (rapid heating), the yield of hexane solubles is slightly higher than from raw coal under rapid heating

but does not exceed the value obtained under slow heating.

CONCLUSIONS

The following conclusions are drawn from this work:

1. Steam pretreatment substantially improves the quality of the liquid product in coal slurry liquefaction. Under low severity conditions, the oil yield is more than doubled, going from 12.5 to 29 wt %.

2. The benefits of steam pretreatment can be realized only if the pretreated coal is rapidly heated to liquefaction temperature. This is necessary in order that the pretreated coal pass quickly through the region of retrogressive reactions. This region, in which retrogressive reactions can mitigate or even destroy the effects of pretreatment, extends downward from 360°C to perhaps as low as 320°C. The upper limit on heating time can not yet be specified, but appears to be about one minute (which was the recovery time for the low severity b series of tests).

3. Pretreated coal must be protected from oxygen to preserve the benefits of pretreatment.

ACKNOWLEDGMENT

This work was supported by the US Department of Energy under contract number DE-AC22-90PC90052.

REFERENCES

Brandes, S.D., Graff, R.A., Gorbaty, M.L., and Siskin, M., 1989, Energy & Fuels, 3, 494

Graff, R.A. and Brandes, S.D., 1987, Energy & Fuels, 1, 84

Graff, R.A. Zhou, P. and Brandes, S.D., 1988, *"Steam Conditioning of Coal for Synfuels Production"*, Final Report, DOE Contract No. DE-AC21-87MC23288.

Witehurst, D.D., Farcasiu, M., Mitchel, T.O., 1976, "The Nature *and Origin of Asphaltenes in Processed Coals"*, Annual Report, EPRI AF-252.

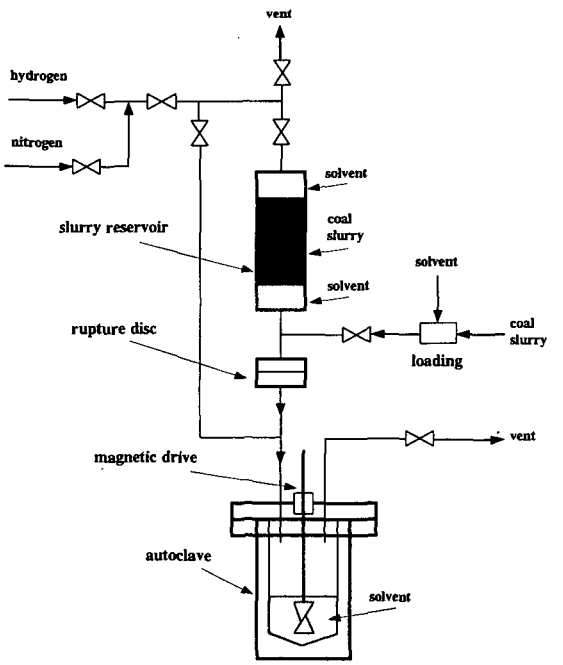

Figure 1. Stirred Autoclave with Coal Slurry Injection (Shown Prior to Coal Slurry Injection)

Table 1.
High Severity Liquefaction of Illinois No.6 coal.
(400°C, 1500 psia, 30 minutes)

		Conversion (%wt)			
Run No.	Conditions	Total (liquid + gas)	Hexane Solubles Oils+Gas	Toluene Solubles Asphaltenes	THF Solubles Preasphaltenes
C2	raw coal slow heating	81.6	37.0	16.9	27.7
2	raw coal	73.8	42.2	10.0	21.6
8	rapid heating	80.0	48.7	16.7	14.6
10	steam treated coal slow heating	73.8	35.2	14.4	24.2
6	steam treated coal	85.7	60.1	17.2	8.4
12	rapid heating	79.3	55.8	14.7	8.8
11	steam treated coal, exposure to air, rapid heating	66.3	38.6	19.8	7.9

Table 2.
Low Severity a Rapid Heating Liquefaction of Illinois No.6 Coal.
(350°C, 1500 psia, 30 min)

		Conversion (wt %)					
			Hexane Solubles			Toluene Solubles	THF Solubles
Run No.	Conditions	Total (liquid + gas)	Total	Gas	Oils	Asphaltenes	Preasphaltenes
28	raw coal	73.9	47.4	5.52	41.88	10.9	15.6
29	steam treated	71.3	47.1	13.52	33.58	9.5	14.7
30	coal	70.9	42.6	12.02	30.58	11.0	17.0

Table 3.
Low Severity b Liquefaction of Illinois No.6 Coal.
(385°C, 1500 psia, 15 min)

		Conversion (% wt)					
			Hexane Solubles			Toluene Solubles	THF Solubles
Run No.	Conditions	Total (liquid + gas)	Total	Gas	Oils	Asphaltenes	Preasphaltenes
32	raw coal	71.6	27.7	13.7	14.0	17.9	26.0
33	rapid heating	71.3	26.5	15.5	11.0	20.2	24.6
31	steam treated coal	71.3	41.8	11.9	29.9	16.4	19.3
34	rapid heating	70.9	38.9	10.3	28.6	15.8	21.5
35	steam treated coal,	71.3	30.5	14.9	15.6	18.9	23.3
36	exposure to air	70.9	31.2	13.8	17.4	17.1	23.1
37	steam treated coal	71.3	35.2	16.4	18.8	20.0	19.7
38	slow heating	70.9	34.1	19.2	14.9	18.6	27.2

EFFECT OF HYDROTREATING CONDITIONS ON HYDROCRACKING OF A COAL DERIVED LIQUID

X. Zhan, H.S. Joo, and J. A. Guin
Department of Chemical Engineering
Auburn University, AL 36849-5127

Keywords: Coal Liquid, Hydrotreating, Hydrocracking

ABSTRACT

Several coal derived liquids produced using different hydrotreating severities were hydrocracked to naphtha over a presulfided commercial hydrocracking catalyst. The feeds had similar boiling range and molecular type distribution but different nitrogen content. Feed nitrogen content had a significant effect on the hydrocracking activity, activity maintenance, and selectivity. Rapid deactivation was observed for feeds with nitrogen content higher than 50 ppm. For the feed with 50 ppm N, the gas oil (+205°C) conversion to naphtha decreased observably in the initial 4 hours. An initial catalytic activity study indicated that first order kinetics can be used to describe the gas oil conversion to naphtha. The initial hydrocracking rate of gas oil was approximately inversely proportional to the feed nitrogen content. Related model compound studies showed that the hydrocracking of cumene and hexadecane was very dependent on feed N content.

INTRODUCTION

Since it has been expected that total petroleum products demand will rise greatly before the end of this century, refiners are increasing the proportion of heavier, poorer quality crude or syncrude in their feedstocks. These feeds include less valuable petroleum stocks such as residua, and fuels derived from coal, shale, and tar sands. However, liquids derived from direct coal liquefaction still have low hydrogen to carbon ratio, high polyaromatic concentrations, and high sulfur and nitrogen concentrations. Upgrading of these liquids is required before they can be blended into refinery feeds. The primary upgrading process usually involves the hydrotreating of either the entire coal liquid or individual fractions obtained by distillation.

Although hydrogen content can be increased and heteroatoms reduced significantly in the hydrotreating process, the hydrotreated coal liquid still has a high boiling point because only minimal hydrocracking occurs in the hydrotreater. Further downstream treatment in the form of hydrocracking is necessary before fuels of high quality can be obtained. The hydrocracking process is required because coal liquids generally have a high content of polycyclic aromatic compounds, which are relatively unreactive in catalytic cracking.

Hydrocracking is a flexible refining process that allows conversion of feedstocks ranging from naphtha to residua into more valuable, lower boiling products. Hydrocracking catalysts are dual functional, consisting of hydrogenation metals on an acidic cracking base. There have been commercial hydrocracking processes using zeolite-based catalysts for converting petroleum distillates and residues.[1] The research on hydrocracking coal liquids is still very limited. In this work, we studied the activity and activity maintenance of a commercial hydrocracking catalyst using coal liquids with different hydrotreating conditions. The objective was to examine how hydrotreating conditions affect hydrocracking reactions. We also performed some model compound hydrocracking experiments to study the effect of N on hydrocracking rates.

EXPERIMENTAL

Model Compound Experiments. Reactions were performed in tubing bomb microreactors (TBMRs) charged with 1000 psig ambient hydrogen pressure. Two solutions were used : (1) 5g of hexane solution containing 2 wt% cumene, (2) 6g of pure hexadecane. Different nitrogen contents were obtained using pyridine. Experiments were performed at 350°C for cumene reactions and at 400°C for hexadecane reactions ; both for 20 min using 0.1g of a commercial NiMo/zeolite catalyst (Akzo KC2600, MoO_3 < 25%, NiO 1-10%, Al_2O_3 30-70%, SiO_2 20-50%).

Coal Liquid Experiments. The coal liquid hydrocracking experiments were carried out in both an upflow continuous reactor and TBMRs to study the deactivation behavior and

initial activity of the catalyst. The feed reactants were hydrotreated coal liquids prepared with different hydrotreating severities in a continuous reactor[2]. Four hydrotreated liquids with similar boiling range distribution and molecular type distribution but with different nitrogen contents, as summarized in Table 1, were prepared as hydrocracking feeds to investigate the effect of hydrotreating conditions on the hydrocracking reaction.

In the continuous reactor, liquid feed and hydrogen were mixed to produce a dispersive stream entering the bottom of the externally heated reactor tube. The catalyst (5 g) was crushed to 16-25 mesh, diluted with 1.0 mm glass beads (20 g), and then placed in the center of the reactor. The reactor was operated at 400°C and 9.7 MPa with a pressure drop across the reactor bed of about 0.1 MPa. Prior to the start of a run the catalyst was presulfided using 5 wt% CS_2 in cyclohexane at a liquid flow rate of 0.05 ccm and hydrogen at 100 sccm.

The TBMR runs were performed at 400°C and 6.9 MPa cold H_2 pressure. For the deactivation runs in TBMR, 4 g of liquid reactant was used with 1 g catalyst for 2 hours. The catalyst was recovered, washed in THF, and dried in air over night. This catalyst was then used for the next run with fresh feed and the same procedure was repeated for five times, so that the total time the catalyst exposed to the reaction environment was 10 hours. Prior to the first reaction, the catalyst was presulfided in the same type of TBMR using 0.5 g CS_2 for two hours at 400°C and 6.9 MPa cold H_2 pressure. For the kinetic experiments, approximately 4 g of liquid reactant was charged to the TBMR with different loadings of catalyst ranging from 0.1 g to 1 g. The reaction time was from 20 to 120 min. The liquid product was collected and analyzed using GC simulated distillation according to ASTM test method D2887. While the detailed GC boiling curve was obtained, for simplicity of discussion, the product boiling range distribution in this study was grouped into three cuts only: gas, naphtha (-205 °C), and gas oil (+205 °C). The gas make was obtained by difference using the weights of feed and liquid products. The percentage of gas make was defined as

$$\text{Gas Make} = \frac{\text{wt. of gases after RXN} - \text{wt. of Initial } H_2}{\text{wt. of liquid feed}} \qquad (1)$$

RESULTS AND DISCUSSION

Model Compounds Experiments. The effect of feed nitrogen content on cumene and hexadecane conversion is shown in Figure 1. Cumene conversion without nitrogen was 96%. It is relatively easy to crack cumene into benzene and propylene due to the tertiary carbon of cumene which can form very stable tertiary carbonium ions on acid sites. The reactions of hexadecane, a straight-chain paraffin, showed about 51% conversion in the absence of nitrogen. In this reaction (0 ppm N), 5% gas, 41% naphtha, and 54% of gas oil were obtained and 82% of the hexadecane converted was in the naphtha fraction. KC2600 catalyst with hexadecane in the absence of nitrogen has very good selectivity for naphtha. Little conversion was observed above 100 ppm N in both reactions. These results show that the hydrocracking activity of KC2600 is completely poisoned by amounts of nitrogen around 100 ppm and nitrogen removal from the high nitrogen containing feeds such as coal derived liquids is required prior to the hydrocracking process. The catalytic cracking and hydrogenation functions of KC2600 (NiMo/zeolite) can be examined by two reaction pathways of cumene hydrocracking.

1: cumene → benzene + propylene → other products
2: cumene → iso-propylcyclohexane → other products

Pathway 1 is cumene cracking to benzene (B) and propylene (PP) by acid sites mainly on the zeolite. In pathway 2, cumene is hydrogenated to iso-propylcyclohexane (IPCH) by metal sites (Ni and Mo) followed by cracking to other compounds such as cyclohexane (CH), PP, etc. From these experiments, the concentrations of cumene, B, and IPCH from cumene reactions as a function of nitrogen content are shown in Figure 2. The concentration of B was about 0.7% at 0 ppm N and decreased to 0 at about 33 ppm N. IPCH was observed to appear at about 13 ppm N. Below 13 ppm, IPCH is probably cracked to form CH and PP. The IPCH concentration increased to a maximum around 33 ppm N and decreased to about 0 above 100 ppm N. These observations show the following. Below 10 ppm N, cracking reactions by acid sites are dominant. As nitrogen content increases from 10 ppm, however, acid sites are poisoned. On the other hand, metal sites have substantial activity in the range of 10-100 ppm N with IPCH being the main product identified. This activity was also poisoned above 100 ppm N. It can be concluded that the acid function for reaction pathway 1 is severely poisoned around 33 ppm N, while the hydrogenation function (Ni and Mo) still has some activity up to

about 100 ppm N.

Coal Liquids Experiments. Figure 3 shows the lumped boiling range distribution of the hydrocracking liquid products from continuous reactor. The feed had a nitrogen content of 230 ppm (Feed B in Table 1), and the reaction conditions have been described previously. It is seen that there is a significant deactivation of the catalyst, and it is completely deactivated in 24 hours on stream, as reflected by the gas oil content. However, very high hydrocracking activity was observed in a TBMR run with fresh catalyst, which is also shown in Figure 3. It is probable that, during the first few hours in the continuous reactor, the liquid produced might contain low gas oil fraction (high naphtha fraction) because of initially high cracking activity. The gas oil content then increased gradually due to catalyst deactivation. As a result, the sample collected in the first 24 hours, which is actually a mixture produced during this period, exhibited some gas oil conversion, but not as high as that in TBMR in which the reaction time was only 2 hours. The rapid deactivation of the catalyst is speculated to be due to nitrogen or polyaromatics in the feed. Therefore, as a follow on to this study, several deactivation runs were performed in TBMRs with different feed nitrogen contents.

Figure 4 shows the experimental runs made to examine the effect of feed hydrotreating conditions on the hydrocracking reactions. In the following, the feed N content is used as a measure of hydrotreating severity, although other feed characteristics, e.g. polyaromatics content, are also important in catalyst activity behavior. Figure 4 shows that the gas oil conversion decreases with the increase of nitrogen in the feed. The deactivation rate also increases with the increase of nitrogen content, except for the 1800 ppm N feed, where gas oil conversion was low. This is consistent with previous results in the literature. Yan[3] reported that for the hydrocracking of heavy gas oil over NiW/REX-NiW/silica-alumina, when the nitrogen content was increased from 1 ppm to 12 ppm, the reactor temperature had to be increased by 16.7°C to maintain the same catalyst activity. Bouchy et al[4] studied the hydrocracking of a model light cycle oil with 480 ppm N in the feed. They found that the inhibiting effect of nitrogen led to a decrease of the reaction rate of about 30%. It is generally agreed that nitrogen compounds will irreversibly adsorb on acidic sites of hydrocracking catalysts and thus reduce their effectiveness and activity maintenance. It thus appears that a more active hydrotreating catalyst must be developed or more severe hydrotreating conditions should be employed for HDN to reduce the nitrogen content to even lower levels. Another option lies in the development of new hydrocracking catalysts which are more resistant to nitrogen poisoning. Yet it should be noticed that the yield of desired product, e.g., naphtha formation, also might be greatly affected by the catalyst activity and reaction conditions, as is seen in Figure 5 where considerable gas formation was accompanied with gas oil conversion. It seems that some nitrogen in the feed may function to temper the catalyst activity towards gas formation. Therefore, it appears that quantitative determination of the hydrocracking rate constant and the nitrogen effect would be meaningful for the optimal design of hydrocracker for the coal liquid.

To quantify the effect of N content on the initial hydrocracking rate, an empirical power-law kinetic model, as shown in equation (2) was used to describe the gas oil conversion.

$$-\frac{dy_A}{dt} = \frac{W_{cat}}{W_{liq}} k y_A^{\ a} p_H^{\ b} \qquad (2)$$

In equation (2), y_A is the weight fraction of gas oil, p_H is the partial pressure of hydrogen which is directly proportional to the weight fraction of dissolved hydrogen, W_{cat} is the weight of catalyst, and W_{liq} is the weight of liquid feed. The term $W_{cat}t/W_{liq}$ is equivalent to the reciprocal of WHSV generally used in flow reactors.

Figure 6, plotted as weight fraction vs. reaction time, suggests that the reactions can be adequately described using the following consecutive reaction scheme, because the initial rate of gas formation is zero, and the reaction rate of naphtha to gases is much slower than that of gas oil to naphtha.

$$\textit{Gas Oil} \longrightarrow \textit{Naphtha} \longrightarrow \textit{Gases}$$

In Figure 6, the data were obtained with catalyst loading from 0.1 to 1g, three particle sizes (16-25, 60-80, 80-200), and reaction time from 20 to 120 min. There was no discernable effect of catalyst loading, particle size, or reaction time, therefore, it is believed that, in our experiments, there is neither internal nor external mass transfer limitation and the data represent the results of reaction kinetics. At $W_{cat}t/W_{liq}$ larger than 0.15 hour, the percentage of naphtha

is essentially stable, but more gas was generated with time at the expense of gas oil. Thus, it appears that a value of $W_{cat}t/W_{liq}$ of no more than 0.15 (or WHSV in flow reactor larger than 6) would be appropriate for the hydrocracking of coal liquid, if the desired product is naphtha. In practice, the value of WHSV in a flow reactor is typically less than 6 because the catalyst will be deactivated somewhat in the initial reaction period.

Since the TBMR is a batch reactor, the hydrogen partial pressure decreases with gas oil conversion. For this reason, the rate constant was evaluated using the low gas oil conversion data. The hydrogen concentration in the liquid, which is approximately directly proportional to its partial pressure, was also assumed constant during this initial stage. Therefore equation (2) is reduced to equation (3).

$$-\frac{dy_A}{d\left(\frac{W_{cat}}{W_{liq}}t\right)} = k' y_A^{\alpha} \qquad (3)$$

The linear plots of Figure 7, $\ln (y_{A0}/y_A)$ vs. $W_{cat}t/W_{liq}$ according to equation 3, indicate that gas oil hydrocracking can be described as a first order reaction. The effect of feed nitrogen content is significant. The reaction rate is approximately inversely proportional to nitrogen content. Since this study considered only the initial reaction rate of gas oil conversion, no quantitative effect of feed nitrogen content on catalyst activity towards gas formation was determined as it was generally less than 1%.

REFERENCES

1 Song, C., Schobert, H.H., and Matsui, H., ACS Fuel Chem. Prepr., 36(4), 1892-1899, 1991.

2. Zhan, X., Joo, H.S., and Guin, J.A., paper in preparation for Energy and Fuels.

3 Yan, T.Y., Ind. Eng. Chem. Res., 28(10), 1463-1466, 1989.

4 Bouchy, M., Peureux-Denys, S., Dufresne, P., and Kasztelan, S., Ind. Eng. Chem. Res., 32(8), 1592-1602, 1993.

Table 1. Properties of Feeds for Hydrocracking

Feed	A	B	C	D
Nitrogen Content (ppm)	50	230	820	1800
Naphtha (-205°C) (wt %)	14.1	11.3	10.5	10.3
Gas Oil (+205°C) (wt %)	85.9	88.7	89.5	89.7
Molecular Type Distribution (wt%)				
Paraffins	17.3	15.3	14.4	11.4
Naphthenes	26.2	24.0	22.6	21.1
Monoaromatics	34.8	37.4	39.3	42.3
Polyaromatics	21.7	23.3	23.7	25.2

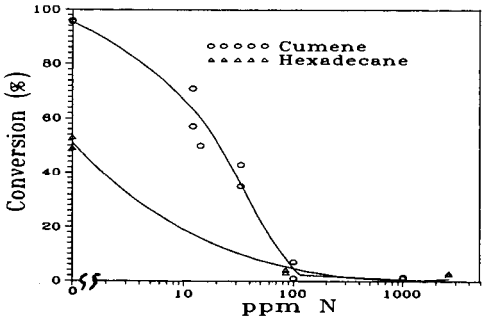

Figure 1 Effect of Nitrogen Content on Cumene and Hexadecane Conversion.

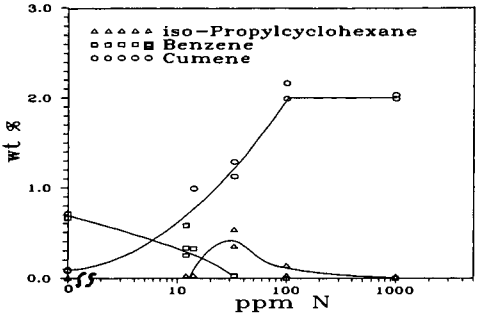

Figure 2 Product Distribution of Cumene Reactions as a Function of Nitrogen Content.

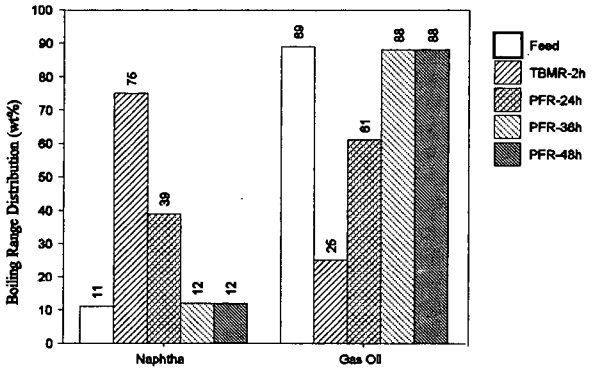

Figure 3 Hydrocracking Catalyst Deactivation in Continuous Reactor with Feed Nitrogen Content of 230 ppm.

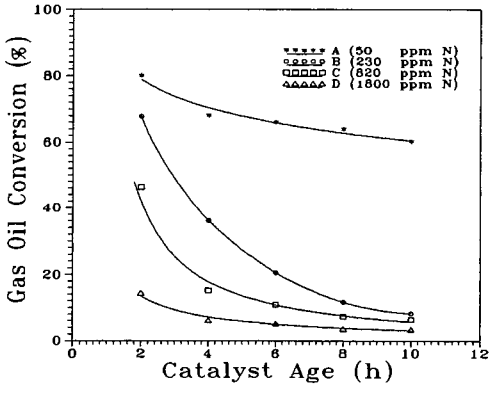

Figure 4 Effect of Feed Nitrogen Content on the Catalyst Deactivation Behavior and Gas Oil Conversion in Successive 2h TBMR Experiments.

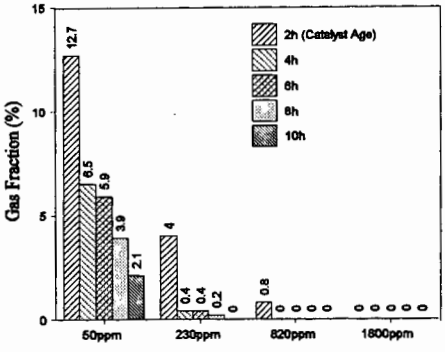

Figure 5 Effect of Feed Nitrogen Content on the Gas Make for Hydrocracking Reactions in TBMR

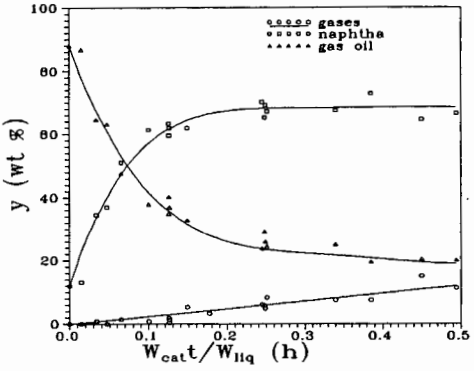

Figure 6 Hydrocracking Product Distribution at 400°C with Feed Nitrogen Content of 230 ppm

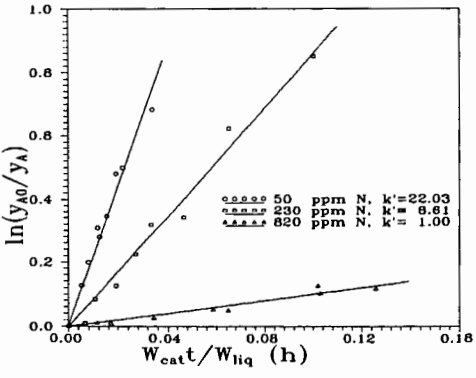

Figure 7 First Order Plots of Gas Oil Conversion with Different Feed Nitrogen Contents

EFFECT OF IRON CATALYSTS ON HYDROGENATION PATHWAYS IN DIRECT COAL LIQUEFACTION

Richard K. Anderson, William J. Clements, Edwin N. Givens and Frank J. Derbyshire
University of Kentucky, Center for Applied Energy Research
3572 Iron Works Pike, Lexington, KY 40511-8433

Keywords: Coal liquefaction, iron catalyst, hydrogenation

Abstract

The effect of a commercially available, high surface area nanometer size iron oxide (SFIO) catalyst on the pathway by which hydrogen is added to a subbituminous coal during direct liquefaction was studied under a variety of conditions. This unique iron oxide, prepared by pyrolyzing volatilized iron carbonyl to produce a finely divided product, is characterized as γ-Fe_2O_3 having a surface area of ~300 m^2/g and particle size of 1-3 nm. Liquefying Wyodak coal in tetralin (0.5 hrs, 415 °C, 2.3 tetralin/dry coal, 6.89 MPa H_2 cold) containing 1.2 wt % Fe as SFIO resulted in an increase in overall coal conversion (77 to 83%) with most of the increase in product being in formation of THF soluble-pentane insoluble product. Adding an excess of sulfur to convert the iron to pyrrhotite further increases conversion to 85% along with a decrease in the THF soluble-pentane insoluble fraction. The presence of catalyst increases the amount of hydrogen added to the product as dihydrogen (H_2) relative to the amount from tetralin via the H-donor pathway. In the absence of catalyst, 60% was added as H_2; adding 1.2% Fe increased H_2 addition to 67%; adding 3 mol S/mol Fe to 1.2% Fe further increased H_2 addition to 82%.

Introduction

Through the use of various types of catalysts, high yields of distillate fuels have been produced in pilot plants from lower-cost subbituminous coal.[1,2,3] The use of high surface area, small particle catalysts has been one area that has been extensively explored in an effort to maximize yields and reduce the cost of catalyst. Fe has been of particular interest as a dispersed catalyst because of its abundance, low cost and its environmental acceptability. Various approaches have been used for preparing disposable nanometer size Fe catalysts, among which are microemulsions,[4,5] aerosols,[6,7,8,9] hydrothermal disproportionation of sulfides,[10] and precipitation of sulfated oxyhydroxides.[11] Highly dispersed iron particles, in various forms as oxides and oxyhydroxides, have been shown to retain their small size upon conversion to pyrrhotite under coal hydroliquefaction conditions.[6,7,12]

In our laboratory, a specially prepared, commercially available superfine Fe oxide (SFIO) was found to have high activity for coal conversion and excellent selectivity for producing distillate product.[13] In the study reported here, the activity of this catalyst for conversion of a Wyodak coal in tetralin was compared with a much lower surface area Fe oxide prepared from Aiusruther spray roast processing of spent acid from steel pickling.[14] The effect of these catalysts on the pathways by which hydrogen (H) is added to the coal and its products was investigated.

Experimental

Samples of the subbituminous coal and powdered iron oxides used at the Wilsonville Advanced Coal Liquefaction Facility in Run 263J[14] were supplied by CONSOL, Inc. The Wyodak coal from the Black Thunder mine in Wright, Wyoming was ground to -200 mesh, riffled and stored under nitrogen at 4 °C. Proximate and ultimate analyses are presented in Table I. The average moisture content measured at the beginning of each run was 21.9 ± 0.72 wt % of as-received coal.

Two iron oxide catalysts were used. One, a sample of SFIO provided by MACH I, Inc., King of Prussia, PA, contained 63 wt % Fe with a γ-Fe_2O_3 structure, average particle size of 1-3 nm, and nitrogen BET surface area of 300 m^2/g.[15] The second, from Bailey Engineers, Fairfield, AL, (IO) was 99% Fe_2O_3 with 0.35 wt % manganese oxide being the largest impurity. The material had a structure of α-Fe_2O_3, nitrogen BET surface area of 8.6 m^2/g, an average particle size of ~140 nm, and bulk density 26 times greater than SFIO (1.37 vs. 0.052 g/ml). Carbon black (CB) was purchased from UIC, Inc. and had a fixed carbon content of 93% with a nitrogen BET surface area of 90 m^2/g.

Liquefaction experiments were conducted by adding 3 grams of coal, 5.4 grams of tetralin, and catalyst to a 50 mL microautoclave. When used, dimethyl disulfide (DMDS) was added at a ratio of 3.0 moles S per mole Fe. The reactor was sealed, pressurized with H_2 to 6.89 MPa, and immersed in a fluidized sand bath set at the specified temperature while continuously agitating at a rate of 400 cycles per minute. After the specified reaction period, the microautoclave was rapidly cooled in a sand bath at room temperature. Gaseous products

were collected and analyzed by gas chromatography. Solid-liquid products were washed from the reactor using tetrahydrofuran (THF) and extracted in a Soxhlet apparatus for 18 hours. The THF-insoluble material (IOM), comprising unconverted macerals and mineral matter, was dried (80 °C/0.1 atm). A pentane insoluble-THF soluble fraction (PA+A) was precipitated from the concentrated THF soluble fraction by adding pentane. The pentane soluble material (Oils) was analyzed with a Hewlett-Packard 5890 gas chromatograph fitted with a DB-5 column to determine the naphthalene-tetralin ratio. Product yields were calculated assuming complete recovery of the inorganic mineral matter plus catalyst, which was demonstrated independently. Fe in the catalyst precursor is presumed to convert to pyrrhotite ($Fe_{0.9}S$) and report to the ash fraction. Oils are calculated by difference, which includes water produced during the reaction and any experimental error. The net product yield equals the amount of maf coal in the feed and coal conversion equals 100 minus the yield of IOM. The average standard deviations for each product fraction were calculated: hydrocarbon gases, 0.1; $CO+CO_2$, 0.4; IOM, 1.4; PA+A, 2.4; Oils, 2.8.

Discussion

The dominant phase of the SFIO, as determined by X-ray absorption fine structure (XAFS) analysis, is $FeOOH{\cdot}xH_2O$ with bulk iron coordinated to six oxygen or hydroxyl groups along with a significant additional fraction of the iron located at the particle surfaces at sites with lower coordination.[16] Extended heating at temperatures >400 °C produces α-Fe_2O_3. Considerable particle growth occurs upon sulfidation in the presence of H_2S and tetralin at 380 °C, with the formation of pyrrhotite having a particle size of several hundred nanometers.[17] However, in the presence of coal, sulfiding produces a much smaller particle size pyrrhotite[6] which has also been observed on Fe-impregnated carbon black.[18]

Approximately 95% of the Fe contained in the residue isolated from runs to which 1.2 wt % Fe was added as SFIO was present as the oxide, even though the amount of sulfur present in the coal (0.39%) was sufficient to convert ~70% of the added Fe to pyrrhotite. However, pyrrhotite would only form when sulfur was added to the reaction mixture. In runs to which a 3-fold excess of sulfur was added along with 1.2 wt % Fe, >95% of the Fe was converted to pyrrhotite within 7.5 min, indicating that when sulfur was present pyrrhotite formed rapidly and was present during almost all of the reaction period. Since particle size of the resulting pyrrhotite was previously reported to be related to the size of the original oxide, SFIO should provide pyrrhotite having a smaller size with correspondingly higher surface area than IO.

As seen in Table II, THF conversion increased when Fe oxides were added to the reaction mixture, while adding sulfur along with the Fe oxides further increased conversion. In the absence of sulfur at 30 minutes runtime, adding SFIO and IO resulted in conversions of 83.4 and 80.2%, respectively, relative to a conversion of 76.7% in the absence of added Fe oxides. The increase was greater for SFIO suggesting a response to the higher surface area. Reactions in which sulfur was added follow the same pattern with SFIO giving higher conversion. At 30 min, addition of sulfur to SFIO and IO increased conversions to 85.4 and 83.6%, respectively, while at 60 min, conversions were 88.8 and 87.0%, respectively.

Oils yields responded quite differently to addition of Fe oxide in the absence of added sulfur. In both cases shown, they actually decreased somewhat, resulting in a buildup of PA+A. When SFIO and IO were present in the 30 min runs, Oils yields decreased to 29.7 and 26.2%, respectively, relative to a yield of 31.8% in the absence of added Fe. When sulfur was added, oil yields increased for both Fe oxides. After 30 min, yields upon addition of SFIO and IO were 36.7 and 37.0%, respectively, while after 60 min, yields were 46.2 and 46.8%, respectively, compared to 42.6% in the absence of added Fe. The sulfided catalyst is clearly better than the oxide for promoting Oils yield.

Adding sulfur to the reaction at the same level as in the other experiments but in the absence of any added Fe oxide caused an increase in conversion from 76.7 to 79.1% and a decrease in Oils yield from 31.8 to 28.2%. At this level of sulfur addition, the calculated initial H_2S partial pressure in the reactor at reaction temperature was 25 psig. The effect on conversion and Oils yield was similar, though less effective than adding Fe oxides in the absence of added sulfur. Since the combined addition of sulfur and Fe oxides was superior to the addition of the Fe oxides alone, the direct contribution from adding sulfur at this level (equivalent to ~1% H_2S in H_2) is small relative to its effect on the chemistry of the Fe in the reaction.

Total H consumption in these reactions was determined from analysis of dihydrogen (H_2) in the gaseous product and the H remaining in the solvent. The latter was calculated from a determination of the change in ratio of naphthalene to tetralin in the pentane soluble fraction. Total H consumption appeared not to increase upon addition of SFIO or IO in the absence of sulfur. Adding sulfur with the Fe oxide had little effect on hydrogen consumption using IO, but a significant effect on hydrogen consumption with SFIO. Total H consumption, based upon maf coal, in the presence of SFIO in the 30 min runs increased from 36 mg/g in the

absence of sulfur to 45 mg/g when sulfur was added. The consumption of H_2 from the gas phase reflected this increased activity. In the 30 min runs, reaction of coal in the absence of additives and in the presence of SFIO gave H_2 consumptions of 23 and 24 mg/g, respectively. Adding sulfur to the SFIO increased H_2 consumption to 37 mg/g. Similar activity changes were observed for the 60 min runs.

The effect of adding 14% of a high surface area carbon (90 m^2/g) on conversion, product yields and H consumption was negligible. Even though the available N_2 BET surface area was more than double the surface area from adding SFIO at a 1.2% Fe level, the reaction did not change. Clearly, the catalytic effect of adding SFIO is not merely a response to added surface area.

Conclusions

Conversion of Wyodak coal to THF soluble product increases in the presence of added Fe oxide, regardless of the presence of sulfur. The higher surface area SFIO is more active than IO for conversion. Both SFIO and IO increase Oils yields when sulfur is added but have little effect in its absence. Since addition of sulfur to coal in the absence of added Fe oxides had little effect on the reaction, the mechanism by which sulfur affects the reaction is presumed to be through sulfiding the Fe. Total H consumption was affected only when both SFIO and sulfur were added to the reaction. The other cases showed little response. The contribution of tetralin to the amount of H consumed in the reaction appears to be relatively constant for reaction times of 30 and 60 min suggesting the reaction pathway involving H-transfer from solvent to coal is important early in the reaction sequence. The effect of SFIO with sulfur, the catalyst that significantly improved H consumption, is to increase direct H_2 addition to the product. The absence of any effect of adding high-surface area carbon indicates that surface area alone is not responsible for the improvement from adding the Fe-oxides.

Acknowledgement

The authors gratefully acknowledge the support of the Department of Energy under contract DE AC22-91PC91040. We also thank Frank Huggins for contributing Mössbauer studies of the liquefaction residues and Z. Feng for her TEM work.

References

1. Southern Electric International, Inc., Technical Progress Report, "Run 262 with Black Thunder Mine Subbituminous Coal" *Document No. DOE/PC/90033-22*, September, 1992.
2. Bauman, R. F.; Coless, L. A.; Davis, S. M.; Poole, M. C.; Wen, M. Y. Continuous Bench-Scale Slurry Catalyst Testing- Direct Coal Liquefaction of Rawhide Sub-bituminous Coal. Proceedings: Coal Liquefaction and Gas Conversion Contractors Review Conference. Pittsburgh, PA. Aug. 1995, p91.
3. Pradhan, V. R.; Lee, L. K.; Stalzer, R. H.; Johanson, E. S.; Comolli, A. G.; Catalytic Multi-stage Liquefaction of Coal at HTI- Bench-scale Studies in Coal/ Waste Plastics Coprocessing. Proceedings: Coal Liquefaction and Gas Conversion Contractors Review Conference. Pittsburgh, PA. Aug. 1995, p75.
4. Wilcoxon, J. P.; Sylwester, A.; Nigrey, P.; Martino, A.; Quintana, C.; Baughman, R. J. *Proceedings, Eighth Annual Inter. Pittsburgh Coal Conf.* 1991, 703.
5. Darab, J. G.; Fulton, J. L.; Linehan, J. C. *Prepr. Pap.- Am. Chem. Soc., Div. Fuel Chem.* 1993, *38(1)*, 27.
6. Andres, M.; Charcosset, H.; Chiche, P.; Davignon, L.; Djega-Mariadassou, G.; Joly, J. P.; Pregermain, S.; *Fuel* 1983, *62*, 69.
7. Andres, M.; Charcosset, H.; Chiche, P.; Djega-Mariadassou, G.; Joly, J-P.; Pregermain, S. *Preparation of catalysts III* (Eds. G. Poncelet and P. Grange), Elsevier: Amsterdam, 1983, pp 675-682.
8. Dadyburjor, D. B.; Stiller, A. H.; Stinespring, C. D.; Zondlo, J. W.; Wann, J.; Sharma, R. K.; Tian, D.; Agarwal, S.; Chadha, A. *Prepr. Pap.- Am. Chem. Soc., Div. Fuel Chem.* 1994, *39(4)*, 1088.
9. Rice, G. W.; Fiato, R. A.; Soled, S. L. 05/26/87. Iron carbide-based catalyst produced in the presence of laser radiation. U. S. Patent 4668647.
10. Dadyburjor, D. B.; Stewart, W. R.; Stiller, A. H.; Stinespring, C. D.; Wann, J. P.; Zondlo, J. W. *Energy Fuels* 1994, *8(1)*, 19.
11. Pradhan, V. R.; Tierney, J. W.; Wender, I. *Energy and Fuels* 1991, *5*, 497-507.
12. Djega-Mariadassou, G.; Besson, M.; Brodzki, D.; Charcosset, H.; Huu, T. V.; Varloud, J. *Fuel Processing Tech.* 1986, *12*, pp 143-145.
13. Quarterly Technical Progress Report, Advanced Direct Liquefaction Concepts for PETC Generic Units, July 1994 through September 1994, DOE/PC/91040-48.
14. Southern Electric International, Inc., Technical Progress Report, "Run 263 with Black Thunder Mine Subbituminous Coal and Dispersed Molybdenum Catalysts" *Document No. DOE/PC/90033-*

23, December, 1992.
15. Srinivasan, R.; Keogh, R. A.; Davis, B. H. "Characterization of Sulfided Iron Catalysts" *Prepr. Pap.-Am. Chem. Soc., Div. Fuel Chem.* 1993, *38(1)*, pp 203-210.
16. Zhao, J.; Feng, Z.; Huggins, F. E.; Shah, N.; Huffman, G. P. "Structure and Phase Transition of an Ultrafine Iron Oxide Catalyst" *Prepr. Pap.- Am. Chem. Soc., Div. Fuel Chem.* 1993, *38(1)*, pp 196-202.
17. Srinivasan, R.- personal communication.
18. Cugini, A.V.; Krastman, D.; Martello, D. V.; Frommell, E. F.; Wells, A. W.; Holder, G. D. *Energy Fuels* 1994, *8(1)*, pp 83-87.

Table I. Black Thunder Coal Analysis

Proximate Analysis	(wt%, as-determined)	Ultimate Analysis	(wt%, dry)
Moisture	21.2	Carbon	68.68
Ash	5.15	Hydrogen	4.76
Volatile Matter	34.4	Nitrogen	1.21
Fixed Carbon	39.3	Sulfur	0.56
Sulfur Types	(wt%, dry)	Oxygen (diff)	18.25
Total	0.39	Ash	6.54
Pyritic	0.07	Ash, SO_3-free	5.42
Sulfate	0.09		
Organic	0.23		

Table II. Product distribution from liquefaction of Wyodak coal in tetralin[a]

Catalyst	none				SFIO			IO			CB[b]
Added Fe, wt% mf Coal	0	0	0	0	1.2	1.2	1.2	1.2	1.1	1.2	0
S/Added Fe mol/mol	0	0	-	-	0	3.0	3.2	0	3.0	3.0	0
H_2S Partial Pressure at temperature, psi			25	24							
Reaction time, minutes	30	60	30	60	30	30	60	30	30	60	30
Products, wt% maf Coal											
HC Gases	0.7	1.0	1.1	1.3	0.8	1.4	2.0	0.8	1.4	1.7	0.7
$CO+CO_2$	5.3	5.2	6.7	5.7	5.3	5.1	7.1	6.1	5.1	4.9	5.2
Oils	31.8	42.6	28.2	34.0	29.7	36.7	46.2	26.2	37.0	46.8	32.4
PA+A	38.9	35.4	43.1	42.2	47.6	42.2	33.5	47.1	40.1	33.6	38.2
IOM	23.3	15.8	20.9	16.8	16.6	14.6	11.2	19.8	16.4	13.0	23.5
THF Conversion	76.7	84.2	79.1	83.2	83.4	85.4	88.8	80.2	83.6	87.0	76.5
n:t ratio	0.26	0.26	0.32	0.40	0.19	0.14	0.16	0.29	0.20	0.24	0.25
Hydrogen consumed, mg/g maf Coal											
from gas	23	30	19	21	24	37	52	22	28	35	20
from solvent	15	15	18	21	12	8	10	16	12	14	16
Total	38	45	37	42	36	45	62	38	40	49	36

a. Liquefaction experiments at 415°C using 3 g Black Thunder coal, 5.4 g tetralin, 6.89 MPa H_2 cold. SO_3-free ash basis.
b. 14% carbon black added (mf coal basis, no Fe).

THE EFFECT OF H_2 PARTIAL PRESSURE AND TEMPERATURE ON CATALYTIC HYDROGENATION WITH MoS_2 CATALYSTS

A. V. Cugini, K. S. Rothenberger, M. V. Ciocco, G. A. Veloski, and D. V. Martello
U.S. Department of Energy, PETC
Pittsburgh, PA 15236

Keywords: Coal Liquefaction, Catalytic Hydrogenation, Molybdenum Catalysts.

INTRODUCTION

Molybdenum-based catalysts have been used extensively for catalytic hydrogenation[1-3]. The type of catalyst, either supported or unsupported, and the preparation and activation procedures can impact catalytic behavior for hydrogenation and coal conversion reactions. This study compared the catalytic hydrogenation and coal conversion observed with preactivated forms of supported and unsupported catalysts. The objective was to utilize model compounds to compare the catalytic hydrogenation activity of these two types of catalysts. The effect of catalyst type, supported or unsupported, on catalytic hydrogenation with and without coal present was studied over a range of pressures, 1.4 MPa (200 psig) - 11.0 MPa (1600 psig) H_2. The results indicated that catalytic hydrogenation activity was observed at H_2 partial pressures as low as 4.8 MPa (700 psig) with both catalyst types.

EXPERIMENTAL

Materials. ACS grade 1-methylnaphthalene from Fisher Scientific Company, found to be 99% pure by gas chromatography, was used without further purification. Blind Canyon coal, (DECS-6) from the U.S. Department of Energy's Coal Sample Program, was used in these studies. The Blind Canyon coal was a low pyrite bituminous coal with 6.3% ash and 3.7% moisture. A unique, high surface area, molybdenum catalyst was prepared at the U.S. Department of Energy's Pittsburgh Energy Technology Center (PETC). The catalyst consisted of the recovered solid from a semi-batch 1-L stirred autoclave reaction of ammonium heptamolybdate, hydrogen sulfide, and Panasol (a mixture of alkylated naphthalenes) under 17.2 MPa (2500 psi) hydrogen at 700 °K [2-4]. The catalyst contained 50% C, 30% Mo, and 20% S by weight, and possessed a BET surface area of approximately 260 m^2/g. Supported molybdenum/nickel catalysts, AKZO AO-60 obtained from HTI, Inc. and Shell-324, were also used. Other catalysts tested included two prepared by impregnating carbon black with Mo or Fe (Mo-C-1 and Fe-C-1, respectively), sulfated Fe_2O_3[5], and carbon black (BET surface area of 490 m^2/g) obtained from Columbian Chemicals Co.

Reactions. Reactions were conducted in a stainless steel batch microautoclave reactor system constructed at PETC. The cylindrical reactor portion has a volume of 43 mL, and the total internal volume, including all tubing and connections, is 60 mL. The reactor was mounted on a rocker arm, which extends into an electrically heated sand bath. In typical experiments, the reactor was charged with various combinations of solvent, coal, catalyst, a sulfur source, and then was pressurized with hydrogen. Unless otherwise stated, a full charge consisted of 6.6 g solvent, 3.3 g coal, 0.1 g catalyst, 0.1 g elemental sulfur, and 6.9 MPa (1000 psi) ambient temperature hydrogen gas. The reactor was then attached to the rocker arm (180 cycles / minute) and plunged into a preheated sand bath, where it was heated up to 700 °K in 2 to 4 minutes. It was held at temperature in the sand bath for 30 minutes, removed and allowed to air cool, typically in less than 5 minutes, to room temperature. The reactor was vented and the gas collected for analysis.

Sample Work up Procedure and Coal Conversion Calculation. During work up, the reactor (including tubing) was cleaned and rinsed with tetrahydrofuran (THF). The material collected was combined and filtered through a 0.45 micron filter under nitrogen gas pressure, yielding the "THF solubles" and "THF insolubles." Coal conversion was calculated based on the mass of MAF coal from the measured mass of THF insolubles adjusted for catalyst and coal mineral matter[6].

Gas and Pressure Analyses. At the completion of each run, product gases were collected and analyzed at PETC by a previously published method [7]. The product gaseous mixture composed mainly of H_2, C_1-C_4, CO_2, and H_2S, was corrected for non-ideal behavior using an equation of state, and the amount of H_2 consumed was then calculated.

Solvent Hydrogenation Analysis. Low-Voltage, High-Resolution Mass Spectrometry (LVHRMS) data were used to calculate solvent hydrogenation. LVHRMS data were obtained on a Kratos MS-50 high-resolution mass spectrometer interfaced to a personal-computer-based data system developed at PETC. Further details on the LVHRMS technique and data reduction routines are provided in references 8 and 9.

RESULTS AND DISCUSSION

The catalytic hydrogenation of 1-methylnaphthalene using various catalysts was investigated in microautoclave reactors. The results from the catalytic hydrogenation experiments are compared in Table 1. The results in Table 1 seem to indicate that supporting the catalyst (either Fe or Mo) is beneficial for solvent hydrogenation. This is somewhat surprising for the Mo system since as shown in Table 2, the dispersion (physical) for the MoS_2 catalyst is about the same or slightly greater for the unsupported than the supported catalyst. Also shown in Table 1 is the synergistic effect of having both the sulfated Fe_2O_3 and carbon black present during solvent hydrogenation. The H_2 consumption is much higher with both the sulfated Fe_2O_3 and carbon black present than with either used alone and is twice the sum of the H_2 consumed for the sulfated Fe_2O_3 and carbon black each employed separately. In addition, hydrogen consumption using the mixed pair of sulfated Fe_2O_3 and carbon black was equal to that of the highly dispersed MoS_2. A possible explanation is that the sulfated Fe_2O_3 may associate with the carbon black allowing absorbed hydrogen to migrate to the carbon surface (i.e., spillover[10]). This hydrogen could be active and could increase the amount of solvent hydrogenated and the H_2 consumption. A second possibility is that the presence of the carbon black resulted in a more dispersed form of pyrrhotite. Experiments are being conducted in order to test these possibilities.

TABLE 1. Effect of Catalyst Type on Solvent Hydrogenation, 6.9 MPa (1000 psig) H_2 cold / No coal)

Catalyst[a]	H_2 Consumed (mMol)	Solvent Hydrogenation (%)
MoS_2 (unsup.)	28	28
Mo-C-1	55	48
AO-60	54	53
Shell-324	52	53
Fe-C-1	38	19
Sulfated Fe_2O_3	10	na
Sulfated Fe_2O_3 + Carbon Black[b]	28	na
Carbon Black[b]	4	1
None	5	1

[a]3000 ppm active metal loading used with respect to solvent weight.
[b]1.0 g of Carbon Black added.

TABLE 2. Catalyst Dispersion

Catalyst	XRD size (002 plane of Mo, Å)	BET Surface Area (m^2/g)
MoS_2 (unsup.)	<25	260
AO-60	30	162
Mo-C-1	47	na

TABLE 3. Effect of Catalyst Type on Coal Liquefaction Experiments

Catalyst[a]	Coal Conversion (%maf coal)	H_2 Consumed (mMol)	Solvent Hydrogenation (%)
MoS_2 (unsup.)	95	55	13
AO-60	87	32	10
Shell-324	81	39	9

[a]1000 ppm active metal loading used with respect to maf coal weight.

In the presence of a complex system, such as coal, the trends are altered, as shown in Table 3. There does not appear to be a significant difference between the supported and unsupported catalysts. If anything, the unsupported catalysts appear to outperform the supported catalysts. This is not surprising in that the effect of the addition of coal on the suppression of catalytic

hydrogenation activity of both the unsupported and supported catalysts has been previously reported [11,12]. The unsupported MoS_2 and supported AO-60 catalysts are compared with respect to the effect of H_2 pressure on H_2 consumption and coal conversion in Figures 1 and 2 respectively. Figure 1 shows that the H_2 consumption for the MoS_2 with no coal present was lower than that of the supported catalyst at all the pressures tested. However, as shown in Figures 1 and 2, the H_2 consumptions and coal conversions, with coal present, are similar for both catalysts.

SUMMARY

The focus of this study was to compare the catalytic hydrogenation observed with supported and unsupported catalysts. In the tests with the 2-ring aromatic solvent (1-methylnaphthalene), the supported catalysts showed superior catalytic hydrogenation performance. Even the case where the support and catalyst precursor were added separately (Sulfated Fe_2O_3 + Carbon Black), the hydrogen consumption was greater than the unsupported catalyst alone. However, the performance of supported and unsupported catalysts in hydrogenation and conversion were comparable when coal was added to the system. Also, at an initial H_2 pressure of 6.9 MPa (1000 psig) cold with coal present, the H_2 consumptions and coal conversions are slightly higher for the unsupported catalyst experiments.

DISCLAIMER

BIBLIOGRAPHY

1. Derbyshire, F. J., Catalysis in Coal Liquefaction: New Directions for Research, IEA CR/08 June (1988).
2. Cugini, A. V., Krastman, D., Lett, R. G., and Balsone, V. D., *Catalysis Today*, **19**(3), pp. 395-408 (1994).
3. Cugini, A. V., Martello, D. V., Baltrus, J. P., and Holder, G. D., *Proceedings of the 17th International Conference on Coal Utilization and Slurry Technologies*, Clearwater, FL, April 28-May 1, (1992).
4. Cugini, A. V., *Ph. D. Dissertation*, University of Pittsburgh (1993).
5. Pradhan, V. R., Herrick, D. E., Tierney, J. W., and Wender, I., "Finely Dispersed Iron, Iron-Molybdenum, and Sulfated Iron Oxides as Catalysts for Coprocessing Reactions," *Energy and Fuels*, **5**(5), pp. 712-720 (1991).
6. Ciocco, M. V., Cugini, A. V., Rothenberger K. S., Veloski, G. A., and Schroeder, K. T., "Effect of Pressure on First Stage Coal Liquefaction with Dispersed Catalysts," Proceedings of the Eleventh Annual International Pittsburgh Coal Conference, Pittsburgh, PA, pp. 500-505, (1994).
7. Hackett, J. P. and Gibbon, G. A. In Automated Stream Analysis for Process Control, Manka, D. P., ed., Academic Press, pp. 95-117, (1982).
8. Schmidt, C. E., Sprecher, R. F., and Batts, B. D., Anal Chem., **59**, pp. 2027-2033, (1987).
9. Schmidt, C. E. and Sprecher, R. F., In Novel Techniques in Fossil Fuel Mass Spectrometry, ASTM STP 1019, Ashe, T. R. and Wood, K. V., eds., American Society for Testing and Materials: Philadelphia, PA, pp. 116-132, (1989).
10. Boudart, M. and Djega-Mariadassou, G., In Kinetics of Heterogeneous Catalytic Reactions, Princeton University Press, Princeton, NJ, pp. 205-206, (1982).
11. Rothenberger, K. S., Cugini, A. V., Schroeder, K. T., Veloski, G. A., Ciocco, M. V., "The Effect of Coal Addition on Solvent Hydrogenation and Coal Conversion in a Model Alkylnaphthalene Solvent," Proceedings; ACS Div. of Fuel Chem., 39(**1**), (1994).
12. Ciocco, M. V., Cugini, A. V., Rothenberger K. S., Veloski, G. A., and Schroeder, K. T., "The Effect of Hydrogen Pressure on First-Stage Coal Liquefaction with Dispersed and Supported Catalysts; the Role of Catalyst in Hydrogen Transfer," Presented at the American Institute of Chemical Engineers, 1995 Annual Meeting, November 12-17, (1995).

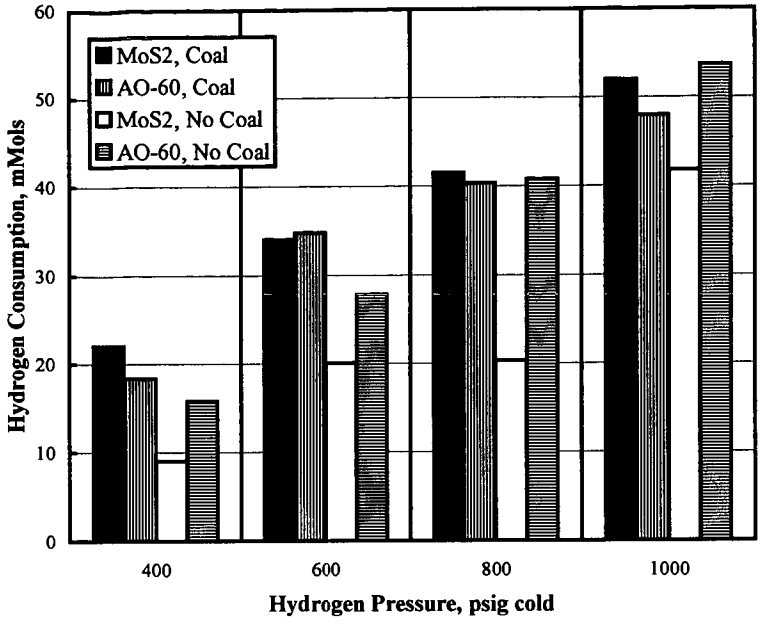

Figure 1. Effect of Pressure on Hydrogen Consumption

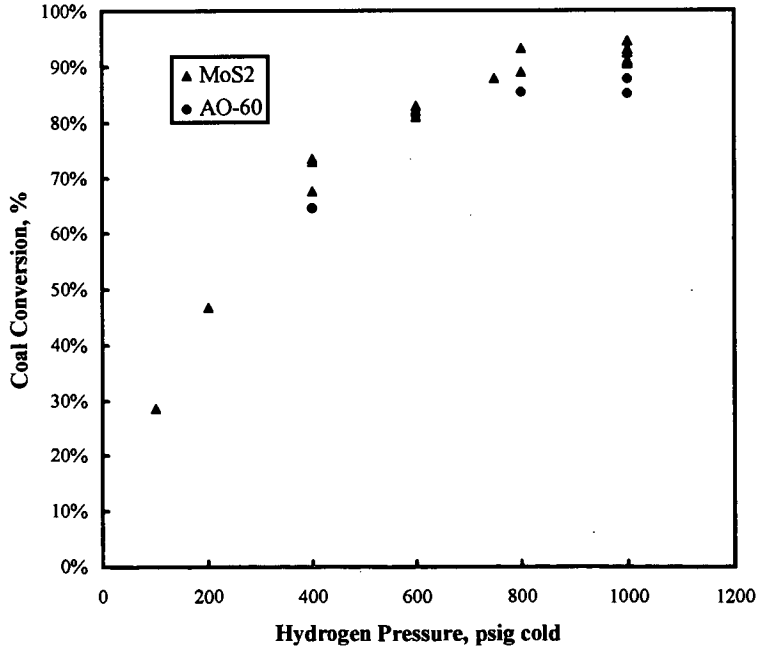

Figure 2. Effect of Pressure on Coal Conversions

COMPONENTS OF OIL DERIVED FROM LIQUEFACTION OF HYDROCARBON-RICH MICROALGAE

Seiichi INOUE, Shigeki SAWAYAMA and Tomoko OGI
National Institute for Resources and Environment, 16-3 Onogawa, Tsukuba, Ibaraki 305, Japan

Keywords: *Botryococcus braunii*, liquefaction, components

ABSTRACT

Botryococcus braunii is a colonial green microalga that produces and accumulates oily hydrocarbons called botryococcenes(C30-36). Liquefaction was applied to *B. braunii* for recovery of hydrocarbons. The liquefied oil was obtained with yield of 64% at 300°C. The oil was fractionated into three fractions by silica gel column chromatography and analyzed to determine its composition. The yields of three fractions were 5% of low molecular weight hydrocarbons, formed by degradation of botryococcenes, 27.2% of botryococcenes and 22.2% of polar substances, produced from organic materials other than hydrocarbons through liquefaction. Further analysis using GC-MS identified some components of the oil. Main components of low molecular hydrocarbons and polar substances were C17-22 hydrocarbons and C14-20 fatty acids, respectively.

INTRODUCTION

The use of biomass for energy is largely motivated from the standpoint of global environmental issues. Biomass-derived fuels would reduce greenhouse gas concentrations to the extent that they could replace fossil fuels currently being used. *Botryococcus braunii* is a unique colonial green microalga that produces and accumulates oily hydrocarbons, called botryococcenes (C30-36), with a dry weight range of 17-86%.[1] These hydrocarbons can be upgraded to transport fuels by hydrocracking[2] or catalytic cracking[3] after being recovered from the algal cells.

On a laboratory scale, the hydrocarbons of algal cells are separated by extraction with organic solvent after their freeze-drying and sonicating. However, this method is not suitable for large scale separations due to the high cost. Therefore, an effective method is needed for separating hydrocarbons from algal cells. We have proposed a new method for separating hydrocarbons from algal cells by direct liquefaction. Applying this process to *B.braunii*, a greater amount of oil than that obtained from *B.braunii* was achieved with yields of 57-64% at 300°C compared to our previous work.[4] Liquefaction could be an effective method for converting the algal cells of *B.braunii* into oil.

The analysis of the oil is important for providing preliminary information about the conversion of organic materials and for the recovery of hydrocarbons produced from the algal cells. In this paper, we analyzed the components of the liquefied oil and determined the suitable reaction conditions needed for the recovery of botryococcenes from *B.braunii*.

EXPERIMENTAL

Algal strain and botryococcenes extraction

The Berkeley strain of *B.braunii* was used for the liquefaction. This strain produces mainly $C_{34}H_{58}$.[5] The algal cells of *B.braunii* were filtered using a 20 μm nylon mesh and then freeze-dried. The algal cells (943 g) were ultrasonically extracted with 50 ml of hexane for 30 min. It gave an oil as hexane extracts (50% of dry cell weight). The extract was chromatographed on a silica gel column with hexane as the eluent in order to obtain Botryococcenes (36% of dry cell weight).

Liquefaction

Liquefaction of *B.braunii* was performed in a 300 ml autoclave at 200, 300 or 340°C, with or without Na_2CO_3 as the catalyst. Liquefied oil was extracted from the reaction mixture with CH_2Cl_2. Details of the liquefaction procedure were reported in a previous study.[4]

Fractionation

The liquefied oil was separated into three fractions. The procedure for fractionation is provided in Fig. 1. The liquefied oil was chromatographed on a silica gel column with 200 ml hexane and 200 ml diethylether. The first 100 ml of the hexane eluate gave F1. The next 100 ml of the hexane eluate was F2, and the 200 ml of the diethylether eluate was F3.

Analysis

The mean molecular weight of the respective fractions was measured using the 117 Molecular Weight Apparatus (Corona, Japan). Elemental composition of the respective fractions was analyzed using a 2400 CHN Elemental Analyzer (Perkin-Elmer, USA). The GC analysis was carried out using a capillary column (DB-1, 30 m x 0.25 mm, Hewlett-Packard, USA). The initial oven temperature was held at 100°C for 10 min, then heated to 220°C at 3 °C min^{-1}. The temperatures of the injector and FID were 220°C and 240°C, respectively. The GC-MS (DB-1, 30 m x 0.25 mm, Hewlett-Packard, USA) analysis was carried out under the same condition.

RESULTS AND DISCUSSION

The properties of F1, F2 and F3 and of botryococcenes extracted from the algal cells are shown in Table 1. The mean molecular weight of F2 was in the range of 438-572, and that of

botryococcenes in the algal cells was 472. The elemental composition of F2 was in good agreement with that of botryococcenes. In addition, the GC retention time of F2 coincided well with the retention time of the botryococcenes. From these results, F2 was identified as the botryococcenes. Elemental analysis showed that F1 was hydrocarbons and the mean molecular weight of F1 was in the range of 197-281. These results suggest that F1 is some kind of degraded product of the botryococcenes. F3 contained oxygenated compounds. Since F3 contained oxygen compounds, they may be produced from organic materials except for the hydrocarbons through liquefaction. From these results, we could confirm that F1, F2 and F3 were low molecular weight hydrocarbons, botryococcenes and polar substances, respectively.

Figure 2 shows the yield of each fraction of the liquefied oil and hexane extracts from the algal cells. The recovery (75%) of the botryococcenes in the liquefied oil was obtained when the liquefaction was carried out at 300°C in the presence of a catalyst (5% sodium carbonate). The yields of the three fractions based on an organic basis were 5% low molecular weight hydrocarbons, 27.2% botryococcenes, and 22.2% polar substances.

The recovery of the botryococcenes was improved with the use of a catalyst at the reaction temperatures of 200 and 300°C (Fig. 2). The quantitative difference in the recovery of the botryococcenes between 200°C and 300°C with a catalyst was very small, but recovery at 340°C decreased. The reaction temperature of 200°C is a preferable reaction temperature from the standpoint of energy use. The liquefaction process can be used for recovery of the botryococcenes as well as the conversion of the algal cells into oil. The total recovery of the fractions (F1, F2 and F3) was in the range of 70-88 wt% for the liquefied oils. The liquefied oil of *B. braunii* had a small amount (1%) of nitrogen, but the fractions (F1, F2 and F3) from the silica gel column contained no nitrogen. The loss is most likely due to the strong adsorption of highly polar components in the liquefied oil onto the silica gel.

Further analysis using GC-MS identified some components of the liquefied oil obtained at 300°C with a catalyst. Table 2 shows the main components of low molecular hydrocarbons and polar substances. The main components of low molecular hydrocarbons were C17-22 hydrocarbons. It is thought that these compounds were formed by degradation of botryococcenes in the algal cells. On the other hand, the main components of the polar substances were C14-20 fatty acids. Except for these compounds, many compounds were identified. From the standpoint of the reaction mechanism during the liquefaction of *B.braunii*, it is very interesting that a methoxyl compound was identified. Ether compounds were found in some strains of *B.braunii*.[6,7] The methoxyl compound may be produced during the liquefaction. Phenol and pyrrolidine compounds, which are absent in the cell, were also identified. They are formed by the degradation and combination of the constituents, such as proteins, in the algal cell.

CONCLUSION

The oil derived from the liquefaction of *B.braunii* consisted of three fractions: low molecular hydrocarbons, botryococcenes and polar substances. From an analysis using GC-MS of the oil obtained at 300°C with a catalyst, the main components of the low molecular hydrocarbons and polar substances were C17-22 hydrocarbons and C14-20 fatty acids, respectively. The recovery of botryococcenes was 75%. The recovery of the botryococcenes was improved using a catalyst at reaction temperatures of 200 and 300°C.

REFERENCES

1. T.G. Tornabene, Microorganisms as hydrocarbon producers *Experientia* **38**, 43-46 (1982).
2. L.W. Hillen, G. Pollard, L.V. Wake and N. White, Hydrocracking of oils of *Botryococcus braunii* to transport fuels. *Biotechnol. Bioeng.* **XXIV**, 193-205 (1982).
3. H. Kitazato, S. Asaoka and H. Iwamoto, Catalytic cracking of hydrocarbons from microalgae. *Sekiyu Gakkaishi* **32**(1), 28-34 (1989).
4. Y. Dote, S. Sawayama, S. Inoue, T. Minowa and S. Yokoyama, Recovery of liquid fuel from hydrocarbon-rich microalgae by thermochemical liquefaction. *Fuel* **73**, 1855-1857 (1994)
5. J. R. Maxell, A. G. Douglas, G. Eglinton, and A. McCormick, The botryococcenes-hydrocarbons of novel structure from the alga Botryococcus braunii, Kützing. *Photochemistry* **7**, 2157-2171 (1968).
6. P. Metzger and E. Casadevall, Botryococcoid ethers, ether lipids from *Botryococcus braunii*. *Photochemistry* **30**, 1439 (1991).
7. P. Metzger and E. Casadevall, Ether lipids from *Botryococcus braunii* and their biosynthesis. *Photochemistry* **31**, 2341 (1992).

Table 1 Properties of the fractionated oil and botryococccenes

	Mean molecular weight	Elemental composition			GC retention time
		C(%)	H(%)	O(%)	(sec)
Fraction 1	197-281	84.5-85.5	14.6-15.5	0.0	-3540
Fraction 2	438-572	85.0-86.5	13.2-14.0	0.0-1.0	4140-4380
Fraction 3	867-2209	73.3-77.3	12.2-13.3	10.1-14.3	4680-
Botryococcenes	472	85.7	14.3	0.0	4140-4380

Table 2 Components of liquefied oil

Low molecular weight hydrocarbon
5-Octadecene
Heptadecane
$C_{19}H_{38}$
$C_{20}H_{40}$
Octadecane
Tetramethyl hexadecene
Docosane
Polar substances
Mesityl oxide
Diacetone alcohol
Phenol
Methyl phenol
Ethyl phenol
2,6-Bis(1,1-dimethylethyl)-4-ethyl phenol
Tetradecanoic acid
Trimethyl pentadecanone
Methyl tetradecanoic acid
Hexadecanoic acid
9-Octadecenoic acid
Octadecanoic acid
Eicosanoic acid
1-(7-Methyl-1-oxopentadecyl)pyrrolidine

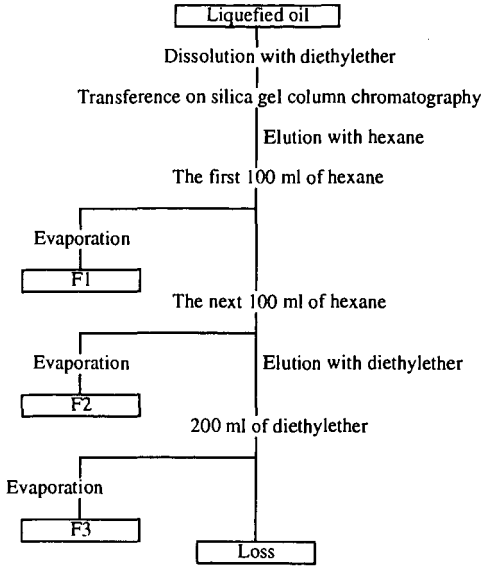

Fig. 1. Procedure for fractionation of liquefied oil

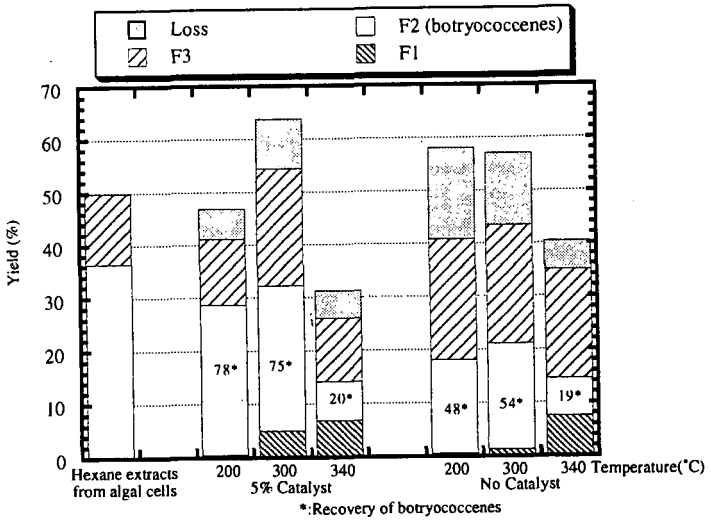

Fig. 2 Yield of each fraction of liquefied oil and hexane extracts from algal cells.

DEMETALLATION OF WASTE OIL WITH COAL

Edward C. Orr, Lian Shao, Edward M. Eyring
Department of Chemistry, University of Utah, Salt Lake City, UT 84112

KEYWORDS: Demetallation, Waste Oils, Coprocessing

INTRODUCTION

The breakdown of coal into liquid fuels has been researched extensively in order to improve upon the economics of the process. To produce liquid fuels from hydrogen deficient coal, hydrogen must be added. Weisz noted that for the most hydrogen deficient coals, it would be necessary to add 8 % by weight hydrogen to produce quality hydrocarbons.[1] One way to decrease the cost of coal liquefaction would be to minimize the need for expensive hydrogen. By coprocessing coal with heavy petroleum resids, the resid may act as a hydrogen donor for the coal diminishing the need for additional costly hydrogen gas.[2] In coprocessing resids with coal it has also been shown that some of the nickel and vanadium that are naturally abundant in the resid reside in the coal char and ash after coprocessing.[3]

More recently, it has been shown that coprocessing waste materials (plastics, rubbers, and waste lubricants) with coal can decrease the cost of coal liquefaction.[4] In addition, coprocessing of coal with waste materials has also been shown to enhance coal conversion to liquids.[5] The addition of waste materials to coal liquefaction reactions also means the addition of heavy metals. Waste rubber tires contain zinc[6] and waste lubricants can contain a variety of heavy metals such as iron, manganese, and zinc.[7] Recent results indicate trace heavy metals found in waste automotive oil will reside in coal char and ash after coprocessing.[7] Demetallation of the trace heavy metals in waste automotive oils was not found to be dependent upon the rank of coal. Out of six different coals used in the demetallation experiments, Illinois #6 coal showed the best demetallation effect. The Illinois #6 has a high content of inorganic matter which has been suggested to have influence on the degree of demetallation. The present paper reports further experiments carried out with Illinois #6 and demineralized Illinois #6 in order to determine the effect of the inorganic portion of the coal on demetallation of waste automotive oil. The extent of the demetallation of the produced oil is reported. X-ray photoelectron spectroscopy (XPS) was used to analyze the surface of the coals before and after demineralization.

EXPERIMENTAL

Illinois #6 was obtained from the Pennsylvania State Coal Sample Bank. The Illinois #6 was used as received (-60 mesh). At all times the coal was stored under a nitrogen atmosphere. The waste automotive oil was obtained from Interline Resources Inc. (Salt Lake City, Utah). The waste automotive oil was stored under ambient conditions and used as received. Demineralization of the Illinois #6 coal was carried out by mixing 500 mL of 6 N HCl with 20 g of Illinois #6 at approximately 45 °C for 1 hour. The coal was then filtered. The filtered coal was then mixed with 250 mL of concentrated HF at ambient conditions for 1 hour. The coal was again filtered. The coal was then treated with 250 mL of 12 N HCl at 45 °C for 1 hour. The coal was then filtered and washed with deionized water until no chloride was precipitated by addition of silver nitrate. The demineralized coal and the untreated coal were dried at 100 °C under vacuum for 2 hours. The dried demineralized and dried untreated coal were then mixed with waste automotive oil in a 1:1 ratio determined by weight. Samples were placed in stainless steel tubing reactors which have volumes of 27 cm^3. Tubing reactors were sealed and then purged with nitrogen gas and finally pressurized to 1000 psig (cold) of hydrogen. Tubing reactors were placed in a fluidized sandbath and shaken vertically at a rate of 160 rpm. The temperature of the sandbath was maintained at 430 °C for 1 hour. After liquefaction the tubing reactor was removed from the sandbath and cooled at room temperature for 5 minutes and finally quenched in cold water. The sample was scraped out of the tubing reactor and placed in a Soxhlet extraction thimble. The internal surfaces of the

tubing reactor were washed with tetrahydrofuran (THF). The THF wash was then placed in the before mentioned extraction thimble. The material was then extracted with THF using a Soxhlet extractor for 48 hours. The nonsoluble portion was dried and weighed in order to calculate the total conversion on a dry ash free. The THF soluble portion was run through a rotary evaporator to remove the THF. The THF soluble portion was then dried under vacuum at 430 °C for 2 hours. The THF soluble portion was extracted with cyclohexane. The portion that is insoluble in cyclohexane is referred to as asphaltenes. The cyclohexane was removed from the cyclohexane soluble portion with a rotary evaporator. The residue was then dried under vacuum at 100 °C for 2 hours. The cyclohexane soluble portion is referred to as oil. The ICP analyses were completed by Data Chem Laboratories, Salt Lake City, UT. The XPS results were obtained from a FISONS ESCALAB 220i-XL using a six channel detection system. Samples were mounted upon double sided 3M tape on top of a metallic sample holder. Charging effects were countered by using an electron flood gun.

RESULTS

Proximate and ultimate analyses of the untreated Illinois #6 coal are given in Table 1.[8] The Illinois #6 coal is a high volatile C bituminous coal. Table 2 shows a comparison of ICP analyses of untreated coal and demineralized coal. There is a significant difference in the amount of inorganic matter present in the untreated coal and the demineralized coal. Table 2 shows a substantial decrease in naturally abundant metals such as aluminum, calcium, iron, and sodium for the demineralized coal. This indicates that the demineralization process was effective in removing a substantial fraction of the inorganic constituents.

XPS analysis of the untreated and the demineralized Illinois #6 coal indicates a decrease in inorganic matter at the surface of the demineralized coal. The XPS analysis of the untreated Illinois #6 coal detected sodium, aluminum, silicon, sulfur, and calcium. XPS analysis of the demineralized coal detected only sulfur and calcium. This indicates that some of the inorganics on the surface of the coal were effectively removed by the demineralization process. From the ICP result, iron makes up over 2 % by weight of the total Illinois #6 coal. Detection of the iron by XPS was not achieved. Past investigators have also reported that detection of iron on the surface of coal is difficult.[9,10] We assume that most of the iron present resides in the bulk coal structure and not upon the coal surface.

The waste automotive oil was analyzed by ICP to determine the type of trace heavy metals present. The results are shown in Table 3. The phosphorous and zinc are present due to an antiwear lubricant, zinc dialkyldithiophosphate, added to the motor oil.[11]

Table 4 shows the liquefaction conversion data for reacting untreated Illinois #6 and demineralized Illinois #6. The untreated Illinois #6 showed better total conversion than the demineralized coal probably because of the decrease in iron in the demineralized coal. Decreasing the iron content decreases the pyrrhotite formation. Pyrrhotites are known to act as coal liquefaction catalysts.[12]

The last two columns of Table 3 shows the ICP analysis of the product oils or the cyclohexane soluble portion of the coal and waste automotive oil reactions. The product oil from both the untreated and the demineralized coal are free of all the elements detected in the untreated waste automotive oil except for some sodium detected in the oil sample from the demineralized coal.

Demineralization of the Illinois #6 decreased the inorganic portion of the coal substantially. The iron content was decreased from 2.3 % to 1.5 % yet the presence of 1 % iron or more would still be sufficient enough for catalytic effects.[13] The remaining iron in the form of iron sulfide will function as a catalyst aiding in dissolution of the coal forming gas, oil, asphaltenes, and char. In coprocessing experiments conducted with resids, Miller et al. concluded that new char formation was responsible for demetallation.[14] In past studies completed in this laboratory, trace heavy metals initially in the automotive oil were found to be more abundant in

asphaltenes.[7] The asphaltenes are precursors to char. Retrogressive reactions allow asphaltenes, laden with heavy metals, to form char which may then trap or embed the heavy metals. Therefor, iron sulfide enhances formation of asphaltenes and indirectly char which traps heavy metals. Thus the iron inherent in the coal may aid in demetallation of the waste automotive oil.

CONCLUSION

Demineralized Illinois #6 coal showed no detectable difference for demetallation of waste automotive oil in coprocessing reactions when compared to untreated Illinois #6 coal. The inorganic portion of the coal, except the iron, seems to have little effect upon the demetallation characteristics of the coal.

ACKNOWLEDGMENTS

We gratefully acknowledge the donation of waste automotive crankcase oil by Professor Larry L. Anderson (Department of Chemical and Fuels Engineering, University of Utah, Salt Lake City, UT) and Interline Resources Inc., (Salt Lake City, UT). Financial support by the U.S. Department of Energy, Fossil Energy Division, through the Consortium for Fossil Fuel Liquefaction Sciences, Contract No. UKRF-4-21033-86-24, is also gratefully acknowledged.

REFERENCES

1 Weisz, P.B., Chemtech, **1982**, 12, 114.
2 Shen, J.; Curtis, C.W., Prepr. Pap. Am. Chem. Soc. Div. Fuel Chem., **1995**, 40 (3), 622.
3 Cugini, A.V.; Lett, R.G., Energy & Fuels, **1989**, 3, 120.
4 Gray, D.; Tomlinson, G., Prepr. Pap. Am. Chem. Soc. Div. Fuel Chem., **1995**, 40 (1), 20.
5 Orr, E.C.; Tuntawiroon, W.; Ding, W.B.; Bolat, E.; Rumpel, S.; Eyring, E.M.; Anderson, L.L., Prepr. Pap. Am. Chem. Soc. Div. Fuel Chem., **1995**, 40 (1), 44.
6 Orr, E.C.; Tuntawiroon, W.; Anderson, L.L.; Eyring, E.M., Prepr. Pap. Am. Chem. Soc. Div. Fuel Chem., **1994**, 39 (4), 1065.
7 Orr, E.C.; Shi, Y.; Liang, J.; Ding, W.; Anderson, L.L.; Eyring, E.M., Prepr. Pap. Am. Chem. Soc. Div. Fuel Chem, **1995**, 40 (3), 633.
8 Pennyslvania State Coal Sample Bank
9 Weitzacker, C.L.; Gardella, Jr., J.A., Anal. Chem., **1992**, 64, 1068.
10 Kelemen, S.R.; Gorbaty, M.L.; George, G.N.; Kwiatek, P.J., Energy & Fuels, **1991**, 5, 720.
11 Tarrer, A.R., Technical Report on DOE Contract No. DE-FC22-93PC93053, Period: May 1, 1994-October 31, 1994, pp. 150.
12 Pradhan, V.R.; Hu, J.; Tierney, J.W.; Wender, I., Prepr. Pap. Am. Chem. Soc. Div. Fuel Chem., **1993**, 38 (1), 8.
13 Sommerfeld, D.A.; Tuntawiroon, W.; Anderson, L.L; Eyring, E.M., Prepr. Pap. Am. Chem. Soc. Div. Fuel Chem., **1993**, 38 (1), 211.
14 Miller, T.J.; Panvelker, S.V.; Wender, I.; Tierney, J.W., Fuel Processing Technology, **1989**, 23, 23.

Table 1 Proximate and Ultimate Analysis of Coals From Pennyslvania State Coal Sample Bank

	Illinois #6
Proximate	
% Ash	16.16
% Volatile	38.14
% Fixed Carbon	45.70
Ultimate	
% Carbon	78.11
% Hydrogen	5.44
% Nitrogen	1.32
% Sulfur	5.39
% Oxygen	9.73
Iron	
% Iron	2.3

Table 2 ICP analyses of untreated Illinois #6 coal and demineralized Illinois #6 coal

Metal	Illinois #6 µg/g	Demineralized Illinois #6 µg/g
Aluminum	1,300	330
Antimony		
Arsenic		
Barium	17	6.6
Beryllium	1.1	.8
Cadmium	1.2	.6
Calcium	6100	320
Chromium	14	15
Cobalt	5.6	
Copper	10	11
Iron	23,000	15,000
Lead	10	
Lithium		
Magnesium	220	42
Manganese	58	13
Molybdenum		
Nickel	14	14
Phosphorous		
Potassium	460	
Selenium		
Silver		
Sodium	770	160
Strontium	24	12
Thallium		
Vanadium	19	20
Zinc	74	4.3

Table 3 First column contains ICP analysis of the received waste automotive oil. The second and third columnss are ICP analyses of oils produced from reacting waste automotive crankcase oil with untreated Illinois #6 coal and demineralized Illinois #6 coal at 430 °C under a 1000 psig (cold) hydrogen for 1 hour.

Metal	Waste Automotive Oil μg/g	Untreated Illinois #6 Coal Oil μg/g	Demineralized Illinois #6 Coal Oil μg/g
Aluminum			
Antimony			
Arsenic			
Barium	11		
Beryllium			
Cadmium			
Calcium	990		
Chromium	2.7		
Cobalt			
Copper	44		
Iron	130		
Lead	47		
Lithium			
Magnesium	410		
Manganese	10		
Molybdenum			
Nickel			
Phosphorous	780		
Potassium			
Selenium			
Silver			
Sodium	450		76
Strontium			
Thallium			
Vanadium			
Zinc	690		

Table 4 Percent conversion of untreated Illinois #6 and demineralized Illinois #6 coal reacted with waste automotive oil mixed in a 1:1 ratio by weight. Liquefaction was carried out in tubing reactors at 430 °C under a 1000 psig (cold) hydrogen for 1 hour.

	Untreated Illinois #6	**Demineralized Illinois #6**
Gas + Oil	38.8	40.2
Asphaltenes	22.1	13.2
Total Conversion	60.9	53.4

VARIABLE TEMPERATURE EPR STUDIES OF ILLINOIS NO. 6 COAL TREATED WITH DONOR AND ACCEPTOR MOLECULES

Robert L. Thompson, Kurt S. Rothenberger, and Herbert L. Retcofsky
U. S. Department of Energy
Pittsburgh Energy Technology Center
P. O. Box 10940
Pittsburgh, PA 15236

Keywords: charge-transfer, EPR spectroscopy, coal extracts

INTRODUCTION

The structure of coal is believed to consist of extended networks of polyaromatic hydrocarbons linked by a wide variety of bonding interactions. In addition to covalent bonds, these networks contain non-covalent interactions, such as hydrogen bonding and charge-transfer interactions. Charge transfer, which can be studied by electron paramagnetic resonance (EPR) spectroscopy,[1] involves the association of electron donors and acceptors. Both donor and acceptor sites are known to exist in coal, although acceptor sites are probably far less common. Such intermolecular associations may play an important role in determining the relaxation behavior of the coal matrix in certain solvents, an important consideration in coal liquefaction.

Charge-transfer interactions between strong donors and acceptors can lead to paramagnetic products, which can be observed by EPR spectroscopy. Any unpaired electrons in the sample can interact to give coupled singlet-triplet states, or they can remain independent of each other to give doublet states. In the former case, if the triplet state lies above the singlet state, it may be too high in energy to be populated at ambient temperature; however, when the interaction lies within the appropriate range, the triplet state can become populated such that the product gives an EPR signal.[1]

Most evidence to date supports the interpretation of EPR results of coal as arising from non-interacting doublet states, but some evidence in support of the existence of thermally accessible triplet states, such as temperature-dependent EPR intensities and the observation of $\Delta M_s = \pm 2$ transitions, has been reported as well.[2,3] In this work, we have studied by variable-temperature EPR spectroscopy, Illinois No. 6 coal, its pyridine extract, and chromatographic fractions of the pyridine extract that have been treated with strong electron donors and acceptors.

The intensity of an EPR signal arising from a doublet-state spin system (I_D) is inversely proportional to temperature according to the Curie Law, whereas the intensity of an EPR signal arising from a ground-state singlet system with a thermally accessible triplet state (I_{ST}) obeys a more complex relationship. Non-Curie Law behavior is often used as a diagnostic for the latter case. We have found that a useful test for non-Curie behavior is to measure the ratio of sample intensity to that of a known doublet state sample under identical conditions. Plots of this ratio versus temperature are useful in illustrating the variable temperature EPR results, as well as accounting for changes within the spectrometer cavity and sample during the experiment.

$$\frac{I_{ST}}{I_D} = \frac{\left[\frac{C_{ST}}{T}\right]\left[\frac{4}{\exp(J/k_BT)+3}\right]}{\left[\frac{C_D}{T}\right]} = \left[\frac{4\ C'}{\exp(J/k_BT)+3}\right] \qquad (1)$$

Equation 1 shows the ideal ratio I_{ST}/I_D as a function of temperature,[1] where J is the energy gap between the singlet and triplet states and k_B is Boltzmann's constant.

EXPERIMENTAL PROCEDURES

The coal used in this work was a high-volatile bituminous coal from the Illinois No. 6 seam in Franklin County, IL (MF analyses: 72.7 %C, 4.7 %H, 1.6 %N, 1.2 %S, 8.0 %ash). The pyridine extract of this coal was obtained by Soxhlet extraction after the coal had been ground to -100 mesh. The pyridine extract was separated into functionality enriched fractions containing aromatics, bases, and acids on an activated Al_2O_3 column according to an adaptation of the procedure developed by Schiller.[4] The yields for samples obtained from these procedures are listed in Table 1.

Samples of the coal, pyridine extract, and chromatographic fractions were treated with donors or acceptors by refluxing a mixture of coal material and reagent (in amounts ranging from 2.5:1 to 5:1) in chlorobenzene for 1 to 2 days, followed by evaporation of solvent and vacuum drying at 50°C until constant weight. Among the donors and acceptors added were tetrathiafulvalene (TTF), tetracyanoquinodimethane (TCNQ), tetracyanoethylene (TCNE), *p*-chloranil (CA), and iodine. EPR measurements were conducted as described elsewhere.[5]

RESULTS AND DISCUSSION

The treated coal and pyridine extract samples were studied by variable temperature EPR spectroscopy. Their EPR intensities were measured over a temperature range from -171°C to 23°C, then adjusted by dividing by the EPR intensities of DPPH obtained at identical temperatures.[5] DPPH is a well-studied, stable, non-interacting doublet-state free radical that obeys the Curie Law over a wide temperature range.[6] This method accounts for any experimental errors due to changes in sample or cavity characteristics with temperature.[7]

In every case, the EPR intensities of the coal, extract, and extract fractions increased upon treatment with the donor or acceptor, although the increase was not commensurate with a new spin for every molecule of reagent added. Neither was the magnitude of increase a function of the donor or acceptor strength of the added reagent; the acceptor with the largest electron affinity did not always give the largest intensity increase.

Only the addition of TTF, a strong donor, resulted in any discernable change in the shape of the EPR spectrum. It gave rise to a another feature at lower field to the original broad, featureless, first-derivative lineshapes of the coal and extract; all other reagents failed to alter the original lineshape. A more definitive spectrum was obtained from the CH_2Cl_2 extract taken from the TTF-pyridine extract sample. The hyperfine structure shown in Figure 1 is strikingly similar to that in the EPR spectrum of $(TTF)_3(BF_4)_2$.[8] In Figure 1, both spectra are centered at a field corresponding to $g = 2$. This spectrum is assigned to the radical cation of TTF; its detection in the extract sample implies that there are acceptor sites in the coal capable of completely removing an electron from TTF.

Variable temperature EPR studies were made of all of the treated coal samples, the results of which are shown in Figure 2. The straight, horizontal plots of I_{sample}/I_{DPPH} as a function of temperature imply that all of the coal samples obey the Curie Law at least as strictly as does DPPH, establishing them as consisting predominantly of doublet-state spins. The temperature range covered was sufficiently wide to have observed any thermally accessible triplet spins, if such had existed. Because the Curie Law was so strictly observed, the newly induced spins must either be doublet state spins or have interactions so weak that they are indistinguishable from doublet state spins.

Similar EPR results were obtained for the pyridine extract samples, shown in Figure 3, and are again indicative of adherence to the Curie Law for all samples. It is significant that coal extracts have a lower spin concentration than the whole coal; thus, were a small portion of thermally accessible triplet spins present in the treated coal, but obscured by a larger portion of native doublet spins, we would expect to observe them more readily in the extract. Because we do not see any deviation from Curie Law even in the extract samples, it is clear that thermally accessible triplet spins play no important role in the EPR behavior of whole coal.

Studies supporting the deviations from Curie Law in coal samples[2,3] have relied upon the mathematical deconvolution of EPR spectra, which is by nature artificial and rests on the questionable assumption that the lineshapes of coal signals are Lorentzian. These studies also observe forbidden $\Delta M_s = \pm 2$ transitions for certain coals. We have observed similar EPR signals in many of our samples under similar spectrometer conditions, but evidence does not support the assignment of these signals to $\Delta M_s = \pm 2$ transitions. The EPR spectra of Illinois No. 6 coal at a field corresponding to $g = 4$ are shown in Figure 4. These signals resonate at the appropriate field, but are extremely weak and their intensities do not vary with temperature. In fact, in some cases the observed signal was larger at -171°C than at 23°C, in contradiction to assignment to a thermally accessible triplet state. The location of these signals suggests that they are due to iron-bearing impurities such as kaolinite, which has been shown to possess a variety of low field signals from Fe(III) substituting in the lattice for Al(III) and Si(IV).[9]

The only non-Curie Law behavior we have observed was associated with certain minor sub-fractions from coal extract. The fractions obtained from the pyridine extract displayed weak EPR signals similar in shape to that of the coal and extract. Variable temperature EPR results for the acidic fraction revealed that it obeys the Curie Law, but the results for the aromatic and basic fractions show some slight deviation. As seen in Figure 5, their EPR intensity ratios are no longer horizontal, but slanted lines. This behavior is indicative of the presence of thermally accessible triplet spins. These fractions represent a minuscule portion of the whole coal and are likely overshadowed by the preponderance of doublet state spins.

The yields of individual fractions from the chromatographic separation were small. With this limited amount of sample, the donors and acceptors added to the fractions were limited to TTF and TCNE only. The EPR results for these treated fractions were surprising in that the aromatic sample obeyed Curie Law after treatment with TTF or TCNE, whereas the untreated aromatic fraction deviated from Curie Law. The acidic samples obeyed the Curie Law both before and after treatment with TTF or TCNE. The intensities of the treated basic samples deviated as strongly after treatment as before, particularly TTF-base, which had a curved rather than linear relationship to temperature, as shown in Figure 6.

The samples treated with TCNQ and TCNE were also studied by IR spectroscopy to monitor changes in the stretching frequency of the nitrile group, which has a frequency located in a region of the spectrum that is relatively free of absorptions for most coals. Larsen and co-workers[10] have shown the location of the stretching frequency for coals treated with these two electron acceptors to be very sensitive to the amount of electron density accepted. The nitrile

stretching frequencies of these samples are summarized in Table 2, which includes TCNQ and TCNE and shows the distinct shift to lower frequencies for all of the treated coal samples.

The IR results imply that electron density is being transferred from the coal to the acceptor, but the EPR results indicate that charge-transfer complexes having thermally accessible triplet states are not being formed in any detectable quantity. Similar results have been obtained by others for coal samples treated with TCNQ.[10] They have demonstrated that, although the IR frequencies of these samples were shifted, the EPR spectra did not show any evidence of formation of the TCNQ radical anion and the intensity increase was much less than would be expected if every added molecule of TCNQ resulted in an additional spin. These results were attributed to the formation of extended electronic valence bands between the coal and TCNQ.

It is possible that the frequency shifts in our samples reflect a distinct donation of electron density to TCNQ and TCNE, but the donations occur in such a way that the electrons remain paired. Alternatively, the formation of charge-transfer complexes may indeed be taking place, but with the EPR active triplet state so high in energy as to be essentially unpopulated at room temperature and below.[5]

We have found that a very small fraction of the spins present in Illinois No. 6 coal deviates from the Curie Law due to the population of thermally accessible triplet states. The vast majority of spins observable by EPR in the whole coal behaves as non-interacting doublet state spins, effectively obscuring the weak non-Curie Law behavior. We have also observed that Curie Law behavior persists even in samples treated with reagents capable of inducing charge transfer. Deviation from Curie Law finally becomes observable in the aromatic and basic fractions of the pyridine extract of the coal, as well as in some of the treated fractions. IR spectra reveal that electron density is indeed donated from the coal to the acceptors TCNQ and TCNE, and the EPR intensities are increased relative to the untreated coal samples, but treatment does not result in any noticeable deviation from Curie Law. Finally, while weak EPR signals are observed at half-field for many of the samples studied above, these signals are believed to arise from Fe(III)-containing impurities rather than from $\Delta M_s = \pm 2$ transitions.

REFERENCES

1. Bijl, D., Kainer, H., Rose-Innes, A.C. *J. Chem. Phys.* 1959, **30**, 765.
2. Duber, S., Więckowski, A.B. *Fuel* 1984, **63**, 1474.
3. Duber, S., Mikosz, J. *Fuel* 1993, **72**, 267.
4. Schiller, J.E., Mathiason, D.R. *Anal. Chem.* 1977, **49**, 1225.
5. Rothenberger, K.S., Sprecher, R.F., Castellano, S.M., Retcofsky, H.L. in 'Magnetic Resonance of Carbonaceous Solids' (Eds. R. Botto, Y. Sanada), ACS Adv. Chem. Ser. 229, Washington, DC, 1992, 581.
6. Singer, L.S., Spencer, E.G. *J. Chem. Phys.* 1953, **21**, 939.
7. Castellano, S., Chisolm, W., Sprecher, R.F., Retcofsky, H.L. *Anal. Chem.* 1987, **59**, 1726.
8. Wudl, F., Kaplan, M.L. *Inorg. Synth.* 1979, **19**, 27.
9. Angel, B.R., Hall, P.L. *Proc. Int. Clay Conf., Madrid* 1973, 47.
10. Flowers, R.A., Gebhard, L.A., Larsen, J.W., Sanada, Y., Sasaki, M., Silbernagel, B. *Energy Fuels* 1994, **8**, 1524.

Table 1. Extraction and Chromatographic Yields
(each value an average of 3 runs)

pyridine extraction yield	16.8	
chromatographic yields:	based on extract	based on coal
aromatics	4.2	0.7
bases	7.4	1.2
acids	17.3	2.9

Table 2. Infrared Frequency Changes for Samples Treated with TCNQ and TCNE

sample	ν(CN)	$\Delta\nu$(CN)	sample	ν(CN)	$\Delta\nu$(CN)
TCNQ	2227	----	TCNE	2236	----
coal-TCNQ	2179	-48	coal-TCNE	2200	-36
extract-TCNQ	2182	-45	extract-TCNE	2201	-35
			aromatics-TCNE	2206	-30
			bases-TCNE	2206	-30
			acids-TCNE	2213	-23

Figure 1. EPR Spectra of (a) CH_2Cl_2 Soluble Portion of Pyridine Extract + TTF and (b) $(TTF)_3(BF_4)_2$.

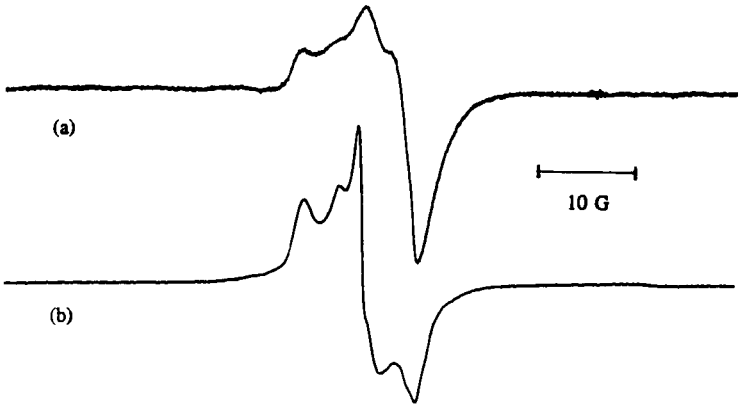

Figure 2. VT-EPR Results for Treated Illinois No. 6 Coal Samples.

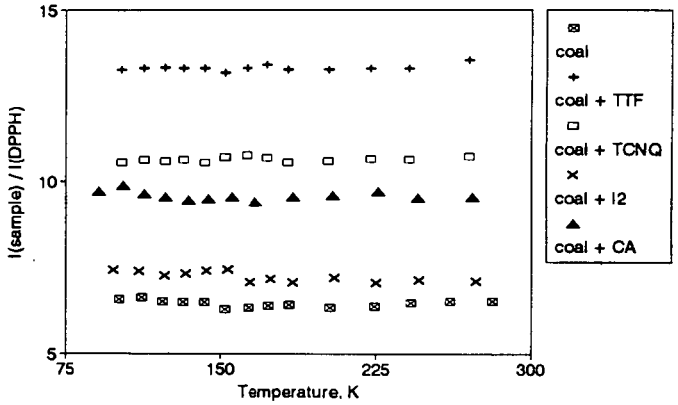

Figure 3. VT-EPR Results for Treated Pyridine Extract Samples.

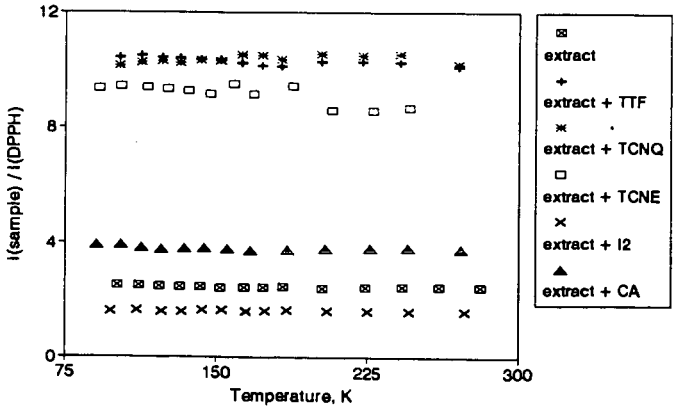

Figure 4. Half Field EPR Spectra of Illinois No. 6 Coal.

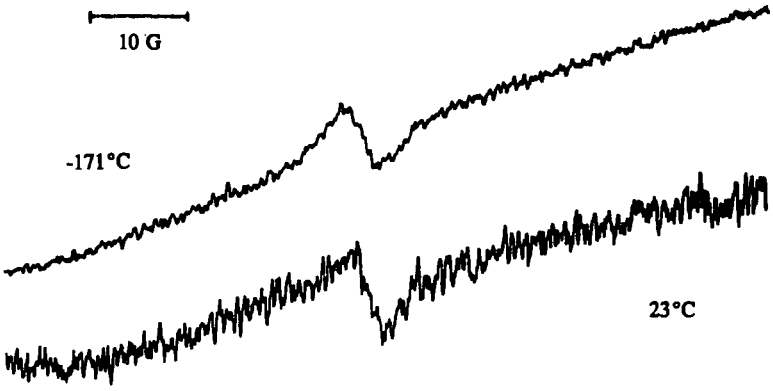

Figure 5. VT-EPR Results for Pyridine Extract Fractions.

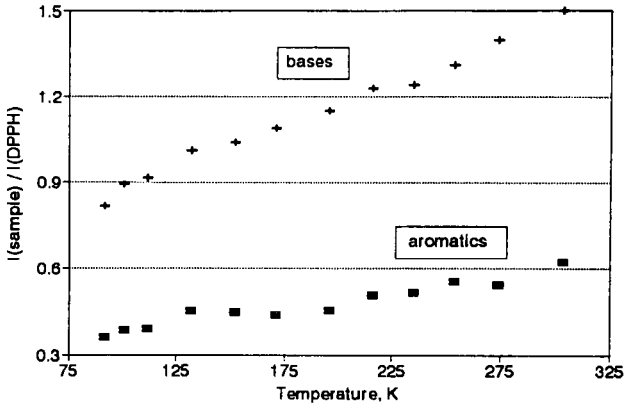

Figure 6. VT-EPR Results for Treated Base Fraction Samples.

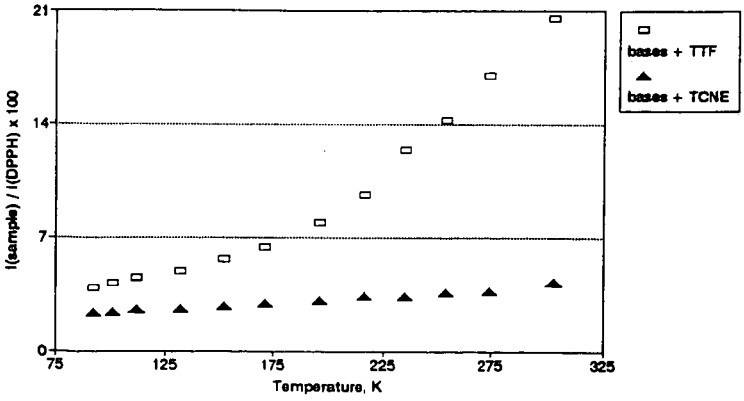

PRODUCTION OF ORGANIC ACIDS IN HIGH YIELDS FROM BROWN COALS THROUGH THE LIQUID PHASE OXIDATION WITH H_2O_2 AT LOW TEMPERATURE

Kouichi Miura, Kazuhiro Mae, Hajime Okutsu and Nori-aki Mizutani
Department of Chemical Engineering, Kyoto University,
Kyoto 606 JAPAN

Key words: Liquid phase oxidation of coal, Fatty acids from coal, H_2O_2 oxidation

INTRODUCTION

Low rank coals such as brown coal and lignite are most abundant fossil resources, but they have not been utilized in a large amount because of their low calorific values. They will not be utilized widely without some method that merits the utilization of such coals. Production of valuable chemicals, such as fatty acids *via* liquid phase oxidation may be a possible way to utilize the coals, judging from their structure.

Many attempts have been performed for decades to obtain organic acids from coal through the oxidation in alkali or acid medium. Kamiya et al. [1,2], Kapo et al.[3] and Bimer et al.[4] oxidized coals by oxygen in an aqueous NaOH or Na_2CO_3 solution at 110 to 270 °C under the pressure of 4.0 to 7.5 MPa. Water-soluble organics could be obtained in 50% yield on carbon basis, but CO_2 was produced in 40 to 50% yield. Montgomery et al.[5] performed the oxidation of a bituminous coal at 150 °C using H_2O_2 as an oxidizing agent, but CO_2 was produced in 60 to 90% yield. Deno et al.[6,7] oxidized four kinds of coals including lignite and several aromatic compounds at 50 to 70 °C using a mixture of trifluoroacetic acid and H_2O_2. They reported that fatty acids and methanol were produced in 5 to 15 % yield.

Thus the attempts for obtaining fatty acids from coal through liquid phase oxidation have not been so successful. A large amount of CO_2 were produced when increasing the decomposition rate by employing severe oxidation conditions such as high temperature, high pressure, and strong acids. A much milder oxidation method seemed to be favorable to produce fatty acids in high yield and in high selectivity. Selection of a suitable coal that is easily degraded in oxidizing agents seemed to be important also.

We have recently found that an Australian brown coal oxidized by H_2O_2 for 2 h at 60°C was extracted by 84 wt% in a mixed solvent of methanol and 1-methylnaphthalene at room temperature[8]. We also analyzed these extracts in detail, then clarified that 40% of carbon in the oxidized coal was aliphatic carbon.[9] This result suggests that a large amount of fatty acids can be recovered if the coal is further oxidized in liquid phase by H_2O_2.

In this paper we show that the liquid phase oxidation of brown coal with H_2O_2 under mild conditions produces water-soluble fatty acids in high yields. We also examine the mechanism by which the organic acids are produced from coal through a detailed study on the product distribution and the coal properties during the H_2O_2 oxidation.

EXPERIMENTAL

Three kinds of coals, an Australian brown coal (Morwell, MW), a Canadian brown coal (Highvale, HV), and a Japanese sub-bituminous coal (Taiheiyo, TC) were used as raw coals. The analyses of the coals are listed in Table 1. The coals were ground into fine particles of less than 74 μm, and dried in vacuo at 110 °C for 24 h before use. Morwell coal as received, which contains more than 60% of moisture, was also used without drying. This was performed to examine the possibility of utilizing the coal without energy-consuming drying process. The oxidation of the coals were performed as follows: 0.5 g of coal particles were mixed with 10 ml of 30% aqueous hydrogen peroxide in a 500 ml flask with a plug. After treating the mixture for several hours in an water bath kept at a constant temperature of 40 °C, 60°C or 80 °C, all the gas in the flask was purged by 10 litre of nitrogen gas and was collected in a gas bag. The gaseous product was analyzed for CO_2, CO and hydrocarbon gases by a gas chromatograph. Next, an excess of cold water was added to the mixture to terminate the oxidation reaction, then the mixture was filtrated to separate it into the solid residue and the aqueous solution. The solid residue was evacuated at 60 °C for 24 h, and was served to the CHN analysis, the F.T.i.r. analysis, and the ^{13}C-n.m.r. analysis. The solid yield on carbon basis was calculated from the CHN analysis. The aqueous solution was served to the TOC, the GPC, and the HPLC analyses. The HPLC analysis detected low molecule fatty acids using a sulfonated polystyrene gel column with an electric conductivity

detector. The content of total organic carbon, the molecular weight distribution, and the composition of fatty acids were estimated from these measurements.

RESULTS AND DISCUSSION

Oxidation of dried MW coal

First, the dried MW coal was oxidized at 60 and 80 °C for different reaction times to examine the validity of the proposed oxidation method. Figure 1 shows the changes in the solid yield with the progress of the oxidation. The height of each bar corresponds to the solid yield at a certain reaction time. Elemental composition at each reaction time is given in the bar. At 60 °C the solid yield decreased to 55% in 2h, and decreased gradually to 19% at 24 h. At 80 °C the coal was decomposed rapidly, and the solid yield was only 15 % at 4 h. The water-soluble oraganics were analyzed by the HPLC and the GPC as stated above. Figure 2 shows a typical chromatogram for low molecule fatty acids obtained using the HPLC. Five components, malonic acid, glycolic acid, formic acid, acetic acid, and a C_2-calboxyl acid, which could not be identified, were separated distinctly and could be quantified. As an another low molecule component methanol was quantified using the GC-MS method. From these analyses the components whose molecular weights (M_w) are smaller than 104 were quantified. Figure 3 shows the change in the number basis molecular weight distribution (MWD) with the progress of the oxidation at 60 °C. Components larger than 60 in molecular weight were detected by the GPC. It is clearly shown that each MWD has two distinct peaks, and that the MWD shifts to smaller molecule region with the increase of the oxidation time. The components detected were separated into two fractions: one is the fraction ranging M_w=105 to 400 and the other is the fracion of M_w>400. The former fraction was quantified by subtracting the amount of the components ranging Mw=60 to 104, which were quantified by the HPLC. The content of the total organic carbon in the water-soluble product was measured separately. Only CO_2 was detected as the gaseous product, and it was quantified by the gas chromatograph. Using these measurements, we could establish the carbon balance during the oxidation.

Figure 4a shows the changes in the product distribution of carbon basis with the progress of oxidation. At 60 °C the yield of water-soluble components increased gradually with the oxidation time, and reached 52 % at 24 h. The yield of the smallest molecule fraction (M_w<104) was surprisingly 28 %. The yield of CO_2 was less than 30 % even at 24 h. At 80 °C the yield of water-soluble components reached 54 % only in 1 h, but the yield decreased gradually with the increase of the oxidation time and CO_2 was produced in 50 % yield at 4 h. Figure 4b shows the product distribution of the smallest molecule fraction (M_w<104) on coal basis. At 60 °C the yield of this fraction increased monotonously with the oxidation time and reached surprisingly 52% at 24 h. At 80 °C, on the other hand, the yield increased little with the increase of the oxidation time, and it was less than 30% at 4 h. The above results clearly indicate that the oxidation of the dried MW coal by H_2O_2 at around 60 °C is a promising method to produce valuable chemicals in high yield and in high selectivity.

Test of the validity of the proposed method for other coals

It was clarified that the proposed oxidation method is very effective to produce valuable chemicals from the dried MW coal under mild conditions. Then the validity of the method was tested for several low rank coals and the wet MW coal (coal as received). The coals were oxidized for 24 h at 40, 60, and 4 h at 80 °C. Figure 5a shows the product distribution on carbon basis for the coals. All the coals were decomposed rapidly and a large amount of water-soluble organics were produced at 40 °C and 60°C. For the MW dried coal, the solid yield was 19 % and the yield of the water-soluble organics reached 52 % at 60°C as stated above. The product distributions for the wet MW coal were similar to the distributions for the dried MW coal, although the decomposition rate of the wet coal was slightly smaller than that of the dried coal. This result shows that the drying process of the low rank coal, which consumes a large amount of energy, can be eliminated when the coal was oxidized by the proposed method. For HV, the solid yield was smaller than that of the dried MW coal, but larger amount of CO_2, 40% in yield, was produced at 60 °C. The main components of the water-soluble organics were high molecular weight compounds. On the other hand, the solid yield was large and the water-soluble organics yield was small for TC coal. This is probably because TC coal (subbituminous coal) consist of more condensed aromatic components as compared with MW coal.

Figure 5b shows the yields of the smallest molecule fraction on coal basis. Only five kinds of fatty acids and methanol were involved in the fraction for all the coals. Such high selectivities for the fatty acids were judged to derive from the structure of coal. Deno et al.[7] performed the H_2O_2-TFA-H_2SO_4 oxidation of model compounds such as toluene and dibenzofuran, and they found that one or two kinds of

particular fatty acids which reflect the structure of the model compound were produced from each compound. The structure of brown coal consists of one or two aromatic rings connected by short chain linkages such as ether, methylene and ethylene bridges. Then the five fatty acids would be produced by the decomposition of the short chains. The total yields of the fatty acids were 10 to 20 wt% at 40°C for all the coals, and they increased to 30 to 50% at 60 °C except for TC coal. The largest yields was obtained for the dried MW coal at 60 °C. It reached surprisingly 52 % as stated earlier, and consisted of 13.1% of malonic acid, 7.8% of glycolic acid, 6.5% of acetic acid, and 19.3 % of formic acid.

Figure 6 shows the MWDs (M_w>60) of the water-soluble compounds for the coals oxidized at 60 °C. They all showed bimodal distributions having peaks at around 200 and 1000. The components of the smaller molecular weight region probably consist of aromatics of one or two aromatic rings. This suggests that much larger amount of fatty acids can be recovered under proper oxidation conditions. Thus it was clarified that the proposed oxidation method is effective to produce valuable chemicals in high yield and in high selectivity especially from the brown coal.

Mechanism of the H_2O_2 oxidation of coal

It is worth while to examine the oxidation mechanism of brown coal for searching optimum oxidation conditions. This was performed by tracing in detail the changes in the solid properties and the product distributions during the oxidation of the dried MW coal. Figure 7 shows the change in the atomic ratios of oxygen to carbon (O/C) and hydrogen to carbon (H/C) with the oxidation time at 60°C and 80°C. The O/C value increased at first, then decreased with the increase of oxidation time. The H/C value increased significantly with the oxidation time at both temperatures. This clearly shows that hydrogen atoms were introduced into the coal by the H_2O_2 oxidation. Figure 8 shows the change in the F.T.i.r. spectra of the dried MW coal during the oxidation. The intensities of the peaks at 1710 cm^{-1} and 1170 cm^{-1}, which are, respectively, assigned to carboxyl groups and alcoholic OH groups, increased with the progress of oxidation. The intensity of the peak at 2890 cm^{-1}, which is assigned to the aliphatic C-H stretching vibration, increased significantly at 24 h. We clarified that the ratio of aliphatic carbon to total carbon of MW coal is 0.43 from the ^{13}C-n.m.r. spectrum[9]. The sum of the yields of CO_2 and the smallest molecule fraction (M_w<104) in Fig. 4a exceeded 0.43 at the oxidation time of 12 and 24 h at 60 °C. This clearly indicates that a part of the aromatic rings of the coal are ruptured by the H_2O_2 oxidation even at 60 °C. The oxidation of coal by air is known to reduces the H/C ratio and the aliphatic proportion in the coal.[10] The above discussion clearly shows that the mechanism of the H_2O_2 oxidation is completely different from the mechanism of the air oxidation. The H_2O_2 oxidation in acid aqueous solutions contains the proton donating reaction.[11] The pH in the mixture of the dried MW coal in the H_2O_2 aqueous solution was below 4.0, so the proton donating reaction surely proceeded to change the coal and the larger molecules of the water-soluble components into aliphatic rich structure. This will surely increase the yields of smaller molecules with the progress of oxidation.

Summarizing the above discussion, the high yield and the high selectivity for the fatty acids were judged to be achieved by the structure of MW coal itself and the proton donating reaction which is realized by H_2O_2 in acid aqueous solutions.

CONCLUSION

A new and effective method for utilizing the low rank coal as chemical resources was presented, in which the coal was oxidized with 30%-H_2O_2 at below 80 °C under ambient pressure. Oxidizing an Australian brown coal for 24 h at 60 °C, five kinds of fatty acids were recovered surprisingly in 52 % in yield. We are expecting that the proposed method will change the conversion technology of brown coal dramatically.

REFERENCES

1. Kamiya, Y., *Kogyo Kagaku Zasshi*, **1956**, 59, 197-202.
2. Kamiya, Y., *Fuel*, **1963**, 42, 353-358.
3. Kapo, G.; Calvert, S.; *Ind. Eng. Chem. Des. Dev.*, **1966**, 5, 97-104.
4. Bimer, J.; Salbut, P. D.; Berlozecki, S., *Fuel*, **1993**, 72, 1063-1068.
5. Montgomery, R.S.; Bozer, K.B., *Fuel*, **1959**, 38, 400-402.
6. Deno, N.C.; Gregger, B.A.; Stroud, S.G., *Fuel*, **1978**, 57, 455-459.
7. Deno, N.C.; Gregger, B.A.; Messer, L.A.; Meyer, M.P.; Stroud, S.G., *Tetrahedron Lett.*, **1977**, 1703.
8. Miura, K.; Mae, K.; Maki, T.; Araki, J., *Chem. Lett.*, **1995**, 901.
9. Mae, K.; Miura, ; K. Maki, T.; Inoue, S., *Proc. Int. Conf. on Coal Sci.*, **1995**, 365-368.
10. Song, C.; Saini, A.K.; Schobert, H.H., *Energy & Fuels*, **1994**, 8, 301-312.
11. Schumb, W.C.; Satterfield, C.N., "Hydrogenperoxide", 1955, Reinhold (New York).

Table 1 Properties of coals

Coal(Abbrev.)	Proximate analysis(wt%)			Ulimate anaysis(wt%,daf)				
	FC	VM	Ash	C	H	N	S	O
Morwell(MW)	48.2	50.3	1.5	64.8	4.5	0.6	0.3	29.8
Highvale(HV)	52.6	35.4	12.0	67.0	4.3	1.0	0.2	27.5
Taiheiyo(TC)	43.2	45.8	11.0	74.5	6.0	1.3	0.4	17.8

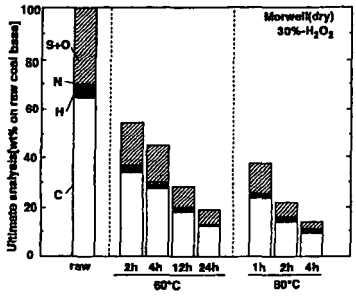

Figure 1 Changes in the solid yield and the elemental composition through the H_2O_2 oxidation of the dried MW coal

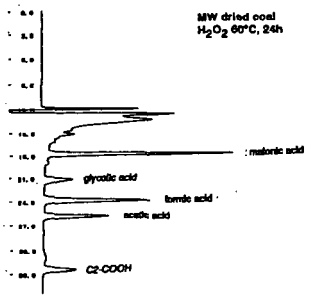

Figure 2 A typical HPLC chart for the organic acid analysis

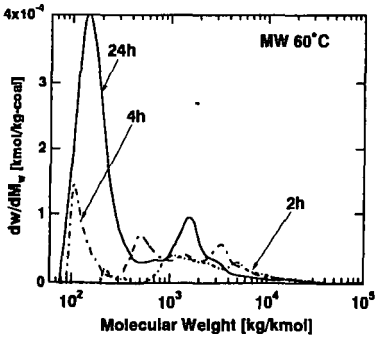

Figure 3 Change in the molecular weight distributions of the water-soluble organics produced through the H_2O_2 oxidation of the dried MW coal

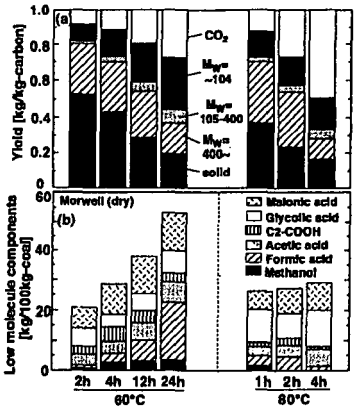

Figure 4 Change in the product distributions through the H_2O_2 oxidation of the dried MW coal

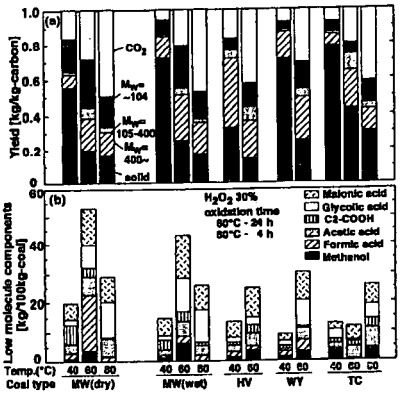

Figure 5 Product distributions through the H_2O_2 oxidation for low rank coals

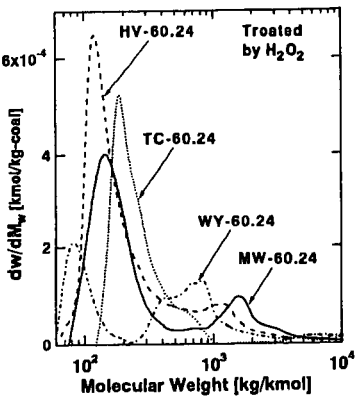

Figure 6 Molecular weight distributions of the water-soluble organics produced through the H_2O_2 oxidation for low rank coals

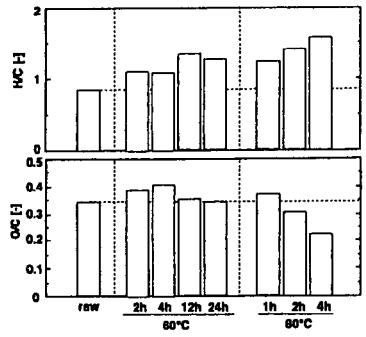

Figure 7 Change in the H/C and O/C atomic ratios through the H_2O_2 oxidation of the dried MW coal

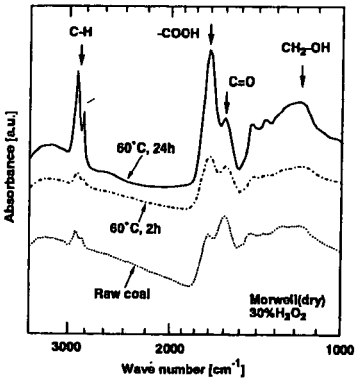

Figure 8 Change in the F.T.i.r. spectra through the H_2O_2 oxidation of the dried MW coal

PYROLYSIS OF SIMPLE COAL MODEL COMPOUNDS CONTAINING AROMATIC CARBOXYLIC ACIDS: DOES DECARBOXYLATION LEAD TO CROSS-LINKING?*

Thomas P. Eskay, Phillip F. Britt, and A.C. Buchanan, III
Chemical and Analytical Sciences Division, Oak Ridge National Laboratory
P.O. Box 2008, MS-6197, Oak Ridge, Tennessee 37831-6197

Keywords: Pyrolysis, Decarboxylation, Cross-Linking, Model Compounds.

Introduction

In recent years, it has been proposed that oxygen functional groups, prevalent in low rank coals, are major actors in retrograde reactions which inhibit their efficient thermochemical processing. In the pyrolysis and liquefaction of low-rank coals, low temperature cross-linking reactions have been correlated with the loss of carboxyl groups and the evolution of CO_2 and H_2O [1,2]. Pretreatments such as methylation, demineralization, or ion-exchange of the inorganic cations reduce cross-linking and CO_2 evolution in pyrolysis, while the exchange of Na^+, K^+, Ca^{++}, and Ba^{++} into demineralized coal increases cross-linking and CO_2 evolution in pyrolysis and liquefaction [3,4]. These results suggest, in part, that decarboxylation pathways in coal may play an important role in the cross-linking of the coal polymer. However, the reaction pathways associated with the decarboxylation and cross-linking events in low rank coal are currently unknown. Furthermore, it is not known whether the reaction pathway that leads to decarboxylation also leads to cross-linking. Radical recombination or addition reactions have been suggested as being involved in retrograde reactions. However, the involvement of radical pathways in thermal decarboxylation reactions has recently been brought into question by the observation that decarboxylation of benzoic acid derivatives under coal liquefaction conditions yielded only small amounts of aryl-aryl coupling products [5]. Therefore, to gain a better understanding of the role decarboxylation plays in cross-linking reactions in low rank coals, we have studied the pyrolysis of several bibenzyls containing aromatic carboxylic acids. The structures currently under investigation are 1,2-(3,3'-dicarboxyphenyl)ethane (**1**) and 1,2-(4,4'-dicarboxyphenyl)ethane (**2**). These compounds are capable of forming reactive free-radical intermediates at *ca.* 400°C through homolysis of the weak bibenzylic bonds. This provides a constant source of free-radicals to potentially assist in the decarboxylation reaction.

Experimental

1,2-(3,3'-dicarboxyphenyl)ethane (1). Into a 1 L oven-dried flask, containing a magnetic stirbar, equipped with an oven-dried addition funnel and kept under positive argon pressure, was placed 3-bromobenzyl bromide (13.0 g, 5.22 x 10^{-2} moles) and dry THF (500 mL). The solution was cooled to -78°C, and the addition funnel was charged with 2.5 M *n*-butyllithium in hexane (54 mL, 1.35 x 10^{-1} moles). The *n*-butyllithium was added dropwise over a period of 20 min and the solution was stirred for 30 min at -78°C. Carbon dioxide, produced from warming dry ice and passing it through two separate drying tubes of $CaSO_4$ and $CaSO_4/CaCl_2$, was bubbled into the solution for 1.5 h. The reaction was warmed to room temperature and quenched with saturated aqueous $NaHCO_3$ (100 mL). The solution was transferred to a separatory funnel and diluted with H_2O (700 mL) and Et_2O (700 mL). The aqueous layer was collected and acidified with concentated H_2SO_4 to precipitate **1**. The white precipitate was collected by vacuum filtration and air dried giving 6.884 g (98 %, GC purity 97 %). Further purification by 4 recrystallizations from isopropyl alcohol and drying over P_2O_5 in a vacuum desicator yielded the product in 99.9 % purity by GC analysis.

1,1,2,2-tetradeutero-1,2-(3,3'-dicarboxyphenyl)ethane (1-d_4) was synthesized by the procedure described above for the synthesis of **1** using 3-bromobenzyl bromide-d_2 which was synthesized as described below. The deuterium content of the product was 97 % d_4 by GC-MS analysis.

3-bromobenzyl bromide-d_2 Into a 1L oven-dried 2-neck flask, containing a magnetic stirbar, equipped with a reflux condenser and an addition funnel, was placed $LiAlD_4$ (Aldrich 98 % deuterium content, 5.00 g, 0.12 moles) and dry Et_2O (300 mL). The solution was stirred and

* This research was sponsored by the Division of Chemical Sciences, Office of Basic Energy Sciences, U.S. Department of Energy under contract DE-AC05-840R21400 with Lockheed Martin Energy Systems, Inc.

3-bromobenzoic acid (20.0 g, 0.10 moles) in dry Et_2O (300 mL) was added from the addition funnel over a period of 30 min. The solution was refluxed for 1 h and was quenched with the cautious addition of H_2O (100 mL). The solution was poured into H_2O (200 mL) containing concentrated H_2SO_4 (16 mL) and stirred until all the solid dissolved. The Et_2O layer was collected and the aqueous layer was extracted with Et_2O (2 x 100 mL). The combined Et_2O extract was washed with dilute aqeous $NaHCO_3$, dried over Na_2SO_4, and the Et_2O was removed to yield 19.4 g of liquid, 3-bromobenzyl alcohol (100 %, crude yield). The deuterium content of the product was 99 % d_2 by GC-MS.

The crude 3-bromobenzyl alcohol (10.1 g, 53.7 mmol) was then placed into a 1-neck (100 mL) flask containing concentrated HBr (26 mL) and concentrated H_2SO_4 (4.0 mL). The solution was refluxed for 6 h, cooled to room temperature, and extracted with hexane (2 x 50 mL). The hexane was passed through a plug of Merck grade 60 silica gel in a (2.5 cm diameter x 2.5 cm long) column and the hexane was evaporated to produce a white solid (11.75 g, 89 % based on crude 3-bromobenzyl alcohol). By GC-MS analysis, the product was 99 % d_2.

1,2-(4,4'-dicarboxyphenyl)ethane (2) was synthesized as described previously [7].

Pyrolyses. Pyrolyses were performed in sealed pyrex tubes (sealed at ca. 10^{-5} Torr) in a Tecam fluidized sandbath at 400 $\pm$ 1.5 °C. Following pyrolysis, the samples were quickly removed from the sandbath and cooled in liquid N_2. The tubes were then cracked open and the solid products were removed with a 2:1 mixture of pyridine:N,O-bis(trimethylsilyl)trifluoroacetamide (BSTFA). Internal standards (2,4,6-trimethylbenzoic acid and 2-phenylbenzoic acid) were added and the reaction mixtures analyzed by GC and GC-MS. Gas chromatography analysis was performed using a Hewlett-Packard 5890 Series II gas chromatograph equipped with a J&W Scientific 30 m x 0.25 mm id, 0.25 μm film thickness DB-1 column and a flame ionization detector. Mass spectra were obtained at 70 eV on a Hewlett-Packard 5972 GC/MS equipped with a capillary column identical to that used for GC analysis. The identities of products from the thermolysis of **1** and **2** were determined by GC-MS analysis and were further confirmed by comparison with commercially available or synthesized authentic materials.

Results and Discussion

Thermolysis of **1** and **2** was conducted at 400 °C in sealed pyrex tubes and analyzed by GC and GC-MS. The major products from the thermolysis of **1** are shown in equation 1 and account for $\geq$ 95 % of the mass balance at conversions of **1** up to 22 %. Several other

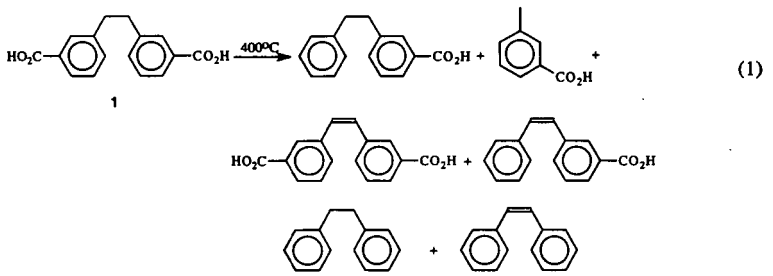

(1)

products are formed in the pyrolysis that have not been identified, but based upon the GC peak area and the good mass balance, the amount of these products are small (< 2 %). The results obtained for the thermolysis of **1** at 400 °C at various time intervals are given in Table 1, entries 1-5. A similar product distribution and mass balance (> 96 %) was obtained in the thermolysis of **2**.

The major product from the thermolysis of **1** and **2** is decarboxylation to 3-carboxybibenzyl and 4-carboxybibenzyl respectively. The good mass balances ($\geq$95 %) suggest that the decarboxylation reaction does not lead to significant quantities of high molecular weight products that might not be observed by GC analysis. Analysis of the methylated (via diazomethane) reaction mixture from the thermolysis of **2** by reverse phase high performance liquid chromatography showed no new products. This result supports the premise that no non-volatile, high molecular weight products are formed. The rate constant for C-C homolysis of the bibenzylic bond was calculated to be 1.8 $\pm$ 0.1 x 10^{-6} s^{-1} for **1** and

$3.8 \pm 0.6 \times 10^{-6}$ s^{-1} for **2** based on the amount of HO_2CPhCH_3 formed at conversions of less than 10 %. The rate constant is slightly lower than reported for homolysis of bibenzyl in tetralin (8.0×10^{-6} s^{-1}) [6]. The apparent first-order rate constant of decarboxylation of **1** and **2** has also been calculated to be $3.7 \pm 0.2 \times 10^{-5}$ s^{-1} and $6.6 \pm 0.2 \times 10^{-5}$ s^{-1}, respectively. The rate constant for decarboxylation of **1** is roughly a factor of 2 slower than that of **2**, suggesting that the decarboxylation mechanism is influenced by the position of the carboxy group on the aryl ring.

On the basis of the product distribution and rate of decarboxylation, the decarboxylation of **1** and **2** is proposed to proceed by an ionic pathway as shown in equation 2. Although the reaction order has not been determined, it is proposed that a second

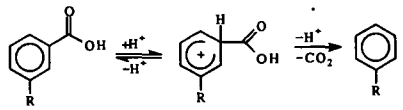

(2)

equivalent of starting material is the source of the acid. Catalysis by residual mineral acid, used to precipitate the diacid during its synthesis, is unlikely based on the similar thermolysis results obtained from the thermolysis of **2** prepared by simple precipitation from mineral acid, and **2** purified by dissolving in NH_4OH, titrating with HCO_2H, and washing with water, ether, and acetone. The difference in the decarboxylation rates of **1** and **2** also supports an ionic pathway. If the rate determining step is protonation of the aromatic ring, the *para*-substituent in **2** would stabilize the carbocation intermediate while the *meta*-substituent in **1** would not. The toluic acid and stilbene derivatives are formed by a free-radical reaction analogous to that reported for the thermolysis of bibenzyl [6,9]. Homolysis of **1** produces 2 (HO_2CPhCH_2•) followed by hydrogen abstraction from **1** to form $HO_2CPhCH_2CH(•)PhCO_2H$ (**3**) and toluic acid (Scheme 1). It is predicted that hydrogen abstraction by HO_2CPhCH_2• or

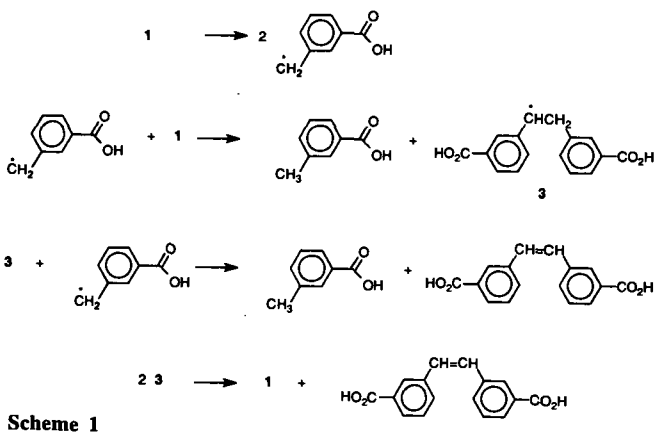

Scheme 1

3 would favor the benzylic C-H bond (86 kcal/mole) over the stronger O-H bond of the carboxylic acid (estimated as 101 kcal/mole). The stilbene derivatives are formed from the disproportionation of **3**, but no products from the coupling of **3** are observed, in contrast to the thermolysis of bibenzyl in which tetraphenylbutane is a major product [9], .

The decarboxylation and cross-linking of aromatic carboxylic acids has been assumed to arise from a free-radical pathway (eq 3), since free-radicals are known to be formed as the

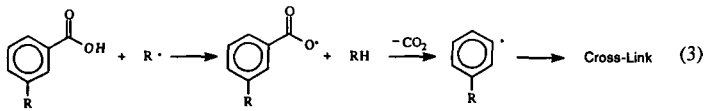

(3)

reactive intermediates in the thermolysis of coal. Aryl radicals are known to add to aromatic rings to form biaryls [6]. The data obtained from decarboxylation of **1** and **2** is inconsistent with a free-radical mechanism. Moreover, it is predicted that the hydrogen abstraction from the carboxylic acid in equation 3 should be the rate determining step in this decarboxylation, since it is known that aryl carboxy radicals undergo decarboxylation at rapid rates (*ca.* 10^6 s^{-1} at 23 °C [8]). Thus a free-radical mechanism should not show a difference in the rate of decarboxylation of **1** and **2**, because the carboxy radical is not in conjugation with the aromatic ring.

To further investigate the mechanism for the decarboxylation of **1**, the thermolysis of **1** containing deuterium in the ethylene bridge (**1-d_4**) was investigated. This molecule should allow us to distinguish if decarboxylation is occuring by an ionic pathway (eq 2) or free-radical pathway (eq 3). Decarboxylation by an ionic pathway would place a hydrogen at the 3-position while the free-radical pathway would place a deuterium at the 3-position of the aromatic ring from D abstraction of the aryl radical (Scheme 2). Preliminary data from a 30

Ionic Pathway

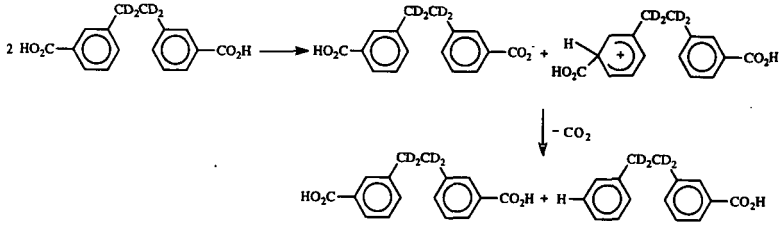

Radical Pathway

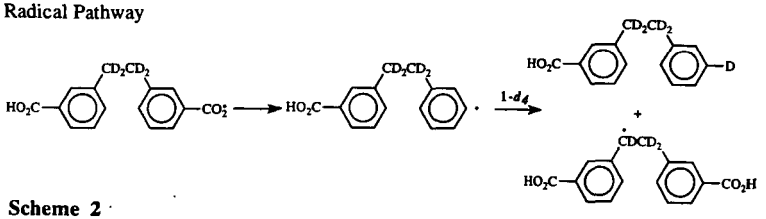

Scheme 2

min thermolysis of **1-d_4** are given in Table 1, entry 6. Analysis of the deuterium content of the major product, 3-carboxybibenzyl, by GC-MS showed that > 97 % of the product was d_4. No d_5 was detected, which strongly supports our assertion that decarboxylation of **1** is occuring by an ionic pathway. The deuterium content of the *m*-toluic acid is currently under investigation to determine if the benzylic radical can abstract hydrogen from the carboxylic acid to give *m*-toluic acid-d_2 as well as from the ethylene bridge to give *m*-toluic acid-d_3.

Summary and Conclusion

The thermolysis of two aromatic carboxylic acids **1** and **2** have been investigated at 400 °C as models of carboxylic acids in low rank coals. The major decomposition pathway observed is decarboxylation, which mainly occurs by an ionic pathway. This decarboxylation route does not lead to any significant amount of coupling or high molecular weight products that would be indicative of cross-linking products in coal. The pyrolysis of **1** and **2** will be investigated under a variety of conditions that better mimic the environment found in coal to further delineate the role that decarboxylation plays in coal cross-linking chemistry.

References

1. Suuberg, E.M.; Lee, D.; Larsen, J.W. *Fuel* **1985**, *64*, 1668.

2. (a) Solomon, P.R.; Serio, M.A.; Despande, G.V.; Kroo, E. *Energy and Fuels* **1990,** *4,* 42. (b) Ibarra, J.V.; Moliner, R.; Gavilan, M.P. *Fuel* **1991,** *70,* 408.
3. (a) Serio, M.A.; Kroo, E.; Chapernay, S.; Solomon, P.R. *Prepr. Pap.-Am. Chem. Soc. Div., Fuel Chem.* **1993,** *38(3),* 1021. (b) Serio, M.A.; Kroo, E.; Teng, H.; Solomon, P.R. *Prepr. Pap.-Am. Chem. Soc., Div. Fuel Chem.* **1993,** *38(2),* 577.
4. Joseph, J.T.; Forria, T.R. *Fuel* **1992,** *71,* 75.
5. Manion, J.A.; McMillien, D.F.; Malhotra, R. *Prepr. Pap.-Am. Chem. Soc., Div. Fuel Chem.* **1992,** *37(4),* 1720.
6. Stein, S.E.; Robaugh, D.A.; Alfieri, A.D.; Miller, R.E. *J. Am. Chem. Soc.* **1982,** *104,* 6567.
7. Britt, P.F.; Buchanan, A.C., III, Hoenigman, R.L. *Coal Science* Pajares, J.A. and Tascon, J. M. D. Eds.; Coal Science and Technology 24; Elsevier Science B.V.: Amsterdam, Netherlands, 1995, 437.
8. Wang, J.; Tsuchiya, M; Sakuragi, H.; Tokumaru, K. *Tetrahedron Letters* **1994,** *35,* 6321.
9. Poutsma, M. L. *Fuel* **1980,** *59,* 335.

Table 1 Product Distributions Observed from the Thermolysis of *m,m*-$HO_2CPhCH_2CH_2PhCO_2H$ at 400°C for Various Time Intervals.

Entry	1	2	3	4	5	6[c]
Products (mole %)	10 min	30 min	60 min	90 min	120 min	30 min
m-CH_3PhCO_2H	8.2	9.9	10.1	10.3	14.1	9.0
m-$CH_3CH_2PhCO_2H$	0.93	1.6	1.4	1.4	1.7	1.3
$PhCH_2CH_2Ph$	b	1.2	2.4	3.2	4.8	1.2
PhCH=CHPh	b	b	0.1	0.1	0.4	b
m-$HO_2CPhCH_2CH_2Ph$	83.7	80.3	76.4	73.3	82.3	84.6
m-HO_2CPhCH=CHPh	0.7	0.6	1.9	2.5	5.6	0.8
m,m-HO_2CPhCH=$CHPhCO_2H$	5.3	5.9	11.2	9.1	11.2	3.2
Conversion[a]	2.6	9.6	17.3	22.3	33.8	8.1
Mass Balance	97.8	96.0	93.0	94.7	90.0	98.4

a-Based on products identified. b-product not detected. c-1-d_4.

RELIABLE CHEMICAL DETERMINATION OF OXYGEN-CONTAINING FUCTIONALITIES IN COAL AND COAL PRODUCTS. CARBOXYLIC ACID AND PHENOLIC HYDROXYL FUNCTIONALITIES

Tetsuo Aida, Yukinari Tsutsumi, and Teiji Yoshinaga
Department of Industrial Chemistry
Faculty of Engineering, Kinki University at Kyusyu
11-6 Kayanomori, Iizuka, Fukuoka 820, JAPAN

Keywords: Coal, chemical determination, oxygen-containing fuctionality

INTRODUCTION

Coal contains various chemical functionalities. Particularly, the oxygen-containing functionalities are considered to play an important role to controle its physical and chemical properties. Recent developement of sophisticated instrumentaion such as FT-ir, ^{13}C-CP-MAS-NMR, XPS, etc., for the direct non-destructive chacterization of a solid coal has made it possible to provide quite reliable information about such hetero-atom-fuctionalites as sulfur-(1), nitrogen-(2) and oxygen-containing fuctionalities. However there still seems to be a problem concerning the selectivity between delicate functiomalities, i.e., a carboxylic, phenolic and alcoholic hydroxyl functionalities.

About 40 years ago, Blom et al.(3) developed chemical determination methods for various ogygen-containing functionalities in coal and coal products, which have often been used in the literatue with some minor modifications. In the course of our studies concerning the solvent swelling of coal, we have learned that this classical method may involve serious experimenntal errors based on the accessibility, particuraly the determination of the carboxylic acid functionality in coals, which used to be carried out in an aqueous solution by using calcium acetate. In general, the coal does not swell very much in a water, furthermore the coals exibit significant steric requirments for the penetrant molecules(4), and its extent of swelling widely varied depending upon the coal rank(5). Usually, a higher rank coal like a bituminous coal exhibits serious penetration restriction. Thus, if one wants to use a chemical reaction on coals, in order to obtain reasonable accessibility of chemical reagent to the functionality in solid coals it is critical to pay maximum attention to the arrangement of the reaction conditions, i.e., reagents and solvents.

Based on our experimental results of coal swelling, we have developed a quite reliable chemical determination method for carboxylic acid and phenolic hydroxyl fuctionalities in coal and coal products. The principle of this method is described as follows: Chemical reactions using various borohydrides were adopted for the determination of these functionalities as shown below, which have very different reactivities and give us a stoichiometric amount of hydrogen gas for each functionality in a pyridine solvent. Thus, we can discriminate each functionalities based upon the difference of thier reactivities to the borohydrides:

$$\text{R-OH} + \text{MBH}_4 \longrightarrow \text{R-OM} + \text{BH}_3 + \text{H}_2$$

(R = Aryl, Alkyl, -CO-, H, etc. ; M = Li, Na, K, n-Bu_4N etc.)

EXPERIMENTAL

The chemical reagents were commercial products(Aldrich's gold label grade) which were used without further purifications. Pyridine was dried over calcium hydride and distilled before use. Coals from the Ames Coal Library were ground, seized, dried at 110°C under vacuum overnight, and stored under a dry nitrogen atmosphere. The pyridine extractions of coals were carried out by using excess amount of pyridine under an ultrasonic irradiation. In order to remove trace amounts of pyridine in the pyridine-extract it was washed by THF/H_2O(30vol%) solution saturated by CO_2, then dried at 110°C overnight , and stored under a dry nitrogen atmosphere.

Volumetric measurements of hydrogen gas evolved through the reactions were carried out by using a gas-buret under hydrogen atmosphere at 25°C. A typical procedure was as follows: Pyridine-extract(0.1g) was throughly groung by using an agate mortar in a dry-box, and placed into a 30ml reaction vessel. Dry pyridine(5ml) was added and the mixture stirred for 30-60minutes prior to start the reaction with excess amount of pyridine/tetra-n-butylammonium borohydride solution. The volume of hydrogen gas generated from the reaction mixture was measured by a gas-buret.

RESULTS AND DISCUSSION

1. Reactivities of various borohydrides toward hydroxyl fuctionalities

In order to evaluate the chemical reactivity of borohydrides, 1-naphthol was chosen as a standard model compound of a phenolic hydroxyl functionality. In Figure 1, the effects of the counter cations of borohydrides are demonstrated. This Figure shows the rate of completion of the reaction vs. reaction time in minute, which were calculated from the volume of the hydrogen gas evolved. Very interestingly, a lithium borohydride reacted very rapidely(completed within 5 minutes under these reaction conditions), compared to the others which were finaly complete only after a prolonged reaction time. Among the experimental data shown in this Figure, it is also quite interesting to note that tetra-n-butylammmonium borohydride reacted with 1-naphthol slowly and stoichiometrically, since the affinity of these types of tetra-alkyl ammmounium compunds for the macromolecular network structure of coals had been well-known to be quite high, i.e., Liotta Methylation(6). There will be a good chance to distinguish kinetically between a phenolic hydroxyl functionality and more stronger hydroxyl functionalities like a carboxylic acid in a solid coal.

2. Reactions of lithium borohydride with various hydroxyl model compounds

The reactivities of various hydroxyl fuctionalities toward lithium borohydride were examined by using model compounds, such as a water, benzyl alcohol, 1-naphthol, catechol and benzoic acid. Figure 2 summerizes the results.

Very interestingly, the reactions with carboxylic acid(benzoic acid) and phenolic compounds(1-naphthol and catechol) proceeded significantly faster than those of others(benzyl alcohol and water), which means that the amount of hydrogen gas evolution within 60 minutes under this reaction condition represents the amount of both carboxylic acid and phenolic hydroxyl functionalities.

3. Reactions of tetra-n-butylammonium borohydride with various hydroxyl model compounds

Figure 3 shows the results obtained from the experiments to examine the reactivities of various model compounds toward tetra-*n*-butylammonium borohydride.

Compared to the previous experiments with lithium borohydride, the reaction rate of benzoic acid was significant. Most of the hydrogen gas evolution at the ininitial stage of the reaction is considered to come from the reaction with a carboxylic acid functionality. Even if it was a mixture of those, we can obtain reasonable analytical values of the acid functionality by a treatment of an extraporation of the curve in the Figure.

4. Quantitative determination of carboxylic acid and phenolic hydroxyl functionalities in the mixture of various hydroxyl model compounds

Coal is believed to contain various hydroxyl functionalities, such as a water, alcoholic, phenolic and carboxylic hydroxyl functionalities. Based on the results described above, we have tried to evaluate the proposed method, "Metal hydride method" using a mixture of the model compound which was prepared with an equivalent amount of the functionalities. Figure 4 exhibits the hydrogen gas evolution from reaction mixtures for both the case of the lithium salt and tetra-n-butyl ammmonium salts. The data shown in this Figure seem to be consistent. The equiliblium value of the reaction(hydrogen gas evolution) with lithium salt must represent the sum of carboxylic acid and phenolic hydroxyl functionalities, meanwhile in the case of tetra-n-butylammmonium salt the extraporated value must be the amount of carboxylic acid functionality. Obviously, the data shown in this Figure seems to be consistent.

5. Quantitative determination of carboxylic acid and phenolic hydroxyl functionalities in the pyridine-extract of coal

In order to minimize the complications of the accessibility of the borohydride molecule to the active sites buried into the macromolecular network structure of coal and inorganic components in coal, we have started the quantitative determination of these functionalities by using pyridine-extract which gives us a homogenenous reaction system. In Figure 5, a typical measurement is demonstrated, in which Illinois No.6 coal was used. Although the rate of the hydrogen evolution seems to be slow compared to those of the model compounds, the pattern was quite similar. The calculated values of the contents of carboxylic acid and phenolic hydroxyl functionalities from the Figure 5 were 0.82 mmol/g amd 2.03 mmol/g which corresponded to 8 units/660-carbon atom and 24 units/660-carbon atom. Although we have no reason to believe that the content of these functionalities in the pyridine-extract is exactly same as the raw coal, it is quite interesting that the content of phenolic hydroxyl functionality was almost equal to the number(25 units/660-carbon atom) of phenolic hydroxyl functionality described in the Shinn Model(7) of Illinois No.6 coal. But there was 8 fold differences in the carboxylic acid functionality(1 unit/ 660 carbon atom in Shinn Model vs. 8 units/660 carbon atom by present work).

Table 1 summarizes the analytical data obtained by this new method for the pyridine-extracts of different rank of coals. The coal-rank dependency of each functionalities appearing in this Table seem to be unusual, based on our previous understanding. The carboxylic acid functionality(which had been believed to be so reactive that it would not survive metamorphism and be detectable in higher ranks of coal) seems to exist significantly in a wide range of coals. On the other hand, the phenolic hydroxyl functionality in coal is reasonably stable over the coal-rank range used in this study. The contradictions on these data revealed here are thought to prove very serious and important problems in reviewing our understanding of the physical and chemical properties of coals.

The accumulation of the experimental data concerning the content of these functionalities in the raw coals is now underway in our laboratory. We are now developing the method for the detemination of an alcoholic hydroxyl functionality in coal.

CONCLUSION

Based on the experimental results of solvent swelling of coal, a reliable chemical determination method both carboxylic acid and phenolic hydroxyl functionalities has been developed by using the reactions of borohydride salts in pyridine solvent. Advantages of this method are considered to be (a) better accessibility of chemical reagent into the macromolecular network of coal (in pyridine solvent), (b) quantitative and direct(one-step) reaction, and (c) accuracy and easiness(volumetric determination of hydrogen gas).

AKNOWLEDGEMENTS

A part of this research was supported by the grant from the Nihon Shigaku Shinkoh Zaidan through The Institute of Environmental Science of Kinki University during 1990-1992.

REFERENCES
(1) Gorbaty, M.L., George, G.N., and Kelemen, S.R., Fuel, **69**, 1065(1990)
(2) Burchill, P., and Welch, L.S., Fuel, 68, 100(1989)
(3) Blom, L., Edelhausen, L., and van Krevelen, D.W., Fuel, **36**, 135(1957)
(4) Aida, T., Fuku, K., Fujii, M., Yoshihara, M., Maeshima, T., and Squires, T.G., Energy & Fuels , **5**, 79(1991)
(5) T. Aida, submitted to Fuel
(6) Liotta, R., Rose, K., and Hippo, E., J. Org. Chem., **46**, 277(1981)
(7) Shinn, J.H., Fuel, **63**, 1187(1984)

Table 1. Contents of carboxylic acid and phenolic hydroxyl functionalities in pyridine-extract of coals

Coal	Carbon content(%,dmmf)		Content of functionality(mmol/g)	
	Raw coal	Pyridine-extract	-COOH	Ar-OH
Hanna No.80	73.1	77.4	0.96	2.04
Adaville No.11	76.6	76.0	1.02	2.08
Illinois No.6	80.6	79.7	0.82	2.03
West Kentucky No.9	82.5	79.9	0.65	1.45
Pittsburgh No.8	85.1	77.8	0.52	1.58

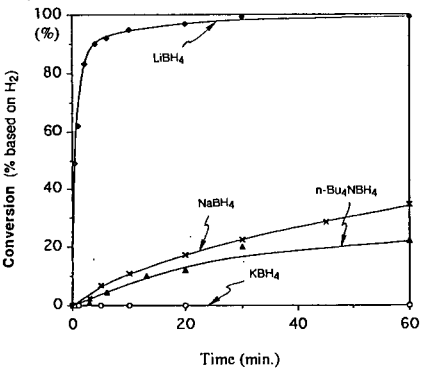

Figure 1. Reactions of 1-naphthol with various borohydrides

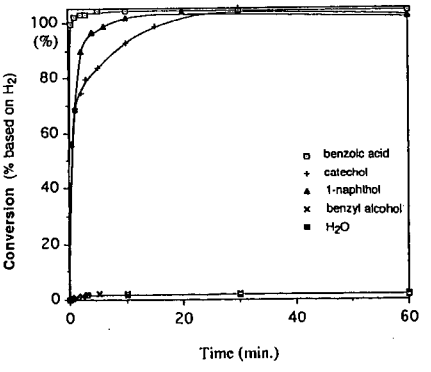

Figure 2. Reactions of $LiBH_4$ with various model compounds

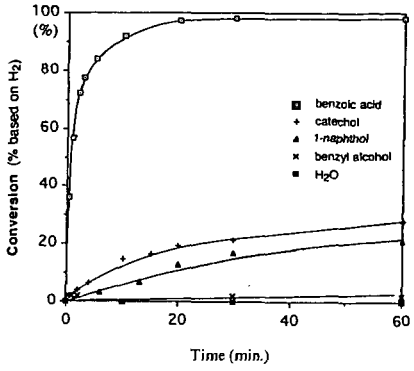

Figure 3. Reactions of n-Bu_4NBH_4 with various model compounds

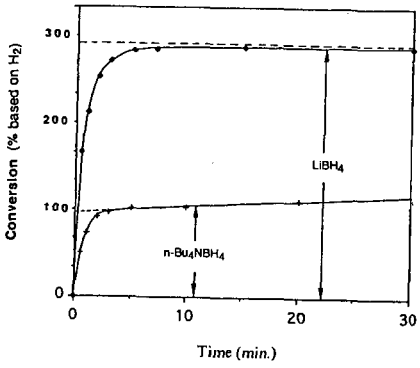

Figure 4. Reactions of $LiBH_4$ and n-Bu_4NBH_4 with model compounds mixture
(benzoic acid / catechol /1-naphthol /benzyl alcohol / H_2O = 1 / 0.5 / 1 / 1 / 1 mol.)

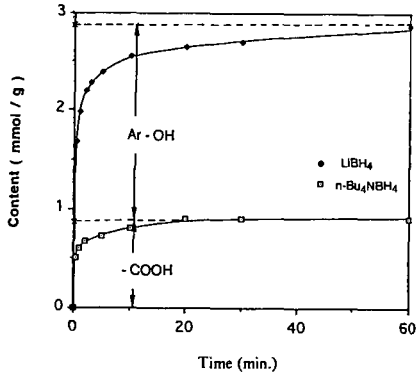

Figure 5. Determination of carboxylic acid and phenolic hydroxy functionalities in pyridine-extract of Illinois No. 6 coal

INTERMOLECULAR INTERACTIONS FOR HYDROCARBONS ON WYODAK COAL

Amy S. Glass and Damon S. Stevenson
Department of Chemistry
University of Dayton
Dayton, OH 45469-2357

(Keywords: Wyodak coal, ionic forces, coal surface interactions)

INTRODUCTION

Low rank coals are abundant in the U.S.[1] Although their calorific values, mineral matter contents, and coking properties make them less desirable than higher rank coals in some industrial applications, low rank coals are used as feedstocks in coal liquefaction and are coprocessed with higher rank coals for other applications.[2-5] The desire to use these coal resources more effectively would be aided by an understanding of the intermolecular and surface interactions at mineral-organic and organic-organic coal interfaces.

Studies of intermolecular forces in low rank coals have concentrated on the coals' ionic properties.[6-10] Schafer quantified the ion-exchange groups in various low rank coals.[6] From swelling studies Nishioka concluded that ionic forces play a role in determining the macromolecular structures of low rank coals.[7] Ahsan et al. studied Wyodak coal's interactions with organic acids before and after the coal was demineralized by citric acid washing (CAW).[8] They found that interactions with aromatic acids increased while those with aliphatic acids decreased as a result of demineralization. From pH studies of coal slurries Vorres found that a range of different ion-exchange sites exist in Wyodak coal.[9] Martinez-Tarazona et al. showed that low rank coals possess ion-exchange sites in the form of both organic (carboxylate and phenolate) and inorganic (clay) components.[10]

In the present work, inverse gas chromatography (IGC) has been used to quantify the intermolecular forces of Wyodak subbituminous coal from the Argonne Premium Coal Sample Bank. It has been found that saturated and unsaturated hydrocarbons experience different intermolecular forces at the coal surface and that these molecules can be used to probe both specific and nonspecific forces in Wyodak coal.

EXPERIMENTAL

The procedure for IGC of coal surfaces has been described previously.[11] About 3g of coal of 40/60 mesh fraction is packed into a 1/8 inch O.D. stainless steel tube ~1.5m in length. GC columns are conditioned at the highest temperatures at which IGC experiments will be performed (150°C, 200°C, or 250°C). Experiments involve obtaining at least 5 peaks every 5-10 degrees over a column temperature range of at least 30 degrees.

Wyodak coal from the Argonne Premium Coal Sample Bank was used as the stationary phase.[12] The coal was extracted in tetrahydrofuran (THF) in a Soxhlet extractor for several days. Citric acid washing and HF-HCl demineralization procedures were those used previously.[13] The alkylation procedure was that of Liotta et al.[14] Adsorbate liquids and reagents were obtained from Aldrich at the highest purities available and used without additional purification. Adsorbate gases were obtained from Aldrich or from Matheson at purities of at least 99.99%.

RESULTS AND DISCUSSION

Figure 1 shows isosteric adsorption heats, q_{st}, for hydrocarbons interacting with Wyodak coal which has been heated to 150°C or 200°C.[15] The data are plotted vs. molecular polarizability of the adsorbates, α'. The molecular polarizability is related to the electron distribution of the adsorbate molecule.[16] For a given class of adsorbate molecules (eg., n-alkanes, chloroalkanes, 1-alkenes), α' increases linearly with increasing adsorbate size or increasing number of carbon atoms in the adsorbate molecule.[16]

The lower plot in Figure 1 shows data for n-alkanes on Wyodak coal. These types of adsorbates can interact with the coal by nonspecific van der Waals dispersion forces only. The adsorption heats for n-alkanes increase linearly with increasing adsorbate polarizability as expected for van der Waals interactions. The slope of the plot for n-alkanes in Figure 1 is a measure of the increase in dispersive van der Waals force with increasing adsorbate size.[16] This information (the slope of the plot) is analogous to a dispersive surface tension, γ_s^d, which gives the strength of the van der Waals interaction normalized to the adsorbate area at a surface.[17] The slope of the plot for n-alkanes in Figure 1 translates into a dispersive surface tension of 25 mJ/m^2. This is a fairly low dispersive surface tension, demonstrating that Wyodak coal presents a low energy surface to saturated hydrocarbons, similar to those found for hydrocarbon oils and bitumens.[18,19]

The two upper plots in Figure 1 show data for 1-alkenes on Wyodak coal that has been heated at 150°C or at 200°C. Comparison of the upper plot, for the 150°C-heated coal, with the plot for n-alkanes demonstrates that alkenes have ~2-4 kcal/mol stronger interaction with the coal than n-alkanes. This difference is most likely the result of a specific interaction between alkenes and the coal, discussed below. The steeper slope of the plots for alkenes (upper plots) compared to the slope for alkanes (lower plot) reflects the stronger nonspecific van der Waals force experienced by alkenes at this surface.[16] On oxidized carbon surfaces which contain polar functional groups, alkenes have more exothermic adsorption enthalpies than alkanes.[20] The stronger nonspecific interactions of alkenes on Wyodak coal likely involve interactions with polar groups on the coal.

As seen by comparing the two upper plots in Figure 1, heating the coal to 200°C causes a constant decrease in the adsorption heat exothermicities for 1-alkenes. The constant decrease in exothermicities of the alkenes' adsorption heats after heating the coal to 200°C suggests that a *specific* interaction between alkenes and the coal has been lost as a result of heating. Heating has caused the adsorption heats for all 1-alkenes to decrease by the same amount, ~1.2 kcal/mol, while it has not changed the slope of the alkenes plot. A specific alkene-coal interaction, as opposed to a nonspecific van der Waals interaction, would be characterized by a constant change in adsorption heat for a particular adsorbate functional group-coal interaction. All of the 1-alkenes in Figure 1 possess a single double bond. Loss of a specific interaction between the double bond of alkenes with the coal surface would result in a constant decrease in the adsorption heat exothermicity. It is likely that a specific interaction is occurring between the double bond of the alkenes and ionic or polar groups on the coal surface. An interaction between the double bond of the hydrocarbon with a positive charge at a surface, a so-called "cation-π" interaction, could be responsible for the specific interactions between unsaturated hydrocarbons and Wyodak coal.[16] Cation-π interactions occur in biological systems and at the surfaces of inorganic solids such as clays and silica.[16,21] When the coal is demineralized by CAW or HF-HCl treatment, the same decrease in adsorption heat exothermicities (~1.2 kcal/mol; data not shown) occurs.[15] This result provides evidence that removing ion-exchangeable cations from Wyodak coal results in the loss of a specific cation-π interaction which involves ion-exchange cations on the coal surface and the unsaturated bond of the hydrocarbon adsorbate.

Figure 2 shows data for n-alkanes and 1-alkenes interacting with the surface of Wyodak coal that has been heated at 250°C. It is seen that heating to 250°C results in the same plot of adsorption heat vs. polarizability for n-alkanes and 1-alkenes. Unlike the case for the 150°C-heated coal (Figure 1) where the different slopes of the plots show that alkanes and alkenes have different nonspecific interactions with the coal, the result in Figure 2 says that heating to 250°C gives the same nonspecific interaction for both types of hydrocarbons on Wyodak coal. Furthermore, a comparison of the data for alkenes on 200°C-heated Wyodak coal

(Figure 1) with data for alkenes on 250°C-heated Wyodak coal (Figure 2) shows that the adsorption heats for alkenes are similar on these two heated coals. These two heated coals have lost their specific interactions with the coal; therefore, this result says that the nonspecific component of the adsorption heat for alkenes is similar for 200°C-heated and 250°C-heated coals. On the other hand, the nonspecific component of the adsorption heat for alkanes has increased in exothermicity as a result of heating the coal to 250°C. The same result (same plot for alkanes and alkenes) is obtained by extracting or alkyating the coal (results not shown).[15] The slope of the plot in Figure 2 corresponds to a dispersive surface tension of ~50 mJ/m². This value is similar to dispersive surface tensions found for flat carbonaceous surfaces.[22] It was shown previously that extracting Illinois No. 6 coal or heating to 250°C gave a dispersive surface tension of ~50 mJ/m² for that coal as well.[23] These treatments cause changes in the concentration and/or polarizabilities of atoms at the coal surface.[16,23] Changes in bulk coal properties have been reported to result from these treatments and it is possible that changes in the bulk are reflected as changes in the coal's dispersive surface tension.[24]

CONCLUSION

In conclusion, IGC data show that three types of forces are experienced by hydrocarbons at the Wyodak coal surface: a nonspecific force experienced by n-alkanes, a nonspecific force experienced by 1-alkenes, and a specific force experienced by 1-alkenes. The nonspecific force felt by n-alkanes gives a dispersive surface tension of ~25 mJ/m² for this coal. The nonspecific force felt by 1-alkenes is stronger and likely involves interactions with polar groups at the coal surface. The specific interaction between alkenes and Wyodak coal is most likely due to an interaction of the unsaturated bond with ionic groups at the coal surface; i.e., a cation-π interaction. Heating the coal to 250°C increases the interactions with n-alkanes so that both types of hydrocarbons, alkanes and alkenes, have the same nonspecific interaction with the 250°C-heated coal. The nonspecific interaction with the 250°C-heated coal gives a dispersive surface tension of ~50 mJ/m².

REFERENCES

1. Van Krevelen, D. W. *Coal*, 3rd. ed.; Elsevier: New York, 1993; Chapter 1.
2. Van Krevelen, D. W. *Coal*, 3rd. ed.; Elsevier: New York, 1993; Chapter 24.
3. Neavel, R. C. In *Coal Structure*, ACS Adv. Chem. Series No. 192; Gorbaty, M. L.; Ouchi, K., Eds.; ACS: Washington, DC, 1981; Chapter 1.
4. Neavel, R. C. In *Coal Science*, vol. 1; Gorbaty, M. L.; Larsen, J. W.; Wender, I., Eds.; Academic: New York, 1982; pp. 1-19.
5. Berkowitz, N. *An Introduction to Coal Technology*; Academic: New York, 1979; Chapter 13.
6. Schafer, H. N. S. *Fuel* 1970, *49*, 271-280.
7. Nishioka, M. *Fuel* 1993, *72*, 1725-1731.
8. Ahsan, T.; Wu, J. H.; Arnett, E. M. *Fuel* 1994, *73*, 417-422.
9. Vorres, K. S. *Prepr. Pap.-Am. Chem. Soc. Div. Fuel Chem.* 1993, *38*, 1045-1057.
10. Martinez-Tarazona, M. R.; Martinez-Alonso, A.; Tascon, J. M. D. *Fuel* 1990, *69*, 362-367.
11. Glass, A. S.; Larsen, J. W. *Energy Fuels* 1993, *7*, 994-1000.
12. Vorres, K. S. *Energy Fuels* 1990, *4*, 420-426.
13. Silbernagel, B. G.; Gebhard, L. A.; Flowers, R. A.; Larsen, J. W. *Energy Fuels* 1991, *5*, 561-568.
14. Liotta, R.; Rose, K.; Hippo, E. *J. Org. Chem.* 1981, *46*, 277-283.
15. Glass, A. S.; Stevenson, D. S. *Energy Fuels*, submitted.
16. Kiselev, A. V.; Yashin, Y. I. *Gas-Adsorption Chromatography*; Plenum: New York, 1969; Chapter 2.
17. Doris, G. M.; Gray, D. G. *J. Coll. Int. Sci.* 1980, *77*, 352-362.
18. Zisman, W. A. In *Contact Angle, Wettability, and Adhesion*,

ACS Adv. Chem. Ser. No. 43; ACS: Washington, DC, 1964; Chapter 1.
19. Drelich, J.; Bukka, K.; Miller, J. D.; Hanson, F. V. *Energy Fuels* 1994, *8*, 700-704.
20. Elkington, P. A.; Curthoys, G. *J. Phys. Chem.* 1969, *73*, 2321-2326.
21. Dougherty, D. A.; Kearney, P. C.; Mizoue, L. S.; Kumpf, R. A.; Forman, J. E.; McCurdy, A. In *Computational Approaches in Supramolecular Chemistry*, Wipff, G., Ed.; Kluwer: New York, 1994; pp. 301-309.
22. Lopez-Garzon, F. J.; Pyda, M.; Domingo-Garcia, M. *Langmuir* 1993, *9*, 531-536.
23. Glass, A. S.; Larsen, J. W. *Energy Fuels* 1994, *8*, 629-636.
24. Brenner, D. *Fuel* 1984, *63*, 1324-1328.

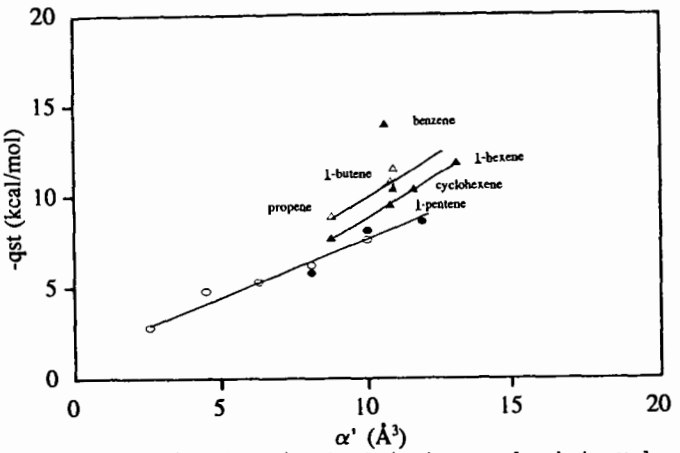

Figure 1. Isosteric adorption heat (q_{st}) vs. adsorbate volume molecular polarizability (α') for n-alkanes, alkenes, and benzene on Wyodak coal heated in helium at 150°C and at 200°C.[15] ○=n-alkanes (methane, ethane, propane, n-butane, and n-pentane) on 150°C-heated coal; ●=n-alkanes (n-butane, n-pentane, n-hexane) on 200°C-heated coal; △=1-alkenes on 150°C-heated coal; ▲=alkenes and benzene on 200°C-heated coal.

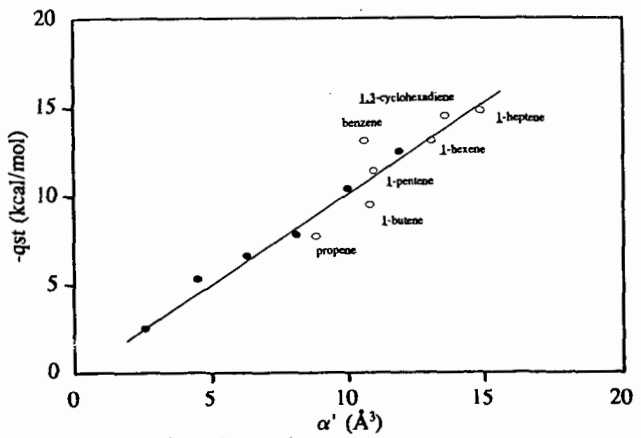

Figure 2. Isosteric adsorption heat (q_{st}) vs. molecular volume polarizability (α') for alkanes and unsaturated hydrocarbons on Wyodak coal heated to 250°C. ●=n-alkanes in order of increasing exothermicity: ethane, propane, n-butane, n-pentane, n-hexane, and n-heptane; ○=alkenes and aromatics on Wyodak coal heated at 250°C.

CHEMICAL STRUCTURE OF COAL TAR DURING DEVOLATILIZATION

T. H. Fletcher[1], M. Watt[1], S. Bai[2], M. S. Solum[2], and R. J. Pugmire[3]

[1]Department of Chemical Engineering Brigham Young University, Provo, Utah 84602
Departments of Chemistry[2] and Chemical and Fuels Engineering[3], University of Utah, Salt Lake City, Utah 84112

Keywords: coal, pyrolysis, ^{13}C NMR

Introduction

Enormous progress has been made in coal pyrolysis research during the last two decades. Models of coal devolatilization have progressed from simple rate expressions based on total mass release[1, 2] to empirical relationships based on the elemental composition of the parent coal[3] to models that attempt to describe the macromolecular network of the coal.[4-6] In the last several years, advancements in chemical analysis techniques have allowed quantitative investigations of the chemical structure of both coal and its pyrolysis products, including the nature of the resulting char. A prominent research goal is to accurately predict the rates, yields, and products of devolatilization from measurements of the parent coal structure. The prediction of nitrogen species evolved during devolatilization is of current interest. These goals necessitate modeling the reaction processes on the molecular scale, with activation energies that relate to chemical bond breaking rather than to the mass of products released from the coal. Solid-state ^{13}C NMR spectroscopy has proven particularly useful in obtaining average values of chemical structure features of coal and char, while liquid phase ^{1}H NMR spectroscopy has been used to determine some of the chemical features of coal tar.[7-10] Pyridine extract residues from coal and partially-pyrolyzed coal chars have also been analyzed by solid-state ^{13}C NMR spectroscopy, and the extracts have been analyzed by ^{1}H NMR spectroscopy.[11]

Several current devolatilization models use some kind of network approach to describe the parent coal structure and subsequent devolatilization behavior.[4-6] Coal is modeled as an array of aromatic clusters connected by labile bridges. Kinetic expressions are postulated for the rate of bridge scission, and statistical representations are used to determine the number of clusters liberated from the coal matrix as a function of the number of bridges cleaved. The vapor pressure of liberated clusters are calculated and used to determine yields of tar versus metaplast. Crosslinking reactions eventually connect the remaining metaplast to the char matrix. Such models require knowledge of the average size of the aromatic clusters in the coal, the number of attachments (bridges and side chains) per cluster, the ratio of bridges to side chains, and the average size of the bridges or side chains. Several reviews of these models have been published.[12, 13] All three of these models use the solid-state ^{13}C NMR data to some extent to guide selection of coal-dependent input parameters to describe the coal matrix. One model demonstrated success in using the solid-state ^{13}C NMR data directly as the only coal-dependent structural input parameters.[6] One of the common assumptions in these models is that the aromatic clusters are not broken during the pyrolysis process, and hence the bridge breaking rate largely controls the devolatilization rate. Therefore, the average number of aromatic carbons per cluster in the coal is equal to that in the char and in the tar.

In a recent paper, Niksa[14] postulated that nitrogen evolution during pyrolysis could be modeled assuming that the mass of nitrogen per aromatic cluster in the coal tar was equal to that in the parent coal. A theoretical analysis was performed using tar data reported in the literature to determine the validity of Niksa's assumption. Elemental analyses of tar samples were reported by Freihaut, et al.[15, 16] and by Chen.[17] It has been shown that the carbon aromaticity of the pristine tar (as estimated from ^{1}H NMR spectroscopy) is similar to that of the parent coal for both lignites and bituminous coals .[8, 9] Assuming that the number of aromatic carbons per cluster in the tar is equal to that in the coal, the mass of nitrogen per cluster $M^{N}_{cluster}$ can be calculated as follows:

$$M^{N}_{cluster} = \frac{x_N}{x_C} MW_C \frac{C_{cl}}{f_{a'}} = MW_{cl}\, x_N \qquad (1)$$

where x_N = wt% N in coal (daf), x_C = wt% C in coal (daf), MW_C = molecular weight of carbon, C_{cl} = # of aromatic carbon per cluster, $f_{a'}$ = carbon aromaticity, and MW_{cl} = molecular weight per aromatic cluster. Results of this analysis are shown in Fig. 1, indicating that the mass of nitrogen per cluster in the tars do not equal the mass of nitrogen per cluster in the parent coal. The results shown in Fig. 1 are pieced together from data reported in several experiments, which may have caused errors. It may also be possible that (a) the number of aromatic clusters in the tar does not equal that in the coal, or that (b) the carbon aromaticity of the tar does not equal that of the coal. This paper describes experiments and analyses of *one* set of coal tars and chars. This is the first time that this high resolution ^{13}C NMR spectroscopy techniquw has been applied to coal tars, and data regarding the number of aromatic carbons per cluster and carbon aromaticities in coal tars are presented.

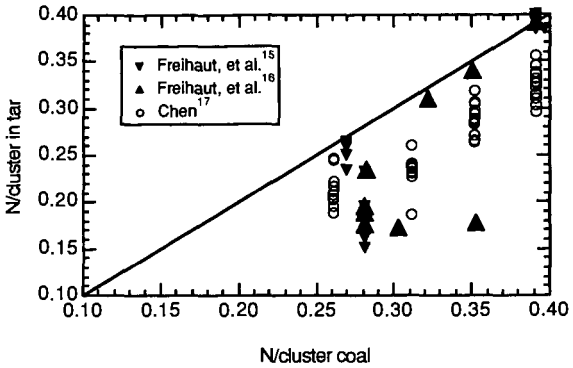

Figure 1. Comparison of the calculated nitrogen per cluster in the tar and in the parent coal.

Experimental Apparatus

Samples of tar and char were produced at atmospheric pressure in the High Pressure Controlled-Profile (HPCP) drop tube reactor.[18] The HPCP drop tube furnace is a laminar flow furnace with a computer-controlled wall temperature profile to create isothermal conditions for reactivity tests. Particles are fed with the primary gas through a water-cooled injector, which can be moved in order to vary particle residence times. The secondary gas flows into a preheater prior to entering the reactor. Wall heaters control the temperature profile in the drop tube furnace. The collection probe collects the entire mass flow and quenches all particle reactions. The collection probe is water-cooled with gas quench jets in the probe tip. A permeable liner inside the main probe tube allows quench gas to be injected radially along the length of the probe to reduce particle and tar deposition. A virtual impactor follows the collection probe to aerodynamically separate the gases from the heavier particles. A cyclone separates char particles from tars and aerosols, and the tars and aerosols are eventually collected on filters.

Table I
Coal Properties

Coal	PSOC ID	Rank	%C (daf)	%H (daf)	%N (daf)	%Ash (dry)
Illinois #6 (IL)	1493D	hvc bituminous	77	5.0	1.5	15.1
Blue #1 (NM)	1445D	sub-bituminous	77	5.7	1.3	3.6
Pittsburgh #8 (PA)	1451D	hva bituminous	84	5.5	1.7	4.1

The HPCP was used to pyrolyze coal samples in 100% nitrogen, at moderate gas temperatures of 930 K, and at residence times of 230 ms and 420 ms. Relatively low temperatures were used in these experiments to minimize possible secondary reactions in the evolved coal tars. Properties of the three coals examined are shown in Table 1. The 63-75 μm size fraction was used in all of these experiments, resulting in heating rates of approximately 10^4 K/s. The "D" on the Penn State coal identification number signifies coals from a suite selected by the DOE Pittsburgh Energy Technology Center's Direct Utilization/AR&TD program. These coals have been well characterized and studied by many other researchers, including those referenced in Figure 1.

^{13}C NMR Analysis

Solid state ^{13}C NMR techniques (CP/MAS and dipolar dephasing) have been used to determine the chemical structure features of coals and coal chars.[7, 19] In addition to carbon aromaticity ($f_{a'}$), the distinction between aromatic carbons with and without attachments (such as hydrogen, carbon, or oxygen) is measured. The specification of the number of aromatic carbons per cluster (C_{cl})[7] provides the basis for the determination of many interesting chemical structure features. Probably one of the most useful quantities is the number of attachments per aromatic cluster, referred to as the coordination number (σ+1).

A high resolution ^{13}C NMR technique was recently developed and applied to model compounds, mixtures, and coal-derived liquid samples.[20] This technique uses spin-lattice relaxation to differentiate protonated from nonprotonated carbons, based on relaxation differences

arising from direct CH dipolar interactions. Average aromatic ring sizes and other lattice parameters are estimated using the procedures used for solid-state ^{13}C NMR.[7, 19]

Tar samples were dissolved in deuterated methylene chloride (CD_2Cl_2) and then filtered. A significant amount of residue was obtained for each tar. This tar residue was subsequently analyzed using the CP/MAS and dipolar dephasing solid-state ^{13}C NMR technique in the same fashion as that used for coal char.

Results and Discussion

Tars collected at 230 ms were analyzed using the ^{13}C NMR spin-lattice relaxation technique; data are presented in Tables 2 and 3. Data for char collected at 420 ms are also presented in Table 2. Analysis of the dissolved tar from the Illinois #6 coal is in progress. As seen in Table 3, 12 to 42% of the tar sample collected was deposited on the filter as residue. Also, lower amounts of tar were collected for the lower rank Illinois #6 and Blue #1 coals than for the hva bituminous Pitt #8 coal. The tar yields seem somewhat lower than reported in the literature, indicating that some tar may have deposited in the sampling apparatus. Other investigators have corrected their measured yields for estimated deposition in the sampling apparatus[17]; this correction will be performed for these data in the future.

Table 2
^{13}C NMR Analysis of Coals, Tars, and Chars[a]

Coal	Sample	f_a	f_a^C	$f_{a'}$	f_a^H	f_a^N	f_a^P	f_a^S	f_a^B	f_{al}	f_{al}^H	f_{al}^*	f_{al}^O
Pitt #8	coal	65	3	62	23	39	5	16	18	35	24	11	7
Pitt #8	dis. tar	69	2	67	38	29	5	15	9	31	2	11	na
Pitt #8	tar res.	83	3	80	34	46	8	18	2	17	1	7	2
Pitt #8	char	81	5	76	24	52	6	18	28	19	11	8	6
Blue #1	coal	6	5	55	19	36	8	13	15	4	29	11	7
Blue #1	dis. tar	63	7	56	27	29	8	16	5	37	27	1	na
Blue #1	tar res.	72	6	66	24	42	9	15	18	28	17	11	12
Blue #1	char	77	5	72	24	48	9	2	19	23	15	8	4
Illinois #6	coal	66	3	63	21	42	7	16	19	34	24	1	8
Illinois #6	tar res.	8	6	74	28	46	8	18	2	2	12	8	3
Illinois #6	char	78	6	72	25	47	8	19	2	22	13	9	4

[a]Percentage carbon (error): f_a = total sp^2-hybridized carbon (±3); $f_{a'}$ = aromatic carbon (±4); f_a^C = carbonyl, $\delta > 165$ ppm (±2); f_a^H = aromatic with proton attachment (±3); f_a^N = nonprotonated aromatic (±3); f_a^P = phenolic or phenolic ether, δ = 150-165 ppm (±2); f_a^S = alkylated aromatic δ = 135-150 ppm(±3); f_a^B = aromatic bridgehead (±4); f_{al} = aliphatic carbon (±2); f_{al}^H = CH or CH_2 (±2); f_{al}^* = CH_3 or nonprotonated (±2); f_{al}^O = bonded to oxygen, δ = 50-90 ppm (±2).

Table 3
Derived Properties of Coal, Tar, and Char[b]

Coal	Sample	X_b	C_{cl}	σ+1	P_o	B.L.	S.C.	V (daf)	Tar (daf)	tar resid.
Pitt #8	coal	0.29	14	4.8	0.48	2.3	2.5			
Pitt #8	tar	0.134	8	2.4	0.45	1	1.4	46	22	
Pitt #8	tar res.	0.25	12	3.9	0.73	2.8	1.1	46	22	0.25
Pitt #8	char	0.368	18	5.7	0.67	3.8	1.9	42	19	
Blue #1	coal	0.27	13	5	0.48	2.4	2.6			
Blue #1	tar	0.09	7	3	0.58	1.7	1.3	23	6	
Blue #1	tar res.	0.273	13	4.7	0.54	2.5	2.2	23	6	0.12
Blue #1	char	0.264	13	5.2	0.72	3.7	1.5	29	7	
Illinois #6	coal	0.3	15	5.5	0.52	2.9	2.6			
Illinois #6	tar res.	0.27	13	4.6	0.69	3.2	1.4	32	6	0.42
Illinois #6	char	0.278	13	4.9	0.67	3.3	1.6	35	11	

[b]X_b = fraction of bridgehead carbons, C_{cl} = aromatic carbons per cluster, σ+1 = total attachments per cluster, P_o = fraction of attachments that are bridges, B.L. = bridges and loops per cluster, S.L. = side chains per cluster, V = total volatiles yield, Tar = tar collected on filters (not corrected for tar deposited in the sampling apparatus), tar resid. = fraction of collected tar that did not dissolve in CD_2Cl_2.

It is interesting to compare the NMR data for the tar, tar residue, and char with that of the coal. The carbon aromaticity $f_{a'}$ of the dissolved tar is similar to that of the parent coal, while that of the tar residue is generally higher (and close to that of the char). Perhaps the most interesting result is that the average cluster size of the dissolved tar is 7 to 8 aromatic carbons, which is much lower than the values of 12-18 found in the coal, tar residue, or char. Previous data on coals and

chars[21] also found that the number of aromatic carbons per cluster in coals and chars (ranging from lignite to lv bituminous coals) ranged from 10 to 18. The fact that the aromatic carbons per cluster in the tar residue is higher in the dissolved tar suggests a wide distribution of species with varying molecular weights in the tar.

The number of aromatic carbons per cluster in the tar residue is very similar to that found in the coal and char. The number of attachments per cluster in the dissolved tar is also significantly smaller than in the coal, while $\sigma+1$ in the tar residue is only slightly less than in the coal. The small number of attachments per cluster in the tars is also reflected in the values of bridges and loops per cluster (B.L.) and side chains per cluster (S.C.).

The average values of chemical structure features for the composite tar can be determined from combining the values for the dissolved tar and tar residue, according to the respective weight fraction of tar residue. This would raise the number of aromatic carbons per cluster in the tar to 8 and 9 for the two coals, which is still more than 35% lower than in the parent coal. It has been shown with repeated data sets that the number of aromatic carbons per cluster in the char does not increase substantially during devolatilization.[8-10, 21] The fact that C_{cl} in the tar is lower than in the coal, coupled with the fact that C_{cl} in the char remains constant at the same value as the coal, *can only be explained by ring breakage and not bridge breaking.* It is known that bond energies in aromatic rings are large, but it is suggested that the heteroatoms (largely oxygen and sulfur) in the clusters weaken the stability of the clusters. This is an interesting development, and suggests that the current view of devolatilization, as explained by current devolatilization models, may be in error.

References

1. Anthony, D. B., J. B. Howard, H. C. Hottel and H. P. Meissner *15th Symposium (International) on Combustion*; The Combustion Institute, Pittsburgh, PA: **1974**; pp 1303-1317.
2. Kobayashi, H., J. B. Howard and A. F. Sarofim *16th Symposium (International) on Combustion*; The Combustion Institute, Pittsburgh, PA: **1976**; pp 411-425.
3. Ko, G. H., D. M. Sanchez, W. A. Peters and J. B. Howard *22nd Symposium (International) on Combustion*; The Combustion Institute, Pittsburgh, PA: **1988**; pp 115-124.
4. Solomon, P. R., D. G. Hamblen, R. M. Carangelo, M. A. Serio and G. V. Deshpande *Energy and Fuels* **1988**, *2*, 405-422.
5. Niksa, S. *Energy and Fuels* **1991**, *5*, 673-683.
6. Fletcher, T. H., A. R. Kerstein, R. J. Pugmire and D. M. Grant *Energy and Fuels* **1992**, *6*, 414.
7. Solum, M. S., R. J. Pugmire and D. M. Grant *Energy and Fuels* **1989**, *3*, 187.
8. Fletcher, T. H., M. S. Solum, D. M. Grant, S. Critchfield and R. J. Pugmire *23rd Symposium (International) on Combustion*; The Combustion Institute, Pittsburgh, PA: **1990**; pp 1231.
9. Pugmire, R. J., M. S. Solum, D. M. Grant, S. Critchfield and T. H. Fletcher *Fuel* **1991**, *70*, 414.
10. Fletcher, T. H., M. S. Solum, D. M. Grant and R. J. Pugmire *Energy and Fuels* **1992**, *6*, 643-650.
11. Fletcher, T. H., S. Bai, R. J. Pugmire, M. S. Solum, S. Wood and D. M. Grant *Energy and Fuels* **1993**, *7*, 734-742.
12. Solomon, P. R. and T. H. Fletcher The Combustion Institute, Pittsburgh, PA: **1990**; pp 463.
13. Smith, K. L., L. D. Smoot, T. H. Fletcher and R. J. Pugmire *The Structure and Reaction Processes of Coal*; Plenum: New York, **1994**.
14. Niksa, S. *Energy and Fuels* **1995**, *9*, 467-478.
15. Freihaut, J. D., W. M. Proscia and D. J. Seery *Energy and Fuels* **1989**, *3*, 692-703.
16. Freihaut, J. D., W. Proscia, N. Knight, A. Vranos, H. Kollick and K. Wicks "Combustion Properties of Micronized Coal for High Intensity Combustion Applications," Final Report for DOE/PETC Contract DE-AC22-85PC80263, **1989**.
17. Chen, J. C. "Effect of Secondary Reactions on Product Distribution and Nitrogen Evolution from Rapid Coal Pyrolysis," Stanford University, HTGL Report No. T-280, **1991**.
18. Monson, C. R. and G. K. Germane *Energy and Fuels* **1993**, *7*, 928-936.
19. Orendt, A. M., M. S. Solum, N. K. Sethi, R. J. Pugmire and D. M. Grant *Advances in Coal Spectroscopy*; H. L. C. Meuzelaar, Ed.; Plenum Press: New York, **1992**; pp 215-254.
20. Bai, S., R. J. Pugmire, C. L. Mayne and D. M. Grant *Analytical Chemistry* **1995**, *67*, 3433-3440.
21. Fletcher, T. H. and D. R. Hardesty "Milestone Report for DOE's Pittsburgh Energy Technology Center," contract FWP 0709, Sandia Report No. SAND92-8209, available NTIS, **1992**.